2022

# Pathfinding Fast Radio Bursts Localizations using Very Long Baseline Interferometry

Pranav Rohit Sanghavi
*West Virginia University*, prs0010@mix.wvu.edu

# PATHFINDING FAST RADIO BURSTS LOCALIZATIONS USING VERY LONG BASELINE INTERFEROMETRY

**by**

**Pranav Sanghavi**

**Dissertation submitted to the**
**Benjamin M. Statler College of Engineering and Mineral Resources**
**at West Virginia University**

**in partial fulfillment of the requirements for the degree of**

**Doctor of Philosophy**
**in**
**Electrical Engineering**

**Kevin Bandura, Ph.D., Committee Chairperson**
**Natalia Schmid, Ph.D.**
**Duncan Lorimer, Ph.D.**
**David Graham, Ph.D.**
**Daryl Reynolds, Ph.D.**

**Lane Department of Computer Science and Electrical Engineering**

**Morgantown, West Virginia**
**2022**

**Keywords: Radio Astronomy, Instrumentation, Fast Radio Bursts, Engineering Pedagogy**

# ABSTRACT

## Pathfinding Fast Radio Bursts Localizations using Very Long Baseline Interferometry

**by Pranav Sanghavi**


Fast radio bursts (FRBs) are millisecond-duration, bright radio transients of extragalactic origin. The Canadian Hydrogen Intensity Mapping Experiment (CHIME) telescope's CHIME/FRB instrument and other radio telescopes across the globe have detected hundreds of FRBs. Their origins are a mystery. Precise localization within the host is critical to distinguish between progenitor models. This can be achieved through Very Long Baseline Interferometry (VLBI). Until now, VLBI localizations have only been carried out in targeted follow-up observations of some repeating sources which comprise a small fraction of the FRBs.

For this work, an interferometric array of 6m dishes was constructed at the Green Bank Observatory as a pathfinder to develop the necessary systems, technology, and techniques to enable VLBI on FRBs. This array called TONE has 8 instrumented dishes and works as a VLBI outrigger for CHIME on a $\sim 3300\,\mathrm{km}$ baseline. This involved construction, commissioning, and integration of the custom analog chains and digital system. TONE is pointed to shadow a portion of the CHIME primary beam at a fixed declination of $22\,\mathrm{deg}$. Upon detection of a single dispersed pulse such as an FRB or a giant pulse from the Crab pulsar, CHIME alerts TONE, triggering a recording of buffered data to disk. In addition to TONE, a single 10-m dish at Algonquin Radio Observatory (ARO10) is set up with a similar infrastructure. Together they form the pathfinders for conducting VLBI for FRBs.

We used these VLBI pathfinders to localize FRB 20210603A at the time of detection. The baseband data from CHIME and TONE are used to synthesize single beams at each telescope. The single-beam data from TONE and data from ARO10 are each cross-correlated with the single beam data from CHIME. We use the Crab pulsar for astrometric calibration and additionally correct for clock errors. The calibrated and corrected cross-correlated data is sampled with a likelihood function of the sky location and ionospheric effects using a Markov Chain Monte Carlo method to estimate the Right Ascension and Declination of the FRB. We localize the burst to SDSS J004105.82+211331.9, an edge-on quiescent lenticular galaxy at redshift z $\approx 0.177$. The localization, dispersion measure, rotation measure (RM), and temporal broadening are consistent with an observed line-of-sight through the host galactic disk, suggesting a progenitor from a population coincident with the host galactic plane.

The development of the TONE telescope has enabled the localization of the FRB within the host. This is a key stepping stone towards constraining the origins and host environments of FRBs.

*I dedicate this dissertation to patience …*

# Acknowledgments

This work is not a solitary endeavor. It has been possible by way of collaboration and constant support from friends and colleagues.

Firstly, I would like to thank Dr. Avinash 'Desh' Deshpande my first mentor in the field of radio astronomy and showing me the door that led me to this opportunity. My doctoral advisor Dr. Kevin Bandura guided me with patience and kindness. He showed me these opportunities and opened several avenues that allowed me to grow into an independent researcher. He has my unending gratitude and respect as we move on to be colleagues. I'd like to thank Dr. Duncan Lorimer, Dr. Maura McLaughlin, and Dr. Natalia Schmid for their countless advice and staunch support. I am also indebted to my advisory and examination committee for lending their time and valuable feedback.

The success and completion of my dissertation project are due to an intense collaboration between my colleagues, friends, Calvin Leung and Dr. Tomas Cassanelli, and me. This work is impossible without either of us. I will never forget that.

The core of this project is the construction of the telescope TONE. I led it but not without a lot of help from several folks. I'd like to thank Dr. John Makous, Howard Chun, Thaddeus Herman, Robert Baker, Michael Stover, John Clarke, Dr. Jose Miguel Jauregui Garcia, and Jacob Hanni. I'm deeply indebted to the scientist and staff at Green Bank Observatory, including but not limited to Dr. Andrew Seymour, Dr. Marty Bloss, Anthony Nucilli, Todd Wright, Emma Yokum, and Carla Beaudet, among others. I'd also like to thank Sue Ann Heatherly and Dr. Glenn Langston for bringing me into the fold of radio astronomy education.

I'd also like to extend my sincerest gratitude to my colleagues in the CHIME/FRB collaboration. I'd reserve a special shout-out to Dr. Jane Kazmerack for assisting me in the nerve-racking process of applying for post-doctoral positions and helping me take the next step after this Ph.D.

The past six years would have gone terribly wrong if it wasn't for my friends Amy Wong-Loomis, David Loomis, Alyssa Knight, and Trisha Russo. KD and Saracha helped me feel at home in a strange town. They were around when things went awry, and helped me find solid ground. They helped me feel joy. I am beyond thankful for them.

Lastly, I'd like to thank my parents for their support and blessings.

— Pranav Sanghavi, 2022

# Contents

# List of Figures

# List of Tables

# Acronyms

**ARO** Algonquin Radio Observatory. 99, 100

**ASKAP** Australian Square Kilometre Array Pathfinder. 17, 27, 28, 30

**CFHT** Canada–France–Hawaii Telescope. 108, 116, 123, 126, 129

**CHIME** Canadian Hydrogen Intensity Mapping Experiment. 17, 19, 30, 39, 100

**CHIME-Pf** Canadian Hydrogen Intensity Mapping Experiment - Pathfinder. 39

**CPU** Central Processing Unit. 91

**DM** Dispersion Measure. 20, 21, 26

**DRAO** Dominion Radio Astrophysical Observatory. 39, 40, 98–100

**FAST** Five-hundred-meter Aperture Spherical Telescope. 29

**FoV** Field of View. 43

**FRB** Fast Radio Burst. 20, 21

**FRBs** Fast Radio Bursts. 20

**FWHM** Full Width Half Maximum. 48, 58

**GBO** Green Bank Observatory. 46, 54, 65, 100, 142

**GBT** Green Bank Telescope. 29

**GPU** Graphic Processing Unit. 91

**HCRO** Har Creek Radio Observatory. 142

**HERA** Hydrogen Epoch Reionization Array. 17

**JVLA** Jansky Very Large Array. 30

**LOFAR** Low Frequency Array. 17, 30

**MWA** Murchison Wide–field Array. 30

**NSF** National Science Foundation. 133

**PAPER** Precision Array for Probing the Epoch of Reionization. 17

**RFoF** Radio Frequency over Fiber. 50–52, 79

**SDR** Software Defined Radio. 137

**SED** Spectral Energy Density. 125, 127, 128, 130

**SEFD** System Equivalent Flux Density. 10, 58

**STARE2** Survey for Transient Astronomical Radio Emission 2. 44

**UTMOST** Molonglo Synthesis Telescope. 30

**VLBI** Very Long Baseline Interferometry. 54, 112

**WSRT** Westerbork Synthesis Radio Telescope. 30

# Nomenclature

## Physics Constants

| | | |
|---|---|---|
| $k_\mathrm{B}$ | Boltzmann constant | $1.38 \times 10^{-23}\,\mathrm{J\,K^{-1}}$ |
| $G$ | Gravitational constant | $6.674\,30 \times 10^{-11}\,\mathrm{m^3\,kg^{-1}\,s^{-2}}$ |
| $c$ | Speed of light in a vacuum | $299\,792\,458\,\mathrm{m\,s^{-1}}$ |
| $h$ | Planck constant | $6.626\,070\,15 \times 10^{-34}\,\mathrm{J\,s}$ |

## Quantities

| | | |
|---|---|---|
| $T$ | Temperature | K |
| $T_\mathrm{b}$ | Brightness Temperature | K |
| $T_\mathrm{a}$ | Antenna Temperature | K |
| $\delta$ | Declination | deg or rad |
| $\alpha$ | Right Ascension | deg or rad |
| $\mathcal{V}$ | Visibilty | |
| $\mathcal{E}, E$ | Electric Field | |
| $\vec{r}, \vec{R}$ | Position Vector | |
| $\hat{s}, \hat{n}$ | Unit direction vectors | |
| $\Omega$ | Solid angle | steradian |
| $\phi$ | phase angle | rad,deg |
| $\nu$ | Frequency of the signal | Hz |

| | | |
|---|---|---|
| $\lambda$ | Wavelength | m |
| $V, v$ | Voltages, (in some upper case instance) cross-relation of electric fields | |
| $f_s$ | Sampling rate | samples per second or Hz |

**Number Sets**

| | |
|---|---|
| $\mathbb{C}$ | Complex numbers |
| $\mathbb{R}$ | Real numbers |

# Preface

Nature inspires awe. The enigma of the night sky has shaped the human story. Early inspiration to human culture was apparent in asterisms coinciding with counts of seasons in frescoed caves of the Palaeolithic eras. Hunter-gatherers and eventually herder-peasants, were required to become experts in the cycle of seasons and the growth periods and location of edible plants and fruits. The sky in these times served as an 'almanac' and a tool of navigation. Human communities grew around agriculture. One can trace the roots of precise astronomical observations with the need for agricultural timing or symbolic icons connected with celestial cycles leading to the development of complex religion and the management of temporal power. This impact of astronomy can be seen in monumental architecture and astronomy being the only 'science' having its own Greek muse, Urania.

The night sky thus inspired generations to build several instruments of increasing sensitivity and complexity. We, as astronomers, have used these instruments to study the night sky over millennia to document its apparent motion, objects, and curiosities such as nebulae and supernovae. Engineering instruments built modern astronomy. It gave us a better understanding of light which opened windows across the electromagnetic spectrum. We have since been acquainted with several phenomena such as quasars, astrophysical masers, pulsars, gamma-ray bursts, and fast radio bursts. Modern astronomy is driven by curiosity and collaboration and is not a solitary pursuit. It spans many disciplines.

This dissertation attempts to append a section to this human story inspired by the heavens by exploring the phenomena of fast radio bursts. They are still inscrutable, at the time of writing.

It forms a sub-field of astronomy, currently only a little over 15 years old, as an exciting avenue for discovery. This work is aimed to demonstrate a landmark scientific detection through new instrumentation and novel algorithms. We used the technique of very long baseline interferometry to localize a fast radio burst to its host galaxy. This is the first measurement of its kind. It uses data from the first and only detection of that particular fast radio burst so far. This is a stepping stone to several such measurements poised to change the field.

## Dissertation Outline

The text is organized to lead the reader to this discovery. Chapters 1 and 2 introduce the observational technique of radio astronomy and the phenomena under study fast radio bursts, respectively. The discussions are succinct but detailed enough to acquaint the reader with the necessary jargon. The core of this work is in Chapters 3 and 4 where we describe and characterise the instrument built (TONE) and the techniques used to enable our detection. Chapter 5 consists of the scientific reporting and discussion of our localization of a fast radio burst (FRB 20210603A). Before concluding in Chapter 7 we discuss the digital signal processing in radio astronomy a research experience for teachers program and its role in facilitating pedagogy based on radio astronomy instrumentation as well as fast radio burst citizen science in Chapter 6. Detailed derivations are appropriately organized into appendices.

# Chapter 1

# Radio Astronomy

Radio astronomy is the branch of astronomy dealing with the lowest frequencies of the electromagnetic spectrum. The part of the spectrum that is not absorbed by our atmosphere makes the radio window (see Figure 1.1). It is generally defined from frequencies of $\mathrm{MHz}$ (limited by the ionosphere) to $\mathrm{THz}$ ($\mathrm{mm}$/sub–$\mathrm{mm}$). Where the upper limit is largely due to the water vapor and the troposphere. Besides these natural limits of the ionosphere and troposphere, human-made sources of interference, i.e., Radio Frequency Interference (RFI) restrict observations in the radio regime.

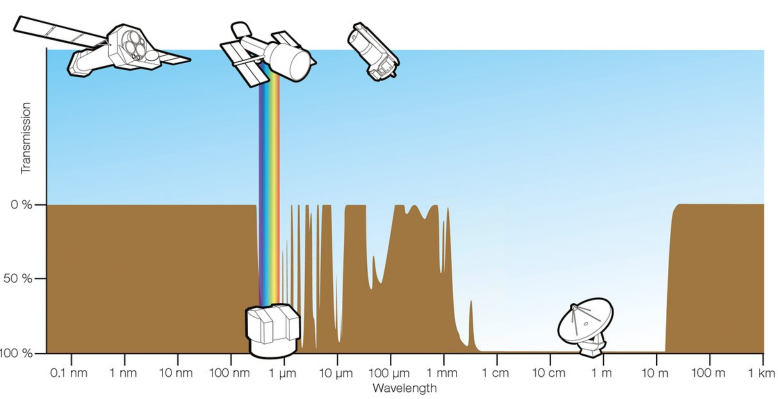


Figure 1.1: **Transparency of the atmosphere:** The brown curve shows the transmission fraction of the atmosphere at the given wavelength to radiation from space. The major windows are at visible wavelengths (marked by the rainbow) and at radio wavelengths from about $\sim 1\,\mathrm{mm}$ to $\sim 10\,\mathrm{m}$. Observations can be done outside the atmospheric windows from space as illustrated by XMM-Newton, Hubble, and the Spitzer Space Telescope in orbit. Credit: ESA/Hubble (F. Granato) https://www.eso.org/public/usa/images/atm_opacity/

## 1.1 The Birth of Radio Astronomy

James Clerk Maxwell published a series of papers in 1861-1862 [1–4] and 1865 [5]. The equations in [5] were cast into the vector representation by Oliver Heaviside in 1884. The vector formulation of these equations of electromagnetism is now known universally as "Maxwell's equations", as first called by Albert Einstein [6]. They predicted that there should be a form of radiation, which came to be known as electromagnetic radiation. Maxwell realized that light was a form of electromagnetic radiation [5]. The equations predicted that electromagnetic radiation could exist with any wavelength. Maxwell's theory was experimentally proven in 1888 when Heinrich Hertz built an apparatus that could transmit and receive electromagnetic waves of about $\sim 5\,\mathrm{m}$ in length. Once Hertz had demonstrated the existence of electromagnetic radiation, the possibility of receiving such radiation from celestial objects especially the sun occurred to many scientists with efforts from Thomas Alva Edison, Nikola Tesla, Sir Oliver Lodge, Charles Nordman, Johannes Wilsing, and Julius Scheiner. Much of these experiments failed due to the lower sensitivity of the instruments of the time and the ionosphere, a radio wave reflecting layer, as suggested by Oliver Heaviside and Arthur Kennelly [8, 9].

Earlier astronomers did not observe radio waves, partly because they were discouraged scientifically. Since the early 1900s, it was known that stars emit as blackbodies in the optical regime. The spectral brightness of a blackbody radiator at an absolute temperature $T$ is given by Planck's law [10, 11], in which the power emitted per unit area per unit frequency per solid angle by a black body,

$$B_\nu(T) = \frac{2h\nu^3}{c^2}\frac{1}{e^{\frac{h\nu}{k_\mathrm{B}\mathrm{T}}} - 1}, \tag{1.1}$$

where $\nu$ is the frequency in Hertz (Hz), c is the speed of light, $h \approx 6.63 \times 10^{-34}\,\mathrm{J\,s}$ is the Planck's constant, and $k_\mathrm{B} \approx 1.38 \times 10^{-23}\,\mathrm{J\,K^{-1}}$ is the Boltzmann constant. In the radio frequencies, $B_\nu$ would be much too low to be detected by the instruments of the time. Additionally, it was discovered the effects of the ionosphere are frequency-dependent.

Despite the discouragement from past efforts, in 1932, Karl Guthe Jansky, a radio engineer working at Bell Telephone Laboratories, serendipitously discovered that the static observed in transatlantic telephone conversations at wavelengths of about 15 m repeated every 24 hours suspecting the source might be the sun [12]. Upon analyzing more data over time he observed the hiss peaked in strength four minutes earlier every day and appeared to come from a fixed point in the sky *"stationary with respect to the stars"*. Thus, this signal must originate from beyond our solar system [13]. By the end of 1933, informed by the shift in the position of the source of this hiss as the year rolled past, Jansky was certain the radio waves arrived from beyond the Solar System. By 1935 he discovered that the *"source of these radiations is located in the stars themselves or in the interstellar matter distributed throughout the Milky Way"* since the antenna received increased energy received when pointed to some part of the Milky way with the most radiation from the center of the Milky Way [14]. Motivated by Jansky's discovery, Grote Reber built a telescope in his backyard that had a parabolic dish reflector and 3 receivers with central frequencies $3300\,\mathrm{MHz}$, $900\,\mathrm{MHz}$ and $160\,\mathrm{MHz}$. Data from the latter receiver confirmed Jansky's discovery of signal from the Milky Way and enabled Reber to plot contour maps of radiation coincident with the Galaxy [15–17].

This marks the beginning of Radio Astronomy. Thorough strides were made in the field after World War II by engineers who were able to build more sensitive radio telescopes establishing a rich discipline for discovery. The possibility of $21\,\mathrm{cm}$ emission from interstellar matter was first suggested as observable by radio telescopes in 1945 [18]. This led to independent experiments by Ewen & Purcell [19] and Muller & Oort [20] detecting the $21\,\mathrm{cm}$ line. Interferometry was introduced to radio astronomy in 1946 by Pawsey *et al.* by using a 'sea interferometer' to resolve sunspots [21]. A sea interferometer measures the interference between the signal from the source and the source signal reflected by the sea. Sea interferometers were used to measure the size of several radio sources such as Cygnus A, Virgo A, Centaurus A, and Taurus A from 1948 to 1949. The first two-element radio interferometer, an analog of the Michelson interferometer, was reported by Ryle & Vonberg. It had a spacing of about $0.5\,\mathrm{km}$, in Cambridge, England. Aperture synthesis [23] improved the performance of radio interferometers. Some seminal discoveries in radio astronomy include quasi-stellar objects, radio galaxies, and cosmic microwave background radiation by Penzias & Wilson [24]. Dame Jocelyn Bell Burnell on reducing the data from Interplanetary Scintillation Array at Cambridge detected the first pulsar [25]. In more recent years, studies of pulsars led to the first indirect measurement of gravitation of waves [26] and the discovery of fast radio bursts [27].

## 1.2 A Brief Primer on Radio Astronomy

This section provides a concise review of the necessary fundamentals, quantities, mathematical primitives, and techniques involved in Radio Astronomy. Detailed discussions including derivations on these topics can be found in the texts, *Tools of Radio Astronomy* by Wilson *et al.* [28] and *Essential Radio Astronomy* by Condon & Ransom [29].

### 1.2.1 Radio Astronomy Observables

Radio observations measure the radiation in the sky generally as a function of the sky position and frequency as well as parameters such as time and polarisation.

The total brightness is the total contribution of all the photons of all frequencies. The brightness per unit frequency is called the specific intensity ($I_\nu$). The energy within the frequency band $d\nu$ from from within the solid angle $d\Omega$ passing through a (for e.g. detector) surface of an an infinitesimal surface area $d\sigma$ flows through the projected area $cos\theta d\sigma$ (see Figure 1.2) in time $dt$,

$$dE = I_\nu \cos\theta d\sigma d\Omega d\nu dt \ [\mathrm{J}]. \tag{1.2}$$

The corresponding power

$$dP = \frac{dE}{dt} = I_\nu \cos\theta d\sigma d\Omega d\nu \ [\mathrm{W}]. \tag{1.3}$$

Thus, the specific intensity,

$$I_\nu = \frac{dP}{\cos\theta d\sigma d\Omega d\nu} \,[\mathrm{W\,m^{-2}\,Hz^{-1}\,sr^{-1}}], \tag{1.4}$$

and the total intensity $I = \int_0^\infty I_\nu d\nu$.

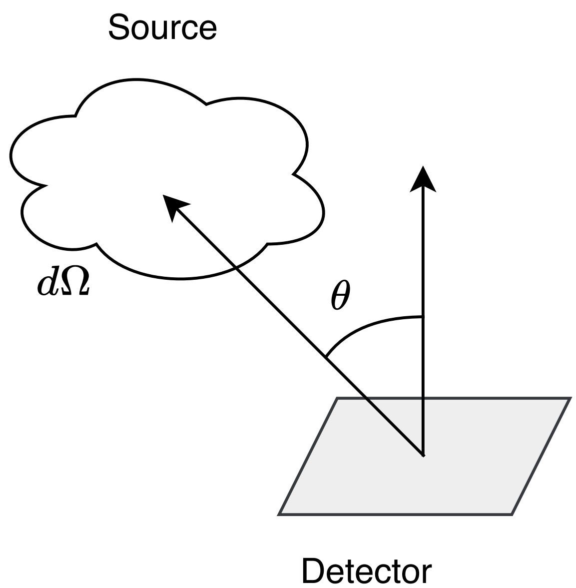


Figure 1.2: **Radiation measured by a detector:** Radiation measured by a detector of infinitesimal surface area of $d\sigma$ whose normal is at an angle $\theta$ from the line of sight to the source subtending a solid angle $d\Omega$.

Telescopes measure the amount of energy incident on a unit surface within unit time per unit frequency. This quantity is called the flux density $S_\nu$ of the source. It is the spectral power received by a detector of unit projected area (Figure 1.2) for a source that subtends a well-defined solid angle. Equation 1.4 implies

$$\frac{dP}{d\sigma d\nu} = I_\nu \cos\theta d\Omega \,[\mathrm{W\,m^{-2}\,Hz^{-1}}], \tag{1.5}$$

so integrating over the solid angle subtended by the source yields

$$S_\nu \equiv \int_{\text{source}} I_\nu(\theta, \phi) \cos\theta d\Omega \,[\mathrm{W\,m^{-2}\,Hz^{-1}}]. \tag{1.6}$$

If the source angular size is $\ll 1\,\mathrm{rad}, \cos\theta \approx 1$ and the expression for flux density is:

$$S_\nu \approx \int_{\text{source}} I_\nu(\theta,\phi) d\Omega \; [\mathrm{W\,m^{-2}\,Hz^{-1}}]. \tag{1.7}$$

The total flux received over all frequencies is $S = \int_0^\infty \mathrm{d}\nu S_\nu$.

Radio waves are measured in flux density are relatively weak and their unit is Jansky (Jy),

$$1\,\mathrm{Jy} \equiv 1 \times 10^{-26}\,\mathrm{W\,m^{-2}\,Hz^{-1}} \tag{1.8}$$

The spectral luminosity $L_\nu$ of a source is defined as the total power per unit bandwidth radiated by the source at frequency $\nu$. For a source at distance $d$,

$$L_\nu = 4\pi d^2 S_\nu \tag{1.9}$$

and the luminosity or total luminosity $L$ of a source is defined as the integral over all frequencies of the spectral luminosity, $L = \int_0^\infty d\nu L_\nu$.

If the radiation is in a Local Thermodynamical Equilibrium (LTE), the specific intensity behaves as a blackbody (Eq. 1.1), $(I_\nu)_{\text{LTE}} \rightarrow B_\nu(T)$. In this case the temperature is known as the Brightness temperature $T_\mathrm{b}$ which corresponds to the temperature of a blackbody to produce the observed specific intensity $I_\nu$. Thus at radio frequencies where $k_\mathrm{B} T_\mathrm{a} \gg h\nu$,

$$I_\nu = B_\nu(T_\mathrm{b}) \approx \frac{2k_\mathrm{B} T_\mathrm{b} \nu^2}{c^2} = \frac{2k_\mathrm{B} T_\mathrm{b}}{\lambda^2}. \tag{1.10}$$

This is the Rayleigh-Jeans approximation and the corresponding brightness temperature,

$$T_\mathrm{a} \equiv \frac{c^2}{2k_\mathrm{B}\nu^2} I_\nu \; [\mathrm{K}] = \frac{\lambda^2}{2k_\mathrm{B}} I_\nu \; [\mathrm{K}]. \tag{1.11}$$

**Noise Generated by a Warm Resistor** A resistor is a passive electronic component. It absorbs the electrical power and converts that power into heat. The motions of charged particles in a resistor at any temperature $T > 0\,\mathrm{K}$ generates electrical noise. This is called the *Johnson* noise. In thermal equilibrium, the frequency spectrum of this noise depends only on the temperature of an ideal resistor and is independent of the material in the resistor. In a system consisting of two identical resistors at temperature $T$ connected by a lossless transmission line of length much larger than the longest wavelength of interest. (see Figure 1.3). The power emitted by the resistor R, in the limit of $k_{\mathrm{B}}T_{\mathrm{a}} \gg h\nu$,

$$P_{\nu} = k_{\mathrm{B}}T. \tag{1.12}$$

This is the Nyquist approximation. The noise generated by a resistor is indistinguishable from the noise coming from a receiving antenna surrounded by blackbody radiation of the same temperature. The temperature of this hypothetical “warm" resistor is used as a standard for calibrating the “noise" of antennas and can be extended to be used for impedances of receiver systems of radio telescopes.

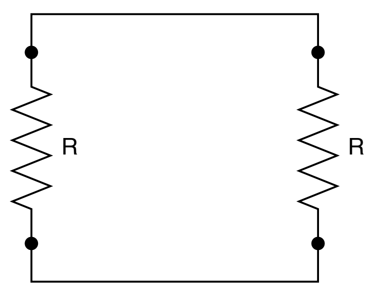


Figure 1.3: **Matched Resitors:** Two resistors connected by a lossless transmission line of length much greater than the longest wavelength of interest. At a temperature $T$ the resistor R on the left provides a power $k_{\mathrm{B}}T$ to a matched load R, on the right.

### 1.2.2 Radio Telescopes

Radio telescopes range from simple wires forming dipole antennas to large structures made of reflectors of all shapes and sizes. The simplest radio telescope (see Figure 1.4) acquires the astronomical signal using an *antenna* converting them to electrical currents. These electrical currents in the “front end” are appropriately conditioned using *amplifiers* and *filters* to be transmitted to a corresponding “*back-end*” for signal processing, detection and data recording. Further signal conditioning may be required before recording the data. Depending on the frequency of observation and limitations of the signal conditioning and processing technology, complex systems can be designed including but not limited to phase-locked systems, and mixers with local oscillators.

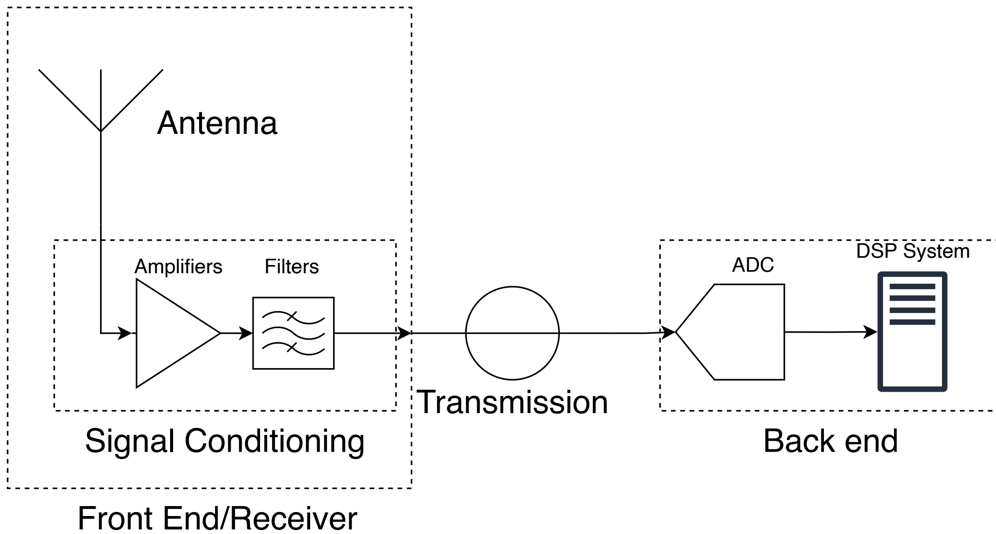


Figure 1.4: **A representation of a simple radio telescope.**

#### 1.2.2.1 Antennas

An antenna is a passive device that converts electromagnetic radiation into electrical currents or vice-versa depending on its use as a receiver or transmitter. Radio telescopes are receiving antennas.

The antenna temperature $T_{\mathrm{a}}$ is used as a practical unit for quantifying the power output per unit frequency. It is defined as the brightness temperature in the Rayleigh–Jeans limit associated with the power received by the telescope. This is the temperature of a matched resistor whose thermally generated power per unit frequency in the Nyquist approximation,

$$\begin{aligned} P_\nu &= I_\nu dA d\Omega \\ &= \frac{2kT_{\mathrm{a}}}{\lambda^2} dA d\Omega. \end{aligned} \tag{1.13}$$

The solid angel $\Omega_a$ and the effective area $A_e$ of all antennas are related by,

$$A_e \Omega_a = \lambda^2, \tag{1.14}$$

where $A_e = \eta_a A_p$ ( $\eta_a$ is the aperture efficiency and $A_p$ is the projected area of the telescope). From equation 1.13 and equation 1.14, the power per unit frequency received by a telescope can thus be given by

$$P_\nu = 2k_\mathrm{B} T_\mathrm{a}. \tag{1.15}$$

We relate the power received by the antenna at a frequency $\nu$, $P_\nu$, to the antenna temperature, $T_\mathrm{a}$, and the observed specific intensity, $I_\nu$, as follows:

$$\begin{aligned} P_\nu &= I_\nu A_e \Omega_a \\ 2k_\mathrm{B} T_\mathrm{a} &= S_\nu A_e \\ T_\mathrm{a} &= \left(\frac{A_e}{2k_\mathrm{B}}\right) S_\nu. \end{aligned} \tag{1.16}$$

The term $A_e/2k_\mathrm{B}$ is called the gain ($G$) of the antenna and for $k_\mathrm{B} = 1830.64\,\mathrm{Jy\,m^2\,K^{-1}}$ has the units of $\mathrm{K\,Jy^{-1}}$.

The system temperature, $T_\mathrm{sys}$ describes the actual power received due to the sky and the receiver $T_\mathrm{R}$.

$$T_\mathrm{sys} = T_\mathrm{a} + T_\mathrm{atm} + T_\mathrm{R}. \tag{1.17}$$

The dominant component is the receiver temperature, $T_\mathrm{R} \gg T_\mathrm{a}$, which includes the *Johnson* noise from the electronics. Detection of our astronomical signal requires us to detect our signal above the noise, i.e. $T_a > \sigma$. From the central limit theorem, the noise or the standard deviation or the root mean square error of $N$ independent samples taken from a signal with the standard deviation or root mean squared error is scaled by $1/\sqrt{N}$. A signal with bandwidth $\Delta\nu$ contains $\Delta\nu$ independent pieces of complex numbered information each second. Thus, for a measurement made over $\tau$, we have averaged $N = \Delta\nu\tau$ independent complex samples. The temperature relates to the variance of a distribution, then the uncertainty of each variance measurement is $\approx T_{\rm sys}$. Thus,

$$\sigma = \frac{T_{\rm sys}}{\sqrt{\Delta\nu\tau}}. \tag{1.18}$$

Thus for the signal $T_{\rm a}$, we have the radiometer equation, where

$$\frac{T_{\rm a}}{\sigma} = {\rm SNR} = \frac{T_{\rm a}}{T_{\rm sys}}\sqrt{\Delta\nu\tau}. \tag{1.19}$$

From equation 1.16, for a detection threshold, SNR, the radiometer equation in terms of the minimum detectable flux $S_{\rm min}$ is,

$${\rm SNR} = \left(\frac{A_{\rm e}}{2k_{\rm B}}\right)\frac{S_{\rm min}}{T_{\rm sys}}\sqrt{\Delta\nu\tau}, \tag{1.20}$$

or,

$$S_{\rm min} = \frac{{\rm SNR}\cdot T_{\rm sys}}{\frac{A_{\rm e}}{2k_{\rm B}}\sqrt{\Delta\nu\tau}}. \tag{1.21}$$

A useful metric of measuring sensitivity of a radio telescope is by defining the System Equivalent Flux Density (SEFD). This is, as the name suggests, the flux equivalent of $T_{\rm sys}$,

$${\rm SEFD} = \frac{T_{\rm sys}}{G} = \frac{T_{\rm sys}}{A_{\rm e}/2k_{\rm B}}. \tag{1.22}$$

More specifically, it refers to the flux of a source that would double the system temperature. If we know the flux $S_\nu$ [Jy] of a source, then the signal-to-noise is,

$${\rm SNR} = \frac{S_\nu[{\rm Jy}]}{\rm SEFD}\sqrt{\Delta\nu\tau}. \tag{1.23}$$

The full width half max or half power beam-width of most radio telescopes observation at wavelength $\lambda$ and aperture $D$ is given as,

$$\theta_{\rm FWHM} \approx 1.2\frac{\lambda}{D}[{\rm radians}]. \tag{1.24}$$

The beams of most radio telescopes are nearly Gaussian with the full width half max or half power beam-width equal to $\theta_{\mathrm{FWHM}}$. Their corresponding beam solid angle,

$$\Omega = \left(\frac{\pi}{4\log 2}\right)\theta_{\mathrm{FWHM}}^2 \approx 1.133\theta_{\mathrm{FWHM}}^2. \tag{1.25}$$

#### 1.2.2.2 Amplifiers

Astronomical signals are faint and usually amplified. Amplifiers for radio astronomy typical must have low internal noise, amplify over several frequencies without any large variations, be linear over the observed bandwidth, and be stable over time. The characteristic of an amplifier is generally expressed as its temperature. $T$. It is the noise that would be added at the amplifier's input to account for the added noise observed following amplification. In practice, this is reported as the noise factor and noise figure. The noise factor is

$$F \equiv \frac{290 + T}{290}. \tag{1.26}$$

The temperature of $290\,\mathrm{K}$ is taken as the standard room temperature as convention. The noise figure is the noise factor expressed in decibels,

$$NF = 10\log_{10}(F). \tag{1.27}$$

**Decibels**: Most amplification and conversely attenuation of a signal is expressed in *decibels*. The power in *decibels* is the ratio of output to input,

$$\text{dB} = 10\log_{10}\left(\frac{P_{\text{out}}}{P_{\text{ref}}}\right). \tag{1.28}$$

In this expression, $P_{\text{out}}$ and $P_{\text{ref}}$ are the output and reference powers respectively. For amplifiers and attenuators $P_{\text{ref}}$ is the power that is fed into the device. Thus a 3dB gain doubles the power, conversely, a 3dB attenuation halves the power, a gain of 10dB increases the power by a factor of

10, 20dB increases the power by a factor of 100, and so on. Many instruments take measurements in dBm which corresponds to the decibels of power with reference to $1\,\mathrm{mW}$. For voltages the decibel value,

$$\mathrm{dB} = 20\log_{10}\left(\frac{v_{\mathrm{out}}}{v_{\mathrm{ref}}}\right). \tag{1.29}$$

So, a 6dB gain doubles the voltage, conversely, a 6dB attenuation halves the voltage, and a gain of 20dB increases the voltage by a factor of 10, 40dB increases the voltage by a factor of 100, and so on.

Typically analog chains have cascading amplifiers to account for design and technical constraints as well as to compensate for attenuation from transmitting a signal across significant distances.

The output power from an amplifier that amplifies the signal by gaining $G$ is

$$P = G k_{\mathrm{B}} T \Delta\nu. \tag{1.30}$$

Thus for an amplifier chain of $n$ amplifiers with gains $G_1, G_2, ..., G_n$ and noise temperatures $T_1, T_2, ..., T_n$ the power,

$$P = G_1 G_2 ... G_n k_{\mathrm{B}} T_1 \Delta\nu + G_2 G_3 ... G_n k_{\mathrm{B}} T_2 \Delta\nu + ..., \tag{1.31}$$

with the corresponding amplifier system temperature

$$T = T_1 + \frac{T_2}{G_1} + \frac{T_3}{G_1 G_2} + ... + \frac{T_n}{G_1 G_2 ... G_{n-1}}. \tag{1.32}$$

The noise temperature of systems is usually calculated using the Y-factor method. From equation 1.30 we see that the power is linear to the noise temperature. So we can thus use two loads at known temperatures $T_1$ and $T_2$ where $T_1 > T_2$ is usually called the hot and cold load. The hot load can be either a resister at a known temperature or a source in the sky or a noise source generated by a calibrated noise diode. We measure the power $P_{\mathrm{out},1}$ and $P_{\mathrm{out},2}$from two known loads corresponding to different known noise temperatures and then linearly interpolate for the noise temperature of the system. So, the Y factor,

$$Y \equiv \frac{P_{\mathrm{out},1}}{P_{\mathrm{out},2}}, \tag{1.33}$$

and the noise temperature of the system.

$$T = \frac{T_1 - YT_2}{Y - 1}. \tag{1.34}$$

#### 1.2.2.3 Signal Processing

The signal paths have a combination of filters and amplifiers to condition the signal to be free from radio frequency interference and additionally restrict the signal to be recorded to specified frequencies of interest. Signals are can be processed through a variety of methods from square law detectors to polarimeters. Many modern radio telescopes employ digital signal processing due to their accessibility and ever-decreasing cost.

Digital signal processing requires the signal to be digitized by sampling the signals at discrete intervals and quantizing the signal to discrete levels. To extract characterizable information from the signal we must sample at a rate, $f_\mathrm{s}$ that is more than twice the maximum frequency to be measured in the signal spectrum, $f_\mathrm{max}$, i.e. $f_\mathrm{s} > 2f_\mathrm{max}$ This is called the Nyquist-Shannon Sampling theorem. For a sample rate of $f_\mathrm{s}$, we cannot differentiate between any tone with frequencies $Nf_\mathrm{s} \pm \Delta f$, where $N$ is an integer. All signal power for these frequencies will 'alias' at $\frac{f_\mathrm{s}}{2} - \Delta f$. This phenomenon of alias allows us to define Nyquist zones every $f_\mathrm{s}/2$ Hz. If a signal is band-limited to each of these Nyquist zones all the analog signals from those frequencies can be recovered. This is employed in the CHIME telescope (see §2.3) where the data are sampled at 800 mega-samples-per-second but band limited to $400$–$800\,\mathrm{MHz}$ placing the acquisition in the second Nyquist zone.

Astronomical signals of interest span several frequencies of electromagnetic radiation and some are narrowband frequencies originating from spectral lines. To facilitate such measurements we use spectrometers. Spectrometers can be constructed by assembling a bank of filters (called filterbanks) that the signal was passed through. This method was employed in early radio telescopes (e.g. 40-foot telescope at Green Bank Observatory). Mathematically, spectrometers measures the power spectral density (PSD) $S_{xx}(\nu)$ in $\mathrm{W\,Hz^{-1}}$ of our signal $x(t)$. The PSD and the autocorrelation function ($r_{xx}(\tau)$) of the signal are related by the Wiener-Khinchin theorem. Assuming the signal $x(t)$ is wide sense stationary the PSD,

$$S_{xx}(\nu) = \int_{-\infty}^{\infty} r_{xx}(\tau) e^{-2\pi i \nu \tau} d\tau. \tag{1.35}$$

Here $\nu$ is the frequency and $\tau$ is the time delay or lag. The autocorrelation function,

$$r_{xx}(\tau) = \Big\langle x(t)x(t-\tau) \Big\rangle\,, \tag{1.36}$$

where the angled brackets denote the expectation value of (i.e. the time average) of the signal.

The autocorrelation function is related to the PSD by a Fourier transform as seen in equation 1.35 which for discrete signals is,

$$S_{xx}(k) = \sum_{m=-\infty}^{\infty} \langle x(n)x(n-m) \rangle e^{-2\pi i m k}. \tag{1.37}$$

The summation is performed over time lag, $m$ and angled brackets average over time sample, $n$. This expression is a convolution and from the convolution property of Fourier transforms:

$$S_{xx}(k) = \Big\langle |X(k)|^2 \Big\rangle \tag{1.38}$$

where $X(k)$ denotes the Discrete Fourier Transform (DFT) of $x(n)$ with $N \to \infty$ discrete points:

$$X(k) = \sum_{n=0}^{N-1} x(n) e^{-2\pi i n k / N}. \tag{1.39}$$

Equations 1.37 and 1.38 represent two types of spectrometers that differ in the order in which the Fourier transform is taken. The first takes the autocorrelation first and then the Fourier transform. It is called the autocorrelation spectrometer or more generally the “XF” correlator. The first autocorrelation spectrometer in radio astronomy was reported in [30]. The second route involves taking the Fourier transform of the signal and then multiplying the Fourier transformed signal. These are generally part of “FX” correlators. The advent of cheaper digital signal processing fuelled by Moore’s law has made these the correlators of choice for modern telescopes. The discrete nature of the Fourier transform in digitally processing signals requires enhanced windowing in the DFT equation 1.39 by constructing Polyphase filterbank spectrometers (PFBs).

### 1.2.3 Interferometers

The resolution of a single dish given by equation 1.24 states a larger dish is required for higher resolutions. Systems scaling from previous projects has shown that the cost of large steerable radio telescopes of diameter increases approximately as $(D)^{2+\alpha}$ where typically $\alpha \in [0, 1]$. Some estimates report $\alpha = 0.7$[1][31]. Thus cost considerations put an upper limit on the largest single-dish systems one can build. Interferometry as a method of observation in radio astronomy was introduced in 1946 in the form of sea interferometers using the reflection from the surface of the ocean to observe the radiation from the sun [21]. The first radio interferometric observations using multiple antennas by Ryle & Vonberg in 1946 and the development of aperture synthesis in 1960 [23] have since enabled us to synthesize an equivalent large telescope that has the best resolution given by $\sim \lambda/B$ where $B$ is the longest baseline between interferometer elements.

Interferometers such as beamformers and very long baseline interferometers are discussed in Chapter 4. For a detailed history of interferometry leading up to very long baseline interferometry, one can refer to ‘The Development of High-Resolution Imaging in Radio Astronomy’ by Kellermann & Moran [31].

Signals from individual elements of interferometers, each with an effective area $A_e$ and field of

[1] https://library.nrao.edu/public/memos/alma/main/memo006.pdf

view $\Omega$ and the sensitivity given by equation 1.20, can be combined in several ways:

- **Incoherent Sum:** The power of the signal from individual elements is computed and then added incoherently. The sensitivity of such a system scales from a single element as $\sqrt{N_{\rm a}}A_{\rm e}$ for $N_{\rm a}$ elements and the field of view is the same as that of each element $\Omega$. For geometrically far away elements, a phase can be applied to the power before summing the signals.

- **Phased Array/Coherent Sum/Correlator beamformer**: The signal from individual elements can have a phase applied and then summed before power is computed for detection. The formed beam of the array has a field of view of $\Omega_{\rm array}$. The phases can be applied such that we can form $N_{\rm b}$ independently pointed beams within the primary beam. The sensitivity of such a system scales from a single element as $N_{\rm a}A_{\rm e}$ for $N_{\rm a}$ elements and the field of view is $N_{\rm b}\Omega_{\rm array}$. The phased array can be an aperture array or a phased array feed on a dish telescope.

- **Incoherent sum of Phased Array stations**: An array made of $M$ subarray stations each with $N_{\rm a}$ elements can be made to have each subarray coherently summing signals to make beams with the field of view $\Omega_{\rm station}$ determined by the substation array geometry and incoherently summing the beamformed signal from each subarray station. The sensitivity scale from a single element as $\sqrt{M}N_{\rm a}$. For a subarray forming $N_{\rm b}$ beams the total field of view is $N_{\rm b}\Omega_{\rm station}$.

- **Coherent sum of Phased Array stations**: An array made of $M$ subarray stations each with $N_{\rm a}$ elements can be made to have each subarray coherently summing signals to a beam essentially synthesizing a data stream from a single element whose sensitivity is scaled by $N_{\rm a}$. Each of these single phased array elements is again coherently added to form beams in the sky. The sensitivty scale from a single element as $MN_{\rm a}$. This instrument can form $N_{\rm b}$ beams within the field of view of a single element with the total field of view achievable as $N_{\rm b}\Omega_{\rm array}$, where each beam's field of view $\Omega_{\rm array}$ determined by the full array geometry.

The data stream of each of these formed signals can be used for searches of varying sensitivities traded off with processing complexities involved to get the fast real-time detection rate for the cost. For example, a real-time search of transients within the incoherent sum data streams is cheaper because of the reduced number of signal streams. Concurrently, a buffered baseband data system can be used to acquire data to be coherently summed. This would achieve greater SNR and better localization of the detected real-time signal, especially when utilizing an array of phased array systems.

## 1.3 Modern Radio Astronomy

Modern radio astronomy is powered by advances in digital electronics and the near-ubiquity of Moore's law [32]. This allows us to sample the electrical fields at a very high cadence. Thus despite the limits on the size of telescope structure due to costs (see §1.2.3) we can scale digital infrastructure at relatively lower costs. One can thus use high-performance computing (HPCs), field-programmable gate arrays (FPGAs), and application-specific integrated circuits (ASICs) to digitally synthesize large radio telescopes and steer their beams. Such modern telescopes include Precision Array for Probing the Epoch of Reionization (PAPER) [33] , Hydrogen Epoch Reionization Array (HERA) [34], Low Frequency Array (LOFAR) [35], Australian Square Kilometre Array Pathfinder (ASKAP) [36], MeerKAT and Canadian Hydrogen Intensity Mapping Experiment (CHIME). These synthesized telescopes based on interferometry essentially measure the visibilities from all the antennas of the telescope arrays. It is the time-averaged correlation of the voltages $v_m$ and $v_n$, from antennas $m$ and $n$ respectively

$$\mathcal{V}_{mn} = \langle v_m v_n^* \rangle \,. \tag{1.40}$$

The computational cost for $N$ antennas for equation 1.40 scales as the number of multiplications. Since there are $N(N+1)/2$ baselines of crosscorrelations and $N$ auto-correlations. The cost scales as $\mathcal{O}(N^2)$. It was however proposed in [37], and formalised in [38, 39], that having a regular grid of antennas allows us to compute 1.40 by considering a vector $\mathbf{v}$ containing signals from all $N$ antennas and cross-correlating them in the spacial Fourier domain as,

$$\mathcal{F}\left(\mathbf{v} \star \mathbf{v}^{\dagger}\right) = \mathcal{F}(\mathbf{v})\mathcal{F}(\mathbf{v}^{\dagger}). \tag{1.41}$$

Here $\mathcal{F}$ is a spatial Fourier transform, and the dagger, $\dagger$, denotes a Hermitian. The inverse of equation 1.41 gives us the visibilities in 1.40. Since the operations occur in the Fourier domain we can use fast Fourier transforms (FFT) algorithms to scale the computations to $\mathcal{O}(N \log N)$ instead of $\mathcal{O}(N^2)$. These telescopes have been termed "Fast Fourier Transform Telescope" and CHIME is the first full-scale FFT Telescope [40].

# Chapter 2

# Fast Radio Bursts

This chapter briefly describes the phenomena of fast radio bursts (FRBs) and introduces the Canadian Hydrogen Intensity Mapping Experiment (CHIME) telescope's CHIME/FRB instrument.

## 2.1 Time Domain Sky

The night sky seems largely static with respect to itself. The stars, within human timescales, do not appear to move relative to each other on the sky. However, new stars, retrospectively identified as supernovae, have been observed on historical records across the world from the 2nd, and 11th up to the 16th century when Tycho Brahe studied a *stella nova*, a new star in the sky, is now termed SN 1572 or colloquially "Tycho's supernova", for two years until it disappeared. Time-domain astronomy as it is now called also invloves the study of time variable stars "cepheid variables" and comets. By their very nature, the discoveries of astronomical transients are serendipitously aided by the opening of observable phase space such as the discovery of radio astronomy as discussed in the previous chapter. Solar and Jovian radio bursts were discovered in the 1940s and 1950s [41], respectively. Radio pulsars were discovered in 1967 by Jocelyn Bell Burnell [25] from observations made with the Interplanetary Scintillation Array which a year later were interpreted as coming from rotating neutron stars. Around the same time as pulsars, gamma-ray bursts (GRBs) were discovered by newly launched US satellites to detect suspected secret nuclear weapon tests by the Soviet Union. The results were only declassified and published in 1973 [42] with [43] measuring GRB redshift placing them unambiguously at an extragalactic distance. Other known radio transients include flare stars [44, 45], rotating radio transients (RRATs) that have been theorised to be extreme cases of pulsars [46, 47] and magnetars [48, 49].

## 2.2 The Fast Radio Bursts phenomenon

Fast Radio Bursts (FRBs) are a class of radio transients that are bright millisecond radio flashes broadly distributed across the sky. The first FRB was reported in [27] (see: 2.1) in archival data of the Parkes telescope. It exhibits the expected behaviour for cold-plasma dispersion assuming a Dispersion Measure (DM) of $375\ \mathrm{pc\ cm^{-3}}$. The frequency dispersion strongly suggests a celestial origins. The DM observed was significantly larger than the value expected along the line sight from the Galaxy ($25\ \mathrm{pc\ cm^{-3}}$) according to the NE2001 model for the Galactic electron density contribution [50, 51]. This suggests an extragalactic origin. Their discovery was met with skepticism but their astronomical origins were confirmed when four more bursts were detected by [52] by the Parkes telescope and finally [53] by the Arecibo telescope. Earlier detections of extragalactic radio bursts [54] failed to be detected in follow-up observations [55]. There have been previously attempted searches for radio bursts from energetic mechanism [56] and gamma-ray bursts [57] with the closest FRB analogs possibly detected as early as 1989[58]. The discovery of the repeating nature of some FRBs [53] led to a distinction between 'one-off' FRBs and repeaters, as other FRBs had been followed up for up to several hours without detecting any repetitions.

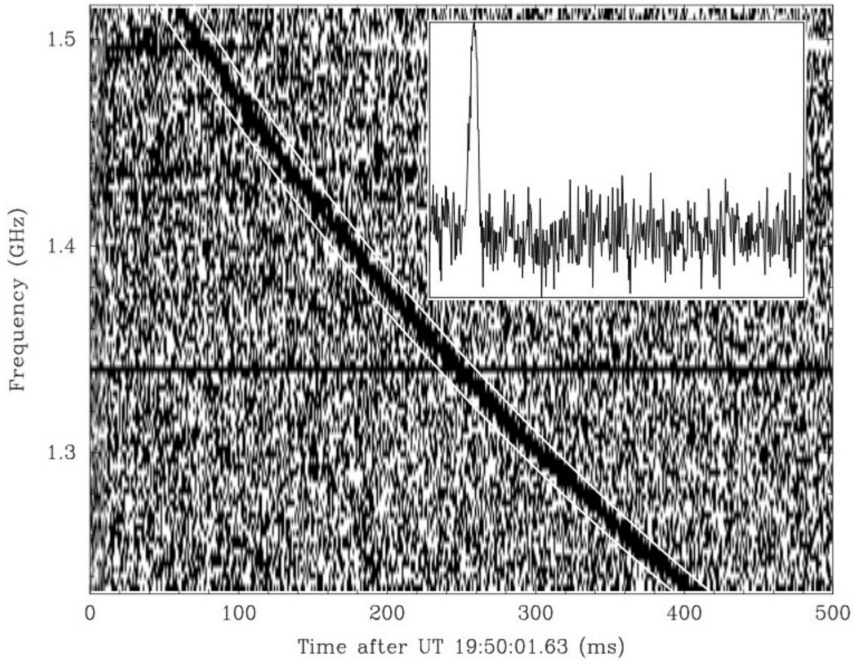


Figure 2.1: **The "Lorimer Burst" [Figure from 27]:** The "waterfall plot" of intensity as a function of radio frequency versus time. Inset, the integrated pulse shape of the radio burst. The dark quadratic sweep across the frequency is the dispersed FRB pulse.

Most FRB pulses arrive with DMs much larger than the estimated Galactic contribution along the line of sight of detection, therefore FRBs are believed to originate in extra-galactic sources (see Figure 2.2). FRBs [59, 60] have been localized and are coincident with galaxies at cosmological redshifts, reinforcing the extragalactic origin hypothesis. Efforts to explain the exceptionally high inferred isotropic brightness temperature of these sources ($10^{38}$ K) along with the all-sky rate have employed extreme astrophysical models [61, 62]. If the few-millisecond duration of the bursts reflects the spatial extent of the source region, these cosmologically distant sources have an angular diameter smaller than $10^{-21}$ radians. The small source size allows FRB spectra to exhibit non-dispersive two-path interference when microlensed [63], as well as scattering and scintillation that does exhibit dispersion as the pulses transit the intervening plasma. FRBs can therefore serve as a unique new probe of the microlensed and ionized universe as well as the Large-Scale Structure of the Universe [64–66]. The events show no Galactic latitude dependence [67]. Most are not shown to repeat. The burst morphology seen in figure 2.4 arranges itself into distinct archetypes suggesting a beaming or propagation effect, or it could be intrinsic to the populations. The CHIME/FRB Catalog [68] reports a sky rate of $[820 \pm 60(\mathrm{stat.})^{+220}_{-200}(\mathrm{sys.})]/\mathrm{sky}/\mathrm{day}$ above a fluence of 5 Jy ms at 600 MHz.

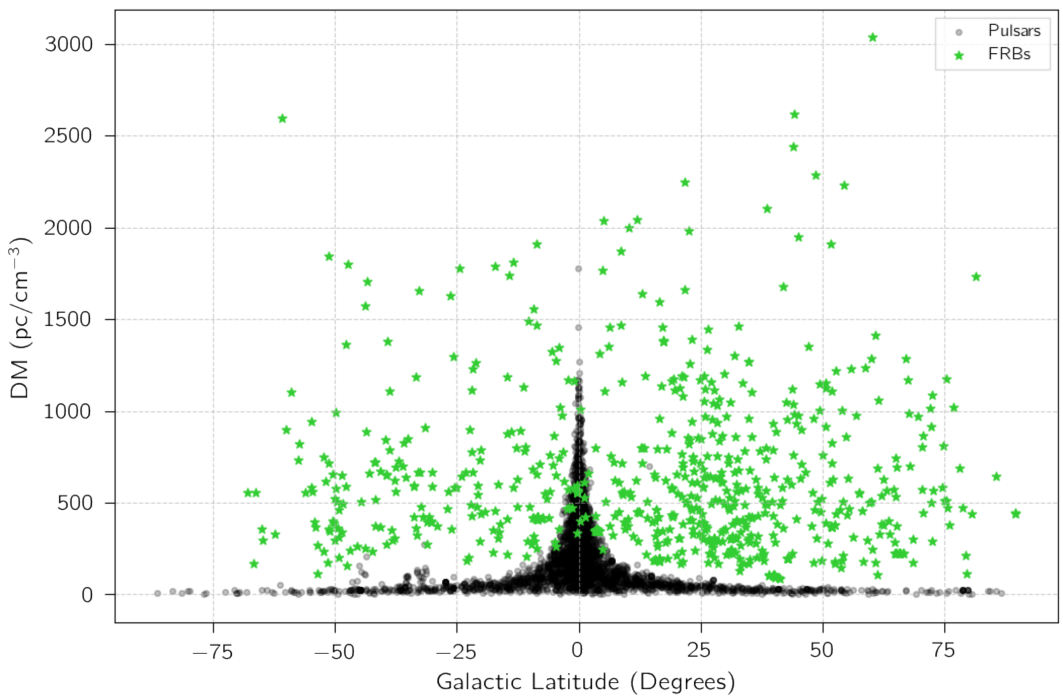


Figure 2.2: **The dispersion measure of pulsars and FRBs as a function of galactic latitude.** The pulsars (in black) have higher DMs closer to the galactic plane and are distinctly grouped enveloped by a curve that proportional to the inverse of the sine of the Galactic latitude $b$ ($sin^{-1}(b)$). Signals from the extragalactic FRBs traverse a distance more than this geometry of the Galaxy.

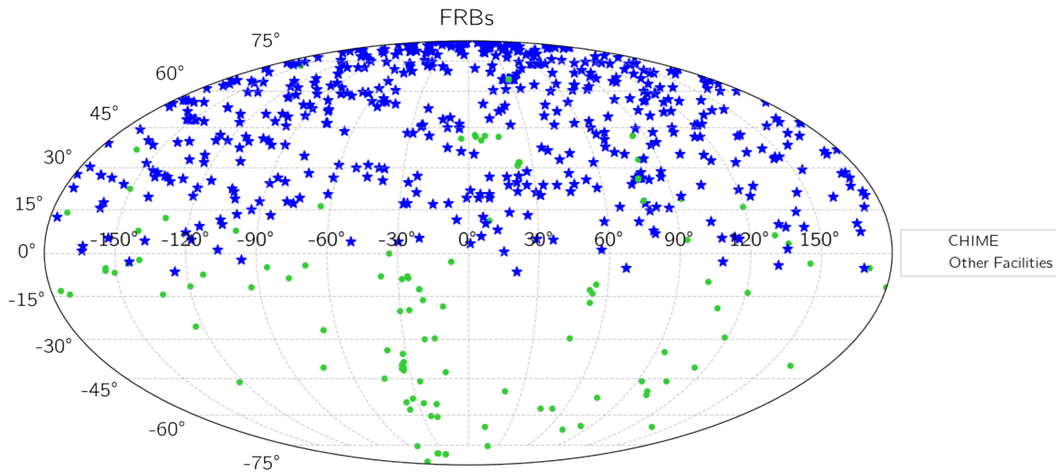


Figure 2.3: **An Mollwiede projection map of the sky positions of all published FRBs (as of July 2022).** Here the right ascension is shown as ranging from –180 to 180 degrees and the declination ranges from –90 to +90 degrees. Blue corresponds to FRBs detected by CHIME and green from the other different telescopes.

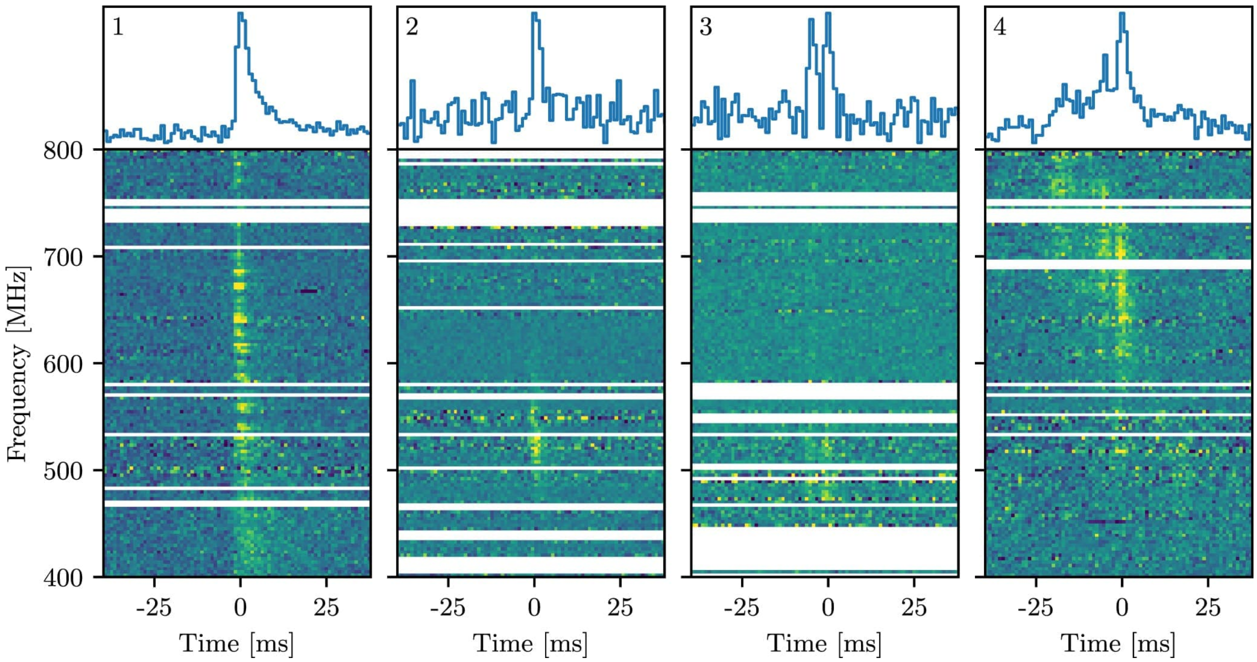


Figure 2.4: **Dedispersed dynamic spectra of the four FRB morphology archetypes:**1) Broadband simple bursts comprised of one peak descibed by a gaussian convolved with an exponential scattering tail; 2.) Narrowband simple bursts; 3.) Complex bursts are comprised of multiple peaks with similar frequency extent, with one of the peaks sometimes being a much dimmer precursor or post cursor – they can be broadband or narrowband; 4.) Complex bursts comprised of multiple sub-bursts that drift downward in frequency as time progresses., as detected by CHIME/FRB. These are FRBs 20190527C, 20190515D, 20181117B, and the 2019 August 10 burst of repeating FRB 20190117A. Knots of intensity in the burst spectra are instrumental in origin. Figure and caption adapted from [69]

.

### 2.2.1 FRB observables

Electromagnetic radiation properties are modified by interactions with the intervening media. The observed properties of the FRBs are a combination of the effects of their signals' path of propagation as well as their intrinsic nature. Understanding propagation properties is thus critical to understanding their progenitors.

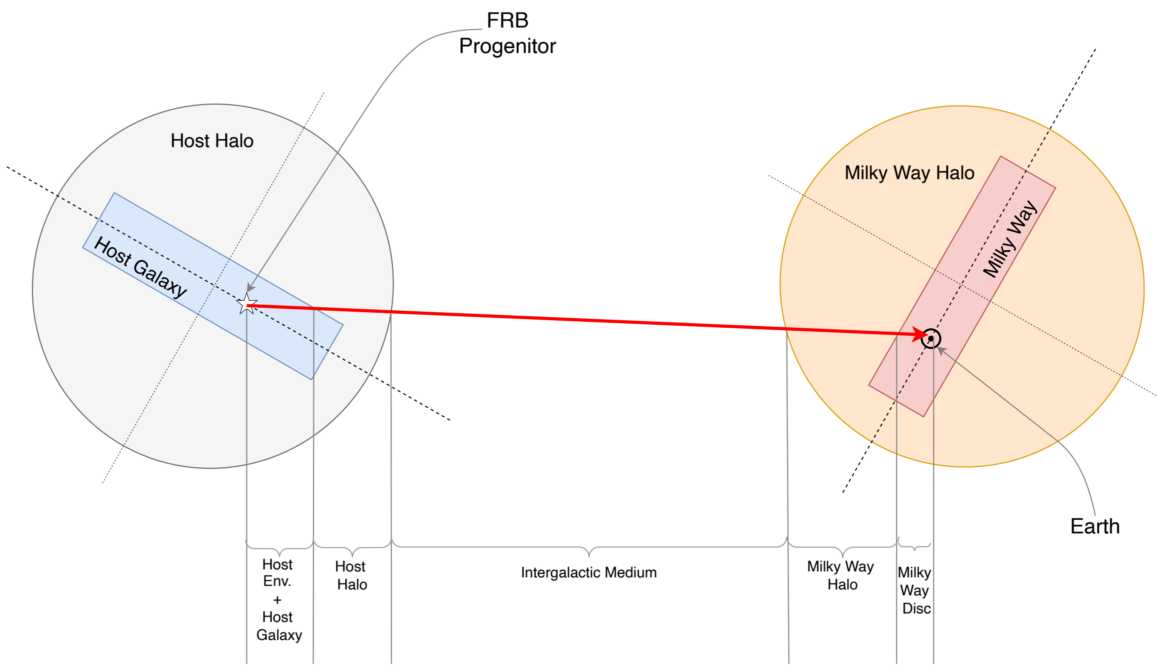


Figure 2.5: **FRB signal propagation:** The signal from a progenitor travels through the host's immediate environment and through the interstellar matter in what is usually the host galaxy. Galaxies have halos that surround the galaxy itself. The signal traverses the intergalactic medium before entering the Milky Way halo, the Milky way disc, and is finally observed by us. Each piece of the propagation path affects the signal and can provide insights into their properties as they are observed in the signal characters.

**Dispersion Measure:** Electrons in the cold tenuous plasma have the refractive index,

$$\mu = \left[1 - \left(\frac{\nu_{\mathrm{p}}}{\nu}\right)^2\right]^{1/2}. \tag{2.1}$$

Here $\nu$ is the frequency and $\nu_{\mathrm{p}}$ is the plasma frequency,

$$\nu_{\mathrm{p}} = \left(\frac{e^2 n_{\mathrm{e}}}{\pi m_{\mathrm{e}}}\right)^{1/2} \approx 8.97\mathrm{kHz} \times \left(\frac{n_{\mathrm{e}}}{\mathrm{cm}^{-3}}\right)^{1/2}. \tag{2.2}$$

For the interstellar medium within the milky way Milky Way, the electron density is $n_e \sim 0.03\ \mathrm{cm}^{-3}$ giving us the plasma frequency of $\nu_{\mathrm{p}} \sim 1.5\ \mathrm{kHz}$. Radiation below this frequency $\nu_{\mathrm{p}}$ cannot propagate. The group velocity of the propagating waves is $v_{\mathrm{g}} = \mu c$, less than the speed of light in a vacuum, as $\mu < 1$. This leads to a frequency-dependent dispersion delay in arrival time $\Delta t$. For two observing frequencies $\nu_1$ and $\nu_2$ $\left(\nu \gg \nu_{\mathrm{p}}\right)$ this is

$$\Delta t \simeq k_{\mathrm{DM}} \mathrm{DM}\left(\nu_1^{-2} - \nu_2^{-2}\right) \mathrm{s}, \tag{2.3}$$

where $\nu_1$ and $\nu_2$ are in MHz and the Dispersion Measure (DM) is given in $\mathrm{pc\,cm^{-3}}$ is the integrated column density of free electrons between the source and the observer, i.e.,

$$\text{DM} = \int_0^d n_e dl. \tag{2.4}$$

In this expression, $d$ is the distance through the plasma and $n_e$ is the free electron density. The constant $k_{\mathrm{DM}} = 4149.377\,59\,\mathrm{s\,MHz^2\,pc^{-1}\,cm^3}$ which has been determine with high accuracy recently in [70]. Dispersion broadens a pulsed signal over the bandwidth of a telescope receiver and “dedispersion" is required to compensate for it to detect a pulse with a modest high signal-to-noise ratio. The DM of a source is unknown and is determined, usually in pulse searches, by dedispersing the intensity data over a range of trial DMs. This “incoherent” dedispersion takes the intensity of the signal, divides the full bandwidth in narrow frequency channels, and delays the signal in every channel with the expected delay for a given trial DM to find the intensity by integrating over the bandwidth of the instrument. Residual smearing of the pulse remains within the finite width of frequency channels. Fully removing the dispersive effect of the ISM “coherent” dedispersion. This is achieved by convolving the full phase and amplitude information of an observation encoding in the complex voltages with the inverse of the ISM transfer function [71].

The observed dispersion measure $\mathrm{DM_{obs}}$ from FRBs is the sum of the dispersion measure from all the intervening cold plasma (see 2.5). This can be written as follows,

$$\mathrm{DM_{obs}} = \mathrm{DM_{MW,disk}} + \mathrm{DM_{MW,halo}} + \mathrm{DM_{cosmic}} + \mathrm{DM_{host}}. \tag{2.5}$$

Here Milky Way contributions, $\mathrm{DM_{MW,disk}}$ is from the Galactic disk and $\mathrm{DM_{MW,halo}}$ from the Galactic dark matter halo. $\mathrm{DM_{cosmic}}$ is the contribution from the intergalactic medium between the Milky Way and $\mathrm{DM_{host}}$ the dispersion contribution of the FRB host. $\mathrm{DM_{host}}$ can be decomposed into the contribution from the FRBs immediate environment as well as its hosts such as the contribution of the host galaxy and its halo.

FRBs and bursts/pulses from Galactic RRATs or pulsars are by definition distinguished by being able to determine the Galactic contribution to DM towards the burst's line of sight $\mathrm{DM_{MW,disk}}$. To aid this we use the result of electron distribution models of our Galaxy described in the NE2001 [50, 51] and YMW16 [72] models. The dispersion measure of the Milky Way halo $\mathrm{DM_{MW,halo}}$ have been estimated by several studies with limits as low as $\sim 6\,\mathrm{pc\,cm^{-3}}$ [73] with the mean value estimated as $\sim$ 43–63 $\mathrm{pc\,cm^{-3}}$ by detailed models [74–76]. $\mathrm{DM_{cosmic}}$ estimations requires assumptions about the ionization fractions of the baryons in the IGM and about the electron-to-baryon fraction [77, 78]. Well-localized FRBs using the Australian Square Kilometre Array Pathfinder (ASKAP) has allowed us to construct a DM-z, or Macquart relation [79]. A reasonable rule-of-thumb estimation can be taken as $\mathrm{DM_{cosmic}} \approx 1000z\mathrm{pc\,cm^{-3}}$. The value of $\mathrm{DM_{host}}$ depends on the type of host galaxy and its geometry with respect to us (an interesting exploration of this is discussed for the FRB localized by our instrument in Chapter 5).

**Turbulent Media:** Small-angle deviations in the path of burst can be caused by inhomogeneities in the turbulent plasma. These result in time delays encoded in the phase of the complex signal that can interfere to create intensity modulations on several bandwidths and timescales (scintillations), broaden the burst in time and increase the observed angular diameter of the burst in the sky. Scattering due to multi-path propagation results in the convolution of a burst with an exponential scattering tail (approximately $\propto \nu^{-4}$). The strong frequency dependence makes scattering much more pronounced at lower frequencies. Scattering is observed ubiquitously among pulsars, and it has been identified in some of the FRBs. Measured scattering timescales of pulsars in the Galaxy are the strongest in the plane of the Galaxy and for sources more distant in the plane, scattering is linked to the DM. Scattering timescales measured for FRBs seem to be larger than those of pulsars at similar Galactic latitudes, indicating that most FRB scattering has an origin outside of our Galaxy.

**Burst width [ms]:** FRB duration or burst widths are of the order of milliseconds. The intrinsic burst width is broadened by propagation effects. The width constrains possible progenitors and emission mechanisms.

**Spectrum:** The spectrum refers to both the extent and the shape of the FRB intesnity as a function of frequency. FRBs have been observed from $110\,\mathrm{MHz}$ [80] up to $8\,\mathrm{GHz}$ [81]. The spectra of bursts can be described by a power-law function $\propto \nu^{\alpha}$, with $\alpha$ the spectral index. ASKAP bursts have been found to have a spectral index of $\alpha = -1.6^{+0.3}_{-0.2}$. Additionally, FRB spectra have been found to have fine intensity-modulated structure due to scintillation as in [82] as well as multiple sub-bursts that sometimes drift down in frequency as time progresses.

**Polarization:** The polarization of an electromagnetic signal relates to the preferred geometric orientation of its oscillating electric and magnetic fields. The intrinsic signal from the source of the FRB passing through magnetic media results in the signal being Polarized. The resulting effect of the magnetic field is to change the phase of the radio signal. This effect is quantified by the faraday Rotation measure (RM) $[\mathrm{rad\,m^{-2}}]$. The RM is the frequency-dependent variation of the linear polarization angle. Most observed FRB RMs range from a few tens to a few hundred $\mathrm{rad\,m^{-2}}$. Linear polarization fractions of FRBs have been observed to be close to or $100\%$. Other quantities characterizing polarization are the linear and circularly polarized fraction, and the position angle (PA). PAs have been observed to stay flat in some cases and change systematically in others. Many FRBs observed with polarization information have no circular polarization, but some do.

**Redshift:** The redshift is the reduced observed frequency $\nu_{obsv}$ of an object emitting at frequency $\nu_{emit}$ moving away relative to the observer $z = \nu_{emit}/\nu_{obsv} - 1$. The redshift of the progenitor of an FRB can be estimated from $\mathrm{DM_{cosmic}}$ by the Macquart relation or it can be measured by identifying spectral lines from optical observations of the host associated with the FRB.

**Drift rate:** Some FRBs have been shown to have sub-bursts that drift with respect to the main pulse. Their morphology in the spectra has earned them the name of the "sad trombone" bursts. It is typically assumed to be linear, Measured drift rates are a few to tens of $\mathrm{MHz\,ms^{-1}}$ around 600 MHz up to almost a $\mathrm{GHz\,ms^{-1}}$ around $6.5\,\mathrm{GHz}$. Drifting subpulses have also been previously observed in pulsars [83].

### 2.2.2 FRB discovery Instruments

Initial discoveries were made in reanalyzed archival data. Existing instruments have been equipped with dedicated or robotic backends enabling FRB searches, as well as dedicated FRB instrumentation, which has since emerged.

### 2.2.3 Single dish telescopes

Since FRBs detected by Parkes in [52] removed significant ambiguity of the phenomenon, several instruments have been searching for FRBs. Large single-dish telescopes including Parkes (64 m), Lovell (76 m), Effelsberg (100 m), Arecibo (305 m) [1], Five-hundred-meter Aperture Spherical Telescope (FAST) ($500\,\mathrm{m}$), and GBT ($110\,\mathrm{m}$) have had FRB searching projects in the past decade with many commensal pipelines. The sensitivity of a radio dish is approximately inversely proportional to its effective area. The diameter of the dish $D$ determines the size of the telescope full width half maximum beam width $\theta_{\mathrm{FWHM}} \approx 1.22\lambda/D$, where $\lambda$ is the observed wavelength. To increase the field of view of single-dish telescopes, some are equipped with multi-beam receivers that sample a larger fraction of the telescope's focal plan like Parkes. The large collecting area gives a larger sensitivity and the signal processing is relatively less complex and can thus be invaluable in the study of FRB emission and polarization. However, the single-dish beam $\theta_{\mathrm{FWHM}}$ is the limiting factor and hence uncertainty in localization persists and the discovery rate is limited.

[1] Until the unfortunate collapse of the telescope in 2020

### 2.2.4 Interferometric arrays

Interferometric radio telescopes are composed of many antennas or dishes. The signals from these elements can be added in several ways [84] with the expressed idea that we can construct a mathematical telescope with the resolution of a single large telescope with a diameter equivalent to the longest baseline (the distance between any two elements). The field of view can be more finely sampled using many mathematically synthesized beams by applying different complex signal weightings between different elements of the array. Interferometric telescopes come in all shapes and sizes – as small radio dishes such as the Jansky Very Large Array (JVLA) ($27 \times 25$ m) dishes), the Westerbork Synthesis Radio Telescope (WSRT) ($14 \times 25$ m dishes), and the Australian Square Kilometre Array Pathfinder (ASKAP) ($36 \times 12$ m dishes), or as cylindrical paraboloids with many receivers sampling along the focal line, such as the Canadian Hydrogen Intensity Mapping Experiment (CHIME) and the Molonglo Synthesis Telescope (UTMOST), 2778m long paraboloids as well as individual stationary dipole antennas such as the Low Frequency Array (LOFAR) and the Murchison Wide–field Array (MWA). Broadly the signals can be combined in two techniques: Incoherent searches, which simply perform summation of the individual element intensities disregarding any phase information with the sensitivity scales as $\sqrt{N}$ for $N$ elements. The field of view is large but the localization is poor. Secondly, Coherent searches provide sensitivity that scales as $N$. It also proffers superior localization by applying weights to different elements and summing the signals in phase. The decreasing cost of digital signal processing costs and sophisticated algorithms give Interferometric instruments an edge and flexibility while designing an experiment.

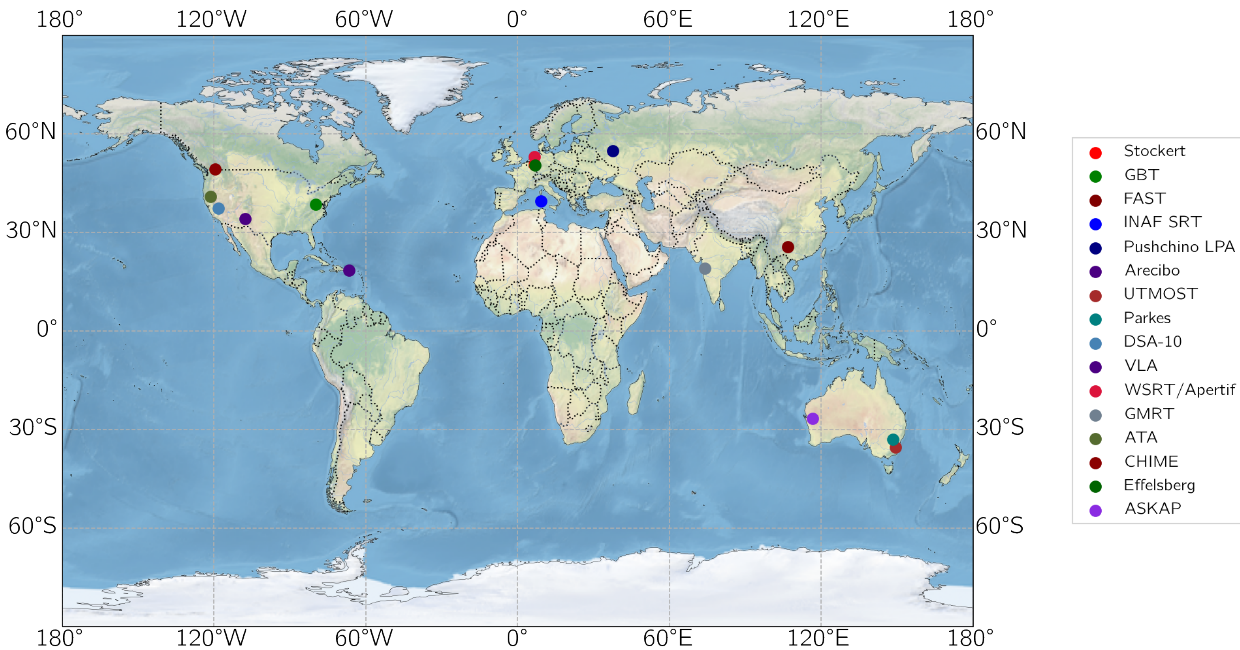


Figure 2.6: **A map of Radio Telescopes that have detected FRBs or have dedicated FRB surveys**

### 2.2.5 What is missing in the story of Fast Radio Bursts and why do we care?

Since the first FRB, the *Lorimer Burst*, several FRBs have been discovered by instruments across the globe [60]. From the considerable majority of the population of FRBs detected only a handful of events repeat and one of them is confirmed to be repeating with a periodicity[85]. Follow-up studies are thus limited and very challenging due to the lack of localization. This is because, radio telescopes that detect FRBs have a field of view that usually large enough to have several host galaxies within them. This is a significant dearth present in the quest to understand this phenomenon despite the many theories proposed [86].

### 2.2.6 What makes a good FRB detector?

*This section is a reproduction of [87] written by Dr. Jeffery Peterson, Dr. Kevin Bandura and me.*

The optimum parameters for a custom FRB telescope may depart substantially from previous telescope designs. Below we examine a set of hypothetical telescope layouts and calculate the dependence of FRB detection rate on array element collecting area as well as survey frequency and the number of elements.

We restrict our analysis to close-packed, drift-scan arrays. Alternatives not considered include Large single dishes with a focal plane array of feeds–these are more expensive than close-packed arrays of the same collecting area; Dilute dish arrays–these have increased processing costs, with a different signal processing system than discussed here; Telescopes with tracking systems–the added cost of the tracking system does not result in an increase in the FRB discovery rate.

#### 2.2.6.1 Projected FRB detection rates

We consider two types of array elements: on-axis paraboloidal dishes and square aperture array tiles with a single-beam[2] coherent analog summing network. Each tile consists of $m = 1, 4, 9...$ dipole-like antennas. $n$ elements are close-packed to form the telescope. We leave cylinder arrays [88] to future analysis since these are phased-array-dish hybrids and should produce rates that fall between the two cases we consider.

Each element covers the same instantaneous field of view $\Omega = 4\pi/G$, defined in terms of the peak antenna gain $G$ [89]. The effective collecting area of each element $A_{\rm el}$ is related to $\Omega$ via the diffraction relation,

$$A_{\rm el}\,\Omega = \lambda^2. \tag{2.6}$$

Diffraction forces a trade-off: while an increase of $A_{\rm el}$ allows dimmer FRBs to be detected, the resulting increase in detection rate is moderated by a decreased field of view $\Omega$. Note that the total effective area of the telescope is $A_{\rm tel} = 2nA_{\rm el}$. The factor of two accounts for the assumption that both polarizations are used.

[2]Suppose, in the interest of increasing sky coverage, a telescope designer decided to form not one but four coherent beams, producing four signals from every tile. The three new beams would each require a new signal processing channel. Given that there are now four times as many signal processors another option would be to increase sky coverage by making each tile smaller by a factor of two in each dimension, keeping one beam per tile, and making four times as many tiles. The two systems would have the same sky coverage, the number of dipoles, signal processor channels, and total collecting area and provide the same FRB rate. However, the multi-beam system would have the added cost of the additional analog beam-formers as well as substantially increased system complexity. The simpler more cost-efficient choice is to form just one beam per tile and adjust the sky coverage using the tile size $m$. We, therefore, proceed with consideration of single-beam tiles, setting aside as redundant the multi-beam options.

The beam solid angle $\Omega$ is limited by the horizon to half the sky. Furthermore, no antenna design allows uniform sensitivity across a full hemisphere, so a practical maximum to the field of view is $\Omega \sim \pi$. The aperture array tile with $m = 1$ is considered the 'all-sky' option since it has the widest beam and also maintains substantial sensitivity from horizon to horizon.

The individual antennas within an aperture array tile are assumed to be dipole-like antennas close to a ground plane. These might be four-squares, clovers, sloping bow-ties, etc. We generically assume $G = 4$ and $\Omega = \pi$ for these individual antennas.

We assume the FRB detection rate can be represented as a power law

$$R(> F_{min}) = R_o \left[\frac{F_{min}}{F_o}\right]^{\alpha} \frac{\Omega}{4\pi}, \tag{2.7}$$

where the all-sky rate normalization $R_o$ is drawn from results of a previous survey with fluence threshold $F_o$. We discuss the limited knowledge of the all-sky rate below. The limiting fluence $F_{min}$ is defined below. The power law index of the integrated source count distribution function $\alpha$ has the value $-3/2$ corresponding to a Euclidean universe, if the median FRBs redshift is well below one, the co-moving FRB rate does not evolve substantially over the observed redshift range and the local universe has negligible density structure. This index can be difficult to measure accurately because it can be difficult to estimate survey completeness near the fluence limit. Worse, estimates of $\alpha$ are often made by comparing surveys, which may have differing RFI cuts and search algorithm efficiencies. To accommodate a range of possible indices we consider $\alpha = -1.0, -1.5, -2.0$.

The limiting fluence $F_{min}$ of a survey is given by the radiometer equation in which

$$F_{min} = \frac{\mathrm{SNR_{min}}\ \mathrm{k_B}\ \mathrm{T_{sys}}\ \tau_\mathrm{b}}{2nA_\mathrm{el}\sqrt{\Delta\nu\ \tau_\mathrm{b}}}. \tag{2.8}$$

Here $\mathrm{SNR_{min}}$ is the signal to noise ratio threshold, which is set by the survey designers, $k_\mathrm{B}$ is the Boltzmann constant, $T_\mathrm{sys}$ is the system temperature, $\tau_\mathrm{b}$ is the burst duration and $\Delta\nu = f\nu_s$ is the bandwidth of the observation, which can be expressed as a fraction $f$ of the center frequency of the survey $\nu_s$.

Equations 2.6 to 2.8 combine to express a scaling law for the FRB detection rate,

$$R(> F_{min}) = \frac{R_o F_o{}^{-\alpha} c^2}{4\pi} \left[ \frac{\mathrm{SNR_{min}}\ \mathrm{k_B T_{sys}}\ \tau_\mathrm{b}}{2\sqrt{f\ \tau_\mathrm{b}}} \right]^\alpha A_\mathrm{el}^{-\alpha-1}\ \nu_s{}^{-\alpha/2-2}\ n^{-\alpha}. \tag{2.9}$$

The quantities in square braces are considered fixed in this analysis. For the frequency range, we consider $T_\mathrm{sys}$ is determined by receiver noise for much of the sky, but at frequencies below about 400 MHz a term should be added to $T_\mathrm{sys}$ to account for Galactic synchrotron emission. Absent cost considerations, for $\alpha \sim -1.5$, equation 4 pushes the design in the direction of increased element area, lower frequency, and higher element count. When costs are considered, below, the optimization is more complicated.

#### 2.2.6.2 Cost Model

We divide construction costs into three components: 1) The Radiation Collector–these costs increase with $A_\mathrm{el}$; 2) The Frequency Channelizer and 3) The Digital Beam Former. For dish arrays we adopt Radiation Collector cost function $C_d = D_o A_\mathrm{el}^{1.25}\ n$, a bit steeper than a linear function of dish area. We assume the dish cost is independent of frequency since many commercially available dishes are more precise than we require at these low frequencies. For aperture array tiles we adopt Radiation Collector cost function $C_a = A_o\ m\ n$, where $A_o$ is the cost of an individual dipole-like antenna. For the Frequency Channelizer we adopt the cost function $C_s = F_o\ f\ \nu\ n$, and for the Beam Digital Former we adopt cost function $B_o\ f\ \nu\ n\ ln(n)$. To set the cost coefficients $D_o$, $A_o$, $F_o$ and $B_o$ we use cost data for an FRB-search array of 12 six-meter dishes we built at Green Bank WV in 2019, scaled to $n \sim 1000$ elements. $D_o = 0.029[\mathrm{m}^{-2.5}]$, $S_o = 2.3 \times 10^{-3}$ [$\mathrm{MHz}^{-1}$], $F_o = 0.067$ and $B_o = 0.0067$.

#### 2.2.6.3 Frequency Dependence

Projected FRB detection rates fall dramatically with frequency, as seen in Figure 2.7, primarily because of the $\lambda^2$ factor in equation 2.6. Note that our calculations show only the instrumental impact

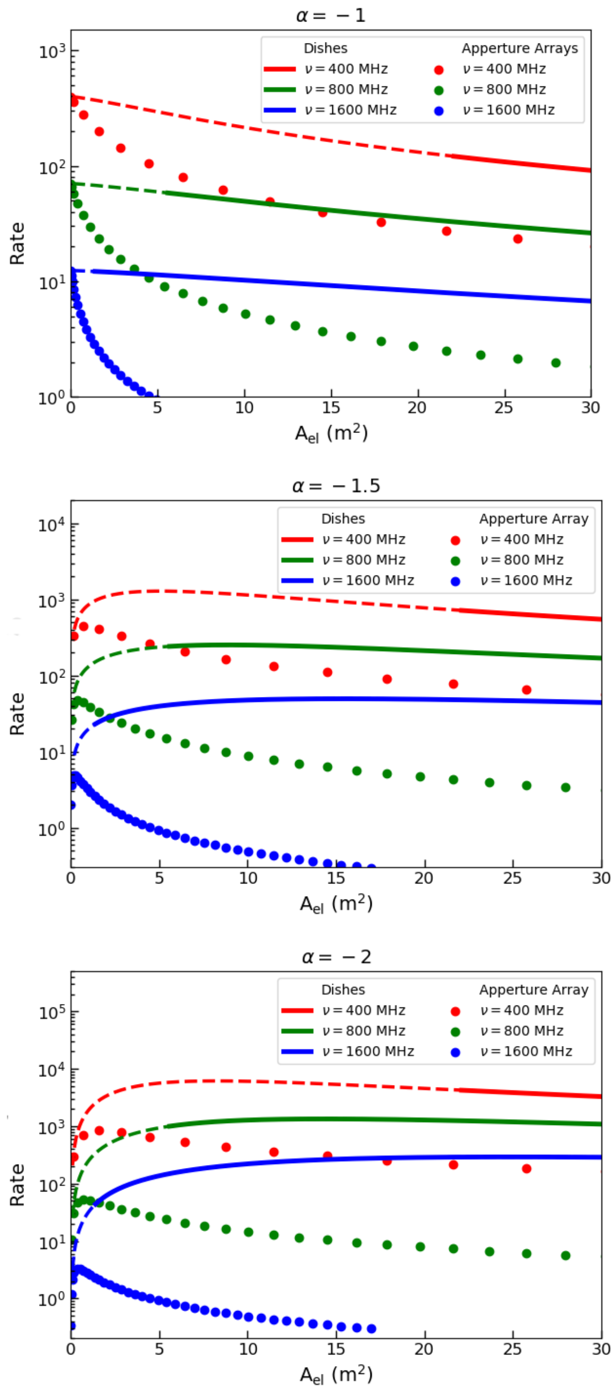


Figure 2.7: **Projected FRB detection rate**, for $\alpha = -1.0, -1.5, -2.0$ with three survey center frequencies: 400 MHz (red), 800 MHz (green), 1600 MHz (blue) and two element choices: Dishes (smooth curves) and Aperture Array Tiles (solid circles). Integer steps of aperture array dimension 1x1, 2x2, 3x3, etc. are shown. On-axis dishes smaller than $d = 5\lambda$ are not commonly used because of feed blockage inefficiency, so these rates are shown as dashed curves

of telescope parameters on the rate, while the on-sky rate also depends on the (unknown) source spectrum and possible pulse broadening during propagation. This scatter-broadening is expected at low frequencies due to plasma structure in the host galaxy or in the Milky Way and may produce a low-frequency falloff of the rate. The observational data on scattering are ambiguous. About 5 % of the entries in FRBCAT [60] have a measured scattering spectral index ($d\, ln\, \tau_{\rm scat}/d\, ln\, \nu$) with values ranging from –3.6 to –4.8, consistent with scattering in turbulent plasma. However, there are also FRB spectra that show no measurable scatter broadening, even at 400 MHz, the lowest detection frequency so far [90].

FRBs have been detected from 400 MHz to 8 GHz. Most archival searching has been done near 1.5 GHz so there is substantial rate information at that frequency. At and below 327 MHz there are reports of non-detection but the fluence limits of these surveys are much higher than for the higher frequency surveys. So far, there is at best weak evidence for any spectral slope of the FRB detection rate.

Since we calculate the instrument-specific impact of telescope parameters on the detection rate, we are implicitly assuming a flat prior distribution for $R_o(\nu_s)$, which is consistent with current data.

#### 2.2.6.4 Number of array elements

Budgets have limits, so we fix the total telescope cost at the arbitrary value of 2000 units, which allows for an interesting detection rate of 100s to 1000s of FRBs per year. This leads to a telescope with $n \sim 1000$ elements. Under this constraint increasing the element collecting area will entail a reduction in the number of elements. This creates a peak in the rate function $R(A_{\rm el})$ at which the cost efficiency is maximized.

#### 2.2.6.5 Element effective area

The dependence of projected FRB detection rate on $A_{\rm el}$ is shown in Figure 2.7. The assumptions used in this plot are: $T_{\rm sys} = 50$ K, $\tau_{\rm b} = 2$ ms, ${\rm SNR}_{\rm min} = 10$ and $f = 0.66$, We used a recent Parkes Survey to normalize the rate: $R_o = 1700/{\rm day}$ , $F_o = 2$ Jy ms. This is a conservative choice since other surveys find substantially higher rates.

#### 2.2.6.6 Discussion

For aperture arrays the optimal rate decreases by 0.062 per frequency doubling for $\alpha = -2$ and 0.20 per frequency doubling for $\alpha = -1$. For dish arrays the decrease is 0.22 per frequency doubling ($\alpha = -2$) and 0.18 per frequency doubling ($\alpha = -1$). All these factors are less than 1/4 so we find the cost efficiency of such telescopes falls with the frequency with at least two powers of $\nu_s$. Once the on-sky rate versus frequency is measured, if low-frequency FRBs are rare, the source spectral slope and/or scattering spectral slope may compensate for the telescope cost-efficiency spectral slope. The optimum frequency can then be determined by locating the point where the combined slope is zero. However, scattering is absent in several published FRB spectra at 400 MHz, indicating that a high throughput search below this frequency should yield FRB detections. If the CHIME team finds an all-sky rate versus frequency with a spectral index greater than 2 they may be able to locate the optimum frequency within their band. If the index is below 2 the optimum lies below 400 MHz.

The source count index $\alpha$ determines which array type (dishes versus aperture array tiles) is most cost-efficient. The critical point is near $\alpha = -1.0$. If dim FRBs are rare enough ($\alpha > -1$) the all-sky array is the most cost-efficient choice. In the future, it is reasonable to assume signal processing costs will continue to fall. As this happens the cost efficiency of the all-sky aperture array will see the greatest improvement to cost efficiency, since this configuration has costs strongly dominated by the signal processor. Paying attention to cost efficiency allows the telescope designer to use funding efficiently, however, there may be scientific goals that push the design away from peak rates. For example, widening the field of view can be useful to increase the event rate of rare, bright, nearby FRBs. Some emission models [91] predict weak x-ray to gamma-ray afterglows which would only be detectable for nearby FRBs. The most constraining test of these models will come from an all-sky FRB telescope. Telescopes with element collecting areas larger than the area at the rate peak may also have a scientific benefit that justifies the increased cost. Increasing the collecting area means the survey will be deep rather than wide, which increases the average redshift of the FRBs detected, providing longer paths on which to study the ionized universe and search for microlensing, while also allowing the study of the cosmic evolution of the FRB event rate.

Throughout this analysis we have focused on the FRB detection rate using a single close-packed array telescope, setting aside the important topic of precise localization of the sources. Outrigger arrays will be needed to provide this localization. These can be built of the same elements as the central close-packed array and placed hundreds to thousands of kilometers away. The outriggers can have a combined area substantially smaller than the central array since the central array provides high SNR waveform templates which can be used to recover the weaker signal from the outriggers.

When designing a telescope specifically to detect FRBs some design constraints can be relaxed. Array telescopes can have aliases and false point source locations. The position of these aliases moves on the sky with frequency while the true source position remains fixed, so for FRBs that sweep in frequency, the aliased positions can be identified and deleted. This means the dipole-like antennas can have spacing wider than the Nyquist spacing needed to eliminate aliases. This increases $A_{\mathrm{el}}$. Compared to intensity mapping telescopes, FRB telescopes also have less stringent requirements for gain calibration precision and low sidelobe response.

#### 2.2.6.7 Conclusion

We have presented optimization calculations for radio telescope arrays used for the detection of FRBs. The instrument-specific detection rates fall with a frequency indicating low survey frequencies are preferred. However, other factors influence the on-sky rate, such as possible low-frequency falloff of rates due to scattering, and the intrinsic source spectral index. These other factors are currently poorly constrained. Current published data is inadequate to identify an optimum survey frequency. The lack of scattering at 400 MHz in some FRB spectra indicates searches at frequencies below 400 MHz should be productive.

If the source count index $\alpha > -1$, cost efficiency favors the minimal element area–the all-sky aperture array designs. For $\alpha < -1$, cost efficiency favors dish arrays over aperture arrays, with the peak in cost efficiency moving to a larger element area for smaller $\alpha$.

Apart from cost considerations, the science goals for wide and narrow field observation differ. All-sky telescopes can be used to understand the FRB emission mechanism, by allowing the detection of rare, nearby, bright events which can be followed up at other wavelengths with high sensitivity and spatial resolution. In contrast, a larger element area allows detection of dimmer FRBs along longer paths through the ionized universe, allowing improved constraints to the evolution of FRB rates over cosmic time, increased occurrence of lensed events, and tighter cosmological constraints.

## 2.3 CHIME/FRB

The Canadian Hydrogen Intensity Mapping Experiment (CHIME) is a transient telescope operating in the 400–800 MHz band (Figure 2.8a), with an $8000\mathrm{m}^2$ aperture area of semi-cylindrical paraboloid reflectors. It is located at the Dominion Radio Astrophysical Observatory (DRAO) near Penticton, British Columbia. The Canadian Hydrogen Intensity Mapping Experiment - Pathfinder (CHIME-Pf), two $36\mathrm{m}$ long $20\mathrm{m}$ wide cylinders of and 128 dual-polarization antennas is a technological precurser to CHIME. The CHIME-Pf, located at DRAO, was a prototype for CHIME (Bandura 2014; Denman 2019).

CHIME was originally designed for the measurement of Baryon Acoustic Oscillation (BAO), to study redshifted neutral hydrogen gas ($z = 0.8 - 2.5$) to precisely constrain dark energy. The choice of operating frequency, collecting area, and angular resolution for the CHIME telescope was driven by the original motivation for the project to measure and map the BAO. Assuming the FRB detection rate can be represented as a power law,

$$R(> F_{min}) = R_o \left[\frac{F_{min}}{F_o}\right]^{\alpha} \frac{\Omega}{4\pi}, \tag{2.10}$$

where the all-sky rate normalization $R_o$ is drawn from results of a previous survey with fluence threshold $F_o$. The power law index of the integrated source count distribution function $\alpha$ has the euclidean value $-3/2$ if the median FRBs redshift is well below one, the co-moving FRB rate does not evolve substantially over the observed redshift range and the local universe has negligible density structure. For this simple model, it is clear that an increased field of view allows for a large FRB detection rate. The large ($\sim 200\,^{\circ 2}$) field of view proves to be invaluable as a prolific FRB detector [90, 92–95].

### 2.3.1 The CHIME telescope

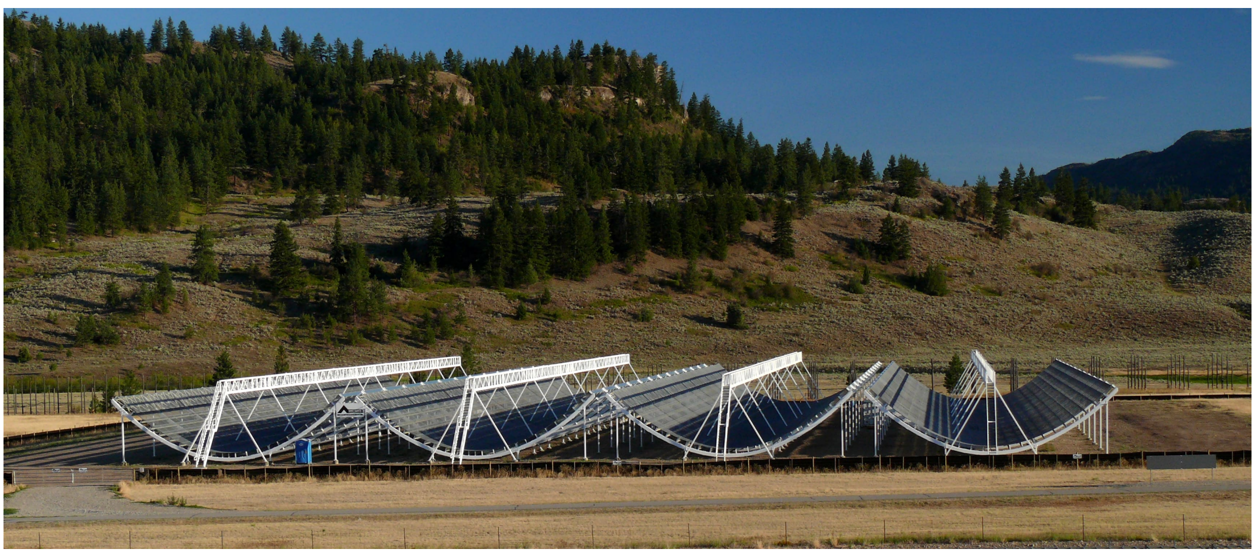

(a) **CHIME Telescope** credit: CHIME/FRB Collaboration

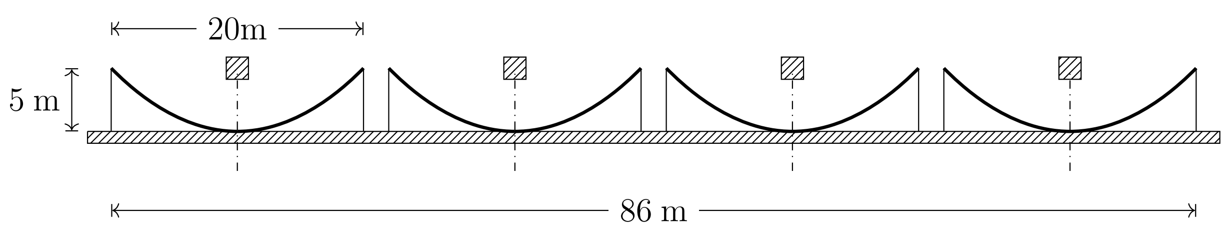


(b) **Cross Section of CHIME**

Figure 2.8: **CHIME Telescope** located at the Dominion Radio Astrophysical Observatory (DRAO) near Penticton, British Columbia, Canada.

The CHIME telescope consists of four $20\,\mathrm{m} \times 100\,\mathrm{m}$ cylindrical paraboloid reflectors oriented with the cylinder axis in the North-South direction [96]. Each cylinder is fitted with $256$ dual-linear-Polarization antennas that are sensitive in the frequency range of $400$–$800\,\mathrm{MHz}$. The $2048$ analog signals from the antennas are amplified and digitized at an array of $128$ field-programmable gate array (FPGA) driven motherboards with mezzanine analog to digital converters (ADCs) called ICE boards [97]. At each ICE board, raw voltages are channelized with a polyphase filterbank (PFB) producing $1024$ complex channels with $2.56\,\mu\mathrm{s}$ time resolution. We refer to the channelized and time-tagged voltage data as raw baseband data. These data are sent to $256$ GPU-based compute nodes comprising the X-Engine correlator driven by the open-source `kotekan`[3] software [98, 99]. The X-engine processes the baseband to different data products for the CHIME/Cosmology and the CHIME/Pulsar backends (see Figure 2.9a) and CHIME/FRB.

[3]The kotekan software repository: https://github.com/kotekan/kotekan.

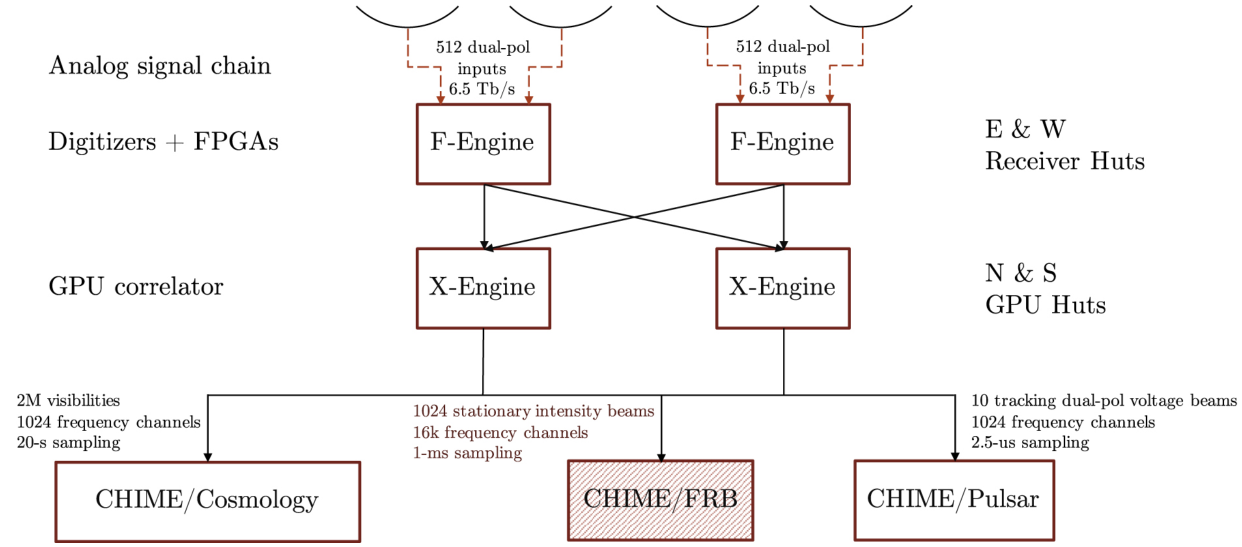


(a) **Schematic of the CHIME telescope signal path.** The four cylinders (black arcs), the correlator (F-and X-Engines), and the backend science instruments are shown. The dashed orange segments depict analog signals carrying coaxial cables from the 256 feeds on each cylinder to the F-Engines in the corresponding East or West receiver huts beneath the cylinders. The black segments depict digital data carried through copper and fiber cables. The CHIME/FRB backend is hatched.

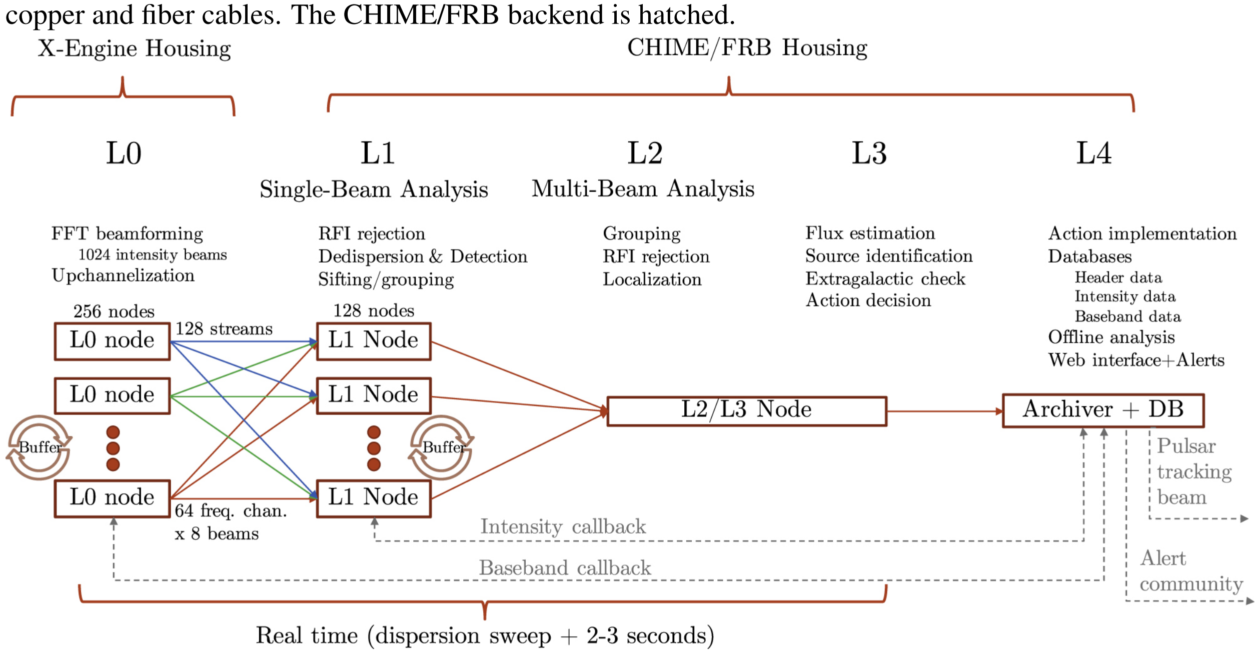


(b) **Schematic of the CHIME/FRB software pipeline.** L0 performs the beam-forming and up-channelization. L1 performs RFI rejection and dedispersion. L2, L3, and L4, assembles data from all beams, classify the detections, provide alerts, and store events. The L1 buffer, available in each node, is for intensity data callback and the L0 buffer is for the baseband callback.

Figure 2.9: **CHIME/FRB System schematic from [88]**

A summary of the CHIME telescope is in Table 2.1.

| Parameter | Value |
|---|---|
| Latitude | $-119.623677\,(43)$ deg |
| Longitude | $49.320709\,(22)$ deg |
| Collecting Area | $8000\ \mathrm{m}^2$ |
| Frequency Range | 400 – 800 MHz |
| Frequency Resolution | 390 kHz, 1024 Channels |
| Focal ratio ($f/D$) | 0.25 |
| East – West FoV | 2.5–1.3 degrees |
| North – South FoV | ∼110 degrees |

Table 2.1: **Instrument parameters for CHIME/FRB.**

### 2.3.2 CHIME/FRB

Here, the spatial correlation is computed and Polarizations are summed, forming $1024$ (256-NS $\times$ $4$-EW) independent beams within the North-South primary beam [40]. These beams are searched for FRBs in real-time using detection pipelines designed for discovering radio transients where each beam is processed to perform RFI excision, dedispersion, detection and event sifting and database management (see Figure 2.9b).

The real-time pipeline and the baseband system collectively make up the CHIME/FRB instrument [100, 101]. The baseband system uses a memory ring buffer system to record (or 'dump') baseband data to disk. The ring buffer holds $\sim$35.5 s of baseband data for subsequent capture by a detection trigger. On successful detection of an FRB candidate by the real-time pipeline above an SNR of 12, a trigger from the real-time pipeline saves a snapshot of $\sim$100 ms of data centered around the pulse at each frequency channel of the baseband buffer. The latency between the time of arrival of a signal and the triggered baseband recording is typically $\sim$14 s. The buffer can record the full band's worth of data when the dispersive sweep of the FRB does not exceed $\sim$20 s (corresponding to a maximum DM of $\sim$1000 $\mathrm{pc\,cm^{-3}}$).

### 2.3.3 CHIME/FRB Results

CHIME/FRB has been pivotal in the contemporary FRB landscape with several interesting results (as of mid-2022) which include:

- an FRB with periodicity [102];
- an 'FRB' from a Galactic magnetar [103] first detected by CHIME/FRB and simultaneously by the Survey for Transient Astronomical Radio Emission 2 (STARE2) instrument [104] paving way to a strong contender for an FRB progenitor;
- an exhaustive FRB catalog from the first year observations [105];
- confirmation of the independence of FRBs' sky position from Galactic latitude [106] solidifying its extragalactic nature;
- confirmation of the presence of FRB morphology archetypes differentiating 'repeaters' from 'one-off' [107] (see Figure 2.4);
- evidence of a statistical cross-correlations with large-scale structure [108];
- in burst sub-second periodicity [109];
- constraining the fraction of primordial blackholes using gravitational lensing [110, 111].

This work expands the capabilities of CHIME/FRB by commissioning outriggers that will enable milli-arcsecond localizations daily.

# Chapter 3

# TONE: A CHIME/FRB Outrigger Pathfinder for localizations of Fast Radio Bursts with Very Long Baseline Ineterferometry

This chapter describes TONE – a CHIME/FRB Outrigger pathfinder. I have worked on every aspect of the TONE telescope. I physically built the structure and assembled, tested, and integrated the analog chain and the digital system. I also developed tools to characterize the telescope. This chapter represents a future system paper with the same title planned to be submitted for publication in an astronomy instrumentation-focused journal shortly.

## 3.1 Introduction

Figure 3.1: **TONE:** The array of dishes at the Green Bank Observatory (GBO).

TONE (see Figure. 3.1) is a new telescope designed to be an outrigger – working in tandem with the CHIME/FRB. The primary consideration was to be able to detect pulses from FRBs at least in cross-correlation with CHIME and localize them to sub-arcsecond accuracy upon the first instance of detection. The secondary goal was to demonstrate key aspects of the hardware and software required for future larger implementations of the CHIME/FRB Outriggers as well as serve as a test for technologies that may enable projects such as HIRAX [112, 113] and CHORD [114].

## 3.2 Location

TONE is located at the Green Bank Observatory (GBO) near the interferometer control building of the Green Bank interferometer. The national radio-quiet zone gives an excellent environment free from radio frequency interference (RFI). Existing radio astronomical infrastructure allows for invaluable resources such as buildings to house the backend with adequate power, gigabit fiber internet link, and access to the site maser clock. The $B_{\mathrm{km}} \sim 3300\,\mathrm{km}$ baseline between CHIME and TONE (see Figure 3.2) gives us an angular resolution,

$$\theta_{\mathrm{FWHM}} \sim 2063 \times \frac{\lambda_{\mathrm{cm}}}{B_{\mathrm{km}}}, \tag{3.1}$$

which at $400\,\mathrm{MHz} \equiv \lambda_{\mathrm{cm}} = 75\,\mathrm{cm}$ gives $\theta_{\mathrm{FWHM}} \sim 50\,\mathrm{mas}$. This would potentially allow us localize the FRBs inside their host galaxies [115].

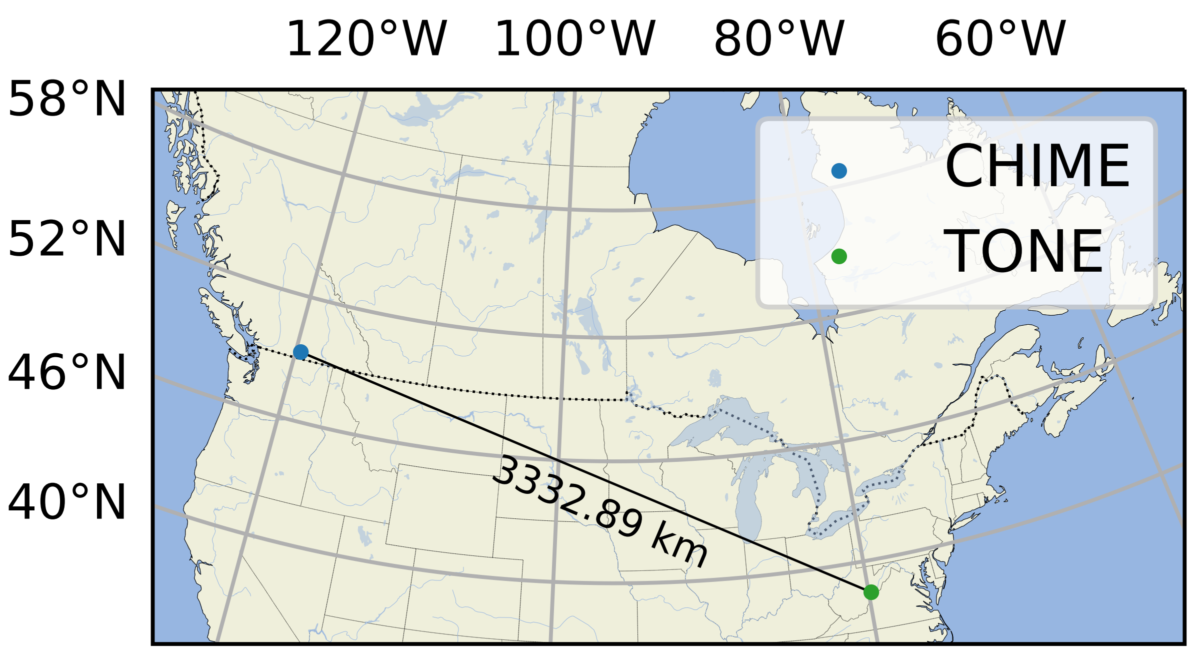


Figure 3.2: **Location of the CHIME and TONE.**

## 3.3 The TONE array

The array was designed to have $12 \times 6$m parabolic dishes arranged in a regular close-packed rectangular pattern. Each dish is an aluminum parabolic design with a steel frame. They were purchased off the shelf significantly reducing cost. We accomplished the assembly of 8 dishes with two dishes that flew away and were damaged beyond repair in a wind storm, one left to be assembled and one is currently redundant. The array bases are positioned along a line 30 degrees from the true north. The layout of the dishes from positions from satellite imagery is shown in Figure 3.3. The dishes are pointed towards the Crab pulsar when it is at the CHIME meridian. We use the continuum radio source from the Crab nebula designated Taurus–A as a calibrator for the array for beamforming. The Crab giant pulse is used as a VLBI astrometric calibrator. Our intended plans for a regular array were impeded by construction logistics and dishes destroyed by strong wind storms. The commissioned array is shown in Figure 3.3.

| **Parameter** | **Value** |
|---|---|
| Number of Dishes | 8 (out of 12 planned) |
| Frequency Range | 400 – 800 MHz |
| Frequency Resolution | 390 kHz, 1024 Channels |
| Dish Diameter | 6 m |
| Dish focal ratio ($f/D$) | $\sim 0.4$ |
| Planned Layout | $4 \times 3$ with $9.1$ m spacing |
| Primary Beam FWHM | $\sim$11 – 5 degrees |

Table 3.1: **Instrumental parameters for TONE.**

(a) Satellite imagery of the TONE dishes Credit: Bing Maps

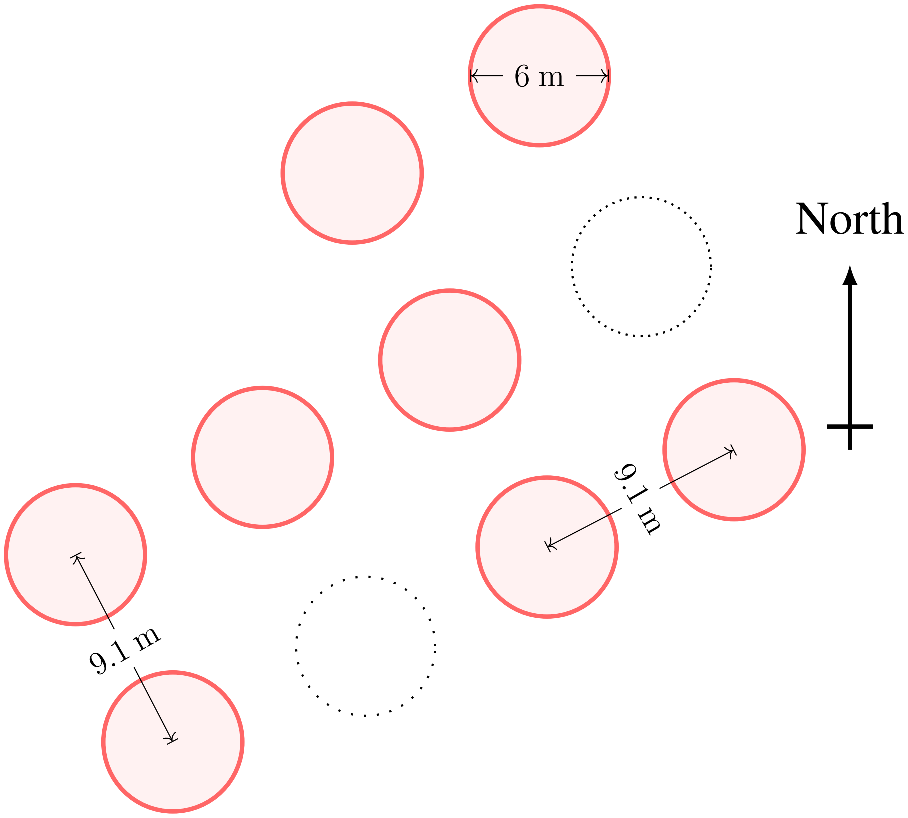

(b) The red circle represent the commissioned dishes.

Figure 3.3: **Arrangement of the currently commissioned Dishes.**

## 3.4 The Analog Chain

The analog chain (Figure 3.4) consists of a dual-polarized clover leaf-shaped dipole antenna with a full octave response between 400 to 800 MHz [116]. The antenna has a low noise amplifier right near the antenna. The amplified signal is passed via a coaxial cable to the Radio Frequency over Fiber (RFoF) transmitter. The signal is sent via fiber in buried conduits to the interferometer control building into the digital backend.

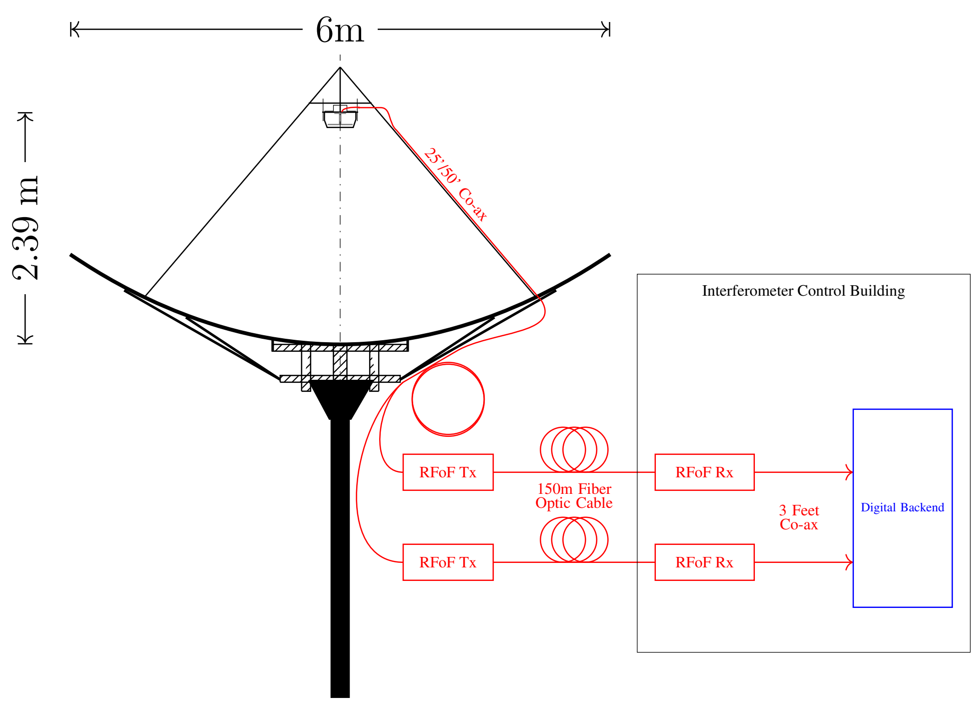


Figure 3.4: **The analog chain of TONE from a single dish:** The analog signal collected by the active feeds from each polarization is sent over 25-50 feet of coaxial cables (not all cables are the same length for all the dishes some are 25 feet and some 50 feet). The signal from the coaxial cables is sent over $150\,\mathrm{m}$ of fiber optic cable to an electromagnetic compliant rack inside the interferometer control building using a custom RFoF system. The receiver converts the light back to an electrical signal that is then digitized by the ICE Boards to be processing.

### 3.4.1 Cloverleaf Antenna & Low Noise Amplifier

We use a dual-polarization cloverleaf feed (Figure 3.5) based on the design that was developed for CHIME and being selected to use for HIRAX [113]. It is an active feed that consists of a balun that uses an Avago MGA-16116 dual amplifier, and the difference between the outputs is amplified using a Mini-Circuits PSA4-5043+ amplifier. Each feed is mounted inside a cylindrical can, which circularizes the beam and helps reduce cross-talk to an extent. Each antenna-can assembly is mounted at the focus by struts extending from the dish and a custom pyramid structure. The active antennae are powered by 2 central power supply units supplying $\sim 7$ Volts directly over copper electrical cables. Over the past year of operations, some feeds have been replaced by CHIME-like passive feeds and new LNA designs. The feeds are protected from the elements by custom vacuum-formed plastic covers and neoprene seals.

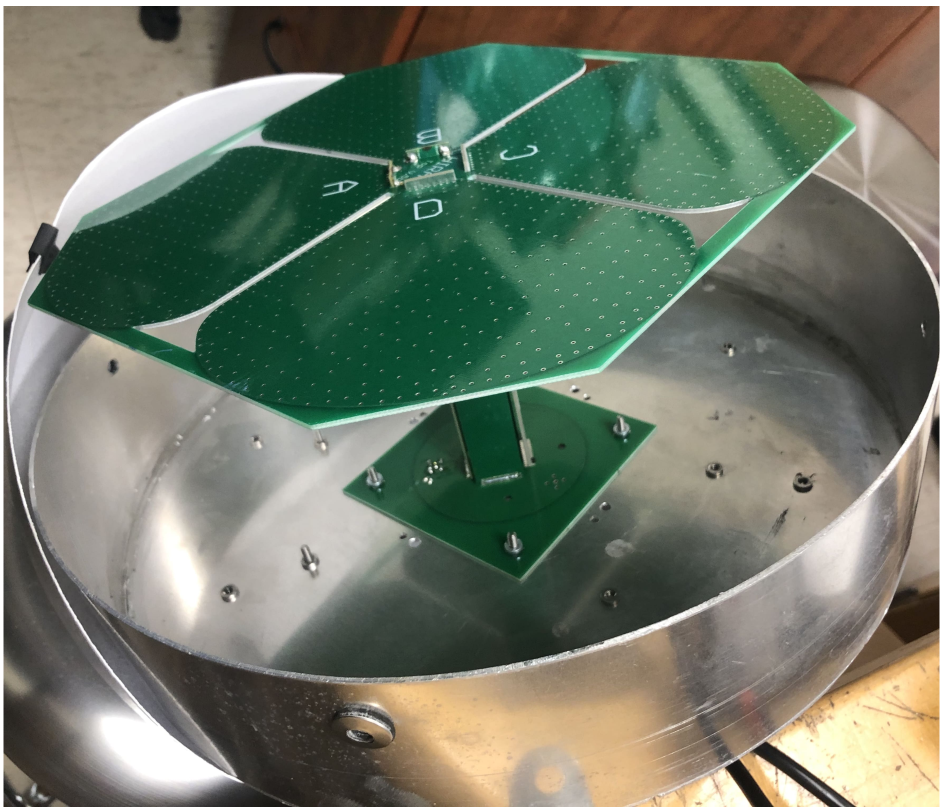


Figure 3.5: **The Feed with the cloverleaf antenna.**

### 3.4.2 Radio Frequency over Fiber (RFoF) system

Signals received by each polarization of the feed are sent over coaxial cables to a junction box at the pole below every dish. This is fed into an RFoF transmitter module (Figure 3.6). It is then band-limited to $400$–$800\,\mathrm{MHz}$ and passed through an amplification stage before being intensity-modulated on an optical carrier. $150\,\mathrm{m}$ of optical fibers carry these signals to the digital backend server rack, where RFoF receivers convert the signals back into electrical voltages. The RF signals are subsequently amplified and filtered again before being passed to the ICE boards. The RFoF transmitter and receiver design is based on technology that was developed by CHIME. The transmitter contains a laser diode (AGX Technologies, FPMR3 series) that is intensity-modulated by the incoming RF signal, and the receiver contains a photodetector (AGX Technologies, PPDD series) that converts the transmitted optical signal into RF.

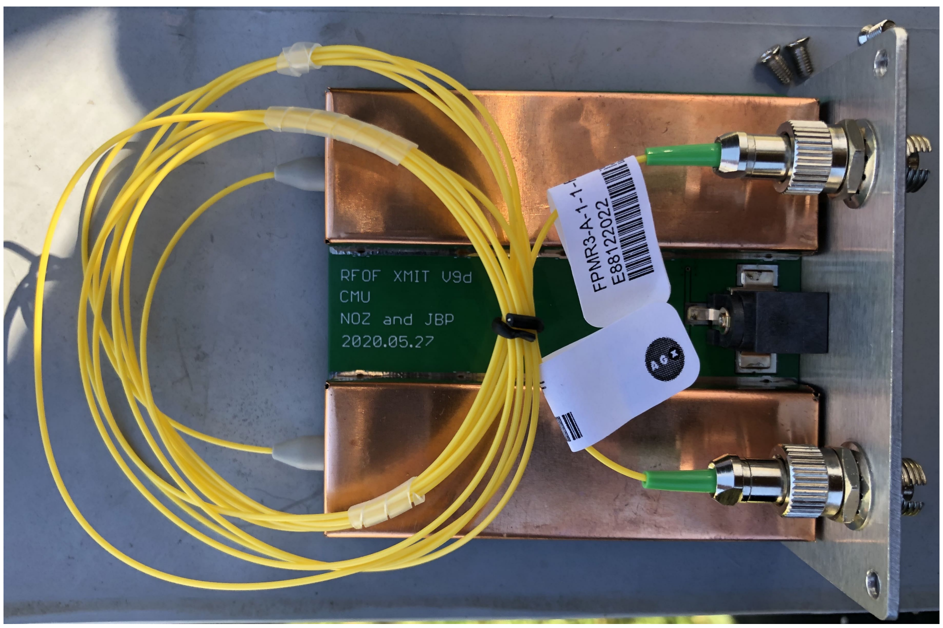


Figure 3.6: **The RFoF system:** Designed by Dr. Jeffrey B. Peterson of Department of Physics, Carnegie Mellon University.

## 3.5 Digital system

Much like CHIME (see 2.3), the TONE backend is operated with an FX correlator architecture without the “X” engine. In the “F” stage, a total of 16 wideband analog signals from the analog chain in the 400-800 MHz frequency band are alias-sampled at 800 Msps into the 2nd Nyquist zone by the analog to digital converters (ADCs) on the mezzanines of the ICE Boards [117, 118].

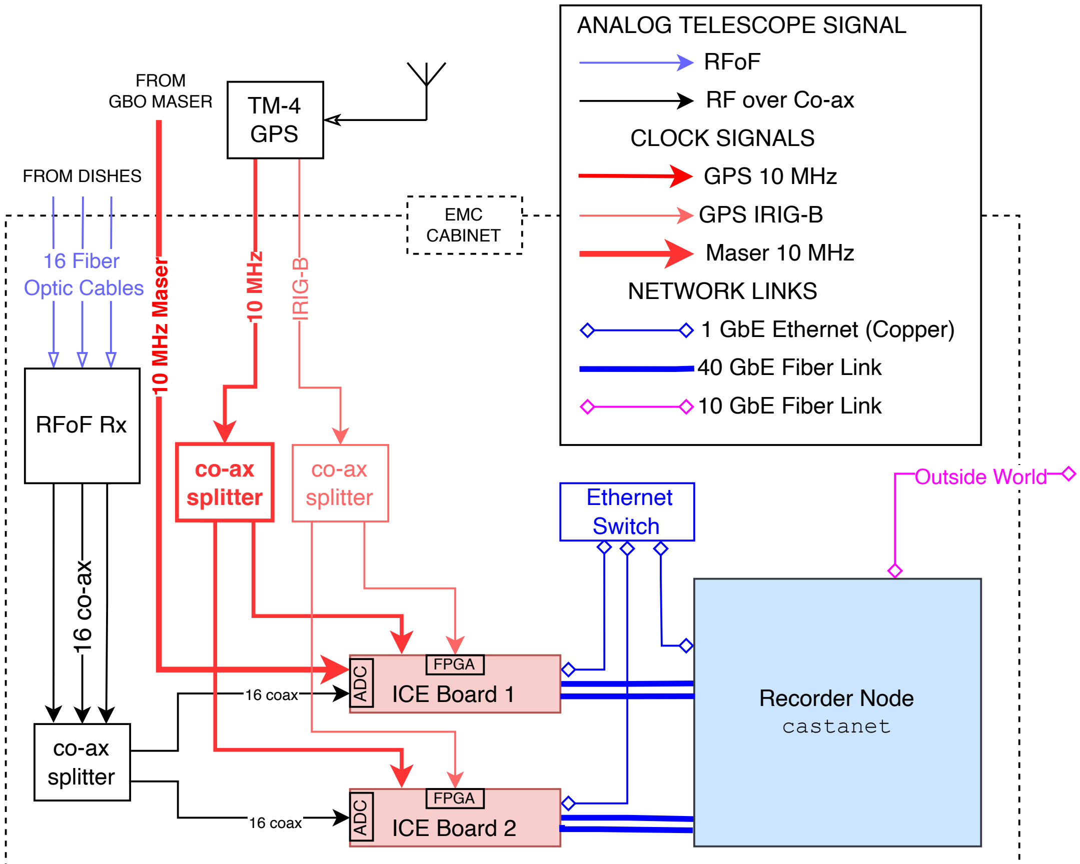


Figure 3.7: **A flow graph of the digital digital backend system.**

### 3.5.1 ICE Board

The F-engine for TONE is based on the ICE system [117, 118]. It is a custom FPGA motherboard that makes use of a Xilinx Kintex-7 FPGA and ARM-based co-processor. It processes 16 digitized inputs from 8 dual-polarization feeds. The ICE boards use custom FPGA-based electronics to digitize the incoming signals from the RFoF system at a precision of 8 bits over the full 400 MHz of bandwidth at 800Msps. For the channelization step, these digitized signals are processed by a polyphase filter bank and FFT-based pipeline, producing the 1024 frequency channels (390 kHz wide) that are passed to the recorder node. This is the `shuffle16` mode where after the channelization the FPGA performs the real-time corner-turn operation, which arranges the outgoing data such that each node of the X-engine receives data streams from all inputs over the subset of the bandwidth to be processed by that node. The mode used for TONE breaks data to be sent to the recorder via two 40GbE QSFP+ fiber links over $8 \times 10$ gigabit lanes sending 128 frequencies in each lane. Additionally, we have a second ICEboard that performs a full correlation and integrates to send all visibilities over a gigabit link to the recorder node. This mode, called the 'corr16' mode or correlator mode, is used for system characterization. Additionally, a snapshot of 2048 raw ADC samples is sent over the gigabit network every second. These boards each are fed inputs from the same analog signals from the RFoF that have been split with a simple resistive coaxial splitter. The ICE boards are controlled by a custom python software, `pychfpga`[1], which is used to communicate with and program the FPGA and the ARM coprocessor.

### 3.5.2 Timing

The ICE boards are synchronized using a 10 MHz signal and are supplied absolute time to the FPGA in the IRIG–B format [2] from a TM-4 GPS receiver [3]. A 10 MHz signal from the GBO site maser, which is a distributed 1 pulse per second signal from the Microsemi MHM 2010 Active Hydrogen Maser, is fed to one of the inputs of the ICE board to measure clock jitter.

### 3.5.3 Recorder node

In a traditional digital radio telescope, the baseband data would be passed along via corner-turn to an X-engine which computes visibilities in real-time. The system design was strictly constrained by the science case of saving baseband data to cross-correlate for VLBI localization. As seen in Figure 3.7 the data from the ICE board is sent via 2 x 40 Gb links to the server code we call `castanet`. In `castanet`, a chime-like baseband readout system is set up where the baseband data is stored in a continuous ∼40 s long ring buffer in a high-density memory that awaits for a "trigger" on receipt of which 500 ms time slice of the buffer is recorded to disk. This is implemented in the open-source high performance data streaming software designed for radio telescopes

[1] https://bitbucket.org/winterlandcosmology/pychfpga/src/master/

[2] https://www.wsmr.army.mil/RCCsite/Documents/200-16_IRIG_Serial_Time_Code_Formats/200-16_IRIG_Serial_Time_Code_Formats.pdf

[3] A modified TM4–D receiver with the time distribution system disconnected and removed https://www.spectruminstruments.net/products/tm4d/tm4d.html

kotekan [4].

| Parts | Part Number | Specifications |
|---|---|---|
| Motherboard | TYAN Tempest EX S7100-EX | 4×PCIeX16, 3×PCIeX8, 2 sockets |
| CPU | 1×Xeon Silver 4116 | 12 cores (hyperthreaded) ×2.1 GHz |
| Memory | 4×HYNIX HMAA8GR7A2R4N-VN | 128 GB |
| Network | 2×Silicom PE 31640G2QI71/QX4 | 2 × 4×10 GbE |

Table 3.2: Components in the baseband recorder server, named castanet, of the digital backend.

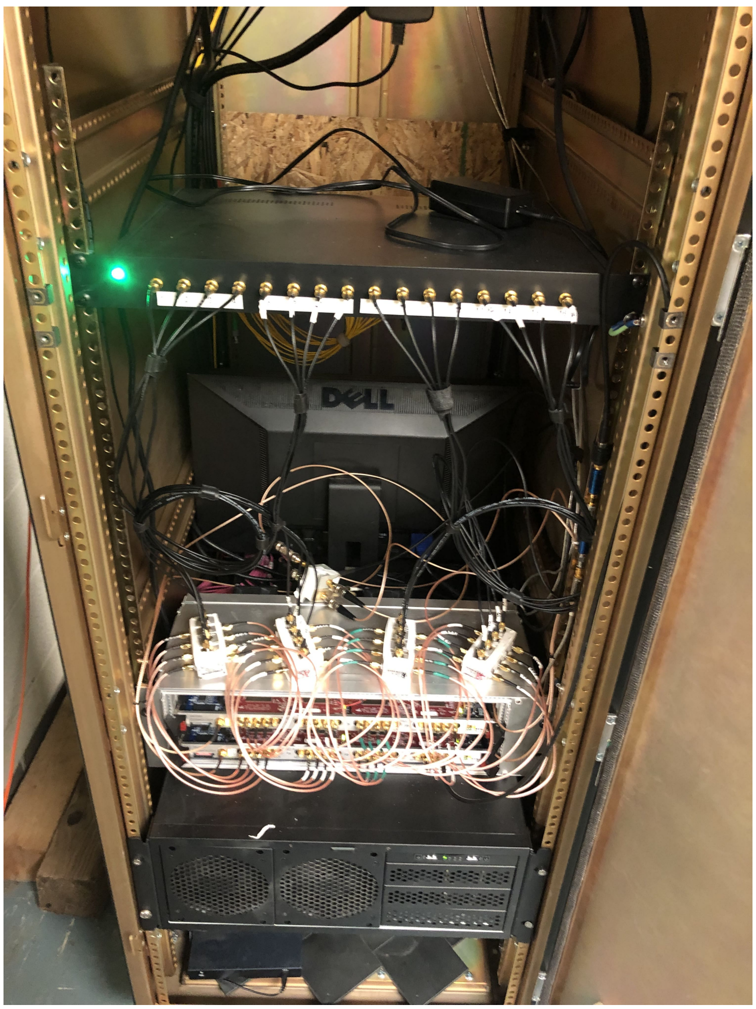


Figure 3.8: **Digital Back-end of TONE:** A picture of the digital backend inside the EMI compliant rack. *From the top:* The RFoF receiver, the ICE boards, and the Recorder node. The base of the rack has power supplies to power the ICE Board and a gigabit switch for the internal network

[4] https://github.com/kotekan/kotekan

### 3.5.4 VLBI Triggering System

To facilitate concurrent observations an asynchronous server is set up such that interfaces with endpoints on `kotekan` of the digital backend. It is called `frb-outrigger`. A reverse ssh tunnel is set up to the CHIME network. A "heartbeat" `frb-outrigger` is sent to CHIME/FRB's backend informing that the outrigger is online as well as the relevant CHIME beams to monitor for FRB detection in the real-time detection pipeline. On a detection in the real-time detection system, a trigger is sent over the reverse ssh tunnel. The script extracts the time of arrival of the pulse, the DM, and the DM error. This information is sent to the `kotekan` baseband endpoint which saves a slice of baseband data centered around the frequency dispersed pulse to disk. Additionally, the trigger script gathers information from the incoming trigger, the path to the recent digital gains, and the path to the appropriate raw ADC data. The latency of the system from data readout to disk against the trigger time is roughly an average of $\sim$14 seconds which is dominated by the CHIME/FRB real-time detection pipeline.

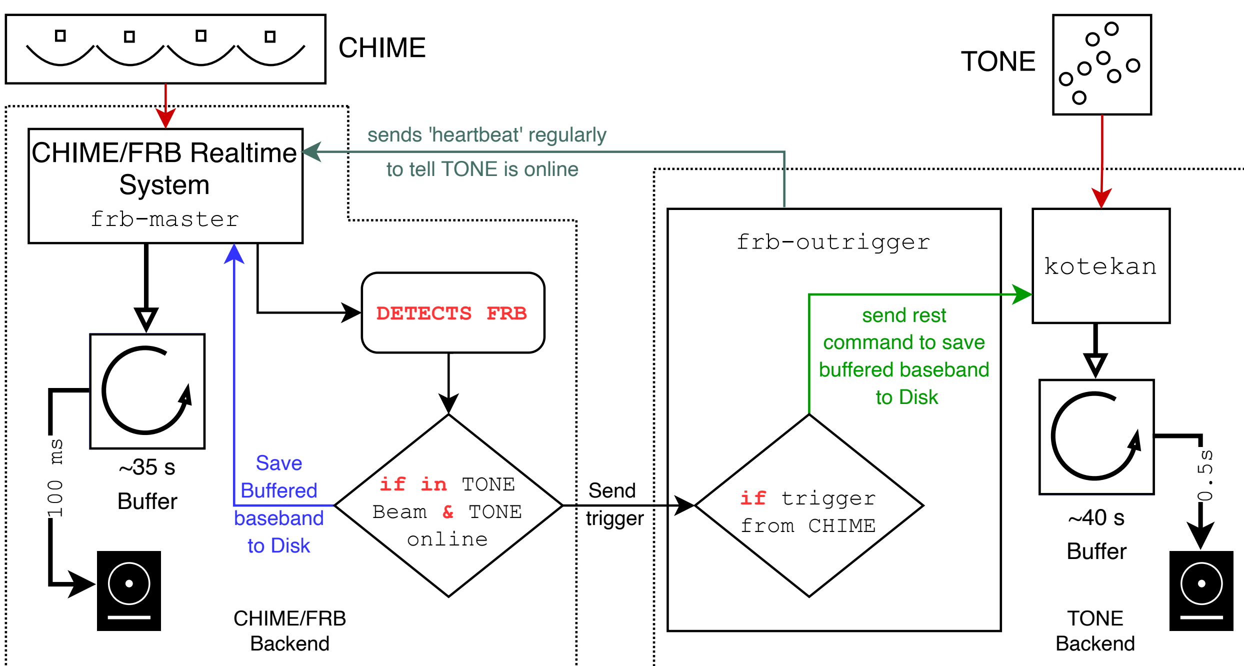


Figure 3.9: **The diagram of the Triggering Infrastructure**

## 3.6 Performance of the Telescope

**The analog chain:** The characteristics of the analog chain were measured in the lab. The gain and the noise figure of the LNA are shown in Figure 3.10. The RFoF chain, the transmitter, and the receiver have the gain shown in Figure 3.11. The gain of the entire analog chain from the LNA to the RFoF chain is shown in Figure 3.12.

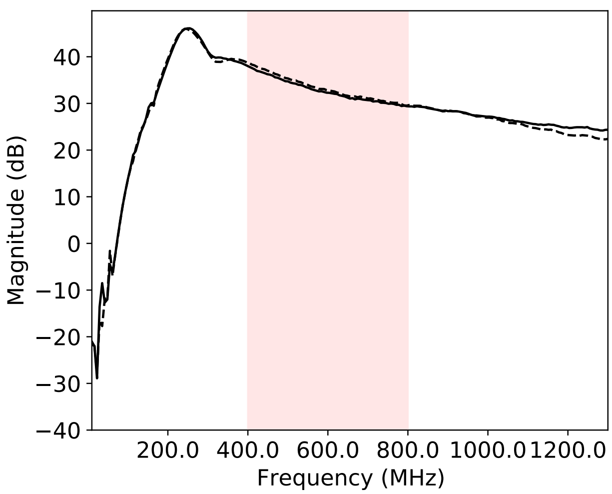


(a) The gain in dB of the LNA.

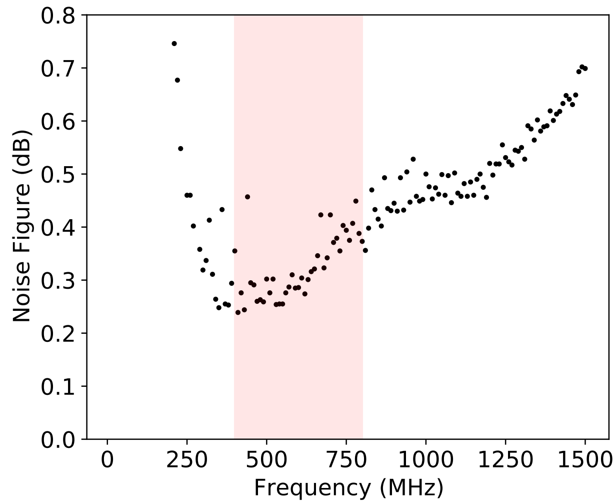


(b) The noise figure in dB of the LNA.

Figure 3.10: **LNA gain and Noise Figure:** The red region shows the frequency of operation of TONE.

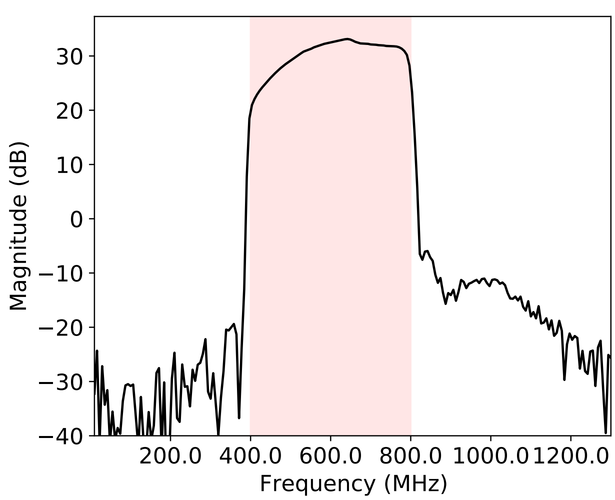


Figure 3.11: **RFoF chain gain:** The gain in dB of the RFoF system. The red region shows the frequency of operation of TONE.

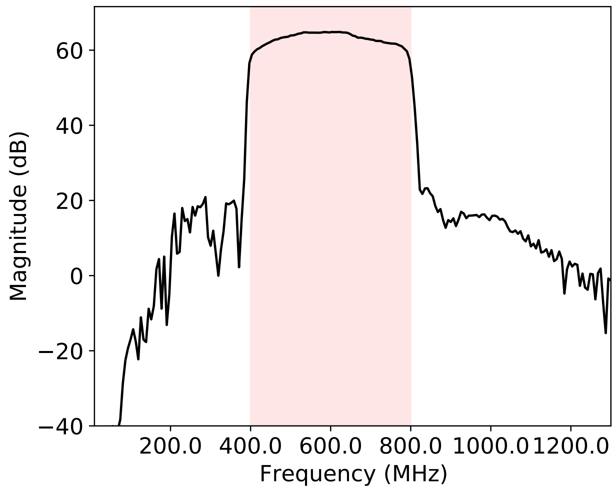


Figure 3.12: **The analog chain gain:** The gain in dB of the entire analog chain from the LNA input to the RFoF receiver output. The red region shows the frequency of operation of TONE.

We can then assess the performance of the on-sky system. We characterize many aspects of the TONE analog state by acquiring data of the Taurus A transit in the correlator mode from the ICE board and analyzing the cross-correlations. We assume that dishes are roughly similar and the beams have circular gaussian symmetry thus the measured characteristic is the geometric mean of the two dishes representing the dishes themselves. We use crosscorrelation between two co-polarizations from two feeds far away from each other to prevent the effects of cross-talk between the feeds and reflections. At each transit cross-correlation, at each frequency, is fit to a gaussian profile (i.e. free parameters offset, amplitude, mean, and width). The amplitude is then calibrated to the flux from Taurus A [119]. The calibration factor is then scaled to the noise, i.e. the off-source sky, in the autocorrelation visibilities to compute the System Equivalent Flux Density (SEFD) is shown in Figure 3.13a. The width of the Gaussian is used to compute the Full Width Half Maximum (FWHM) $\theta_{\mathrm{FWHM}}$ at each frequency shown in Figure 3.14b. The solid angle of a gaussian beam, $\Omega \approx 1.113\theta^2_{\mathrm{FWHM}}$ is then used to compute the system temperature at each frequency $T_{\mathrm{sys}} = (10^{-26}\lambda^2)/(2k_{\mathrm{B}}\Omega) \times \mathrm{SEFD}$ [Jy] shown in Figure 3.13b. The mean of the fitted gaussian corresponds to the time of the transit through the bore-sight of the beam we can thus estimate offset from the correct pointing at each frequency as seen in Figure 3.14a. The pointing of the dishes' structure is within a degree as determined limited by the accuracy of compasses. These values of the system temperature, beam offsets, FWHMs, and SEFDs were computed for several pairs of all active dishes in the data. They were similar for every dish. The system temperature is conservative since the data is affected by the Galaxy, spillover, and the ground.

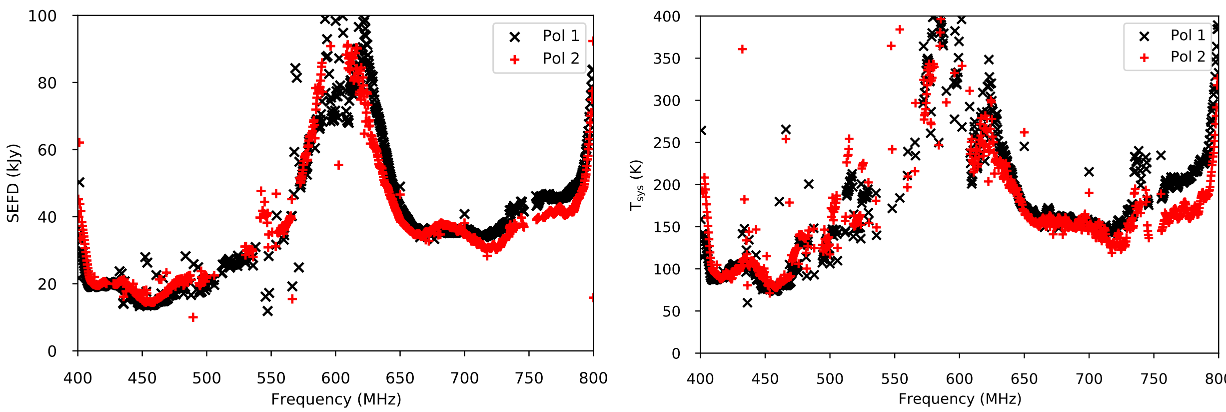


(a) System Equivalent Flux density

(b) System temperature

Figure 3.13: **System equivalent flux density (SEFD) and system temperature**

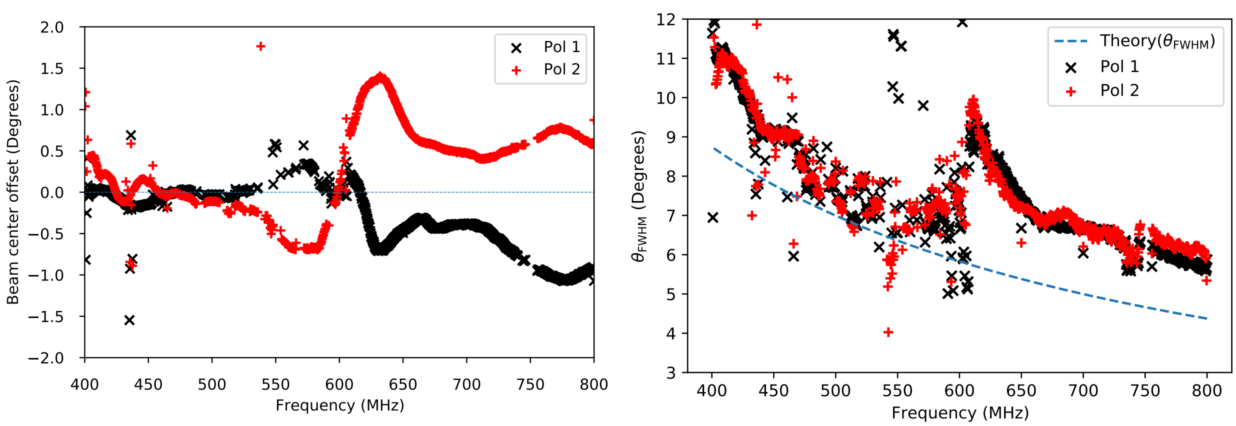


(a) The beam center offset.

(b) Full width half maximum of the dish beam.

Figure 3.14: **TONE beam properties**

**Timing:** The timing system requires us to maintain high precision of the digital sampling and absolute time[120]. To characterize the jitter of the GPS 10 MHz clock as seen in Figure 3.15 caused by the algorithms internal to the GPS to stabilize the clock. This information is stored in the raw ADC snapshots sent by the ICE Board with one of the ADC inputs fed a clock from the GBO site maser. The Fourier transform of the time-stream of the maser input is taken with the phase of the aliased $10\,\mathrm{MHz}$ frequency is channel encoding the offset from the maser. The overlapping Allen deviation [121] of the clock against the reference maser is shown in Figure 3.16. It is assumed the active hydrogen maser tone does not change significantly over the scales of several hours.

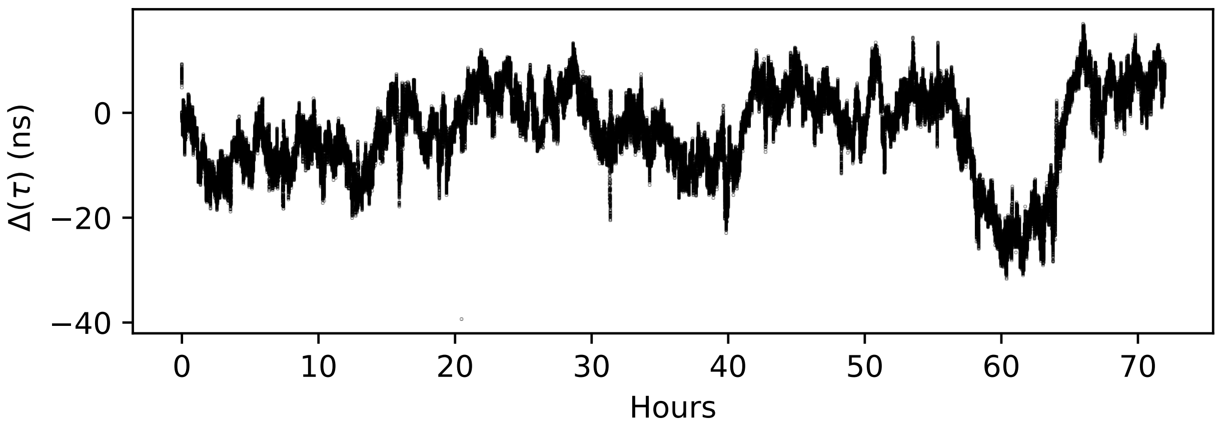


Figure 3.15: **The deviations of the GPS** $10\,\mathrm{MHz}$ **clock against the maser** $10\,\mathrm{MHz}$**.**

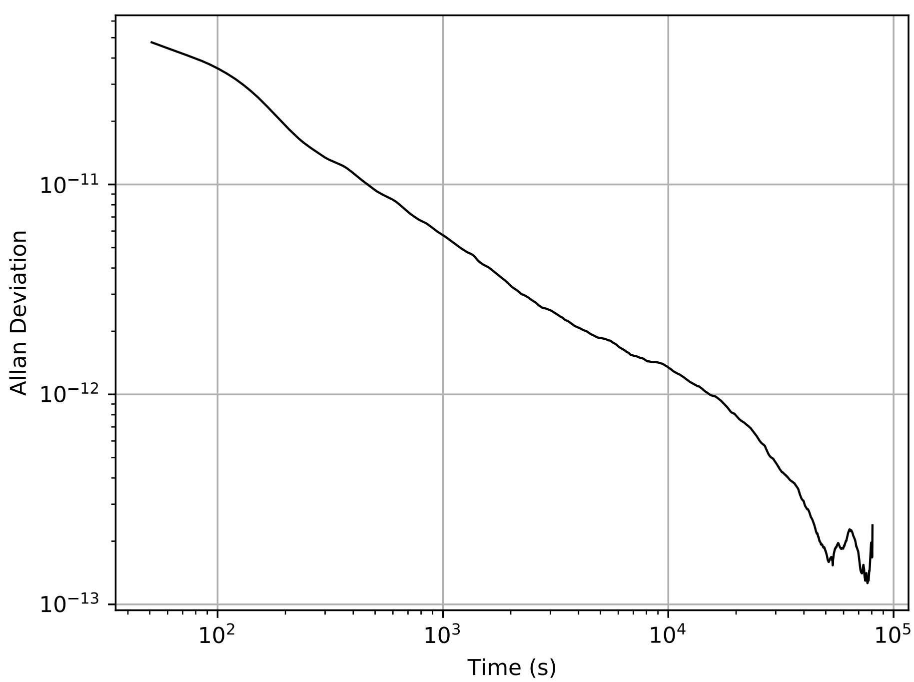


Figure 3.16: **The measured overlapping Allan deviation of the TM-4 GPS unit.**

**Instrumental delays:** Finally, we measure the performance of the analog chain, colloquially referred to as 'cable delays', over many days. These delays include the effects of varying temperatures on transmission cables as well the analog electronics. They contribute to the overall systematic error of the VLBI localization. We use the beamforming calibration methods outlined in §4.2 to compute the array gain. These gains essentially represent the phasing that needs to be applied to data from the dishes to form a beam directly at the zenith i.e. compensating for the instrumental delays for each dish. Thus, we unwrapped the phase of the complex gains and fit a line to get the corresponding delay. Since, for the phase given by $\phi = 2\pi i\tau\nu$, the delay $\tau$ is the slope of the fitting line divided by $2\pi$. Computing the gains for all the baseband data recorded for Taurus us we get the delays shown in Figure 3.17 referenced to the delay from the first day. The outliers, on inspection, correspond to bad gain solutions of data with RFI in the beam or bad weather or the sun in the beam. The best case of consecutive gains solutions corresponds to $\sim 0.064\,\mathrm{ns}$ of deviation of instrumental delays over a month with the worst-case corresponding to $1.6\,\mathrm{ns}$.

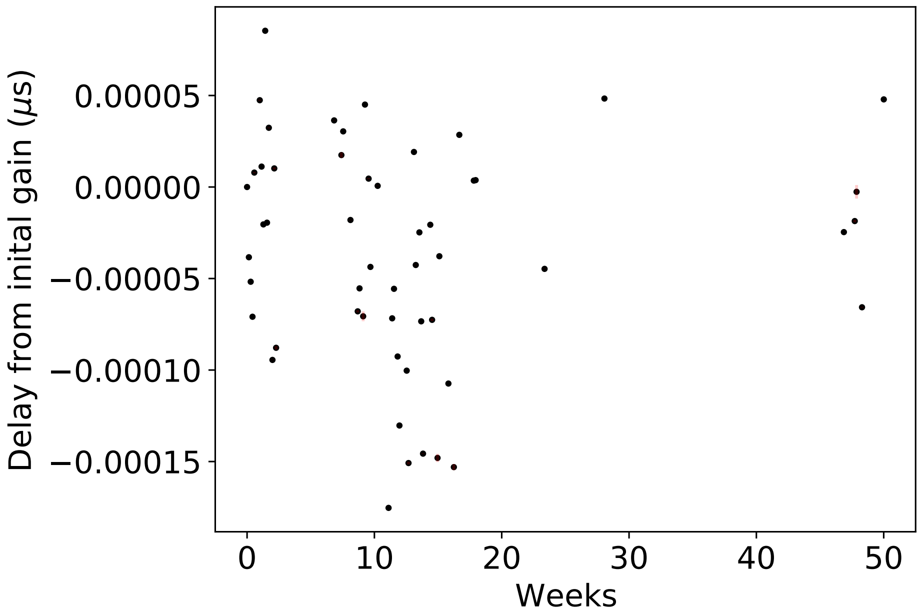


(a) The instrumental delays determined from the phase of the gains.

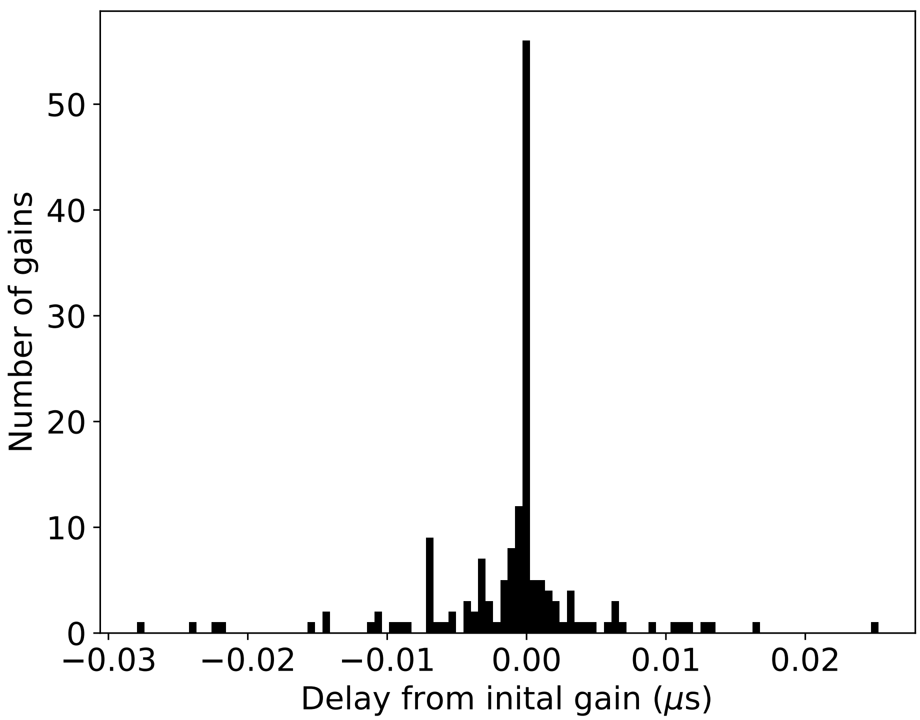


(b) Histogram of the instrumental delays

Figure 3.17: **The characteristics instrumental delays of a typical input:** 3.17a show delays relative ti the first day after throwing away outliers corresponding to “bad gains solutions" due to RFI, bad weather, and the sun in the beam. These outliers resulting in gains with high errors show up as large outliers in 3.17b.

## 3.7 TONE: Operations

The system designed is fairly automated. It has worked almost uninterrupted for months except for the months when the power to the site had been disrupted due to a failed transformer. as seen in the gap in received triggers in Figure 3.18. Within a year of operations as seen in Figure 3.19 we have had at least two high SNR events. The operation involves checking if all services are working and moving daily calibrator data off-site.

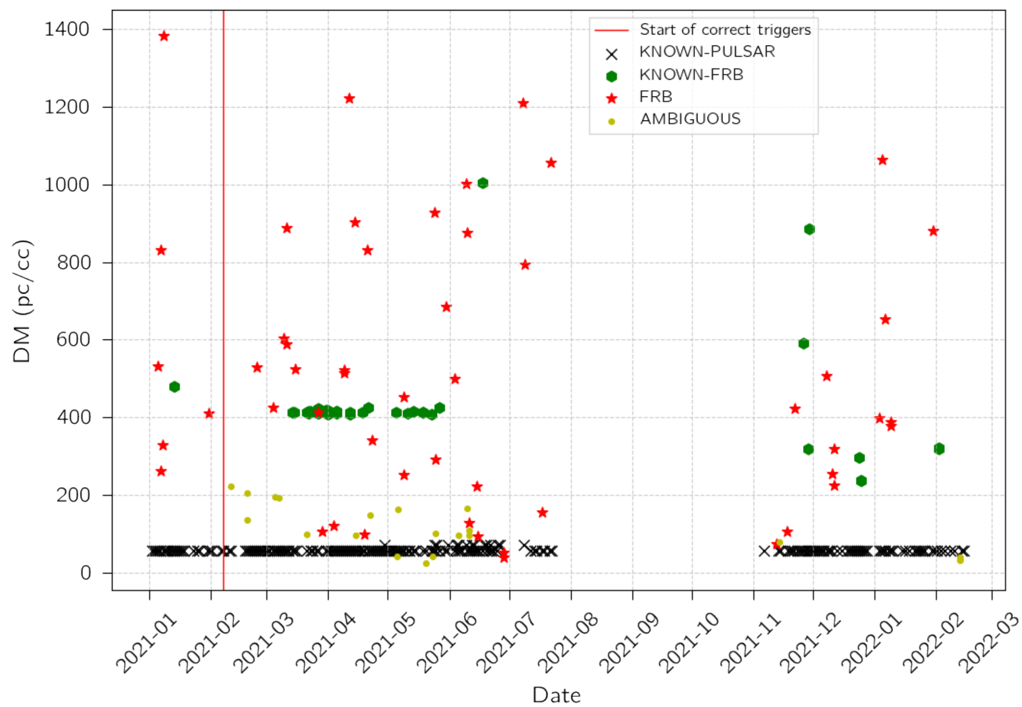


Figure 3.18: **The DMs of Events triggered at TONE from February 2021 - February 2022.**

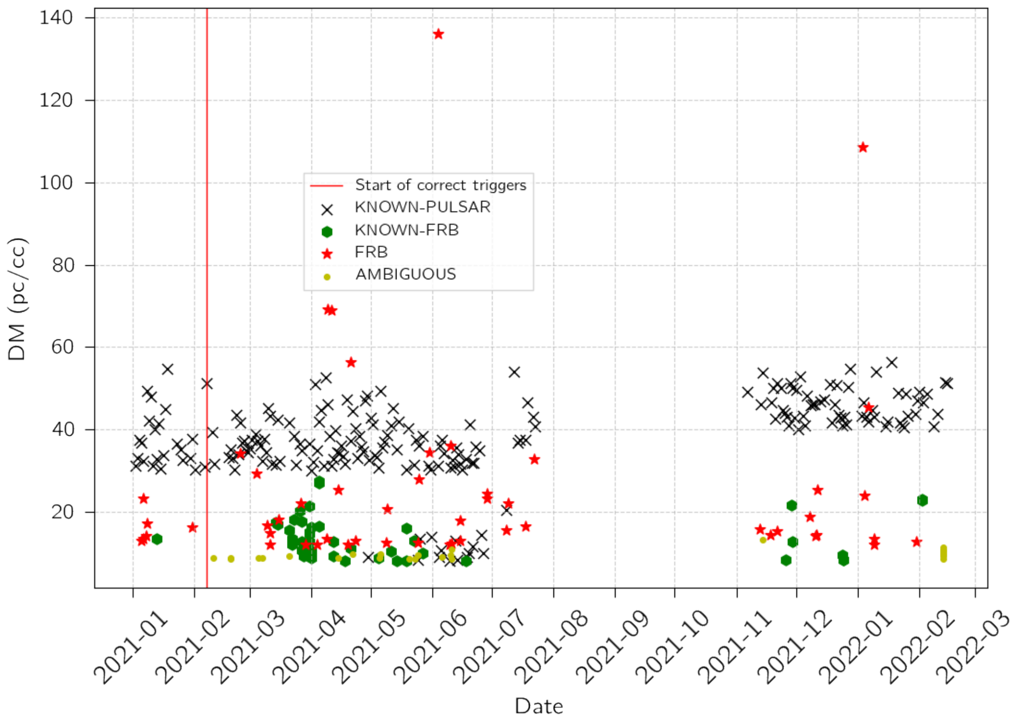


Figure 3.19: **The SNR of Events triggered at TONE from February 2021 - February 2022.** Note two FRB with CHIME/FRB SNR $\gtrsim 100$.

### 3.7.1 Good Input Checks

The feeds and the RFoF transmitters are not indoors and are prone to physical shaking from winds as well as daily weather changes. We proxy the health of the analog chain by recording the root mean square of the raw ADC snapshots. We can compute the ADC count root mean square (RMS), which is very low for a disabled input and very high close to saturating all bins typically corresponding to RFI. Additionally, waterfalls computed from the snapshots are inspected for any tones from errant analog chain oscillations. Plotting a histogram of raw ADC counts is another useful diagnostic visualization wherein counts bins close to zero correspond to a disabled input, a gaussian distribution from random noise for a typical input, and a gaussian with steep edges at the highest bin numbers for saturated inputs typically from a bright sine wave in the data from an oscillating input. Diagnostic products from a typical period from good and bad inputs are shown in Figures 3.20 and 3.21 respectively. These checks are critical for determining inputs to beamform for cross-correlation as well as for compliance with the radio-quiet zone site regulation at the Green Bank Observatory.

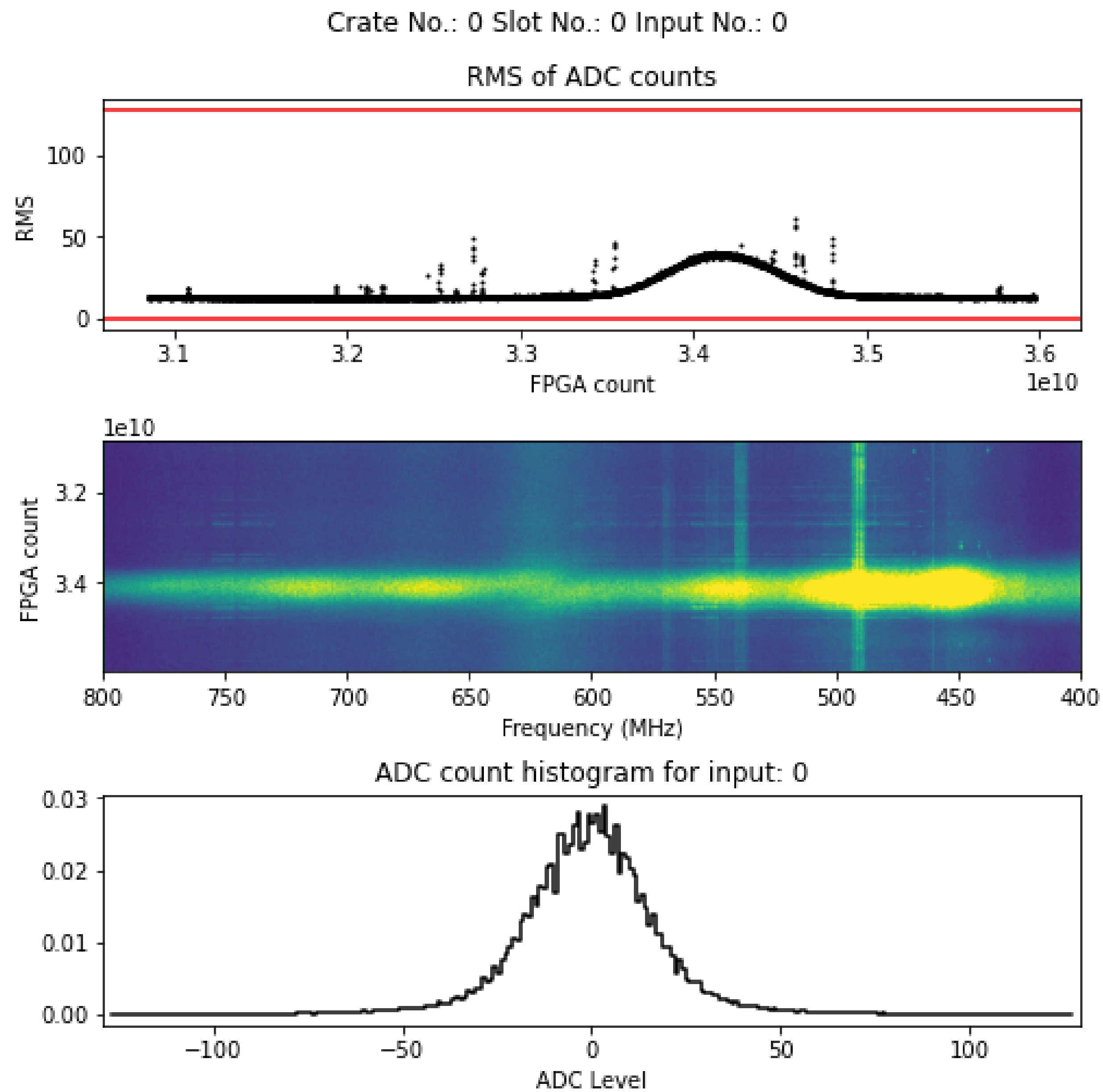


Figure 3.20: **Diagnostic plots acquired from the raw ADC of a typical input.** Note, that the data includes the transit of the sun through the beams of the dish. *From top to bottom:* The RMS of the ADC counts, the waterfall of the data, and the histogram. The ADC quantizes the data to 8 bits leading to 256 bins.

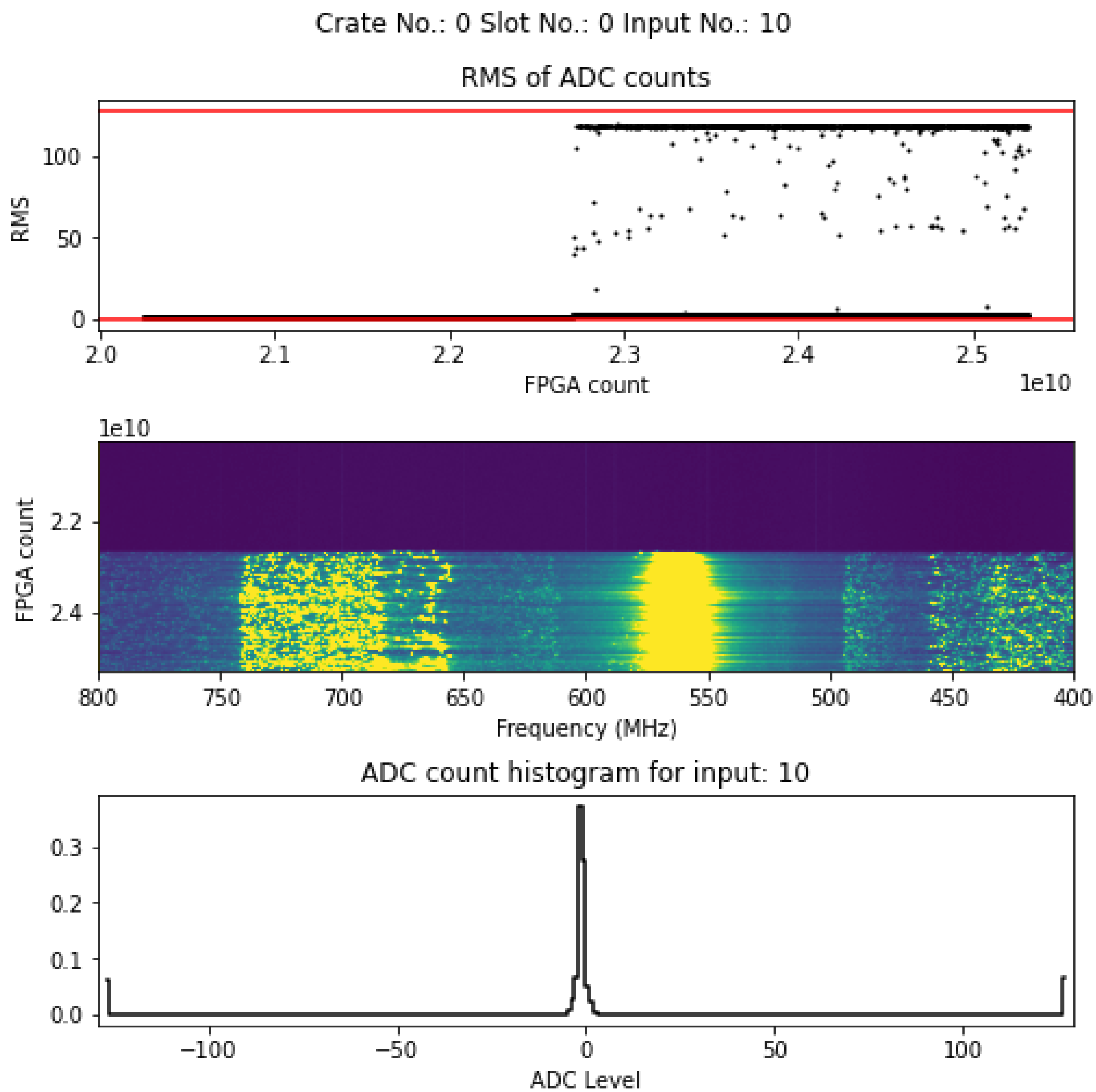


Figure 3.21: **Diagnostic plots acquired from the raw ADC if a bad input.** The first half of the acquisition corresponds to a period wherein the array was turned off. *From top to bottom:* The RMS of the ADC counts, the waterfall of the data, and the histogram. The ADC quantizes the data to 8 bits leading to 256 bins.

### 3.7.2 Incoherent Sum quick-look and RFI excision

The incoherent sum involves is computed by taking the absolute squared of the inputs and discarding predetermined "bad" inputs. Before squaring and summing the median and mean are subtracted for each frequency to normalize the data. A simple detection method was applied to the time series. We compute the signal-to-noise ratio, $\mathrm{SNR} = \mathrm{time\_series}/\sigma$, where the standard deviation $\sigma$ was computed by choosing a section of the time series away from the center of the dump. A more robust method of calculating the standard deviation is by computing the median absolute deviation (MAD) as described below.

**RFI flagging using Median of MAD** 99.9% of random data are contained within three standard deviations of the mean. As the signal from RFI is much stronger than the background noise, we would expect it to fall outside the standard Gaussian distribution. A simple RFI detector would detect signals above three standard deviations from the mean as RFI. However, the mean and the standard deviations skew towards outliers in the data. The more RFI is present, the larger the upper and lower bounds will be, and this ends up RFI not being identified. TO its end we can use the median absolute detection as a statistic. It is calculated for a set of random variables X:

$$\begin{aligned} M &= \mathrm{Median}(X) \\ \mathrm{MAD} &= \mathrm{Median}\,|X - M| \\ \sigma_X &= 1.4826 * \mathrm{MAD} \end{aligned} \tag{3.2}$$

We can then use this standard deviation $\sigma_X$ as a metric for the RFI threshold to remove RFI or compute the median of the MAD in every frequency channel. Any signal above this Median(MAD) can be classified as RFI. This has been empirically demonstrated on many datasets from TONE. This method removes RFI frequency channels where RFI dominated more than 50% of the channel and is quite aggressive.

## 3.8 First light

The array was commissioned to achieve the first light at the end of August 2020 with the real-time trigger system implemented and working by the end of October 2021. The first attempts at characterization involved running the system in the correlator model of the ICE board and capturing the correlated visibilities from all the inputs. The Stokes I data from all the inputs was used to assess the beam and the time of transit. This was used for adjusting the pointing of the dishes. Representative drift scans of the Crab nebula and the sun are shown in Figure 3.22 and Figure 3.23 respectively.

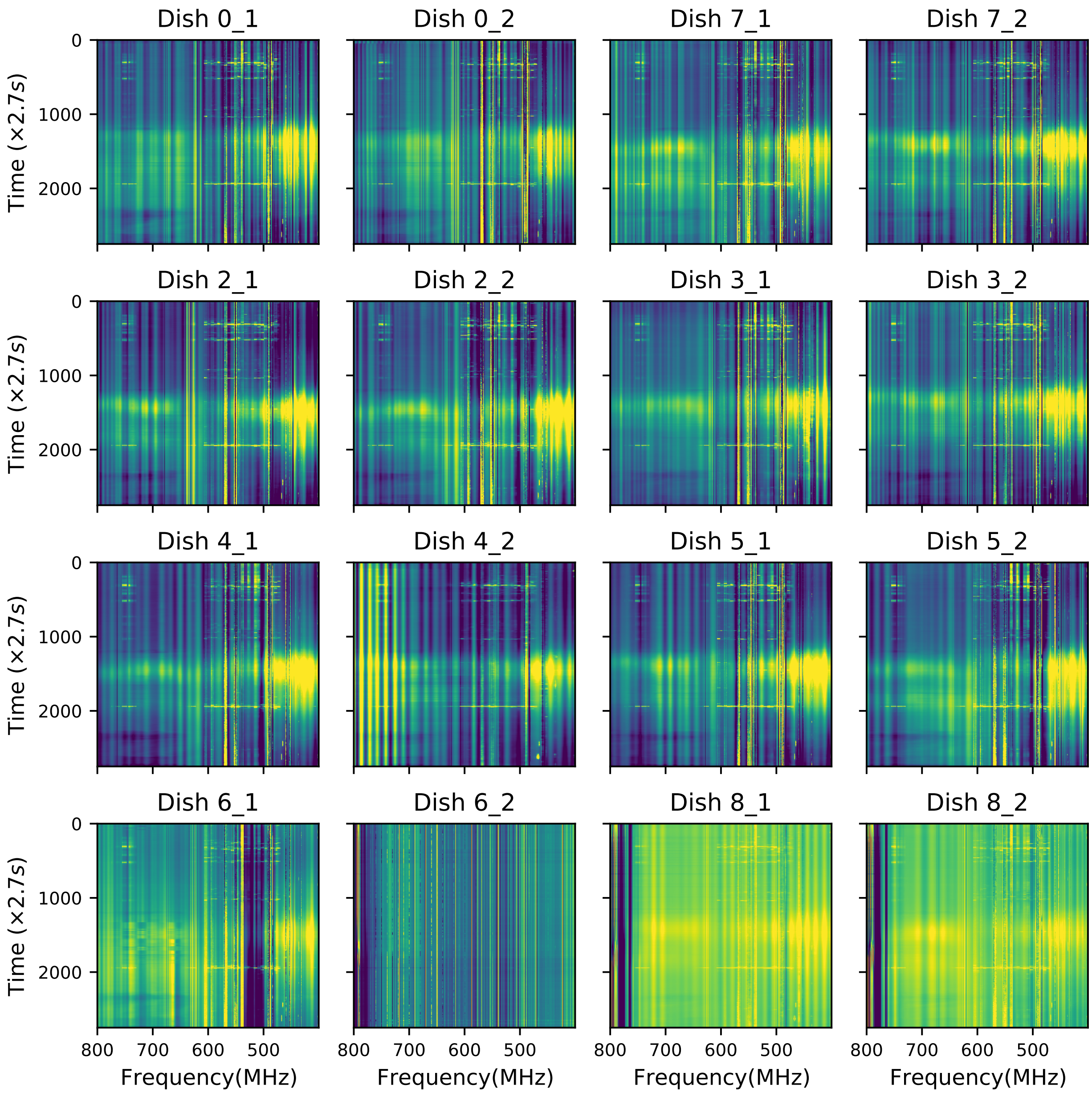


Figure 3.22: **A drift scan of the Taurus A/Crab Nebula/M1.**

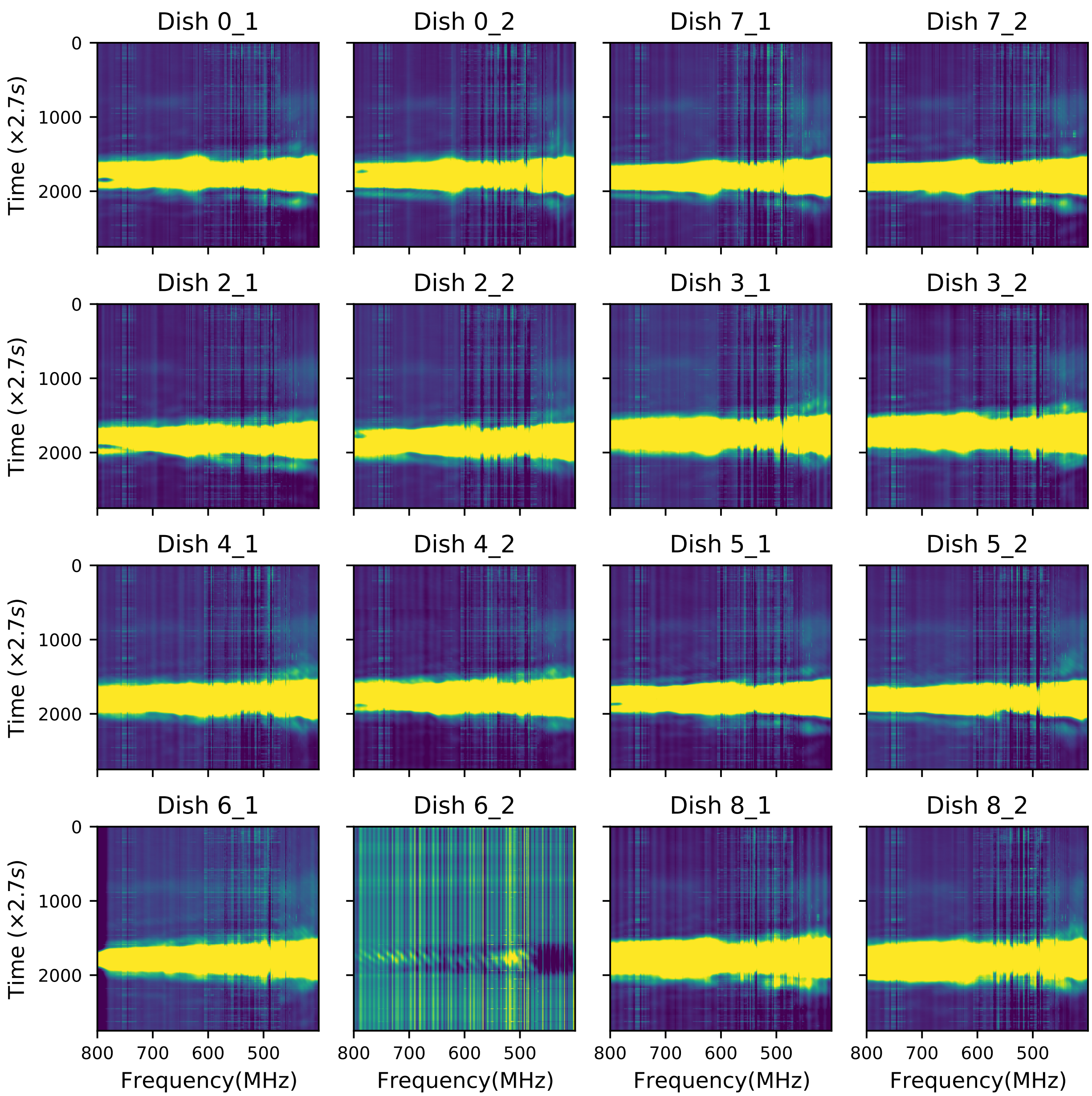


Figure 3.23: **A drift scan of the Sun.**

After resolving bugs in the system in early February 2021, TONE detected its first Crab giant pulse triggered by CHIME in the baseband data dump. The first pulses were recorded February 10, 2021 (see Figure 3.24) in the incoherent sum. The incoherent sum results for some of the brighter Crab giant pulses from February 2021 are shown in Figure 3.25 and 3.26.

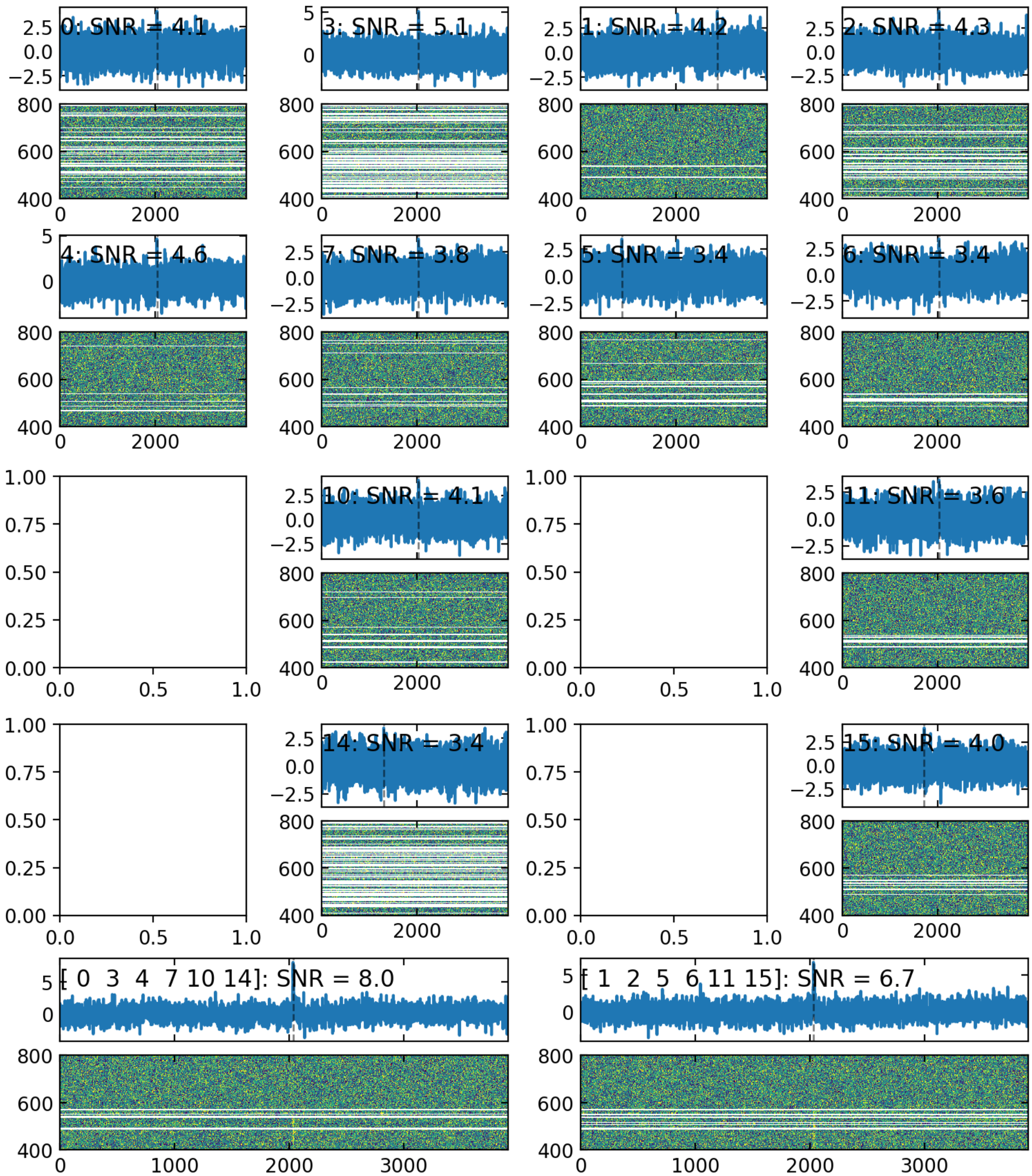


Figure 3.24: **First Detection of a Crab pulsar giant pulse from February 10, 2021.** The top 16 panels show the waterfall of the power of the data at the bottom and a sum of all the frequency channels on the top. The bottom two are the incoherent sums of each polarization group. The blank plots are flagged inputs.

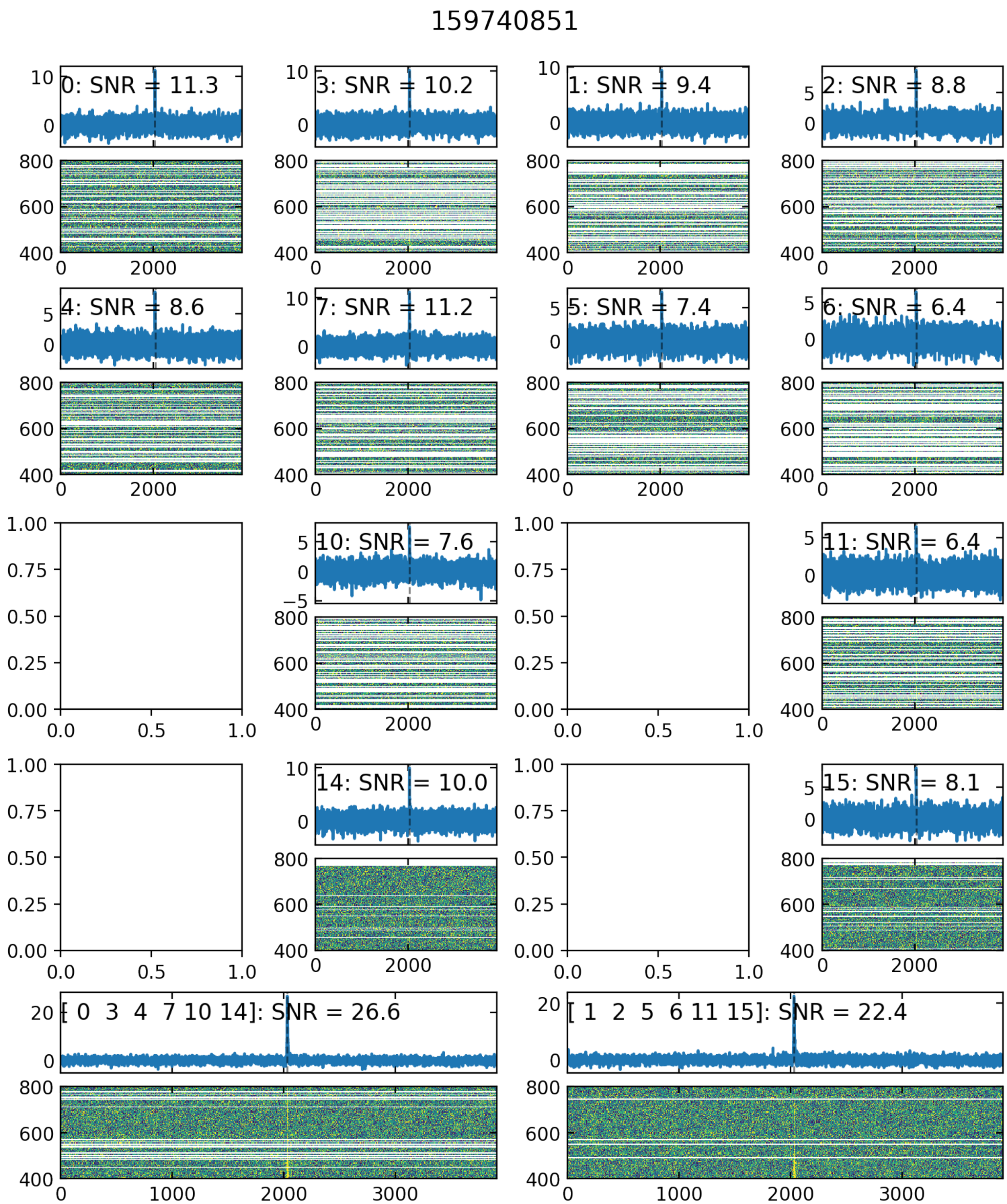


Figure 3.25: **Detection of a Crab pulsar giant pulse from February 18, 2021.** The top 16 panels show the waterfall of the power of the data at the bottom and a sum of all the frequency channels on the top. The bottom two are the incoherent sums of each polarization group. The blank plots are flagged inputs.

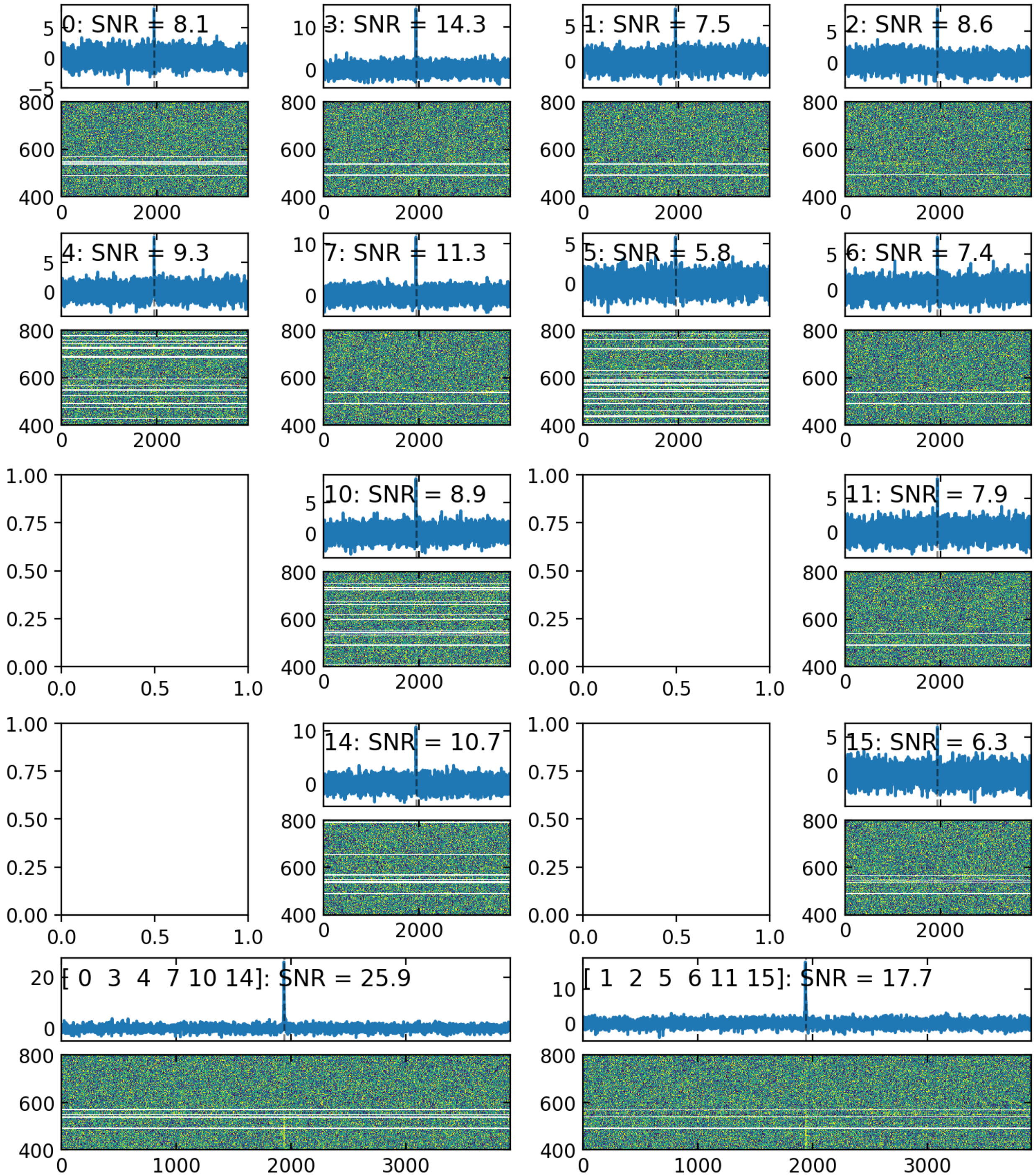


Figure 3.26: **Detection of a Crab pulsar giant pulse from February 23, 2021.** The top 16 panels show the waterfall of the power of the data at the bottom and a sum of all the frequency channels on the top. The bottom two are the Incoherent Sums of each polarization group. The blank plots are flagged inputs.

# Chapter 4

# Beamforming and Very Long Baseline Interferometery

Phased arrays and very long baseline interferometry (VLBI) have become fixtures in modern interferometry in radio astronomy. Phased arrays are the basis of most modern wide-field telescopes like CHIME and HIRAX as well as key design elements of modern observatories such as the Australian Square Kilometre Array Pathfinder (ASKAP)[36]. VLBI has led to monumental observations such as that from the Event Horizon Telescope [122].

In the context of Fast Radio Bursts, these techniques are crucial for the most prolific instruments detecting FRBs (i.e. CHIME). Additionally, a meticulous host association of FRBs is required to truly constrain their origins. Precise host localization from radio data can be achieved by using VLBI.

The large number of analog signals involved in our instruments of interest, CHIME (see §2.3) and TONE (see §3), makes it infeasible to correlate them all for VLBI. To reduce the computational burden of correlating such a large array, we coherently add, or beamform, the raw baseband data from each station.

This chapter outlines the basic theory behind digital beamforming and the results from beamforming at TONE including the first coherent light from a Crab pulsar giant pulse. We then discuss the VLBI methods we use to achieve sub-arcsecond level astrometry of FRBs. The VLBI methods detailed in §4.3.4 are factored from a paper, submitted, and currently being reviewed. The results are discussed in the following chapter.

## 4.1 Measuring using an interferometer

The electric field at a position $\vec{r}$ from a quasi-monochromatic source from a very far distance, at a location $\vec{r}_p$, is given by

$$E_\nu(\vec{r}) = \int \mathcal{E}\left(\vec{r}_p\right) \frac{e^{i2\pi v\left|\vec{r}-\vec{r}_p\right|/c}}{\left|\vec{r}-\vec{r}_p\right|} dS, \tag{4.1}$$

with $\mathcal{E}\left(\vec{r}_p\right)$ representing the electric field at the emitted location. The correlation for two receivers at $\vec{r}_1$ and $\vec{r}_2$ is given by

$$V\left(\vec{r}_1, \vec{r}_2\right) = \left\langle E_\nu\left(\vec{r}_1\right) E^*_\nu\left(\vec{r}_2\right)\right\rangle. \tag{4.2}$$

The asterisk indicates a complex conjugate. We use the expression for $E_\nu$ from equation 4.1 and evaluate the expectation over surface element dummy variables,

$$V\left(\vec{r}_1, \vec{r}_2\right) = \left\langle \iint E_\mu\left(\vec{R}_1\right) E_\nu\left(\vec{R}_2\right) \frac{e^{2\pi i\nu\left|\vec{R}_1-\vec{r}_1\right|/c}}{\left|\vec{R}_1-\vec{r}_1\right|} \cdot \frac{e^{-2\pi i\nu\left|\vec{R}_2-\vec{r}_2\right|/c}}{\left|\vec{R}_2-\vec{r}_2\right|} dS_1 dS_2 \right\rangle. \tag{4.3}$$

If we assume that astronomical signals are not spatially coherent i.e $\left\langle \vec{E}_\nu\left(\vec{R}_1\right) \vec{E}_\nu\left(\vec{R}_2\right)\right\rangle$ is zero for $\vec{R}_1 \neq \vec{R}_2$. Equation 4.3 is thus,

$$\vec{V}_\nu\left(\vec{r}_1, \vec{r}_2\right) = \int \left\langle |\vec{E}(\vec{R})|^2\right\rangle |\vec{R}|^2 \frac{e^{2\pi i\nu\left|\vec{R}-\vec{r}_1\right|/c}}{\left|\vec{R}-\vec{r}_1\right|} \frac{e^{-2\pi i\nu\left|\vec{R}-\vec{r}_2\right|/c}}{\left|\vec{R}-\vec{r}_2\right|} dS. \tag{4.4}$$

Astronomical sources are very far away and hence $|\vec{R}| >> |\vec{r}|$ and define the intensity of the signal as $I = |\vec{R}|^2 \left\langle\left|\vec{E}_v\right|\right\rangle^2$. Additionally we define a unit vector, $\hat{s}$, in the direction of $\vec{R}$ (that is, $\hat{s} = \vec{R}/|\vec{R}|$), and replace the element of integration, $dS$, with the element of solid angle, $d\Omega$. This yields,

$$
\begin{aligned}
V_\nu\left(\vec{r}_1, \vec{r}_2\right) &= \int I_\nu(\hat{s}) e^{-2\pi i \nu \hat{s}\cdot(\vec{r}_1-\vec{r}_2)/c} d\Omega \\
&= \int I_\nu(\hat{s}) e^{-2\pi i \nu \hat{s}\cdot\vec{b}/c} d\Omega,
\end{aligned}
\tag{4.5}
$$

where $\vec{b} = \vec{r_1} - \vec{r_2}$, is what we call the baseline vector. Equation 4.5 in the literature is called the spacial coherence function or the space auto-correlation function of the field $E(\nu)$. In addition to the effect of travelling through the medium the received electrical field is convolved with the telescope transfer function (in other words the primary beam of the telescope) which we denote by $A_\nu(\hat{s})$, the coherence function is thus,

$$
\mathcal{V}_\nu\left(\vec{r}_1, \vec{r}_2\right) = \int A_\nu(\hat{s}) I_\nu(\hat{s}) e^{-2\pi i \nu \hat{s}\cdot\vec{b}/c} d\Omega. \tag{4.6}
$$

This is is generally called the 'visibility'. The visibility function has encoded within the information of the astronomical source. In the most ideal sense one can retrieve information from the visibility by inverting equation 4.6 to get $I_\nu$. Assuming a flat sky and small angles, where-in angles from the source vector positions are given by direction cosines $(l, m, n)$ and the baselines defined in the $(u, v, w) = \nu(\vec{r_1} - \vec{r_2})/c$, we can write equation 4.6 as

$$
\mathcal{V}_\nu(u, v) = \iint A_\nu(l, m) I_\nu(l, m) e^{-2\pi i(ux+vy)} dl dm. \tag{4.7}
$$

This equation is a fourier transform, thus its inversion is,

$$
A_\nu(l, m) I_\nu(l, m) = \iint \mathcal{V}_\nu(u, v) e^{2\pi i(ux+vy)} du dv. \tag{4.8}
$$

In practice, the visibilities are not known everywhere but rather sampled at particular places to what is called the u–v plane in the aforementioned coordinate system corresponding to individual radio telescopes being part of the interferometer. The sampling can be described by a sampling function $S(u, v)$, which is zero where no data have been taken. The inverted visibilities in equation 4.8 take the form,

$$I_\nu^D(l, m) = \iint \mathcal{V}_\nu(u, v) A_\nu(l, m) S(u, v) e^{2\pi i(ux+vy)} du dv. \tag{4.9}$$

In radio astronomy $I_\nu^D(l, m)$ is called the dirty image. Its relation to the desired intensity distribution $I_\nu(x, y)$ is given by using the Fourier convolution theorem:

$$I_\nu^D = I_\nu \star B. \tag{4.10}$$

The value $B = \iint A_\nu(l, m) S(u, v) e^{2\pi i(ux+vy)} du dv$ is called the synthesized or dirty beam of the interferometer. De-convolving the dirty beam from the dirty image gives us the true sky intensity of the astronomical source. This process is called synthesis imaging and is the basis of most modern radio interferometry applications. Detailed discussions and topical coverage of interferometry can be found in *Interferometry and Synthesis in Radio Astronomy, 3rd Edition* by Thompson *et al.* [123] and *Synthesis Imaging in Radio Astronomy II* [124].

## 4.2 Beamforming

Beamforming is a signal processing technique for arrays of sensors (antennas) that allows for spatial filtering i.e. discriminating signals from a specified direction. It has played an important role in several fields of study such as,

- Radar (radio detection and ranging),
- Communications,
- Sonar(sound navigation and ranging),
- Communications,
- Direction of Arrival Estimation,

- Seismology,
- Medical Imaging, and
- Radio Astronomy.

In the most naive sense, a beamformer is an interferometer system where signals are coherently added at different phases such that the summed signal is a spatially filtered signal with sensitivity towards a certain direction in the sky. The reader is directed to *Optimum array processing: Part IV of detection, estimation, and modulation theory* by Van Trees [125] and 'Beamforming: a versatile approach to spatial filtering' by Van Veen *et al.* [126] for an expansive and detailed reference on the topic.

To illustrate the beamforming process, let us consider an ideal system where we capture the system voltages perfectly wherein the voltages are equivalent to the electrical fields at the antenna. For the 2-element interferometer given in Figure 4.1 we have voltages from the antennas $V_1$ and $V_2$ we have a summed signal:

$$V = V_1 + V_2. \tag{4.11}$$

To get the most optimal beam we must constructively combine the signals by compensating for the extra time the signal from the source needs to travel $\tau$ as seen in Figure 4.1. This excess travel time, called the geometric delay, depends on the baseline $\vec{B}$ and the position of the source of the signal in the sky defined by the source vector $\hat{s}$. This delay compensation is represented in the phase of the signal at frequency $\nu$ and is given by the factor $a \cdot \exp(2\pi i\nu\tau)$. Here $a$ is a real number that can be used as amplitude weighting. Thus, for the 2 element system we have,

$$V = V_1 + V_2 \times e^{2\pi i\nu\tau} = V_1 + V_2 \times \left(a \times e^{2\pi i\nu\frac{\vec{B}.\hat{s}}{c}}\right), \tag{4.12}$$

and for $N$ elements we have the beamformed signal $V_{\mathrm{BF}}$ pointing to $\hat{s}$ at frequency $\nu$,

$$V_{\mathrm{BF}} = \sum_{n=0}^{N} V_n \times a_n \times e^{\frac{2\pi i\nu\left(\overrightarrow{B_{0n}}\cdot\hat{s}\right)}{c}}. \tag{4.13}$$

The vector $\overrightarrow{B_{0n}} = \overrightarrow{B_n} - \overrightarrow{B_0}$ represents the baseline between the antenna ($n = N$) with the position vector $\overrightarrow{B_N}$ and the reference antenna ($n = 0$) with the position vector $\overrightarrow{B_0}$ in the given reference frame.

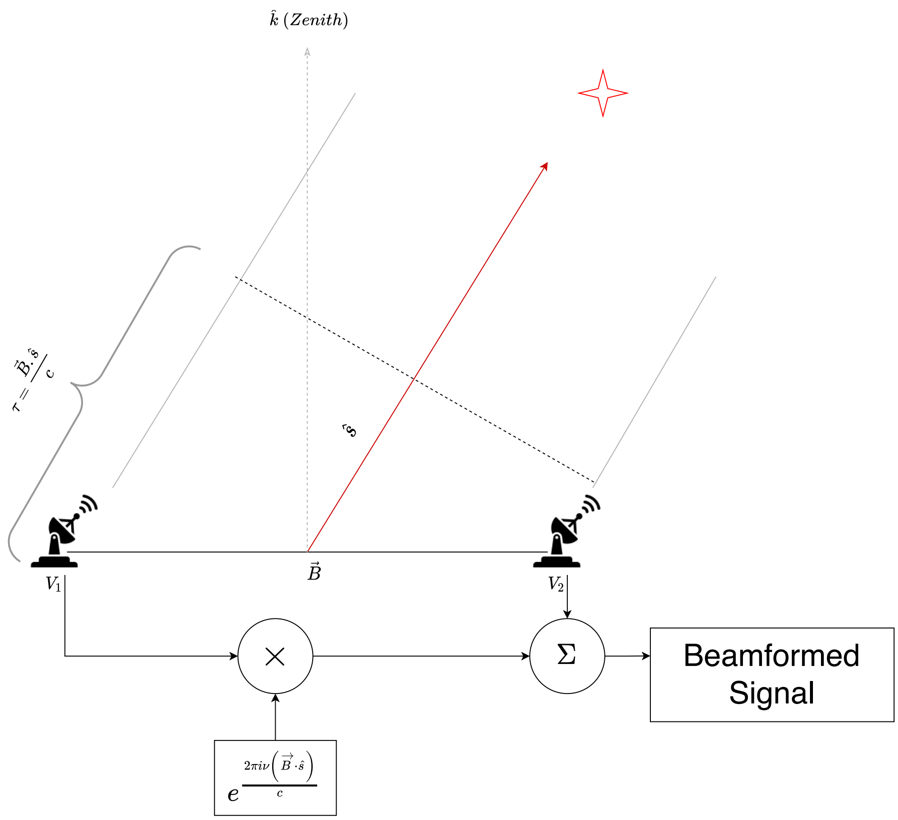


Figure 4.1: **A simple 2 element beamformer** that forms a beam towards the source $\hat{s}$.

In a real system, the voltage measured by the backend $V_n$ includes delays from the instrument $\tau^n_{\text{inst}}$ i.e. the real measured voltage at frequency $\nu$ including the delays from the instrument, so that

$$V_n' = V_n \times a_n \times e^{2\pi i\nu\tau^n}. \tag{4.14}$$

The instrumental delay $\tau^n_{\text{inst}}$ is decomposed as,

$$\tau_{\text{ints}} = \tau_{\text{cable}} + \tau_{\text{a}^{\text{n}}_{\text{inst}}} + \tau_{\text{dig}}, \tag{4.15}$$

which includes components $\tau_{\text{cable}}$, $\tau_{\text{an}}$ and $\tau_{\text{dig}}$ resulting from phases originating from the cables, the analog chain (active dual polarisation feed, RFoF) and the digital electronics (e.g. the ICE Board) respectively. Factoring out the the phases from the instruments, $g_n = a^n_{\text{inst}} \times e^{2\pi i \tau^n_{\text{sys}}}$, we have the measured voltages,

$$V'_n = g_n \times V_n. \tag{4.16}$$

Calibration is simply computing the aforementioned instrumental delays represented by the term $g(\nu)$ which we call the complex gains. Dividing $V'_n$ by $g_n(\nu)$ and multiplying by the steering factor $\times e^{2\pi i \tau^n_{\text{geo}}}$ we obtain a beamformer system as described by equation 4.13, in which

$$\sum_{n=0}^{N} \frac{V'_n}{g_n(\nu)} \times e^{2\pi i \tau^n_{\text{geo}}} = \sum_{n=0}^{N} V_n \times e^{\frac{2\pi i \nu \left(\overrightarrow{B_{0n}} \cdot \hat{s}\right)}{c}}. \tag{4.17}$$

This expression forms a beam that points to the source vector $\hat{s}$ at frequency $\nu$ where $V_n$ are calibrated voltages that if summed together constructively add plane waves that are coincident parallel to the plane of the array i.e. form an optimal beam to the zenith.

### 4.2.1 Calibration

The process of calibration of our array involves computing the complex gains $g(\nu)$. We achieve this by employing an eigenvector decomposition method as described in [127]. Informed by our discussion in §4.1, voltage recorded from a source with the electric field $\mathcal{E}(\hat{s})$ coming from the direction given by unit vector $\hat{s}$ by the backend of the telescope element $i$ with the reviever noise $n_i$ can be given by,

$$V_i = g_i \int d^2\hat{s} A_i(\hat{s}) \mathcal{E}(\hat{s}) e^{2\pi i \vec{u}} + n_i, \tag{4.18}$$

where $g_i$ is the complex gain attributed to the system, $A_i(\hat{s})$ is the primary beam of the element, and $\vec{u_i}$ is the position vector of the element given in the unit of wavelengths (i.e. $\vec{r}/\lambda$). With the assumption that the astronomical signals are spacially and mutually uncorrelated and independent from the noise, the measured visibility from a pair of telescopes with the baseline $\vec{b_{ij}} = (\vec{u_i} - \vec{u_j})[\lambda]$

is

$$\begin{aligned}
\mathcal{V}_{ij} &\equiv \langle V_i V_j^* \rangle \\
&= g_i g_j^* \int d^2\hat{s} A_i(\hat{s}) A_i^*(\hat{s}) \langle \mathcal{E}(\hat{s}) \mathcal{E}^*(\hat{s}) \rangle e^{2\pi i \vec{b_{ij}}} + \langle n_i n_j \rangle \\
&= g_i g_j^* \int d^2\hat{s} A_i(\hat{s}) A_i^*(\hat{s}) I(\hat{s}) e^{2\pi i \vec{b_{ij}}} + \langle n_i n_j \rangle,
\end{aligned} \tag{4.19}$$

Consider an ideal case without noise and if we have knowledge of the primary beam $A_i$ and the sky source $I_\mathrm{s}$ can isolate the gains dividing our measured visibility with a 'model' visibility $\widehat{\mathcal{V}_{ij}}$ as follows

$$\frac{\mathcal{V}_{ij}}{\widehat{\mathcal{V}_{ij}}} = g_i g_j^* = g_{ij}. \tag{4.20}$$

In matrix form, where the vector g where the i-th element is $g_i$, the above expression is,

$$\mathbf{g}\mathbf{g}^\dagger = \mathbf{G}, \tag{4.21}$$

here the dagger implies a Hermitian. This is an outer product representation that can be rewritten as, $\mathbf{g}(\mathbf{g}^\dagger \cdot \mathbf{g}) = (\mathbf{G} \cdot \mathbf{g})$. Since $\mathbf{g}^\dagger \mathbf{g} = ||\mathbf{g}||^2 \in \mathbb{R}$, this presents us with the relation $\mathbf{g} \cdot ||\mathbf{g}||^2 = \mathbf{G} \cdot \mathbf{g}$, implying $\mathbf{g}$ is an eigenvector of $\mathbf{G} \in \mathbb{C}$ with $||\mathbf{g}||^2$ as their corresponding eigenvalue.

However, in practice noise is not negligible and the beam response for each is not sufficiently known. For point source with flux $S$ in the sky the intensity $I(\hat{s_0}) = \delta(\hat{s_0}) * S$ make equation 4.19 for our measured visibilities take the form

$$\mathcal{V}_{ij} = g_i g_j^* A_i(\hat{s}) A_i^*(\hat{s}) S e^{2\pi i \vec{b_{ij}}} + \langle n_i n_j \rangle. \tag{4.22}$$

Since $S$ is a scalar, first term of the right hand side of the equation is again an outer product,

$$\begin{aligned}
\mathcal{V}_{ij} &= \mathcal{V}_0 + \langle n_i n_i \rangle \\
\mathcal{V} &= S\mathbf{G}\mathbf{G}^\dagger + \mathbf{N}
\end{aligned} \tag{4.23}$$

and,

$$G_i = g_i A_i(\hat{s_0}) e^{2\pi i \vec{u_i}}. \tag{4.24}$$

Assuming our calibrator source flux $S$ is brighter than the correlations between the noise $\mathbf{N} = \langle n_i n_i \rangle$ we can use principle component analysis (PCA) of the visibilty matrix $\mathcal{V}$ to get the eigenvectors $x_i$ and eigenvalues $\lambda_i$ with the eigenvector $x_1$ corresponding to the largest eigenvalue $\lambda_1$ representing our solution such that,

$$\mathcal{V}_{\mathbf{ij}} = x_1 x_1^\dagger \lambda_1 + \sum_{k>1} x_k x_k^\dagger \lambda_k \equiv S\mathbf{G}\mathbf{G}^\dagger + \mathbf{N} \tag{4.25}$$

This solution includes the complex gains and the beam response. For a close-packed array-like TONE, nearby feeds interact with each other and the noise terms are not completely uncorrelated this PCA solution may not present itself. For this reason, strong correlations for example between $i$ and $j$ are set to zero, the gain solutions are obtained and the corresponding visibility replaced with the solution as $V_{ij} = G_i G_j^*$ until the solution converges on a value or threshold for the number of iterations set.

Applying these gains to our recorded voltages like in equation 4.17 points our beam to the zenith. The solutions are calculated for every frequency of the baseband data and independently for the two different orthogonal polarizations. We can estimate the error on the calibration solution as the ratio of the second largest eigenvalue, $\lambda_1$, to the largest, $\lambda_2$. The typical error on the gains solution is shown in Figure 4.2. The phases of the normalized gains are shown in Figure 4.3. The typical error on the gains solution is shown in Figure 4.2.

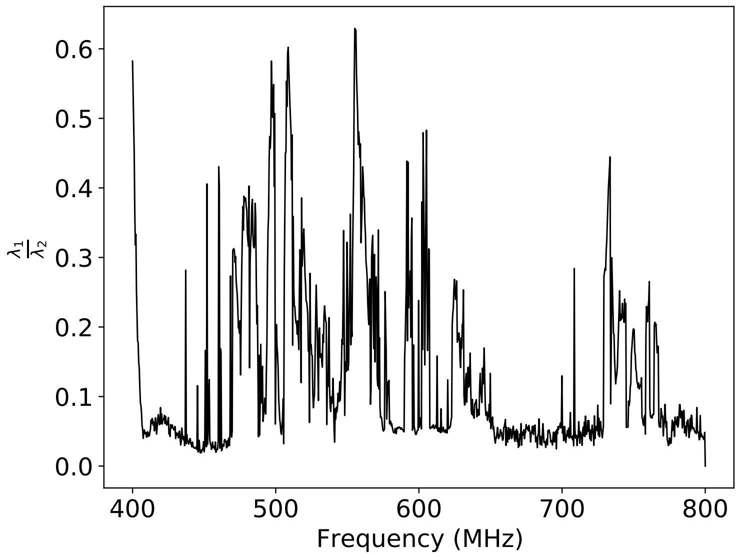


Figure 4.2: **Error of the gains solutions:** The error of a typical gains solution calculation measured as the ratio of the largest $\lambda_1$ and the second largest eigenvalue ($\lambda_2$). Note for frequencies where $\lambda_1/\lambda_2$ are low, show smooth phases in Figure 4.3.

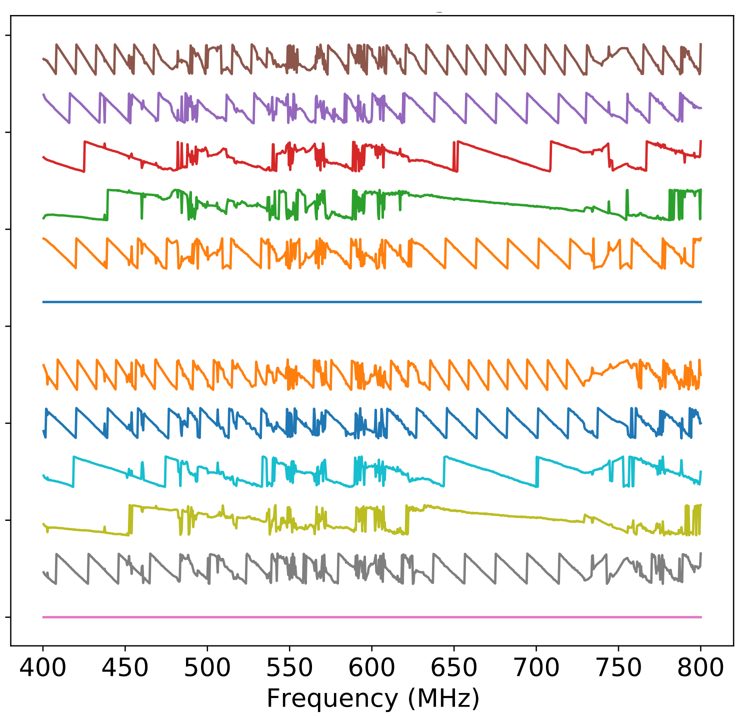


Figure 4.3: **Phase of the normalized gains solutions:** A gains solution of 6 dishes is shown. Each line is the phase of the gains solution. The bottom 6 are from one co-polarizations and the top 6 are from the other co-polarizations indexing upwards. Note the zeroth index has a flat zero phase and the rest, representing a phase for this zeroth input, wrap between $-\pi$ to $\pi$ and are arbitrarily offset for readabilty.

An alternative to solving gains can arise from forming visibilities directly, i.e. without taking into account the direction $\hat{s_0}$ of the calibrator source, from the measured voltages such as

$$
\begin{aligned}
\mathcal{V}_{ij} &\equiv \langle V_i V_j^* \rangle \\
&= g_i g_j^* \int d^2\hat{s} A_i(\hat{s}) A_i^*(\hat{s}) \langle \mathcal{E}(\hat{s}) \mathcal{E}^*(\hat{s}) \rangle + \langle n_i n_j \rangle \\
&= g_i g_j^* \int d^2\hat{s} A_i(\hat{s}) A_i^*(\hat{s}) I(\hat{s}) + \langle n_i n_j \rangle .
\end{aligned}
\tag{4.26}
$$

Solving for gains for these visibilities assuming a point source calibrator with flux $S$, thus the intensity $I(\hat{s_0}) = \delta(\hat{s_0}) * S$, gets gains solutions of the form

$$
G_i = g_i A_i(\hat{s_0}). \tag{4.27}
$$

So dividing this from equation 4.18 gives us a beam that points at the calibrator. For TONE we have implemented both of these beamformer variations. Since we are adding voltages in the phase we scale the sensitivity of the combined array by the order of $N$ where $N$ is the number of co-polarized inputs coherently added together. This can be evidently seen in beamformed signal from six inputs for each polarization in Figures 4.6 and 4.7 which is $\sim \sqrt{N}$ times the incoherent signals seen in Figures 4.4 and 4.5.

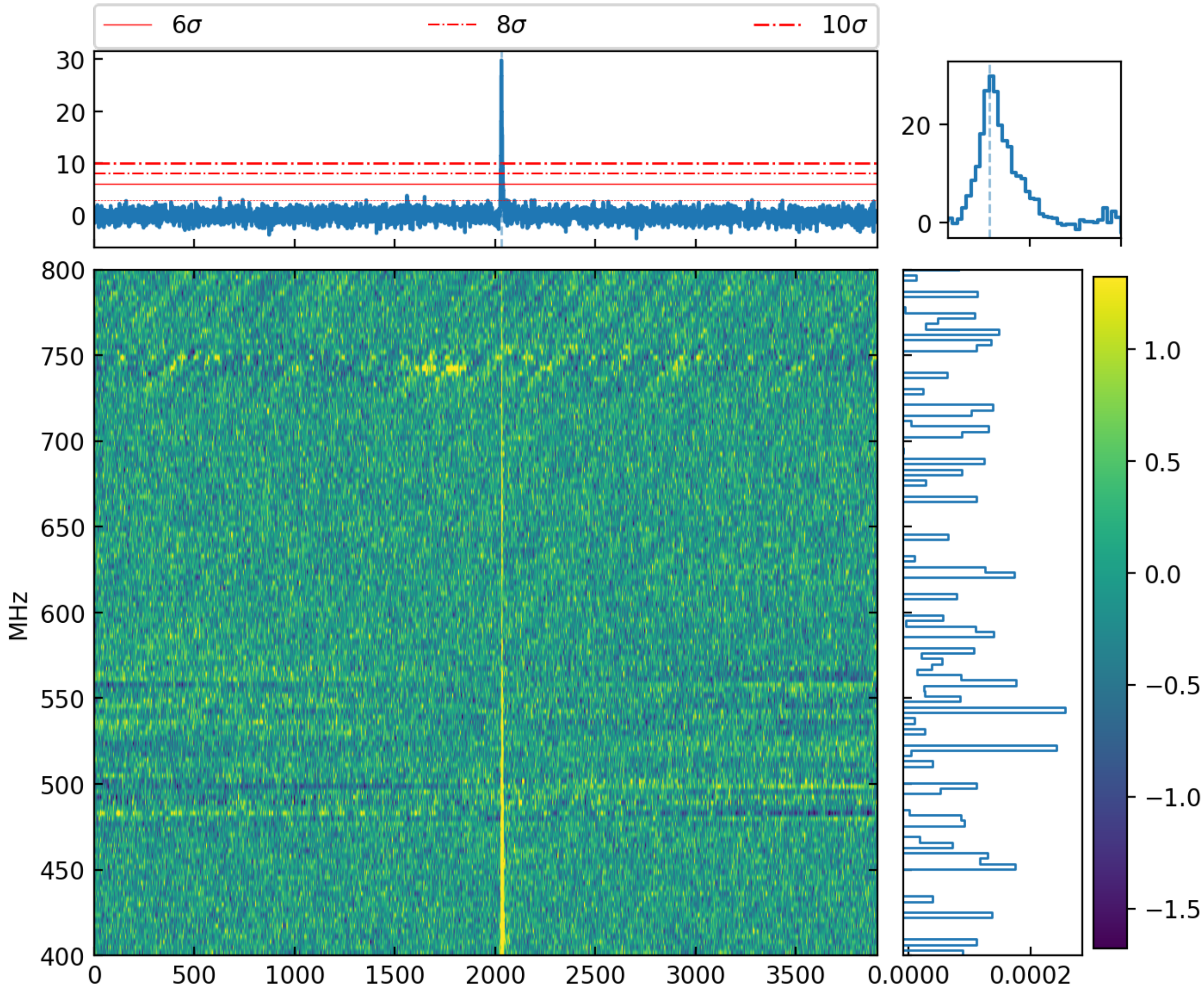


Figure 4.4: **Incoherent sum of a Crab giant pulse from the first set of co-polarized inputs:** The bottom left is the waterfall of the incoherent sum of the data that has been 50-time bins and 8 frequency channels are integrated. The top left panel is the sum of all the frequency channels. In the top right is a zoomed-in view of the frequency stacked pulse. The bottom right panel is the sum of all the data in every frequency channel. The data have been incoherently dedispersed.

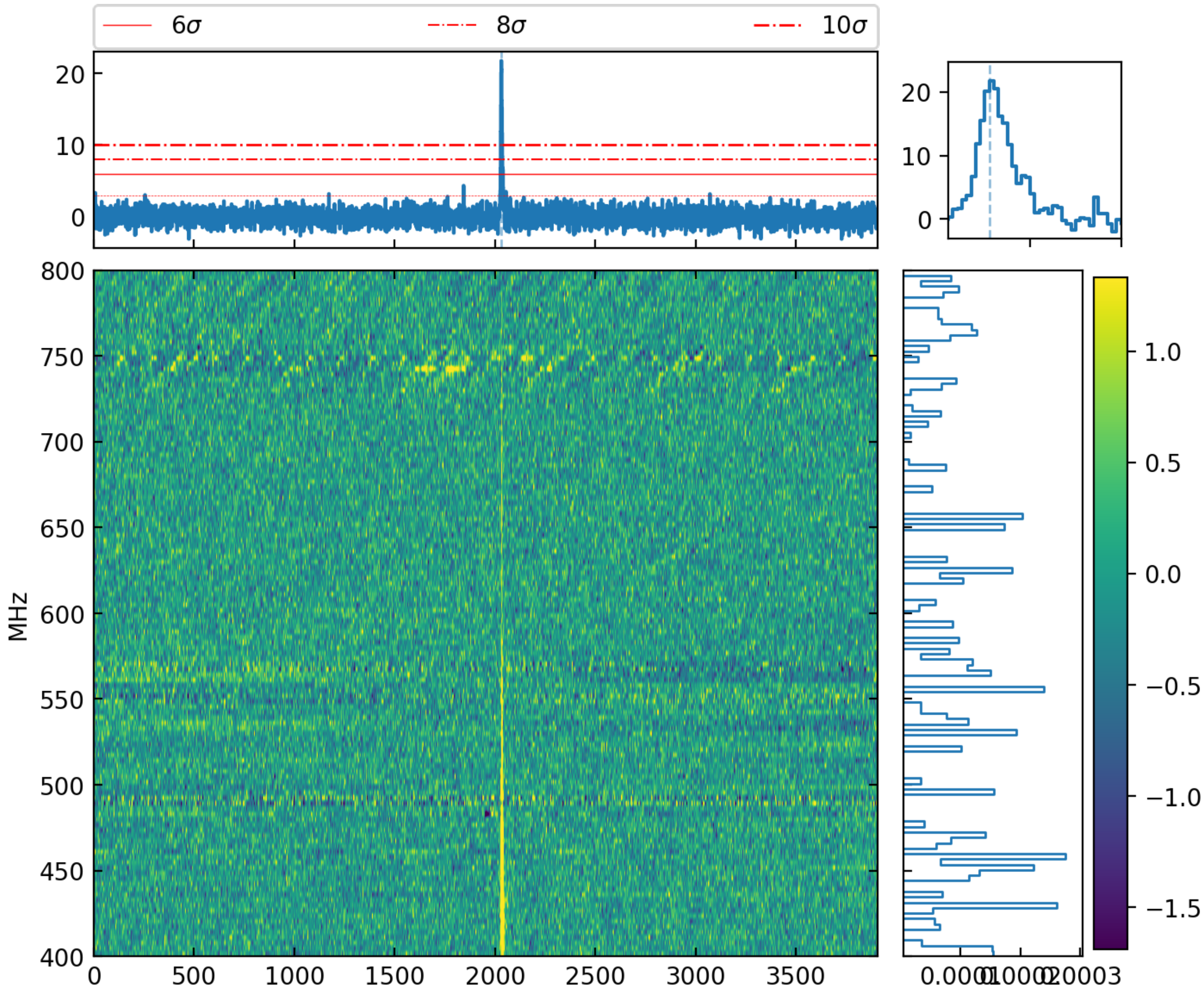


Figure 4.5: **Incoherent sum of a Crab giant pulse from the second set of co-polarized inputs:** The bottom left is the waterfall of the incoherent sum of the data that has been 50-time bins and 8 frequency channels are integrated. The top left panel is the sum of all the frequency channels. In the top right is a zoomed-in view of the frequency stacked pulse. The bottom right panel is the sum of all the data in every frequency channel. The data have been incoherently dedispersed.

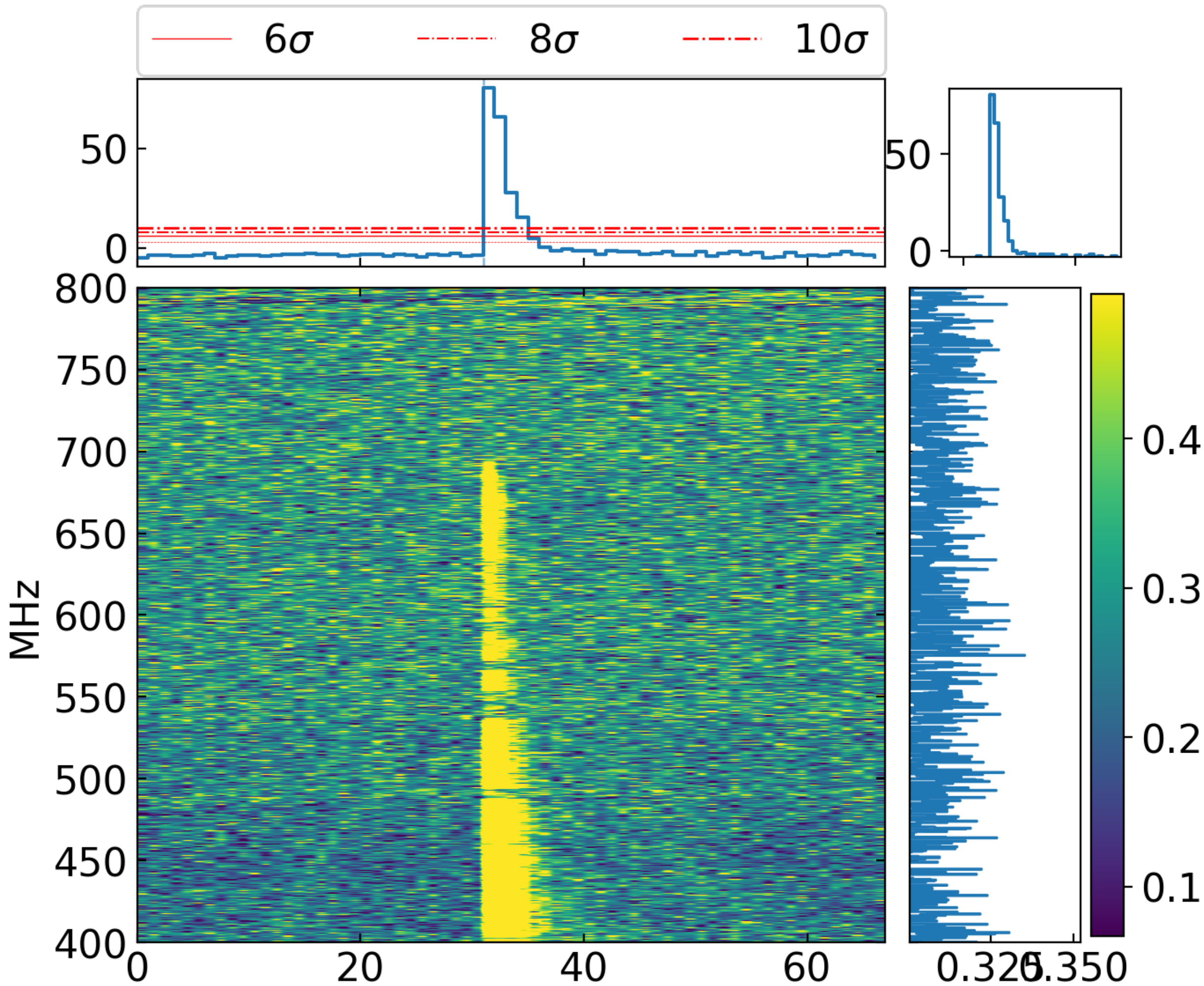


Figure 4.6: **Beamformed single-beam data of a Crab giant pulse from the first set of co-polarized inputs:** The bottom left is the waterfall of the coherent sum of the data that has been 50-time bins and 8 frequency channels are integrated. The top left panel is the sum of all the frequency channels. In the top right is a zoomed-in view of the frequency stacked pulse. The bottom right panel is the sum of all the data in every frequency channel. The data have been coherently dedispersed and rolled to align the pulse in every frequency channel.

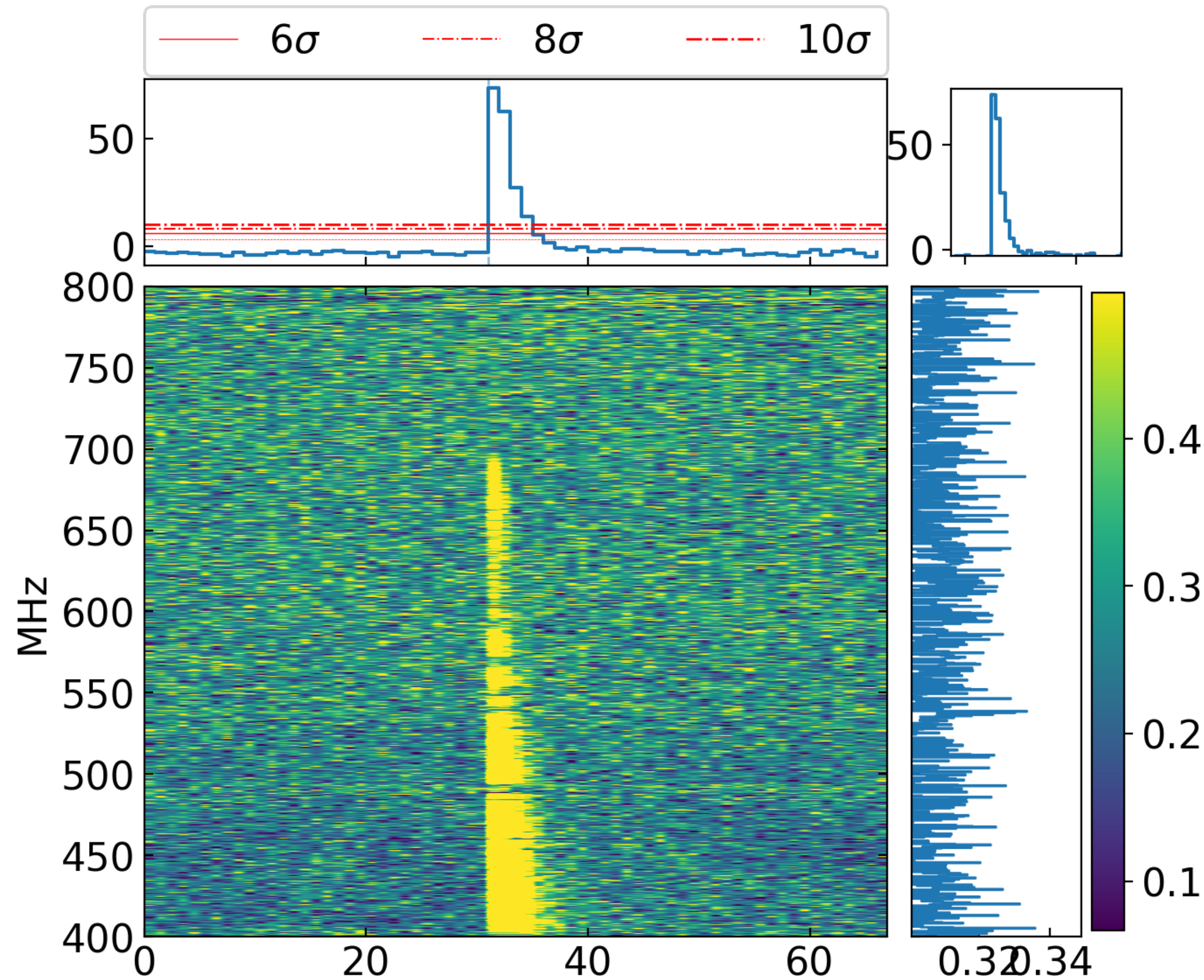


Figure 4.7: **Beamformed single-beam data of a Crab giant pulse from the second set of co-polarizations:** The bottom left is the waterfall of the coherent sum of the data that has been 50-time bins and 8 frequency channels are integrated. The top left panel is the sum of all the frequency channels. In the top right is a zoomed-in view of the frequency stacked pulse. The bottom right panel is the sum of all the data in every frequency channel. The data have been coherently dedispersed and rolled to align the pulse in every frequency channel.

### 4.2.2 Beam Steering

Consider on calibrating complex voltages $V'$ we compute gains $g(\nu)$ for every frequency. We would like to point the beam to the FRB's location in the sky denoted by the vector $\hat{s}'$. This is simply multiplying the phase $e^{2\pi i \vec{b}\cdot\hat{s}'}$ to the calibrated voltages $V$

We assert a cartesian coordinate system centered on our defined zero-th telescope element that corresponds to the computed gains having zero phases. The $x - y - z$ direction is defined by the unit vectors $\hat{i}$, $\hat{j}$ and $\hat{k}$ point to East, North, and Zenith respectively.

The vector to the elements are written as follows,

$$\overrightarrow{B^n} = B_x^n \hat{i} + B_y^n \hat{j} + B_z^n \hat{j}, \tag{4.28}$$

where the vector to the first element is $\overrightarrow{B^0} = \vec{0}$ because it is our defined origin. So our baseline vectors

$$\overrightarrow{B_{0n}} = B_x^n \hat{i} + B_y^n \hat{j} + B_z^n \hat{j} = \vec{B}_n. \tag{4.29}$$

Consider an object in the sky with Azimuth $Az$ and Altitude $Alt$. In our defined coordinate system illustrated in Figure 4.8 the source vector for that object is given by

$$\hat{s} = (\sin(Az)\cos(Alt))\vec{\hat{i}} + (\cos(Alt)\cos(Az))\vec{\hat{j}} + (\sin(Alt))\vec{\hat{k}}, \tag{4.30}$$

where $Alt \in [-\pi, \pi]$ and $Az \in [0, 2\pi]$.

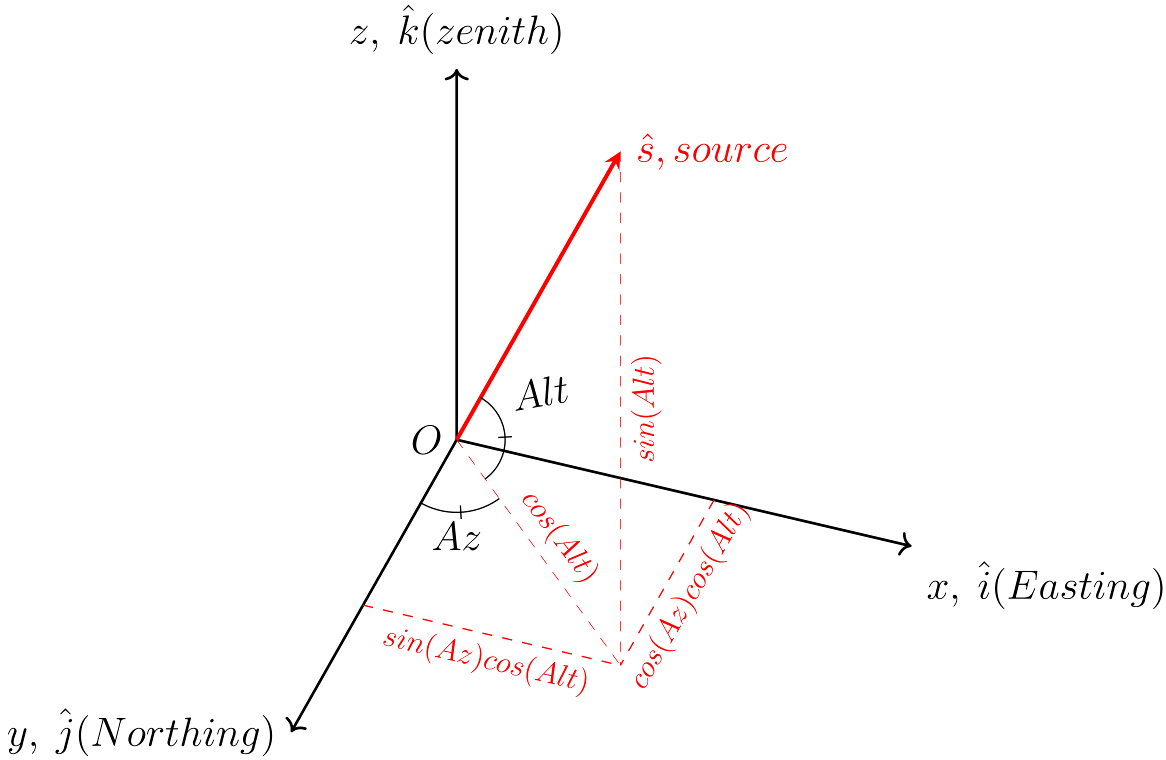


Figure 4.8: **Beam steering coordinate system:** The source unit vector $\hat{s}$ defined in the cartesian co-ordinate system convention defined by the unit vectors $\hat{i} - \hat{j} - \hat{k}$. In this reference system with the vectors $\hat{i}$,$\hat{j}$ and $\hat{k}$ point to East, North and Zenith respectively.

As we noted in §4.2.1, applying gains forms the beam at the zenith, in other words, it compensates for instrumental delays. The point to the source we simply apply the phase to the source

$$V_{BF}(\nu) = \sum_{n=0}^{N} \frac{V'_n}{g_n(\nu)} \times e^{\frac{2\pi i\nu\left(\overrightarrow{B_{0n}}\cdot\hat{s}'\right)}{c}}. \tag{4.31}$$

For a planar array, the exponent

$$\frac{2\pi i\nu}{c}\vec{B_{0n}} \cdot \hat{s}' = \frac{2\pi i\nu}{c}(B_x(\sin{(Az_e)}\cos{(Alt_e)}) + B_y(\cos{(Alt_e)}\cos{(Az_e)})). \tag{4.32}$$

If we computed gains in the alternative order described in §4.2.1, we form the beam at the calibrator, in other words, the complex gains include both the instrumental and geometric contribution in the phase. We remove the geometric contributions of the calibrator by essentially steering the beam to zenith $\hat{k}$. Finally, we steer to the position of the FRB in the sky $\hat{s}'$. So steering our calibrated voltages $V_n'/g_n$ to $\hat{s'}$ the beamformed signal at frequency $\nu$ is

$$V_{BF}(\nu) = \sum_{n=0}^{N} \frac{V_n'(\nu)}{g} \times e^{\frac{2\pi i \nu \vec{B_n} \cdot \left(-\hat{s}+\hat{s'}\right)}{c}}. \tag{4.33}$$

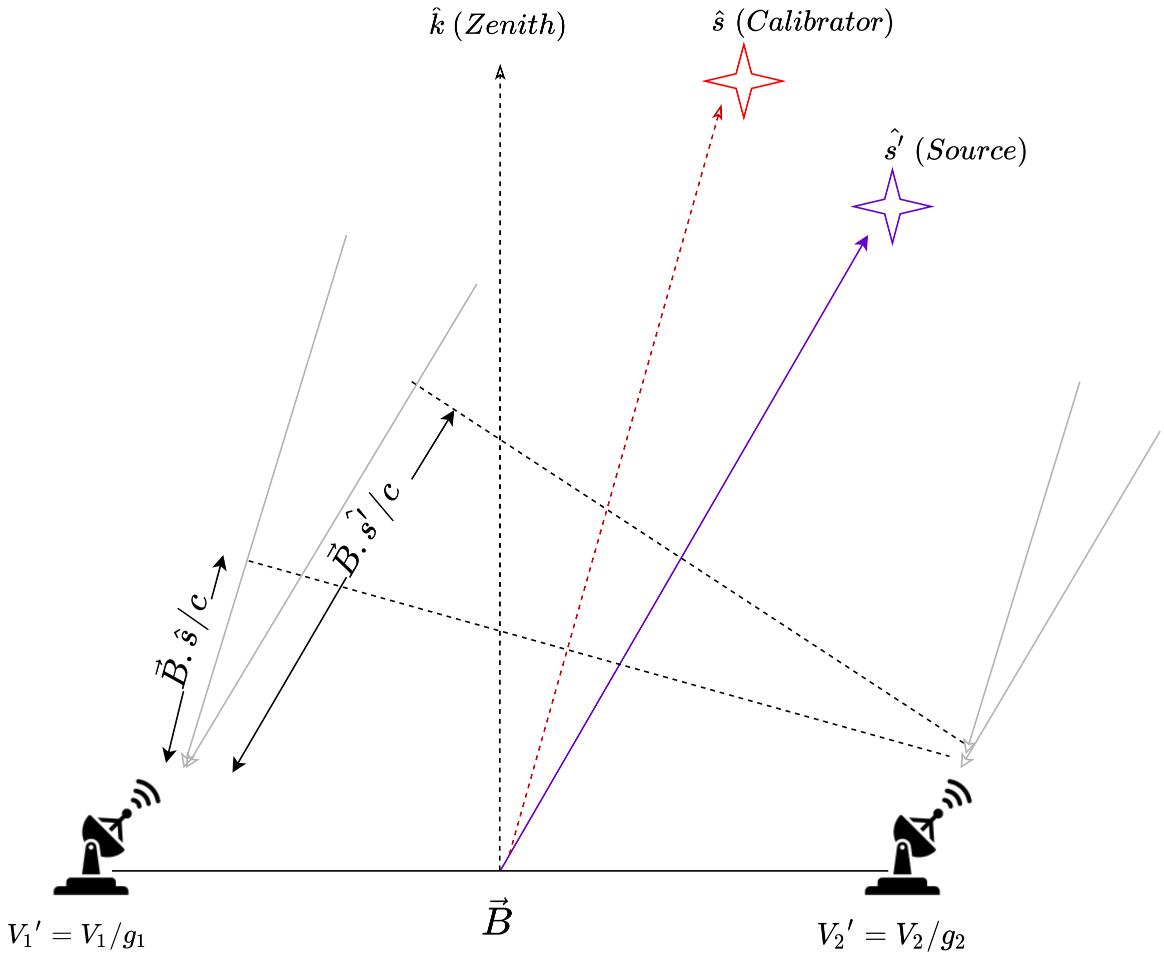


Figure 4.9: **A schematic of beam steering:** For gains computed as in §4.2.1, steering to the source $\hat{s'}$ involved 'removing' the phases from the geometric delay $\vec{B}.\hat{s}/c$ of the calibrator or steering to zenith followed by compensating for the geometric delay $\vec{B}.\hat{s'}/c$ of the source.

So the expression in the exponent given $B_z = 0$ for a planar array is,

$$
\begin{aligned}
&2\pi i\nu \vec{B_n} \cdot \left(-\hat{s} + \hat{s'}\right)/c = \\
&\qquad 2\nu\pi i(B_x \left(\sin\left(Az_e\right)\cos\left(Alt_e\right) - \sin\left(Az_g\right)\cos\left(Alt_g\right)\right) \\
&\qquad + B_y \left(\cos\left(Alt_e\right)\cos\left(Az_e\right) - \cos\left(Alt_g\right)\cos\left(Az_g\right)\right))/c
\end{aligned}
\tag{4.34}
$$

### 4.2.3 Beamforming for TONE

The infrastructure to calculate these complex gains called the "$N^2$-gain calibration" and a tied-array beamformer have already been developed for the CHIME/FRB experiment[96]. We generalised several of CHIME's software frameworks [101, 128, 129], to use the same basic $N^2$-gain calibration algorithms [130] for the data at TONE. Additionally an independent GPU optimised, parallelised-across-CPU-cores implementation of the beamformer was developed for independent verification and redundancy. The beamformed waterfalls of the Crab pulsar giant pulses can be seen in Figures 4.12, 4.13, 4.14, 4.15, 4.16 and 4.16. Finally, for an FRB we compute gains for the nearest Crab Pulsar data, apply the gains and steer to the FRB (see Figure 4.10).

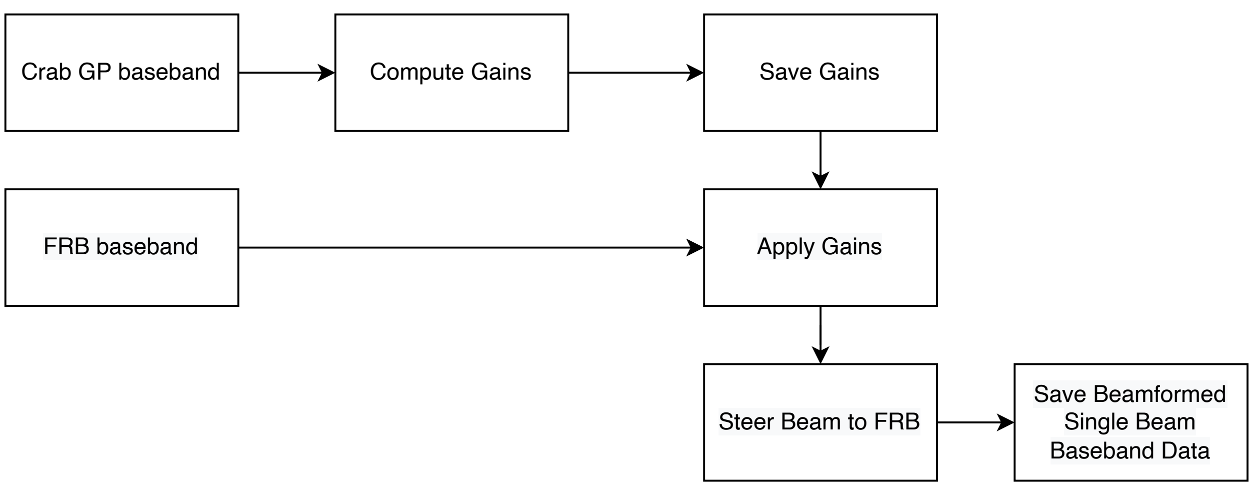


Figure 4.10: **Flow diagram of beamforming a FRB:** The beamforming process leading to a single beam of the FRB baseband data At CHIME and TONE.

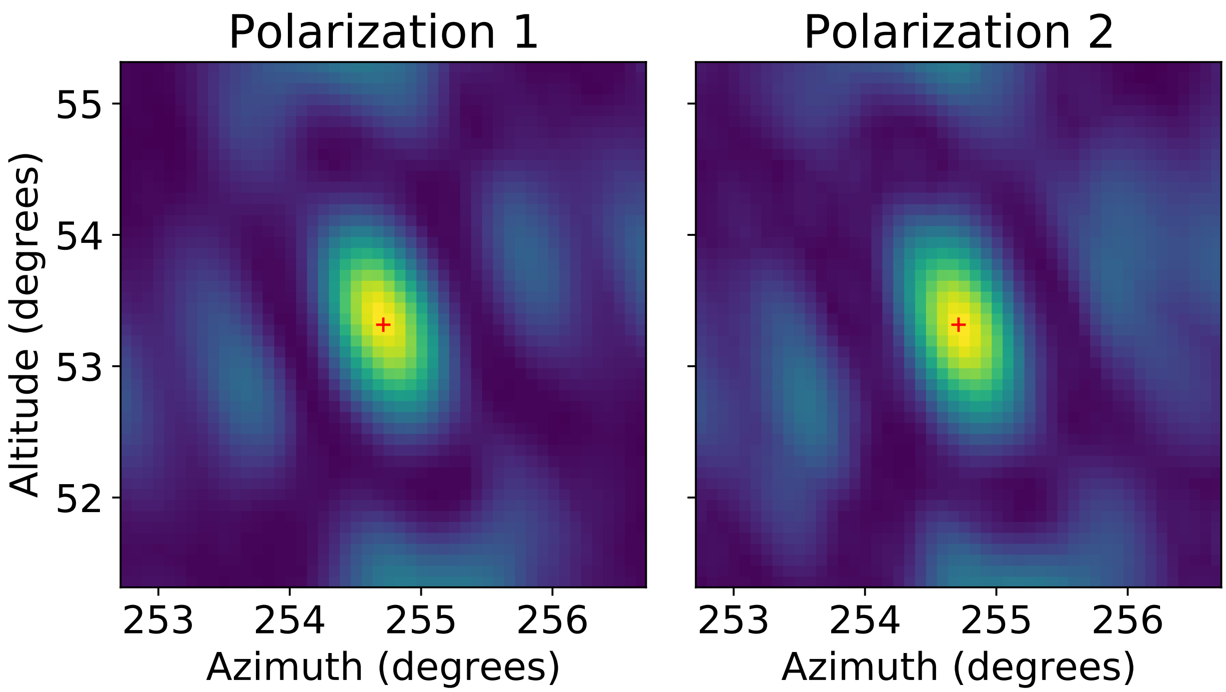


Figure 4.11: **A representation of the synthesized beam:** The SNR of the Crab pulsar giant pulse signal averaged across all frequencies from February 18 (see 4.14 and 4.14) is plotted in a grid of pointings $\pm 2\,\mathrm{deg}$ around the Crab pulsar position marked by the red plus marker. Since the SNR of the pulse at each point is convolved with the synthesized beam pattern of the array, this represents the beam.

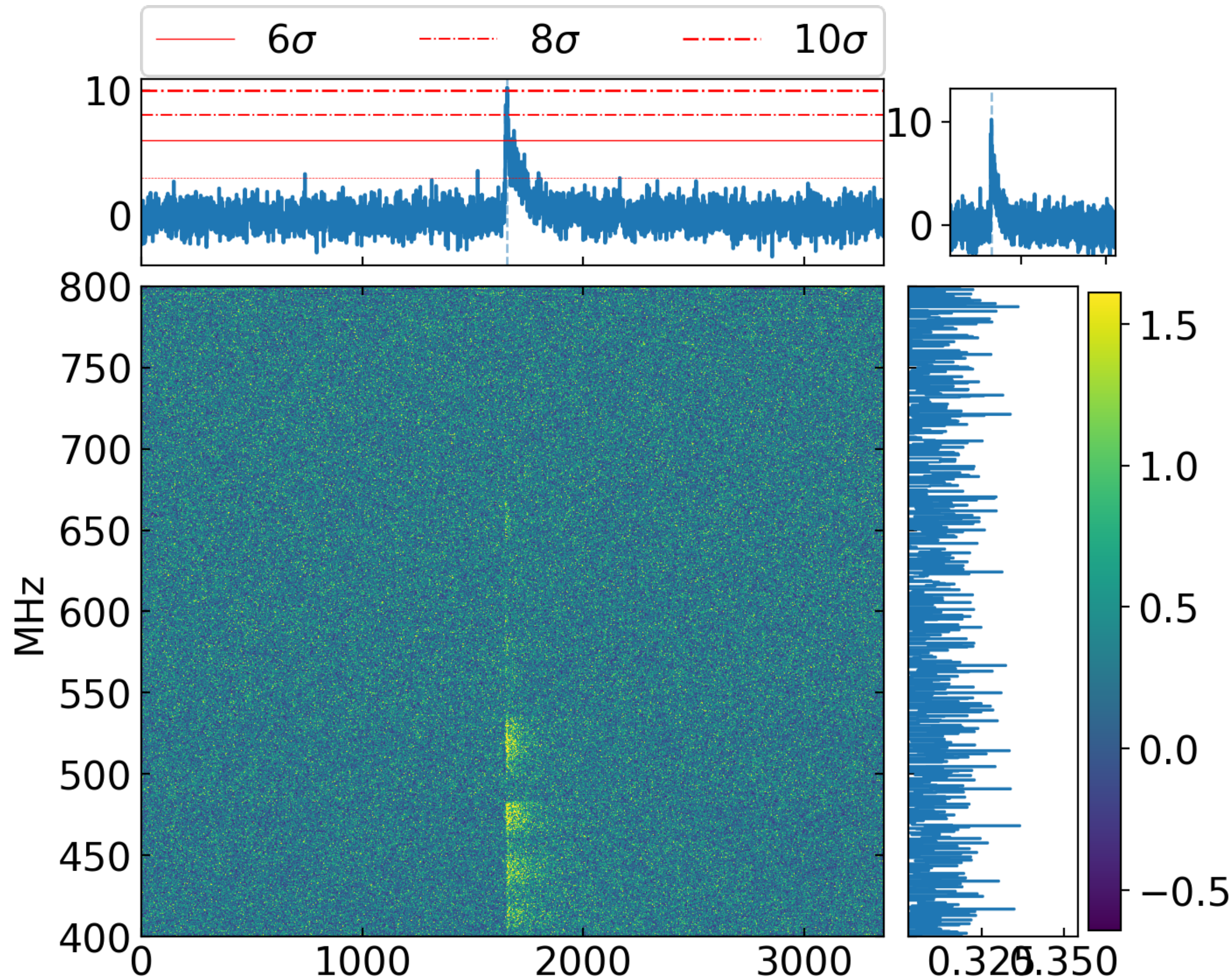


Figure 4.12: **Beamformed data from a Crab pulsar giant pulse for the first set of co-polarizations from February 10, 2021:** The top plot is the 'time-series' produced by summing all the frequency channels. The top-right plot is the zoomed-in region of the time series around the pulse. The right plot represents the sum of all the frequency channels.

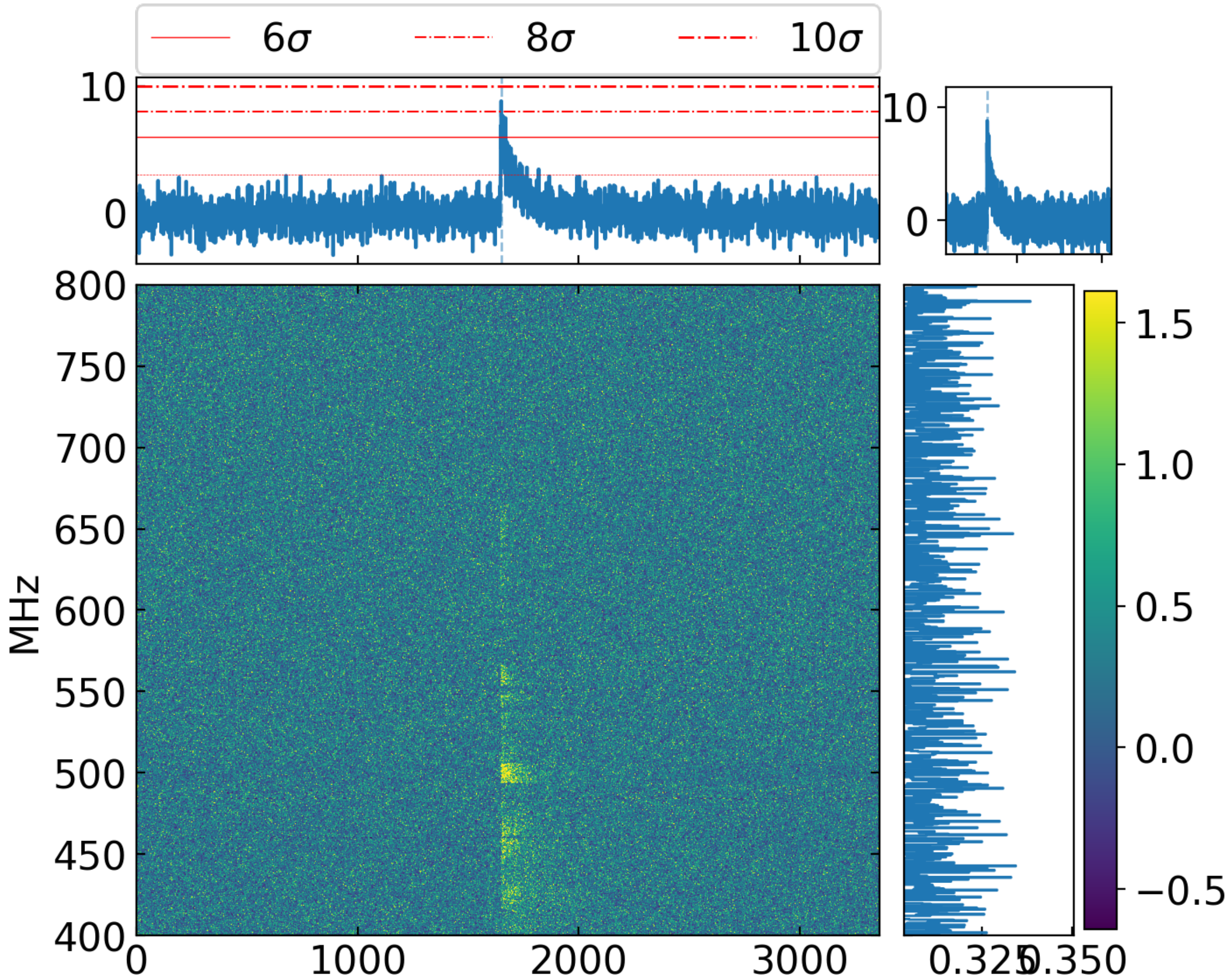


Figure 4.13: **Beamformed data from a Crab pulsar giant pulse for the second set of co-polarizations from February 10, 2021:** The top plot is the 'time-series' produced by summing all the frequency channels. The top-right plot is the zoomed-in region of the time series around the pulse. The right plot represents the sum of all the frequency channels.

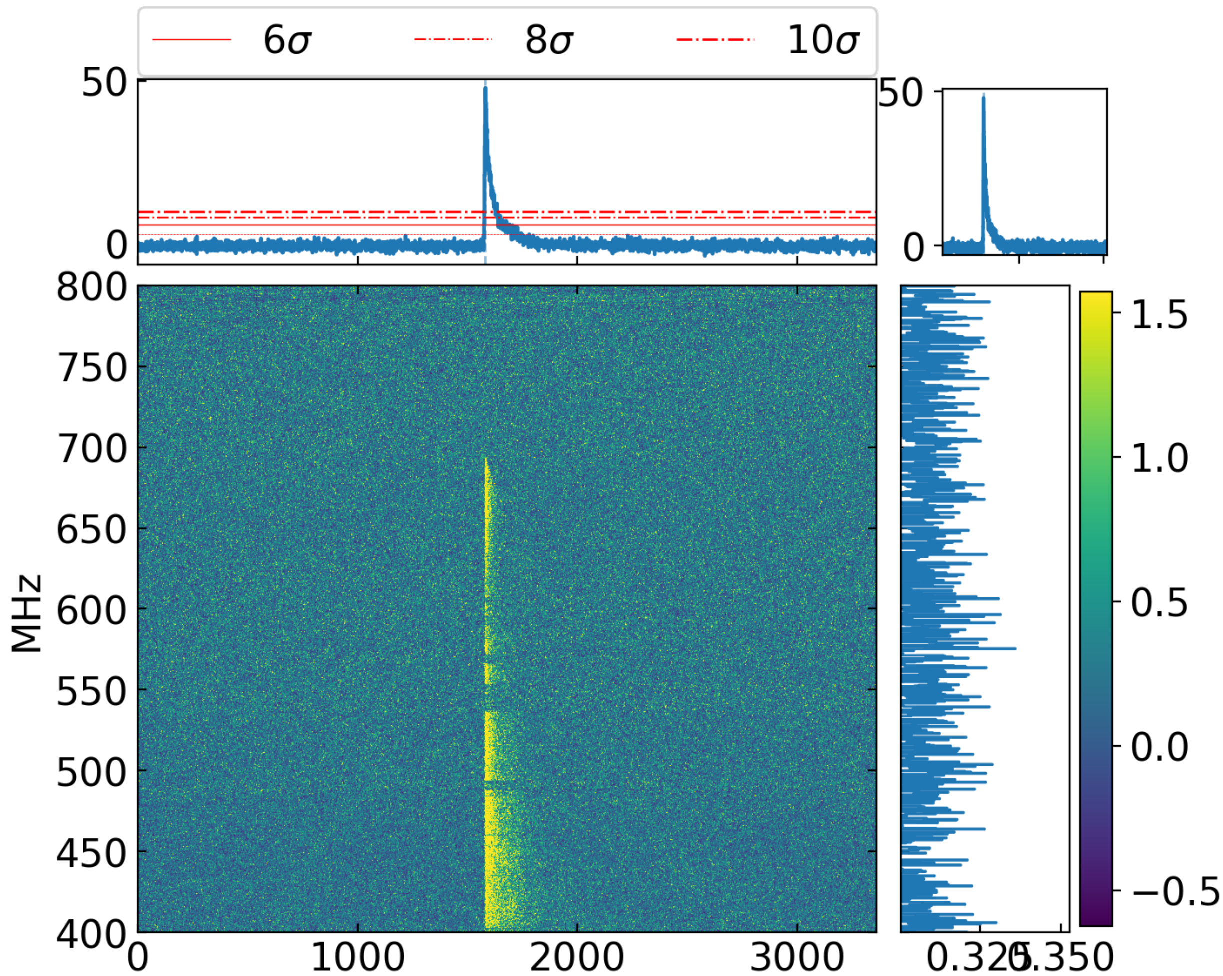


Figure 4.14: **Beamformed data from a Crab pulsar giant pulse for the first set of co-polarizations from February 18, 2021:** The top plot is the 'time-series' produced by summing all the frequency channels. The top-right plot is the zoomed-in region of the time series around the pulse. The right plot represents the sum of each frequency channel.

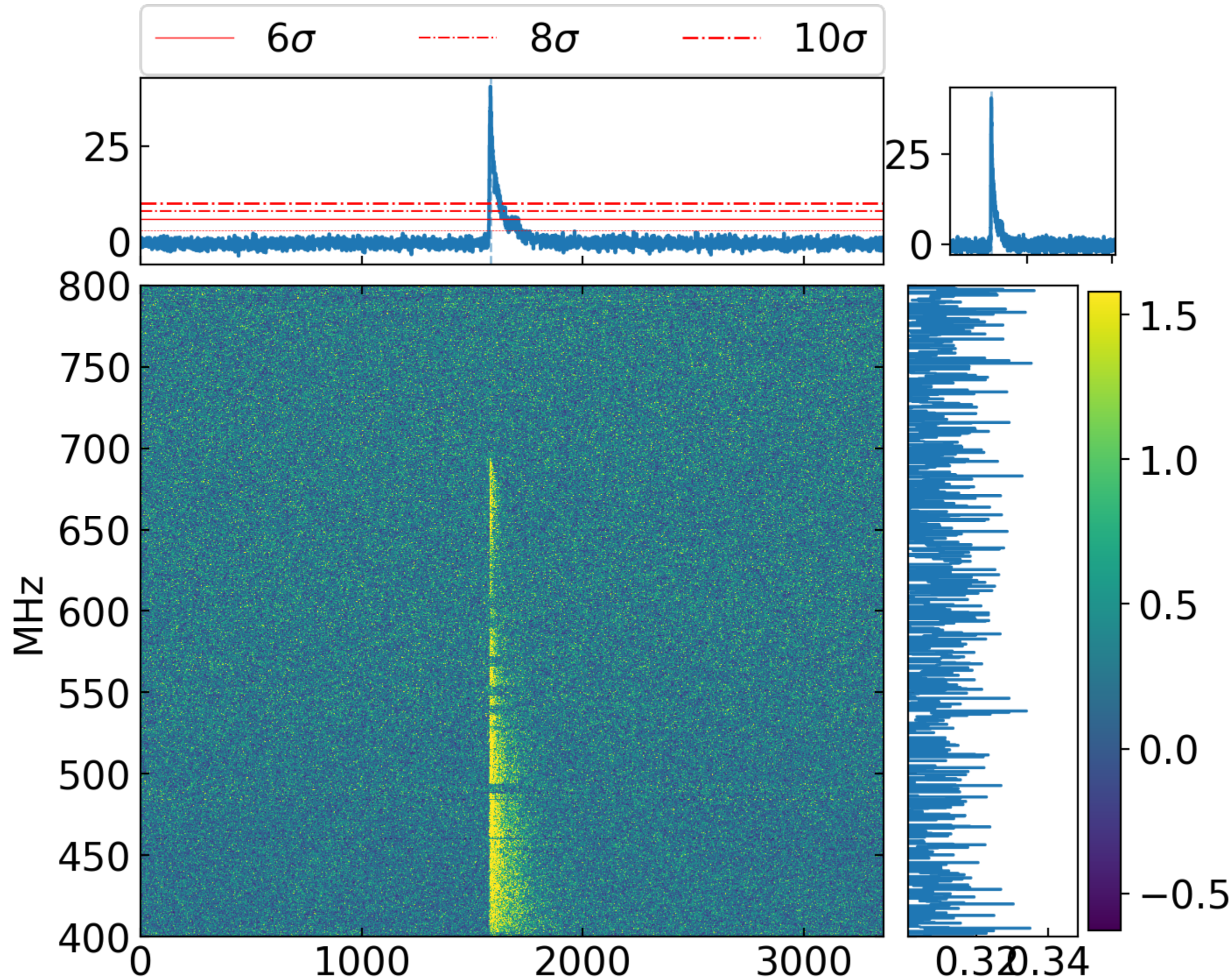


Figure 4.15: **Beamformed data from a Crab pulsar giant pulse for the second set of co-polarizations from February 18 2021.** The top plot is the 'time-series' produced by summing all the frequency channels. The top right plot is the zoomed in region of the time series around the pulse. The right plot represents the sum of each frequency channel.

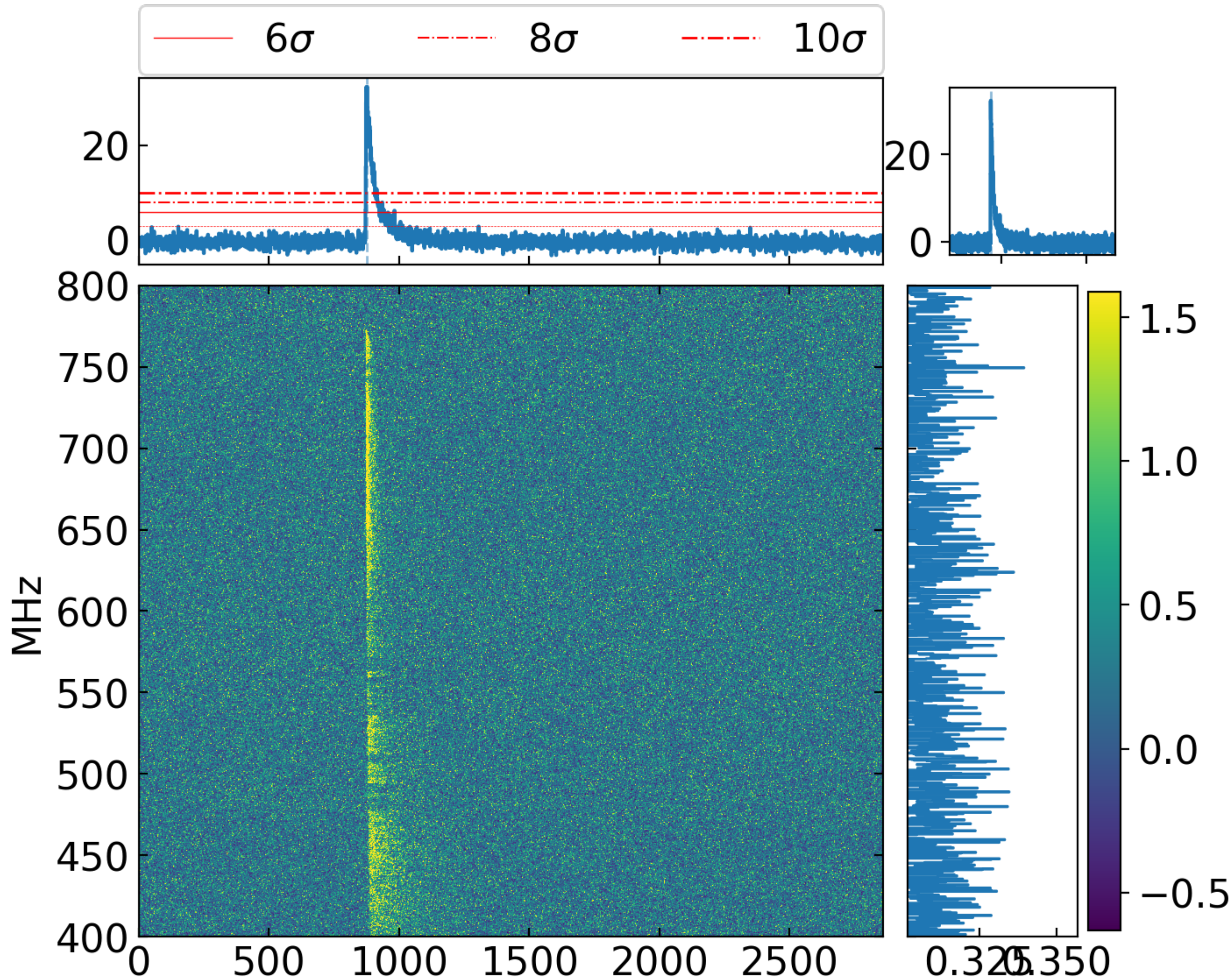


Figure 4.16: **Beamformed data from a Crab pulsar giant pulse for the first set of co-polarizations from February 23, 2021.** The top plot is the 'time-series' produced by summing all the frequency channels. The top-right plot is the zoomed-in region of the time series around the pulse. The right plot represents the sum of each frequency channel.

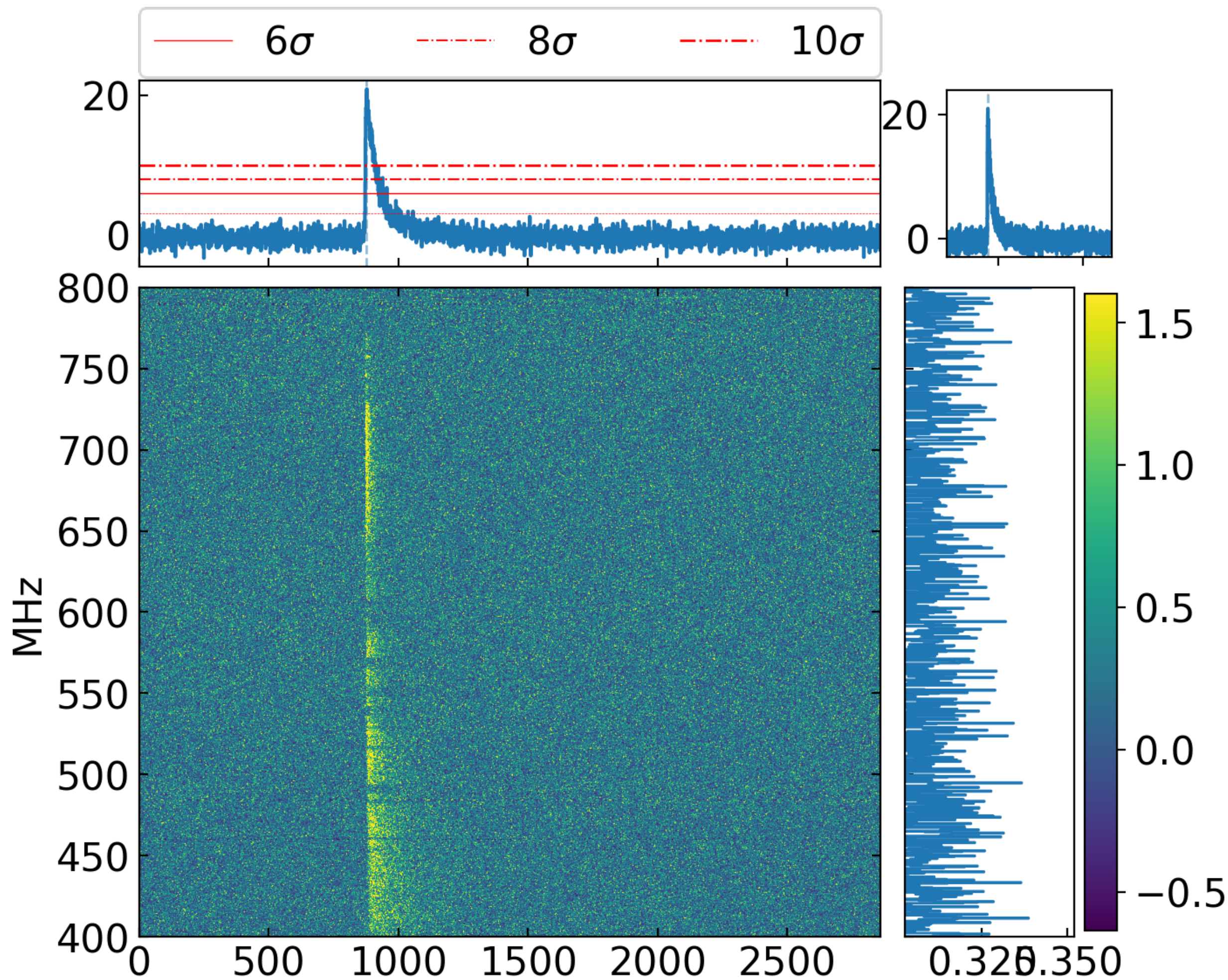


Figure 4.17: **Beamformed data from a Crab pulsar giant pulse for the second set of co-polarizations from February 23 2021.** The top plot is the 'time-series' produced by summing all the frequency channels. The top right plot is the zoomed in region of the time series around the pulse. The right plot represents the sum of each frequency channel.

## 4.3 Very Long Baseline Interferometery (VLBI)

In the 1960s, phenomena such as interplanetary scintillation, time variability of the radiation from quasars, maser emission from OH molecules, and radio bursts from Jupiter were all found to have sub-arc-second angular scales. The motivation to develop VLBI came from the indications that their radio sources have structures that cannot be resolved by connected interferometers with ever-increasing baselines. Since the first VLBI observations using a 26 m radio telescope at Dominion

Radio Astrophysical Observatory (DRAO) and a second $43\,\mathrm{m}$ one at the Algonquin Radio Observatory (ARO) located $\sim 3074\,\mathrm{km}$ away [131–134], it has been used to resolve increasingly small celestial angular scales. Additionally, it has been used for several varied astrometric and geodesy science cases such as

- Motion of the Earth's tectonic plates,
- Regional deformation and local uplift or subsidence,
- Definition of the celestial reference frame,
- Variations in the Earth's orientation and length of the day,
- Maintenance of the terrestrial reference frame,
- Measurement of gravitational forces of the Sun and Moon on the Earth and the deep structure of the Earth, and
- Improvement of atmospheric and ionospheric models.

FRB localization at VLBI scales so far has only been achieved with great success for prolific repeaters [135–137] and 'one off' at few kilometer baselines using the same local clocks and oscillators by instruments such as ASKAP [138], DSA-10 [139] and the VLA [140]. Daily sub-arcsecond localizations of FRBs are still elusive [1]. Some follow-ups can associate hosts and redshifts be determined by using preexisting wide-field instruments and other FRB properties [115] but for robust follow-ups of hosts and to leverage FRBs as probes precise localization is critical. This is due to be standard once the CHIME/FRB outriggers are online piggybacking on the prolific detection rate of CHIME/FRB.

Localization of all FRBs (repeaters and 'one-offs') using VLBI has several challenges:

- Short pulse width represents a minuscule amount of signal to be used for correlation.
- The sky location of FRBs are unknown and hence choosing appropriate VLBI calibrator is tricky.

[1]The handful (as of mid-2022) FRBs localized to their respective hosts are hosted here http://frbhosts.org

- Most FRBs do not repeat, $\lesssim 3\%$ of the current corpus of FRBs are knwon to repeat at least once.
- Most repeating FRBs do not repeat with a given periodicity which makes scheduling observations difficult.
- The pulses are dispersed which implies the energy of the pulse at different frequencies arrives at a different time at every station in a way that is not trivially determined. Additionally, for high DM FRBs, several seconds of baseband would be required for traditional voltage correlations.
- Localising at sub GHz frequencies poses challenges resulting from the frequency dependence and daily variability of the ionosphere.
- Dissimilar clocking systems at the VLBI stations require thorough characterizations.

### 4.3.1 CHIME/FRB Outrigger Pathfinders

Before the full outriggers are online we test technologies and algorithms at testbeds or pathfinders. We use a VLBI network consisting of three stations: Canadian Hydrogen Intensity Mapping Experiment (CHIME) at the Dominion Radio Astrophysical Observatory (DRAO) [100], ARO10, a ten-meter single dish at Algonquin Radio Observatory (ARO) [141], and TONE, a compact array of eight six-meter dishes at Green Bank Observatory (GBO) [142].

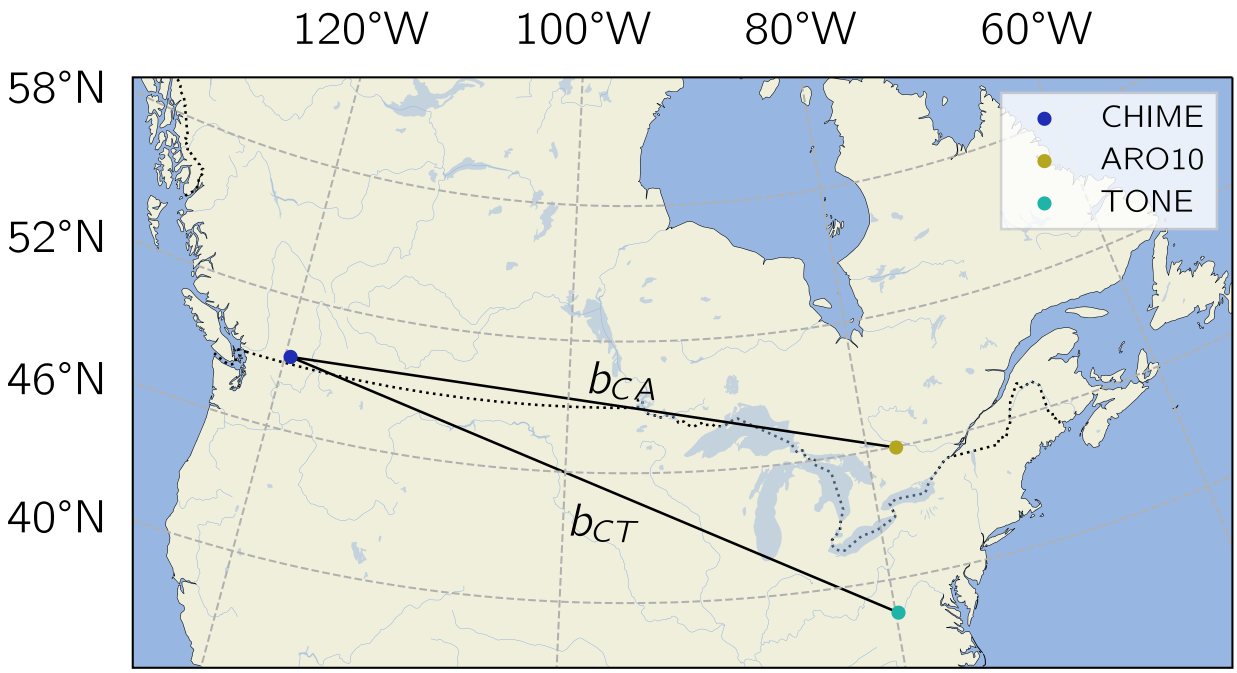


Figure 4.18: **Map of baselines formed between CHIME and ARO10 ($CA$) and TONE ($CT$).** The baselines span from Penticton, BC to Algonquin, ON, and Green Bank, WV with lengths $b_{CA} = 3074\,\mathrm{km}$ and $b_{CT} = 3332\,\mathrm{km}$. For our localization analysis, we omit the $848\,\mathrm{km}$ baseline between ARO10 and TONE because the FRB was not sufficiently bright to be detected on that baseline.

#### 4.3.1.1 CHIME/FRB

The CHIME telescope and the CHIME/FRB instrument are discussed in §2.3. The outriggers rely on a triggering system that waits for a trigger from a CHIME detection to save buffered data to disk for offline cross-correlation. It involves asynchronous servers running at ARO10 and TONE. Each station sends a "heartbeat" to the CHIME/FRB backend. The CHIME/FRB backend then registers each outrigger with a heartbeat as an active outrigger. Upon detection by the real-time pipeline of an FRB or a Crab pulsar giant pulse (GP)[143] in the field of view (FoV) of TONE and ARO10, a trigger is sent to the active outriggers. To prevent overwhelming the baseband readout system with thousands of Crab pulsar GPs, we record Crab GPs triggers with a detection SNR greater than $40$ (near CHIME's zenith) with a duty cycle of $1\,\%$. This results in a Crab GP dump rate of about once per day.

#### 4.3.1.2 Algonquin Radio Observatory 10-m telescope

ARO10 is located at the Algonquin Radio Observatory in Algonquin Park, Ontario. The CHIME-ARO10 baseline is over $b_{CA} \gtrsim 3000\,\mathrm{km}$ (see Figure 4.18). It is a single-dish telescope. The two analog signals from the polarization of the single CHIME cloverleaf feed [144] are digitized and acquired with a digital infrastructure is the same as CHIME and TONE except for the large ring buffer, $\sim$24 h long, being stored in hard disks. A complete description of the radio frequency (RF) chain and the digital system is provided in [141]. The data at ARO10 exhibit a delay drift relative to DRAO amounting to $\sim 0.1\,\mu\mathrm{s}\,\mathrm{day}^{-1}$. This extra shift in addition to the $\sim 2\,\mathrm{ms}$ geometrical delay is predictable and can be corrected (see Figure 15 of [141]).

#### 4.3.1.3 TONE

TONE is located at GBO near the Green Bank Interferometer Control Building. The CHIME-TONE baseline is $b_{CT} \approx 3332\,\mathrm{km}$ long (see Figure 4.18). TONE is an array of 6-m dishes placed in a regular $4 \times 3$ grid with $9.1\,\mathrm{m}$ spacing with the shorter side aligned $60°$ off true north. Details of the TONE system are shown in §3.

### 4.3.2 Clock Calibration

There exist timing errors intrinsic to the digital backends at each station, which are locked to different clocks with varying degrees of stability. The severity of timing errors depends on the type of clock used at each station and varies from unit to unit. Timing errors are characterized in terms of the Allan deviation ($\sigma(\Delta t)$) as a function of timescale $\Delta t$ (e.g., the time to the nearest synchronization) [145]. The CHIME digital system is locked to a single $10\,\mathrm{MHz}$ clock signal provided by a GPS-disciplined, oven-controlled crystal oscillator. While sufficient for the operations of CHIME as a stand-alone telescope, this clock does not meet the stringent stability requirements for VLBI with CHIME/FRB Outriggers. To overcome this limitation, we sample the more stable passive hydrogen maser during FRB VLBI observations [145] on a regular cadence. This minimally-invasive clocking system was developed as part of the effort to expand CHIME's capabilities to include VLBI with CHIME/FRB Outriggers. It works by digitizing the signal from an external maser using one of the inputs of the GPS-clock-driven ICE board. We read out a $2.56\,\mu s$ snapshot of maser data at a cadence of once every $\Delta t_{\text{C,sync}} = 30\,\text{s}$ at CHIME. The data readout from the maser is processed offline to measure the drift of the GPS clock between calibrator observations. A similar readout system records a $10\,\text{MHz}$ clock at TONE at a cadence of $\Delta t_{\text{T,sync}} = 1\,\text{s}$. In contrast, the digital system of ARO10 is directly clocked by an actively-stabilized hydrogen maser.

At CHIME and TONE, observations are referenced to the maser by interpolating between the maser readouts directly before and after the observation. The slow cadence of maser readout at these stations induces an interpolation error of size $\sigma_{\text{GPS}}(\Delta t_{\text{sync}}) \times \Delta t_{\text{sync}}$ when transferring time from the local GPS clocks to the local maser [146]. Referencing all observations to the maser at each station is necessary to take advantage of the maser's stability on $\sim$hour timescales. We use the maser to bridge the $\Delta t_{\text{C2,FRB}} \approx 4\,\text{h}$ gap between the observation of FRB 20210603A and C2. This introduces an additional timing deviation of size $\sigma_{\text{maser,C}}(\Delta t_{\text{C2,FRB}}) \times \Delta t_{\text{C2,FRB}}$.

The total clock errors include the slow, stochastic wandering of the masers over $\Delta t_{\text{C2,FRB}}$ as well as the interpolation required by the maser readout systems. We add these contributions in quadrature for both baselines (denoted CA for CHIME-ARO10 and CT for CHIME-TONE):

$$\begin{aligned}\sigma^2_{\tau,\text{CA}} = \; & \big(\sigma_{\text{GPS}}(\Delta t_{\text{GPS,C}}) \times \Delta t_{\text{GPS,C}}\big)^2 + \big(\sigma_{\text{maser,C}}(\Delta t_{\text{C2,FRB}}) \times \Delta t_{\text{C2,FRB}}\big)^2 \\ & + \big(\sigma_{\text{maser,A}}(\Delta t_{\text{C2,FRB}}) \times \Delta t_{\text{C2,FRB}}\big)^2\end{aligned} \tag{4.35}$$

$$\begin{aligned}\sigma^2_{\tau,\text{CT}} = \; & \big(\sigma_{\text{GPS}}(\Delta t_{\text{GPS,C}}) \times \Delta t_{\text{GPS,C}}\big)^2 + \big(\sigma_{\text{maser,C}}(\Delta t_{\text{C2,FRB}}) \times \Delta t_{\text{C2,FRB}}\big)^2 \\ & + \big(\sigma_{\text{GPS}}(\Delta t_{\text{GPS,T}}) \times \Delta t_{\text{GPS,T}}\big)^2 + \big(\sigma_{\text{maser,T}}(\Delta t_{\text{C2,FRB}}) \times \Delta t_{\text{C2,FRB}}\big)^2\end{aligned} \tag{4.36}$$

### 4.3.3 Local Calibration and Beamforming

CHIME has $1024$ antennas, and TONE has $8$ antennas. It is infeasible to correlate such a large number of antennas as independent VLBI stations. To reduce the computational burden of correlating such a large array, we coherently add, or beamform, the raw baseband data from the antennas within each station. Beamforming calibration and beam steering are discussed in §4.2. Once the gains are characterized, they are used to beamform the raw baseband data from CHIME and TONE towards the best-known positions of the Crab and the FRB provided by the baseband pipeline, which we refer to as $\widehat{\mathbf{n}}_0$. The synthesized beam at CHIME is $\sim 1\,\mathrm{arcmin}$ wide, and the synthesize beam at TONE is $\sim 0.5°$ wide (see Figure 4.11). Since the FRB's true position is well within a synthesized-beam width away from $\widehat{\mathbf{n}}_0$, our final sensitivity only depends weakly on $\widehat{\mathbf{n}}_0$.

### 4.3.4 FRB Localization

After beamforming is completed at each station, the beamformed baseband data are correlated with a custom VLBI correlator. We use the standalone delay model `difxcalc` to calculate geometric delays towards the fiducial sky location $\widehat{\mathbf{n}}_0$ of the FRB. Next, we delay-compensate the data as a function of time. The total delay is broken into an integer number of $2.56\,\mu\mathrm{s}$ frames and a sub-frame (or sub-integer) component ranging from -1.28 to $1.28\,\mu\mathrm{s}$. The integer shift is applied to the data via an array shift, and the sub-integer shift is applied by a phase rotation to each $2.56\,\mu\mathrm{s}$ sample. Applying the integer shift and time-dependent phase rotation is equivalent to Lorentz boosting each outrigger station into the same (CHIME's) reference frame within a $2.56\,\mu\mathrm{s}$ time bin.

Each of the $1024$ frequency channels of data is then de-smeared by a coherent dedispersion kernel [147]. While several conventions may be used (see e.g., Eq. 5.17 in [148]), we use the following kernel in our VLBI correlator:

$$H(\nu) = \exp\left(2\pi \mathrm{i} k_{\mathrm{DM}} \mathrm{DM} \frac{\nu^2}{2\nu_k^2(\nu_k + \nu)}\right). \tag{4.37}$$

In Eq. (4.37), we take $k_{\mathrm{DM}} = 4149.377\,59\,\mathrm{s\,MHz^2\,pc^{-1}\,cm^3}$ (for consistency with previous conventions in the pulsar community [148, 149]), and the fiducial DM of the FRB is taken to be $500.147(4)\,\mathrm{pc\,cm^{-3}}$. We choose this dedispersion kernel in order to avoid introducing delays into each frequency channel (i.e. it preserves times of arrival at the centre of each channel).

The chosen DM adequately resolves the pulse within each frequency channel. This concentrates the signal into a narrow temporal duration to maximize the correlation SNR. The argument $\nu \in [-195.3125\,\mathrm{kHz}, +195.3125\,\mathrm{kHz}]$ indicates the offset from the reference $\nu_k$, chosen to be the centre of each frequency channel $\nu_k \in [800.0, 799.609\,375, ..., 400.390\,625]\ \mathrm{MHz}$.

After the delay compensation towards the fiducial sky position $\widehat{\mathbf{n}}_0 = (\alpha_0, \delta_0)$ and coherent dedispersion, we form VLBI visibilities for each frequency channel (indexed by $k$) independently on both long baselines involving CHIME ($b_{\mathrm{CA}}$ and $b_{\mathrm{CT}}$, hereafter indexed by $i$) by multiplying and integrating the complex baseband data. To reject noise and RFI, we integrate only $\sim 100\,\mu\mathrm{s}$ of data on either side of the pulse in each of $1024$ frequency channels. This produces $1024$ complex visibilities per baseline which are used for astrometry (hereafter referred to as $V\,[i,k]$). We integrate $5$ other windows of the same duration in the same dataset but shifted to off-pulse times to estimate the statistical uncertainties on the visibilities. The statistical uncertainties are hereafter referred to as $\sigma\,[i,k]$.

The complex visibilities $V\,[i,k]$ must be phase-calibrated before the localization analysis. We use a phase calibration and fringe-fitting algorithm that removes static instrumental cable delays, and long-term clock drifts, and significantly suppresses unwanted astrometric shifts related to baseline offsets [141].

In addition to forming visibilities for the FRB ($\mathcal{V}_{\mathrm{FRB}}\,[i,k]$), we collect baseband data and correlate it towards the absolute position of the Crab pulsar [150] during the two Crab pulsar GPs, which we refer to as C1 and C2 respectively. This leaves us with three sets of visibilities ($\mathcal{V}_{\mathrm{C1}}\,[i,k]$, $\mathcal{V}_{\mathrm{FRB}}\,[i,k]$, $\mathcal{V}_{\mathrm{C2}}\,[i,k]$) with their corresponding uncertainties for each baseline. C1 is the brighter of the two Crab pulsar GPs; we therefore use a smoothed version of $\mathcal{V}_{C1}\,[i,k]$ as a phase calibration template $V'\,[i,k]$. All visibilities are multiplied by $\overline{V'}\,[i,k]$, where the overline denotes the complex conjugate. This removes static instrumental phases as a function of frequency, static clock offsets, and static cable delays.

After removing static delays, there still remains a slowly-varying clock drift which changes the measured delay by $\sim 0.1\,\mu\mathrm{s}\,\mathrm{day}^{-1}$ on the CHIME-ARO10 baseline [141] and a smaller drift of

$\sim 9\,\mathrm{ns\,day^{-1}}$ on the CHIME-GBO baseline. This delay drift does not show any significant deviations from linearity over 12 Crab transits. To compensate for these linear drifts in time, we measure delays from the Fourier transforms of $\mathcal{V}_{\mathrm{C1}}\,[i,k]$ and $\mathcal{V}_{\mathrm{C2}}\,[i,k]$. We linearly interpolate between the two delay measurements per baseline to estimate the instrumental delays at the epoch of the FRB ($\tau_{\text{inst,i}}$. Then, we apply a phase rotation of $2\pi\nu_k\tau_{\text{inst,i}}$ to the calibrated visibilities $\mathcal{V}_{\mathrm{FRB}}[i,k]$. Any other linear delay trends are absorbed into this fitting.

We refer to the fully-calibrated visibilities as $\mathcal{V}\,[i,k]$ (not to be confused with the un-calibrated visibilities $V\,[i,k]$). The calibrated visibilities $\mathcal{V}_{\text{FRB}}\,[i,k]$, the correlation start times in each channel $t_0\,[i,k]$, the baseline vectors $\mathbf{b}_{CA}$, $\mathbf{b}_{CT}$, and the fiducial sky position used to correlate the data $\widehat{\mathbf{n}}_0$ can be used to determine the FRB's true position $\widehat{\mathbf{n}}$. Several approaches have been taken in the literature [137, 141, 151], reflecting the significant challenge of astrometry with sparse $uv$-coverage. For example, the traditional method of making a dirty map of a small field and using traditional aperture synthesis algorithms to de-convolve the instrumental response is not well-suited to the present VLBI network with its extremely sparse coverage of the $uv$-plane. We extend the analysis of [141, 151] by fitting a model (Eq. 4.38) to the phases of the $\approx 1024$ visibility phases in each frequency channel on each of the two baselines. The phases $\phi\,[i,k]$ depend on the true two-dimensional position $\widehat{\mathbf{n}} = (\alpha,\delta)$, the fiducial position $\widehat{\mathbf{n}}_0$ and two ionospheric parameters for the CHIME-ARO10 ($\Delta\mathrm{DM}_{CA}$) and CHIME-TONE ($\Delta\mathrm{DM}_{CT}$) baselines as,

$$\phi\,[i,k] = 2\pi\nu_k\mathbf{b}_i\cdot(\widehat{\mathbf{n}}-\widehat{\mathbf{n}}_0)/c + 2\pi k_{\text{DM}}\Delta\mathrm{DM}_i/\nu_k. \tag{4.38}$$

To fit the model we compute the likelihood as in [141, 145, 151, 152],

$$\log\mathcal{L} \propto \sum_{i=\text{CA,CT}}\sum_{k=0}^{1023}\mathrm{Im}\left(\mathcal{V}\,[i,k]\exp\left(-\mathrm{i}\phi\,[i,k]\right)/\sigma\,[i,k]\right)^2. \tag{4.39}$$

To localize the FRB, we sample the posterior likelihood using publicly-available with Markov chain Monte Carlo sampling [153]. We use a prior which is uniform over a $1\,\mathrm{arcmin}\times 1\,\mathrm{arcmin}$ rectangle centred on $\widehat{\mathbf{n}}_0$, and impose a zero-mean Gaussian prior on both $\Delta\mathrm{DM}$ parameters:

$p(\Delta\mathrm{DM}_i) \propto \exp\left(-\Delta\mathrm{DM}_i^2/(2\sigma_{\mathrm{DM}})^2\right)$.

The rectangular prior can be understood as an approximation to the sub-arcminute scale localization provided by the CHIME/FRB baseband pipeline. The ionospheric prior can be understood as follows. In the limit that $\sigma_{\mathrm{DM}} \to 0$, we recover a fit that does not allow for any ionospheric contribution to the phases, and in the opposite limit $\sigma_{\mathrm{DM}} \to \infty$, we recover a completely unconstrained ionospheric model. In previous works, the European VLBI Network (EVN) localization of FRB 20201124A has been used to explore the astrometric reliability of FRB localizations in the limit of extremely sparse $uv$-coverage [137]. Fitting Gaussians to the fringe pattern along each baseline and fitting another Gaussian to their collective intersection was found to produce the most robust estimate of the FRB's position as validated by astrometry using all baselines together. This procedure implicitly assumes that the dispersive delay of the ionosphere does not wash out the fringe pattern entirely. Our procedure makes this assumption more quantitative by using a prior on the ionospheric delays to constrain the expected range of ionospheric fluctuations.

To quantify the expected severity of the ionospheric fluctuations, we turn to a Low-Frequency Array (LOFAR) study of the ionosphere on continental-scale baselines at $\approx 150\,\mathrm{MHz}$ [154]. At LOFAR frequencies, the ionosphere varies by at most $\sim 0.04\,\mathrm{TECu}$ ($\sim 1 \times 10^{-8}\,\mathrm{pc\,cm^{-3}}$) over the course of several hours [155]. At LOFAR frequencies, the ionospheric diffractive scale is larger by a factor of $\sim 5$ than at CHIME frequencies due to its frequency scaling of $\nu^{6/5}$ [156]. We, therefore, expect an ionospheric phase shift on the order of $\sim 0.04\,\mathrm{TECu}$ in either direction in our calibrated data. We take $\sigma_{\mathrm{DM}} = 5 \times 10^{-8}\,\mathrm{pc\,cm^{-3}}$ as a conservative estimate of the size of the ionospheric contribution. Finally, we sample the likelihood with $125$ walkers for $3.2 \times 10^5$ steps – 25 times the chain's autocorrelation length. We obtain an acceptance fraction of $16\,\%$, which is lower than the $23\,\%$ expected of optimal sampling but sufficient in light of our highly-multimodal likelihood [157, 158]. The localization contour is given by marginalizing over the two $\Delta\mathrm{DM}$ parameters.

# Chapter 5

# Detection

This chapter is the exciting culmination of all the work presented in the previous chapters. It is the result of an expansive collaboration between individuals, institutes, and instruments. These are the results of the first FRB, FRB 20210603A, localized to its host with the data collected at its first (and to date, only detection). The contents of this chapter are adapted from the paper, currently, *submitted and under review*, that I co-led with my colleagues Calvin Leung and Tomás Cassanelli. The contents of the paper are *near verbatim* but rearranged to better flow with the format of this dissertation. The VLBI procedure from the aforementioned paper has been refactored to the previous Chapter: 4. The analysis of the optical image and spectra obtained from CFHT and Gemini Observatory respectively was led by Savannah Cary with observations triggered by Mohit Bhardwaj. The polarization analysis was done by Ryan McKinven.

## 5.1 FRB 20210603A

FRB 20210603A, which we localize to the host galaxy in Figure 5.5, was initially detected by the Canadian Hydrogen Intensity Mapping Experiment (CHIME), located at the Dominion Radio Astrophysical Observatory. The CHIME/FRB instrument [100] searches for dispersed single pulses within CHIME's wide field of view. The detection of FRB 20210603A triggered the recording of voltage data at CHIME [96], as well as at a 10-m dish at Algonquin Radio Observatory (referred to as ARO10 hereafter) [141], and TONE, a compact array of eight, six-meter dishes at Green Bank Observatory (GBO)[142]. These three stations operate in tandem as a triggered very-long baseline interferometry (VLBI) array observing between $400$–$800\,\mathrm{MHz}$.

### 5.1.1 Observations

CHIME/FRB detected FRB 20210603A at 2021-06-03 15:51 UTC. In Figure 5.1 we show the Stokes-I dynamic spectrum of the beamformed data from FRB 20210603A as observed at CHIME. Between August 2018 and May 2021, $35.6\,\mathrm{h}$ of exposure were accumulated in the direction of FRB 20210603A; however only the burst reported here was detected. For calibration purposes, we observe two Crab Pulsar Giant Pulses (GPs), denoted by C1 and C2, at 2021-05-29 20:41 UTC and 2021-06-03 20:37 UTC respectively. While C1 and C2 are detected at all stations in autocorrelation, FRB 20210603A is only detectable in autocorrelation at CHIME (see Figure 5.2).

FRB 20210603A has a broadband, main pulse of duration of $\sim 220\,\mu\mathrm{s}$, with a signal-to-noise ratio of $\sim 136$ as detected by the CHIME/FRB real-time detection pipeline. In addition, two trailing emission components are visible in the data ( Figure 5.1). Using the `DM_phase` algorithm [159], we line up substructures in the main dispersed pulse, yielding a DM of $500.147(4)\,\mathrm{pc\,cm^{-3}}$. The DM is input to `fitburst`, which then finds that the main burst (excluding the two trailing emission components) can be described by three closely-spaced sub-bursts.

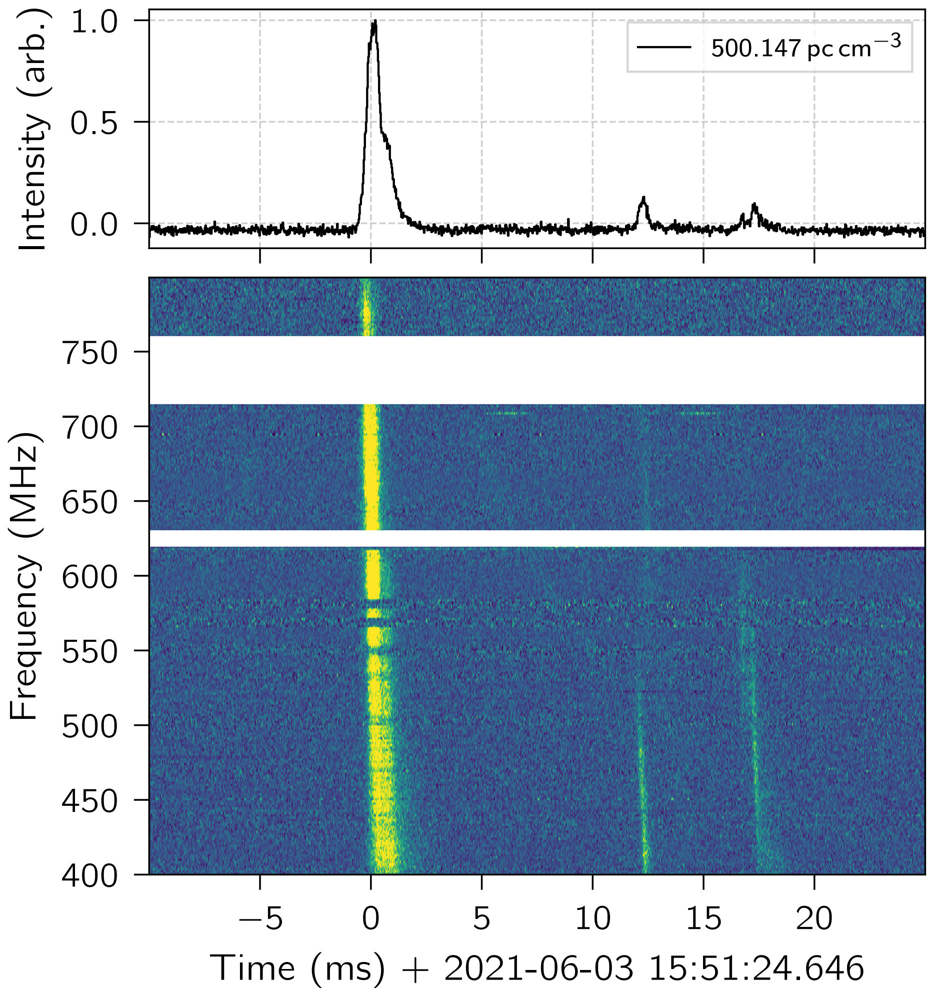


Figure 5.1: **The Stokes-$I$ dynamic spectrum of FRB 20210603A.** We detect the single pulse in autocorrelation at CHIME/FRB with a signal-to-noise ratio exceeding $100$. The data are shown at a time resolution of $25.6\,\mu\mathrm{s}$ with pixel colours scaled to their $1$–$99$ percentile values. To remove dispersion, we use a DM derived by lining up three closely-overlapping sub-burst components within the main pulse using `fitburst` [160]. In addition to the main burst, fainter emission components occurring $\sim 12\,\mathrm{ms}$ and $\sim 18\,\mathrm{ms}$ afterwards are visible in CHIME/FRB baseband data, but are neglected for VLBI localization. The faint dispersed sweeps left and right of the main pulse are known instrumental artifacts from spectral leakage. The masked regions correspond to RFI from cellular communication and television transmission bands between $700$–$750\,\mathrm{MHz}$ and $600$–$650\,\mathrm{MHz}$, respectively.

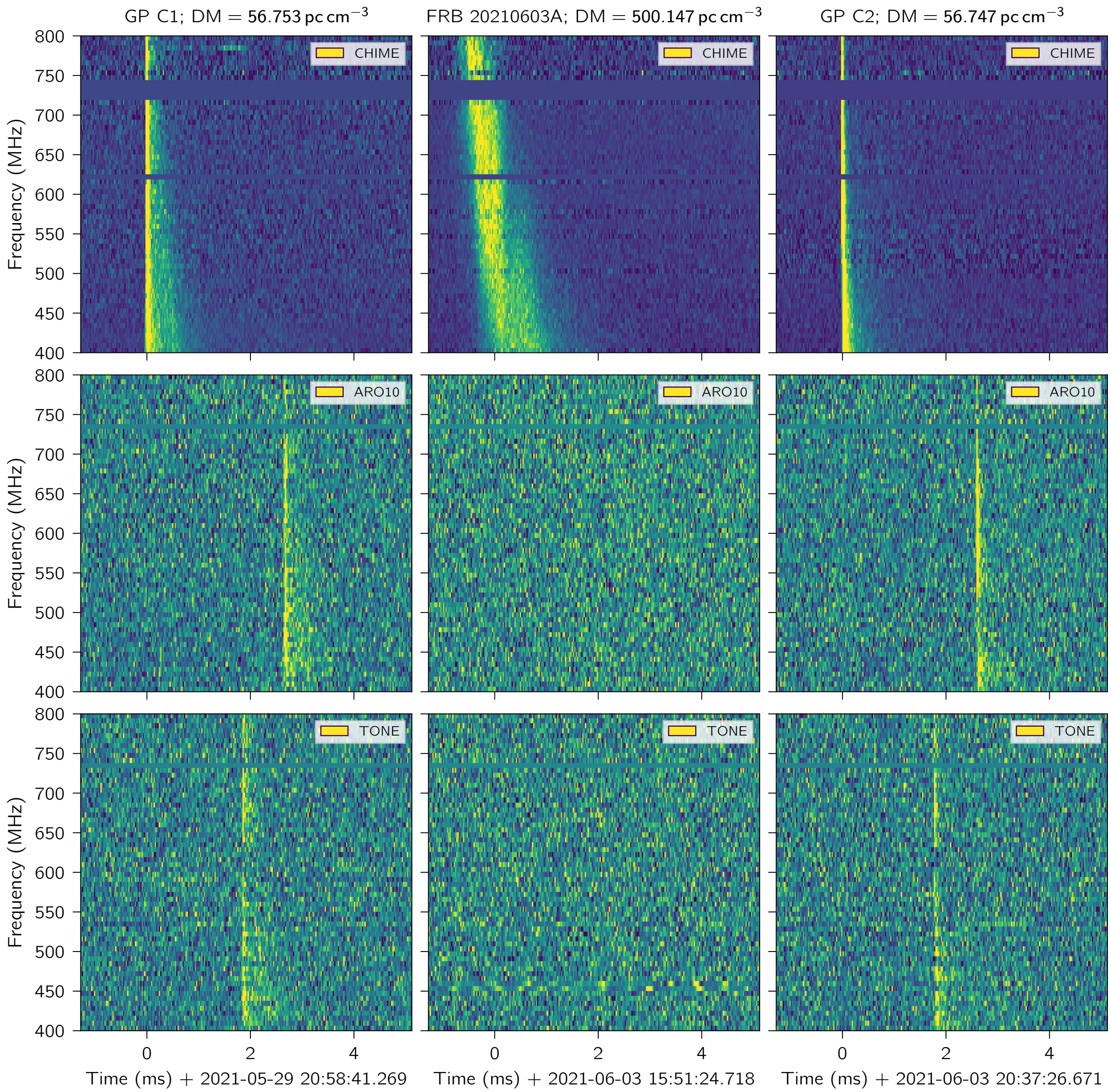


Figure 5.2: **Dynamic spectra of all observations.** At each VLBI station we record three bursts: FRB 20210603A (center column), and Crab pulsar giant pulses several days before (C1; left column) and several hours after (C2; right column) the FRB's arrival, which we refer to as C1 and C2 respectively. Each row corresponds to a different VLBI station (CHIME at the Dominion Radio Astrophysical Observatory, ARO10 at the Algonquin Radio Observatory, and TONE at the Green Bank Observatory). Timestamps show site-local clocks, not synchronized, and aligned to within $2.56\,\mu s$. Though the FRB is too faint to be detected at the testbeds alone, it is robustly detected in cross-correlation with CHIME. The intensity was adjusted by normalizing its standard deviation and setting the color scale limits to the $1$ and $99$ percentile values of the data. Waterfall plots are shown downsampled to a frequency resolution of $25\,\mathrm{MHz}$ and a time resolution of $25.6\,\mu s$. The noisy radio frequency interference (RFI) channels in $700$–$750\,\mathrm{MHz}$ correspond to the cellular communications bands and the RFI channels at lower frequencies correspond to television transmission bands.

## 5.2 Localization

*This section factored from a paper, co-led by me. It has been submitted and is currently being reviewed. The VLBI FRB localization method is described here and the results are discussed in the following chapter.*

We use a VLBI network consisting of three stations: the Canadian Hydrogen Intensity Mapping Experiment (CHIME) at the Dominion Radio Astrophysical Observatory (DRAO) [described in 100, & §2.3], ARO10, a ten-meter single dish at Algonquin Radio Observatory (ARO) [described in 141, & §4.3.1.2], and TONE, a compact array of eight six-meter dishes at Green Bank Observatory (GBO) [see 142, & §3]. For the observations of the FRB and the Crab giant pulses at TONE, $7$ signals from one polarisation and $6$ signals from the other were used to synthesize a single beam for VLBI. This VLBI array is dominated by east-west separations and has a maximum baseline length of $\sim 3300\,\mathrm{km}$ (CHIME-TONE). Of the three stations, only ARO10 is a traditional single-dish telescope. CHIME and TONE are compact interferometric arrays consisting of $1024$ and $8$ dual-polarisation antennas, respectively. All three stations observe the sky in drift-scan mode. The primary beam of CHIME at $600\,\mathrm{MHz}$ is approximately a $\sim 110°$-long strip of width $\sim 2°$ oriented along the local meridian [100]. Simultaneously, ARO10 and TONE are pointed to shadow a portion of the CHIME primary beam at a fixed declination ($\sim 22°$). This common field of view is chosen because it contains the Crab pulsar (PSR B0531+21), which we use as an astrometric calibrator.

### 5.2.1 VLBI

Upon detection of a single dispersed pulse such as an FRB or a giant pulse (GP) from the Crab pulsar, CHIME/FRB forwards low-latency alerts over the internet to the TONE and ARO10 systems, triggering a recording of buffered data to disk (see §4.3). The current network and triggered observing strategy serves as a pathfinder for CHIME/FRB Outriggers: three CHIME-like telescopes located across North America whose primary purpose will be to perform triggered VLBI on FRBs [141, 145, 151].

Since CHIME and TONE are interferometers, we localize FRB 20210603A using "cluster-cluster" VLBI, a specialized type of VLBI that uses beamforming to combine multiple antennas within a single station (or "cluster") into an effective single-dish station (see §4.3). Afterward, the beamformed data are analyzed with conventional VLBI techniques. We calibrate cable delays for the antennas within CHIME and TONE and phase them up towards the most precise estimate of the FRB's position available from CHIME alone, computed with the baseband localization pipeline [101], which we denote as

$$\widehat{\mathbf{n}}_0 = \left(10.2741(70)^\circ, 21.2266(32)^\circ\right). \tag{5.1}$$

After beamforming at CHIME and TONE to $\widehat{\mathbf{n}}_0$, we apply appropriate geometric delays and phase rotations to each of the $1024$ frequency channels. Then, we correlate the delay-compensated baseband data on the CHIME-ARO10 and CHIME-TONE baselines. We use a custom VLBI correlator to coherently dedisperse the FRB to a fiducial DM (see §4.3), and form on- and off-pulse visibilities. FRB 20210603A is detected in CHIME autocorrelation, but not in autocorrelation at the other stations (See §5.1.1). In cross-correlation, the FRB is detected on both the CHIME–ARO10 and CHIME–TONE baselines with a signal-to-noise ratio (SNR) of $\approx 35$ after coherently combining all frequency channels. Similarly, we record GPs from the Crab pulsar and form visibilities using its known position, updated to the current epoch by its proper motion [150]. We use that position of the Crab pulsar to calibrate static instrument delays, clock offsets, and drifts. We then fit an astrometric delay model for both baselines in visibility space, where statistical uncertainties are uncorrelated. The model includes differential dispersive delays between the stations from the ionosphere, on which we put a Gaussian prior of $\sigma_{\mathrm{DM}} = 5 \times 10^{-8}\,\mathrm{pc\,cm^{-3}}$ (see §4.3.4).

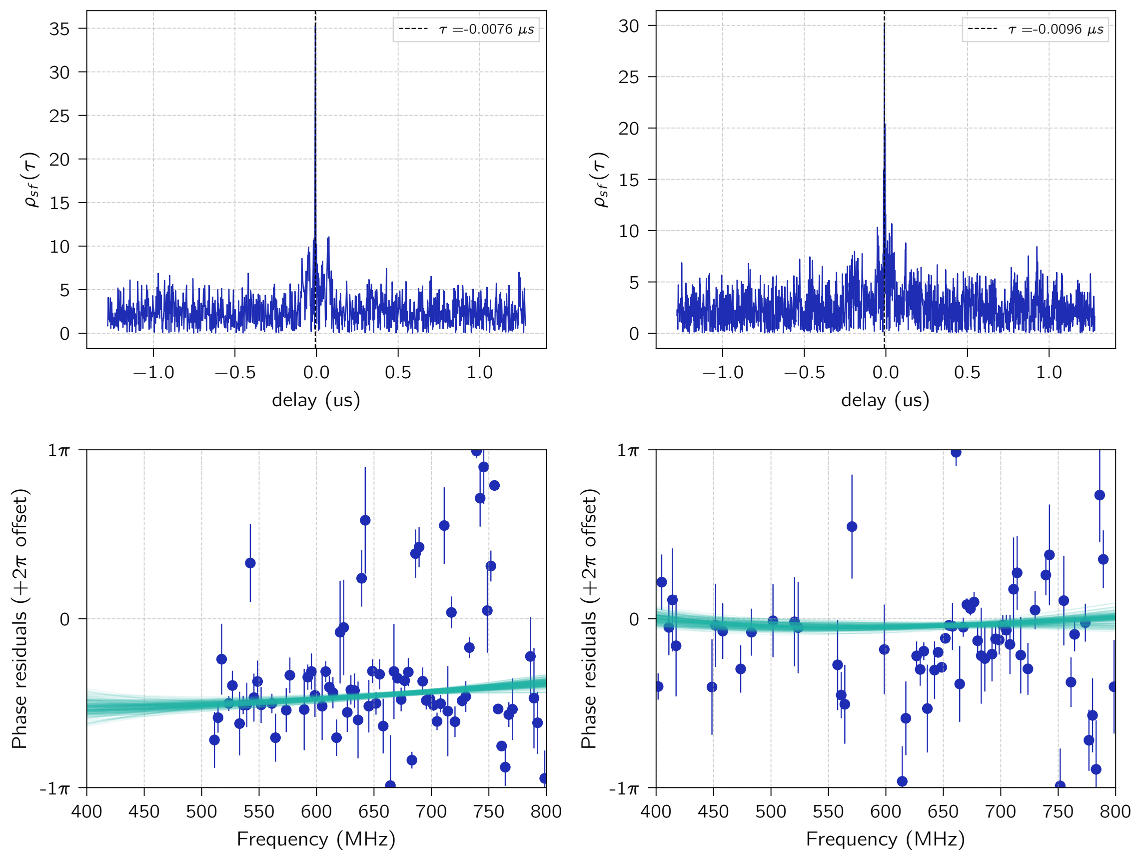


(a) (b)

Figure 5.3: **Cross-correlation visibilities from the CHIME-ARO10 (left) and CHIME-TONE (right) baselines respectively.** In each top panel, we plot the time-lag cross-correlation function $\rho(\tau)$ as a function of delay (ranging from $\pm 1.28\,\mu\text{s}$), showing a detection SNR exceeding $30$ on each baseline. In each bottom panel, we plot the phase of the calibrated and fringestopped visibilities $\mathcal{V}[i,k]$, binned to $6.25\,\text{MHz}$ resolution. We overlay model traces within the $95\,\%$ confidence region surrounding the best-fit values (corresponding to the contour in the inset of Figure 5.5) .

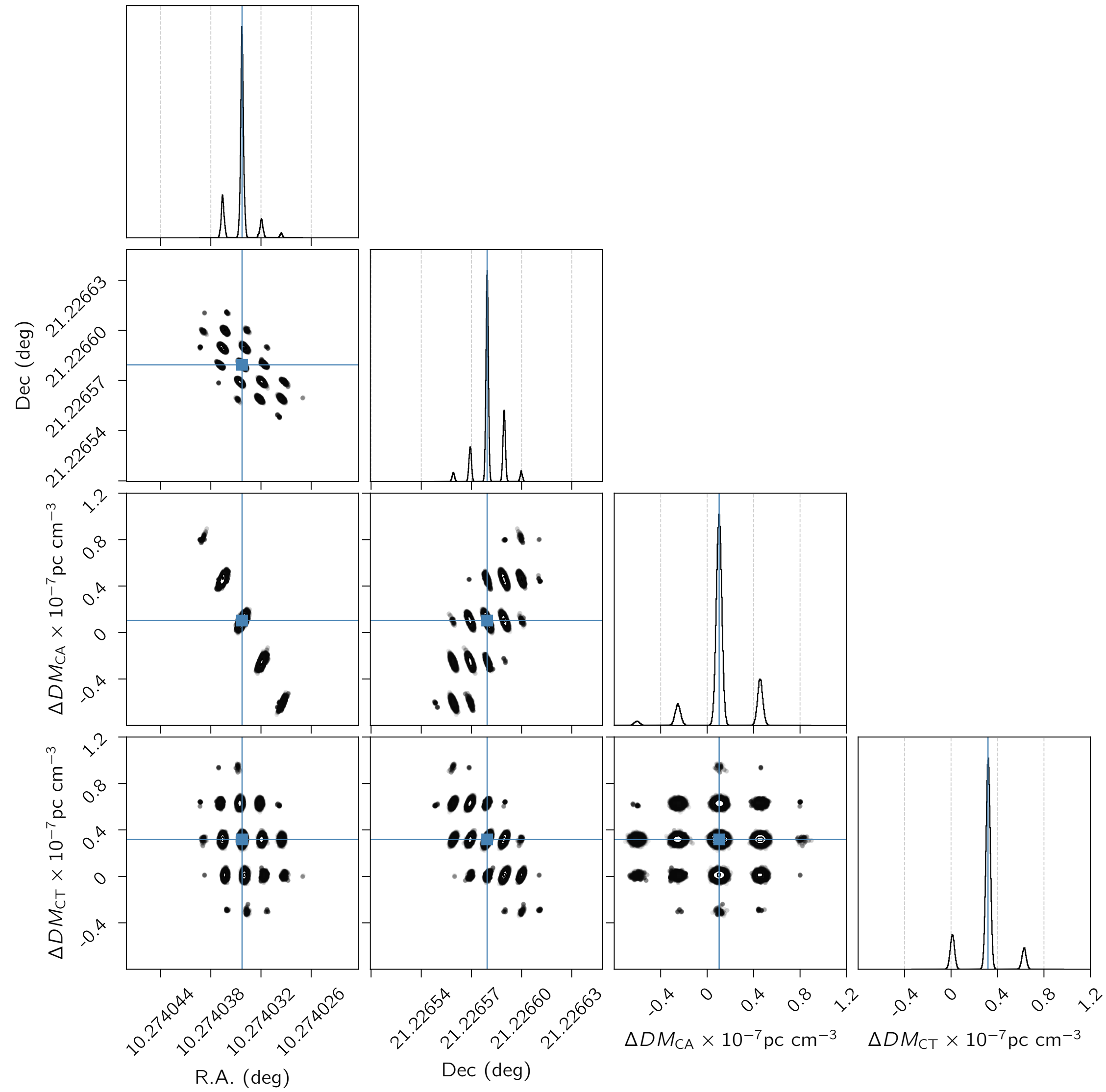


Figure 5.4: **Localization posterior likelihood as a function of R.A., Dec, and $\Delta\mathrm{DM}_{\mathrm{CA}}$, and $\Delta\mathrm{DM}_{\mathrm{CT}}$:** Due to the extremely sparse sampling of the $uv$-plane, we bypass traditional astrometry methods through imaging, and perform astrometric fits directly on the visibility data $\mathcal{V}[i, k]$ shown in Figure 5.3.

We estimate the systematic errors to be $51$ mas and $43$ mas for the CHIME-ARO10 and CHIME-TONE baselines respectively (see §5.2.1.1). The derived coordinates of FRB 20210603A in the International Celestial Reference Frame (ICRF) are Right Ascension $(\alpha) = 0\mathrm{h}41\mathrm{m}05.768\mathrm{s}\pm0.002\mathrm{s}$ and Declination $(\delta) =$ +21d13m35.686s$\pm$0.2s. (Table 5.3). These coordinates coincide with SDSS J004105.82+211331.9 [161], a disk galaxy with a nearly edge-on orientation (see Figure 5.5).

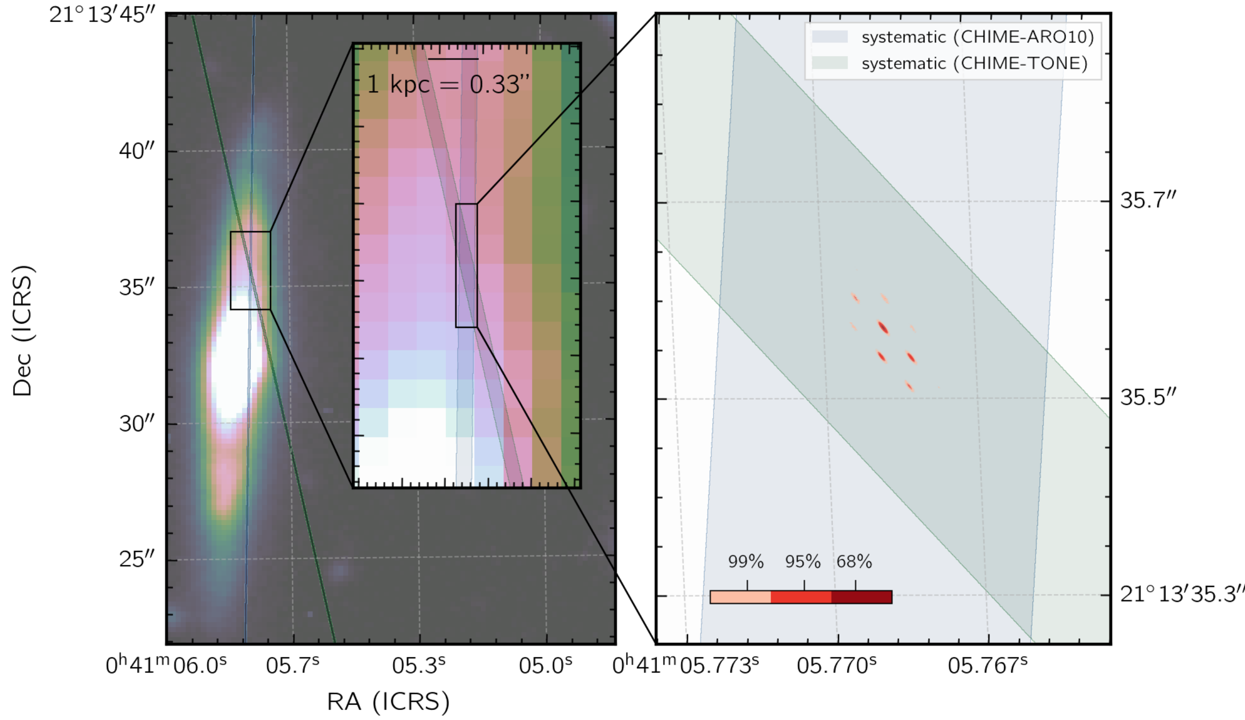


Figure 5.5: **VLBI Localization of FRB 20210603A**. The localization region is overlaid on a CFHT MegaCAM $gri$-band image of its host galaxy: SDSS J004105.82+211331.9. **Left:** the edge-on geometry of the host galaxy is apparent. We use an arcsinh scaling of pixel values, and allow the pixel colors to saturate in the bulge, to accentuate the faint structure in the outskirts of the galaxy. Systematic error bands for the two baselines are shaded (see Table 5.3). **Right:** A zoomed-in view of the localization contour, which includes uncertainties from the fringe-fitting analysis (statistical uncertainty). Our statistical uncertainties are represented by $68\,\%$, $85\,\%$, and $99.7\,\%$ contours of the likelihood function. The localization and burst properties point towards a progenitor located in the disk.

#### 5.2.1.1 Astrometric Error Budget

To precisely define the VLBI localization for FRB 20210603A, we have tabulated the largest sources of unwanted astrometric shifts that can arise from our measurements in Table 5.1. The largest contribution to our systematic uncertainty is the clock error (see §4.3.2). In addition, our systematic error budget includes station positioning errors, the position of the Crab pulsar at its current epoch, residual ionospheric fluctuations, and time-variable instrumental errors. Station positioning errors arise from not knowing the geocentric Earth location of each station to full precision, which arises from time-varying drifts of the phase center of the two interferometers (CHIME and TONE). In addition, the ARO10 Earth location is poorly constrained. The FRB localization error due to baseline offsets depends on the separation between the FRB and the calibrator (in the case of Crab GP C2, $1.7°$), the elevation of the calibrator, and the uncertainty on the baseline vector ($\sigma_b$). The Crab pulsar position error includes the pulsar position error ($\sigma_{\hat{\mathbf{n}}}$) and the proper motion ($\boldsymbol{\mu}$) error ($\sigma_{\boldsymbol{\mu}}$) extrapolated over $\Delta t \approx 10\,\mathrm{yr}$ from recent Crab pulsar astrometry [150]. We sum the absolute position error at the archival observing epoch and the uncertainty in the proper motion, scaled by the time between our observations ($\sim 10\,\mathrm{yr}$), in quadrature for the RA and DEC components individually. The uncertainties in the Crab position turn into equally-sized positional uncertainties of the FRB.

The ionosphere also introduces frequency-dependent delays, with a maximum deviation $\sigma_{\mathrm{DM}} = 5 \times 10^{-8}\,\mathrm{pc\,cm^{-3}}$. In addition to including the ionosphere explicitly in the fringe fit, we insert an ionospheric contribution of $1 \times 10^{-7}\,\mathrm{pc\,cm^{-3}}$ in the systematic budget to reflect the ionosphere's effects on the statistical contours as well as the systematic bands in Figure 5.5.

Table 5.1: Systematic error contributions to our astrometry.

| **Error type/station** | **ARO10** | **TONE** |
|---|---|---|
| Station position error | $21\,\mathrm{mas}$ ($\sigma_b \approx 10\,\mathrm{m}$) | $7\,\mathrm{mas}$ ($\sigma_b = 3\,\mathrm{m}$) |
| Crab pulsar position error | $2\,\mathrm{mas}$ | $2\,\mathrm{mas}$ |
| Clock error (see §4.3.2) | $40\,\mathrm{mas}$ | $37\,\mathrm{mas}$ |
| Ionospheric error ($\sigma_{\mathrm{DM}} = 1 \times 10^{-7}\,\mathrm{pc\,cm^{-3}}$) | $23\,\mathrm{mas}$ | $21\,\mathrm{mas}$ |
| Instrumental error (e.g., thermal expansion) | $2\,\mathrm{mas}$ | $2\,\mathrm{mas}$ |
| **Total** | $51\,\mathrm{mas}$ | $43\,\mathrm{mas}$ |

All quantities have been computed for the particular case of the observed FRB and added in quadrature to derive the total systematic error.

## 5.3 Burst Properties of FRB 20210603A

Our localization allows a detailed accounting of contributions to the observed DM, RM, and scattering (i.e., pulse broadening) in FRB 20210603A. Our determination of the pulse dispersion and scattering, which we measure as the frequency-dependent temporal broadening of the pulse, are broadly consistent with a sightline passing almost directly through the host galaxy's disk. In this scenario, the FRB should experience enhanced dispersion and pulse broadening due to the long line-of-sight path through the host galaxy's disk. The geometry increases the path length through the disk by a factor of $\csc\left(7(3)^{\circ}\right) = 8(3)$ compared to if the host galaxy were oriented face-on.

We estimate the DM from the host galaxy halo, disk, and the FRB local environment to be $\mathrm{DM}^{\mathrm{r}}_{\mathrm{host}} = 302(109)\,\mathrm{pc\,cm^{-3}}$, where the superscript denotes that $\mathrm{DM}^{\mathrm{r}}_{\mathrm{host}}$ is defined in the host galaxy's rest frame. We determine $\mathrm{DM}^{\mathrm{r}}_{\mathrm{host}}$ by subtracting DM contributions from the Milky Way, the Milky Way halo, and the intergalactic medium (IGM) from the measured DM (see §5.3). We make a simple estimate of the host galaxy disk and halo DM contributions by scaling the equivalent Milky Way contributions to the stellar mass of the host galaxy. Our simple model predicts $\mathrm{DM}^{\mathrm{r}}_{\mathrm{host}} = 264(97)\,\mathrm{pc\,cm^{-3}}$ for an FRB traveling out of the host galaxy through its disk, and is consistent with the estimate from the decomposition of the measured DM (see §5.3).

We quantify the total pulse broadening in the FRB dynamic spectrum by fitting a pulse model to the baseband data. The complex time-frequency structure of the main burst requires three sub-pulse components, temporally broadened by the same characteristic timescale, to obtain a robust fit to the data ( [160]). The best-fit scattering timescale is $\tau_{600\,\mathrm{MHz}} = 155(3)\,\mu\mathrm{s}$ at a reference frequency of $600\,\mathrm{MHz}$, whereas the pulse broadening due to the Milky Way is expected to be $\sim 1.0(5)\,\mu\mathrm{s}$ at that frequency [162, 163]. We conclude that the observed pulse broadening is dominated by extragalactic contributions, likely in the host galaxy rather than the Milky Way [164]. When scaled to the rest frame and scattering geometry of the host galaxy, the pulse broadening implies a scattering efficiency similar to a typical sight-line toward a pulsar through a galactic disk with Milky Way-like density fluctuations (see §5.3). In addition, this interpretation is consistent with our measurement of the burst RM. After subtracting Galactic and terrestrial contributions ($\mathrm{RM_{MW}}, \mathrm{RM_{iono}}$; see Table 5.3), the excess is $\mathrm{RM_{excess}} = (+198 \pm 3)\,\mathrm{rad\,m^{-2}}$. Since no intervening systems (e.g., galaxy groups/clusters) are observed along this sightline, the RM contribution from the IGM is likely negligible [165]. The excess RM could be dominated by contributions from the host galaxy interstellar medium (ISM), including the source's local environment. These properties suggest that the source of FRB 20210603A is located close to its galactic plane, consistent with our localization.

### 5.3.1 Dispersion and Scattering Analysis

In general the observed DM of an FRB can be split into four components as,

$$\mathrm{DM}_{\mathrm{FRB}} = \mathrm{DM}_{\mathrm{MW-disk}} + \mathrm{DM}_{\text{MW-halo}} + \mathrm{DM}_{\text{cosmic}} + \mathrm{DM}_{\text{host}}, \tag{5.2}$$

where $\mathrm{DM}_{\text{MW-disk}}$ is the contribution of the disk of the Milky Way, $\mathrm{DM}_{\text{MW-halo}}$ is that from the extended hot Galactic halo and $\mathrm{DM}_{\text{cosmic}}$ is from the intergalactic medium. The DM contribution of the host, $\mathrm{DM}_{\text{host}}$, is a combination of the contributions from the interstellar medium (ISM) of the host galaxy $\mathrm{DM}_{\text{host-disk}}$, the halo of the host galaxy $\mathrm{DM}_{\text{host-halo}}$ and the contributions from the source environment $\mathrm{DM}_{\text{host-env}}$.

To interpret unknown contributions to the total DM, we subtract known contributions from the total. The contribution from the Milky Way disk estimated from the NE2001 model [162, 163] is $\mathrm{DM}_{\text{MW-disk,NE2001}} = 40(8)\,\mathrm{pc\,cm^{-3}}$[1]. We estimate the contribution of the Galactic halo to be $\mathrm{DM}_{\text{MW-halo}} = 30(20)\,\mathrm{pc\,cm^{-3}}$ using the model described in [166]. We can treat this estimate as conservative, and it can be as low as $6\,\mathrm{pc\,cm^{-3}}$[73]. The IGM contribution is estimated to be $\mathrm{DM}_{\text{cosmic}} = 172(90)\,\mathrm{pc\,cm^{-3}}$ [167], where the range is due to cosmic variance in the Macquart relation out to $z \approx 0.18$ [168]. This leaves the contribution to the DM from the host galaxy halo, disk, and the FRB local environment as $\mathrm{DM}_{\text{host}} = 257(93)\,\mathrm{pc\,cm^{-3}}$.

The large value of $\mathrm{DM}_{\text{host}}$ is consistent with a long line-of-sight traveled through the host galaxy disk, resulting from the galaxy inclination angle. We can estimate the DM contributions of the host galaxy disk and halo by scaling the Milky Way's properties. We assume the disk size ($R$) scales with the galaxy stellar mass $\mathrm{M}^{\star}$ as a power law $R \propto (\mathrm{M}^{\star})^{\beta}$ where for simplicity we choose $\beta \sim 1/3$. This value of $\beta$ is close to the measured value in the literature for galaxies with $\mathrm{M}^{\star} = 10^{7} - 10^{11}\ \mathrm{M}_{\odot}$[169]. Thus the galaxy size scales as $\left(\mathrm{M}^{\star}/\mathrm{M}^{\star}_{\mathrm{MW}}\right)^{1/3} = (1.4(3))^{1/3} = 1.12(8)$,

[1]The Milky disk contribution as determined by from the YMW16 electron density model [72] is $\sim 31\,\mathrm{pc\,cm^{-3}}$ which changes our budget by $\sim 10\,\mathrm{pc\,cm^{-3}}$.

where $\mathrm{M}^{\star} = (8.5(8)) \times 10^{10}\ \mathrm{M}_{\odot}$ and $\mathrm{M}^{\star}_{\mathrm{MW}} = (6.1(11)) \times 10^{10}\ \mathrm{M}_{\odot}$ are the present-day stellar masses of host galaxy and Milky Way [170] respectively. Assuming the halo size also scales as $\left(\mathrm{M}^{\star}/\mathrm{M}^{\star}_{\mathrm{MW}}\right)^{1/3}$, the average Milky Way halo DM contribution $43(20)\,\mathrm{pc\,cm^{-3}}$ [166] can be scaled to estimate $\mathrm{DM}^{\mathrm{r}}_{\text{host-halo}} = \mathrm{DM}_{\text{MW-halo}} \times (\mathrm{M}^{\star}/\mathrm{M}^{\star}_{\mathrm{MW}})^{1/3} = 48(23)\,\mathrm{pc\,cm^{-3}}$ in the host galaxy's rest frame.

Similarly, we can conservatively estimate the rest frame DM due to the disk of the host galaxy, $\mathrm{DM}^{\mathrm{r}}_{\text{host-disk}}$. A first approximation is to assume that the FRB originates from close to the midplane of the disk, and scale the DM contribution of the half-thickness of the Milky Way ($N_{\perp}(\infty) \approx 24(3)\,\mathrm{pc\,cm^{-3}}$ [171]) by a factor of $\csc\left(7(3)^{\circ}\right) = 8(3)$ to account for the viewing geometry.

We assume the electron density stays equivalent to that of the Milky Way and scale for the host galaxy size. This yields an estimate of $\mathrm{DM}^{\mathrm{r}}_{\text{host-disk}} = N_{\perp}(\infty) \times \csc\left(7(3)^{\circ}\right) \times \left(\mathrm{M}^{\star}/\mathrm{M}^{\star}_{\mathrm{MW}}\right)^{1/3} = 193(82)\,\mathrm{pc\,cm^{-3}}$ in the host galaxy rest frame. We can sum these estimates of the $\mathrm{DM}^{\mathrm{r}}_{\text{host-disk}}$ and $\mathrm{DM}^{\mathrm{r}}_{\text{host-halo}}$ to give the DM in the observer's frame as $\mathrm{DM}_{\text{host}} = (\mathrm{DM}^{\mathrm{r}}_{\text{host-disk}} + \mathrm{DM}^{\mathrm{r}}_{\text{host-halo}})/(1+z) = 224(82)\,\mathrm{pc\,cm^{-3}}$ which is consistent with the observed $\mathrm{DM}_{\text{host}}$. If the FRB is behind the galaxy, the expected contribution from the host galactic disk could be increased by up to a factor of 2 yielding $448(164)\,\mathrm{pc\,cm^{-3}}$; however, this possibility is inconsistent with the observed DM excess.

The pulse broadening is measured to be $\tau_{600\,\mathrm{MHz}} = 155(3)\,\mu\mathrm{s}$ and is consistent with expected contributions from the host galaxy disk. In this scenario, the observed scattering and DM through the host disk should be commensurate with known pulsar lines of sight through the Milky Way at similar Galactic latitudes. We compare the FRB's scattering to archival measurements of Galactic pulsars as follows. First, we scale $\tau_{600\,\mathrm{MHz}}$ to $1\,\mathrm{GHz}$, and multiply by $(1+z)^3$ to account for time dilation and the un-redshifted frequency at which the pulse is scattered. This gives $\tau_{\text{proper},1\,\mathrm{GHz}} = 45\,\mu\mathrm{s}$ in the rest frame of the host galaxy. Further dividing this by 3 converts the geometric weighting from that of extragalactic (plane-wave) scattering to Galactic (spherical-wave) scattering [172]. Finally, subtracting $\mathrm{DM}_{\text{host-halo}}$ from the observed DM excess in the host galaxy rest frame yields $\mathrm{DM}^{\mathrm{r}}_{\text{host-disk}} = 254(111)\,\mathrm{pc\,cm^{-3}}$. We then calculate the ratio of observables

$$\frac{\tau_{\mathrm{proper,1\,GHz}}}{3(\mathrm{DM}^{\mathrm{r}}_{\mathrm{host-disk}})^2} \approx 4(3)\times 10^{-7}\,\mathrm{ms\,pc^{-2}\,cm^{6}} \propto \widetilde{F}G. \tag{5.3}$$

This ratio characterizes the efficiency of the scattering along the line of sight. It is proportional to the product of the fluctuation parameter $\widetilde{F}$ and an order-unity geometric factor $G$. The proportionality constant is $\Gamma(7/6)r_e^2c^3\nu^{-4}$, where $\Gamma(7/6)\approx 0.9277$, $c$ is the speed of light, $r_e = 2.8\,\mathrm{fm}$ is the classical electron radius, and $\nu$ is the frequency at which the scattering is observed [173]. This proportionality constant captures the microphysics and the frequency dependence of the scattering and relates it to the ratio of observables. The bulk properties of the gas are captured by $\widetilde{F}$, which depends on the volume filling factor of gas cloudlets, the size distribution of cloudlets doing the scattering, the size of the density variations within a cloudlet, and the inner/outer scales of the turbulence [172]. For the Milky Way's disk, typical values of $\widetilde{F}$ range from $0.001$–$1\ \mathrm{pc^{-2/3}\,km^{-1/3}}$ for low-latitude sightlines, roughly corresponding to scattering-DM$^2$ ratios of $1\times10^{-8}$–$1\times10^{-5}\,\mathrm{ms\,pc^{-2}\,cm^{6}}$ [172]. $G$ can vary by an order of magnitude because it depends on the relative position of the scattering media to the source and observer, which is poorly constrained for extragalactic sources of scattering. For example, for the geometry of a homogeneous scattering medium between the FRB and the edge of the host galaxy and a distant observer at infinity, $G = 1$. However, for a spiral arm of thickness $L \approx 1\,\mathrm{kpc}$ at a distance $d \approx 10\,\mathrm{kpc}$ in front of the FRB, $G = L/d \approx 0.1$. We observe that the host DM and scattering properties are consistent with those of an FRB sightline through a host-galactic disk with Milky Way-like density fluctuations. These properties are suggestive of a source close to the host galaxy's plane as opposed to an FRB progenitor significantly displaced from the host galaxy's disk.

Another interpretation is that the DM excess and scattering are partially contributed by the source's local environment. The DM excess observed is not extreme: it is only a factor of two greater than the median measured in population studies ($\mathrm{DM}_{\mathrm{host}} \approx 145\,\mathrm{pc\,cm^{-3}}$ [174]). Furthermore, the scattering timescale and low rotation measure are not outliers within the diverse population of FRBs. In this scenario, the FRB could be produced by a progenitor significantly displaced from the host galactic plane relative to the electron scale height ($1.57(15)\,\mathrm{kpc}$), reducing the host disk contribution to a fraction of our estimate ($224(82)\,\mathrm{pc\,cm^{-3}}$). This displacement would imply an old progenitor since young progenitors typically have low scale heights, $\sim 30\,\mathrm{pc}$ and $100\,\mathrm{pc}$, for young magnetars and massive stars respectively [175, 176]).

### 5.3.2 Polarisation Analysis

The polarisation analysis follows a similar procedure to that previously applied to other FRBs detected by CHIME/FRB [177, 178]. In particular, an initial RM estimate is made by applying RM-synthesis [179, 180] to the Stokes $Q$ and $U$ data of the burst. This initial estimate is then further refined through a judicious selection of time and frequency limits that optimize the SNR of the polarised signal. We then apply a Stokes $QU$-fitting routine that directly fits for the modulation between Stokes $Q$ and $U$ from Faraday rotation but is further extended to capture additional features in the Stokes spectrum.

We analyze FRB 20210603A using the CHIME/FRB polarization pipeline, identical to that recently employed on FRB 20191219F [181]. We determine an RM $= -219.00(1)\,\mathrm{rad\,m^{-2}}$ and find the lower limit of the linear polarised fraction ($\Pi_{\mathrm{L}}$) differs between the top ($\gtrsim 96\,\%$ at $800\,\mathrm{MHz}$) and the bottom of the CHIME band ($\gtrsim 87\,\%$ at $400\,\mathrm{MHz}$). This is counteracted by a very small but changing circular polarised fraction that becomes more significant at the bottom of the band. While this result may reflect the intrinsic properties of the burst at the source or be an imprint of some unknown propagation effect [182–184], it is also not possible to rule out instrumental effects such as cross-polarization between CHIME's orthogonal feeds. For this reason, we do not report on the circular polarisation and conservatively set our $\Pi_{\mathrm{L}}$ measurements as lower bounds (see Table 5.3).

The Galactic $\mathrm{RM_{MW}} = -22.4(3)\,\mathrm{rad\,m^{-2}}$ contribution can be estimated from recent all-sky Faraday Sky maps [185]. The RM contribution of Earth's ionosphere, $\mathrm{RM_{iono}} = +1.4\,\mathrm{rad\,m^{-2}}$, is determined from the `RMextract` package[2] [154]. The uncertainty on this value is not provided,

[2] https://github.com/lofar-astron/RMextract

however, the variability in $\mathrm{RM_{iono}}$ is expected to be $\lesssim +1\,\mathrm{rad\,m^{-2}}$ based on observations of pulsars and repeating FRB sources.

Given that the Galactic pulsar population preferentially occupies the Milky Way disk, this similarity, while not ruling out alternative scenarios, is consistent with the notion that FRB 20210603A resides in or near the disk component of its host galaxy. Figure 5.6 further explores this analysis by locating our $\mathrm{DM_{host}}$, $|\mathrm{RM_{host}}|$ and $\tau_{\mathrm{scatt}}$ estimates of FRB 20210603A within the equivalent phase space of the Galactic pulsar sample. Galactic pulsar data are obtained from the latest Australia Telescope National Facility (ATNF) pulsar catalogue [186][3] using the `psrqpy` package [187][4]. FRB 20210603A occupies a well sampled region of this phase space, however, the distribution is also seen to be highly dependent on the Galactic latitude. We estimate a quasi-latitude value for FRB 20210603A, determined from a simple transformation of the inclination angle of the host galaxy (i.e., $4^\circ \leq 90^\circ - \mathrm{inclination\,angle} \leq 10^\circ$), and find that the average pulsar properties of DM, $|\mathrm{RM}|$ and $\tau_{\mathrm{scatt}}$ at this equivalent latitude agree well with what is observed from FRB 20210603A. The agreement is further improved by rescaling DM, $|\mathrm{RM}|$ to account for the larger disk mass of the host galaxy relative to the Milky Way. This scaling factor corresponds to the ratio of the disk mass of the host galaxy and Milky Way and is found to be $\left(\mathrm{M}^{\star}/\mathrm{M}^{\star}_{\mathrm{MW}}\right)^{1/3} = 1.12(8)$ (See Dispersion and Scattering analysis). Such a result suggests that most of the observed $\mathrm{DM_{host}}$, $|\mathrm{RM_{host}}|$ and $\tau_{\mathrm{scatt}}$ observed from FRB 20210603A can be supplied by the host galaxy ISM with little additional contribution needed from the source's local environment.

## 5.4 The host galaxy of FRB 20210603A

We observed SDSS J004105.82+211331.9 with the Canada–France–Hawaii Telescope (CFHT) MegaCam on 10 September 2021 using the wideband *gri* filter [188]. Figure 5.5 shows the location of the FRB within the host galaxy. In contrast to other FRB host galaxies that have been robustly identified so far, this galaxy is viewed nearly edge-on; it has an inclination of $83(3)^\circ$ (Inclination-

[3] http://www.atnf.csiro.au/research/pulsar/psrcat
[4] https://psrqpy.readthedocs.io/en/latest/

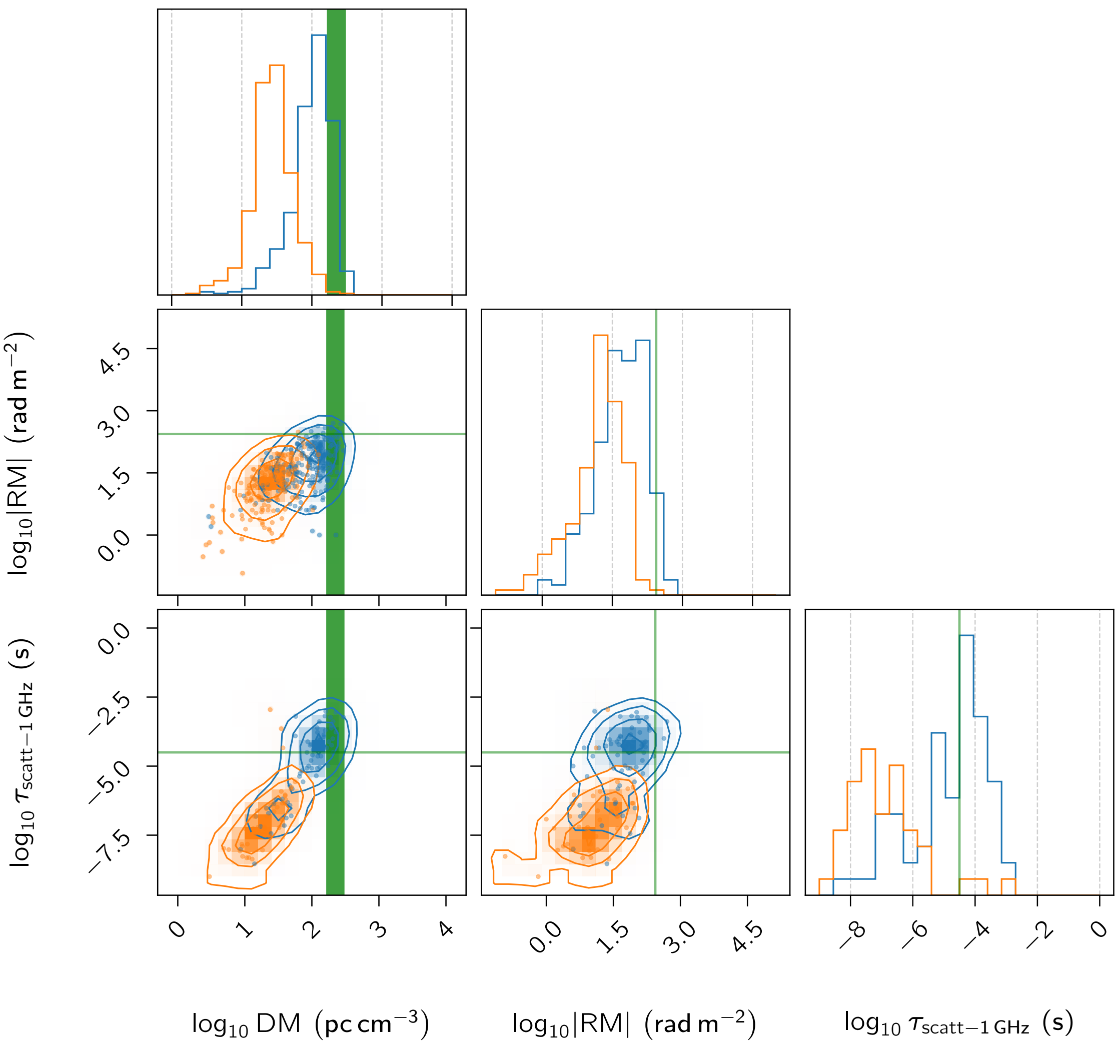


Figure 5.6: A comparison of selected properties of FRB 20210603A with equivalent measurements from known pulsars listed in the ATNF Pulsar Catalogue [186]. Joint distributions of DM, $|\mathrm{RM}|$ and $\tau_{\mathrm{scatt}}$ for the Galactic pulsar sample are shown for two different latitude ranges: $4^\circ \leq |b| \leq 10^\circ$ (blue) and $|b| \geq 20^\circ$ (orange). Contour lines indicate 1, 2 and $3\sigma$ regions of this parameter space. Green regions/lines indicate estimates of equivalent quantities determined for FRB 20210603A, namely: $\mathrm{DM_{host}}, |\mathrm{RM_{host}}|$ and $\tau_{\mathrm{scatt}}$. $\mathrm{DM_{host}}, |\mathrm{RM_{host}}|$ and $\tau_{\mathrm{scatt}}$ estimates are in the source frame with $\tau_{\mathrm{scatt}}$ referenced at $1\,\mathrm{GHz}$ assuming a $\tau_{\mathrm{scatt}} \propto \nu^{-4.4}$ relation used by ATNF. The burst properties of FRB 20210603A ($\mathrm{DM_{host}}$, $|\mathrm{RM_{host}}|$ and $\tau_{\text{scatt-1 GHz}}$) are similar to that of low-latitude ($4^\circ \leq |b| \leq 10^\circ$) Galactic pulsars.

Zoo, [189]). Our localization places the FRB within its disk. We determine the *r*-band half-light radius and Galactic extinction-corrected apparent magnitude to be $8.2(9)\,\mathrm{kpc}$ and $17.90(1)$, respectively, using photometric data provided by the Sloan Digital Sky Survey (SDSS [161], see §5.4.1 ).

Additionally, we acquired long-slit spectra with the Gemini Multi-Object Spectrograph (GMOS, [190]) over the wavelength range $\sim$4500–9000 Å. Fitting Gaussian line profiles to the H$\alpha$ and N II lines (rest wavelengths of $6564.6\,$Å and $6585.2\,$Å) yields a redshift of $z = 0.1772(1)$. Assuming the Planck 2018 cosmology [191], this redshift implies a Galactic extinction- and K-corrected absolute $r$-band magnitude of $-22.03(2)$.

The measured redshift of the galaxy implies an angular diameter distance of $639\,\mathrm{Mpc}$ and a transverse angular distance scale of $3.1\,\mathrm{kpc\,asec}^{-1}$. Using these values, we measure a projected spatial offset for the FRB of $9.5(5)\,\mathrm{kpc}$ from the host galactic center along the host galactic plane. This offset is consistent with the distribution of projected offsets measured from a sample of both repeating and non-repeating FRBs localized by the Australian SKA Pathfinder (ASKAP, see e.g., Figure 9 in [192]). Combining Gemini spectroscopy data with archival photometry from the Two Micron All Sky Survey (2MASS) [193] and the Wide-Field Infrared Space Explorer (WISE) [194] extends our wavelength coverage redwards to $1 \times 10^5\,$Å (see §5.4.1). We fit a Spectral Energy Density (SED) model to the combined spectral and photometric data using the Bayesian SED-fitting package `Prospector` [195]. We estimate best-fit values and uncertainties for the present-day stellar mass, mass-weighted age, V-band dust extinction, and metallicity of our host galaxy using Markov-Chain Monte Carlo (MCMC) posterior sampling [153]. The parameters determined by `Prospector` and the star formation rate (SFR) are shown in Table 5.3. From the H$\alpha$ luminosity measured with Gemini data, we determine the galaxy's overall SFR ($0.24 \pm 0.06\ \mathrm{M_{\odot}yr^{-1}}$) and note that a substantial fraction – 9–36 % of the total star formation, as traced by H$\alpha$ flux – comes from the kiloparsec-scale vicinity of the FRB (see §5.4.1). The detection of H$\alpha$ emission is potentially a sign of recent ($\sim$ 10 Myr) star formation and young stellar populations. However, as with the case of FRB 20180916B [196], spatially-resolved spectroscopic studies of this galaxy are needed to further constrain the age and nature of the progenitor.

### 5.4.1 Host Galaxy Analysis

Optical images of SDSS J004105.82+211331.9 were taken with the CFHT MegaCam using the wide-band *gri* filter. The data were reduced using the standard bias, dark, and flat corrections using the Elixir pipeline [197, 198]. Several exposures were combined using this filter to create an image with a total exposure of 2500 s.

The half-light radius of the host galaxy was determined using the given Petrosian radii fluxes provided by SDSS Data Release 12 [161] and Eq. 7 of [199]. The half-light radius in the $r$-band using these values was found to be $8.2(9)\,\mathrm{kpc}$. Furthermore, the SDSS-provided apparent magnitude in the $r$-band was corrected for Milky Way extinction using the model from Fitzpatrick & Massa 2007 [200]; this gave us an absolute magnitude of $-22.03(2)$ after k-corrections [201].

In addition to imaging, we conducted Gemini spectroscopic observations consisting of two $1000\,\mathrm{s}$ exposures, one centered at $6750$ Å and the other centered at $6650$ Å. This wavelength offset was to account for the gap between the detectors. The images were reduced using standard bias and flat corrections and combined using the Gemini `IRAF/PyRAF` package tools [202, 203]. Using the same package, we also wavelength- and flux-calibrated the spectrum, and accounted for skylines and cosmic rays in the data. We extract spectra with various aperture sizes along with the galaxy. The redshift was determined by extracting a spectrum from a $1\,\mathrm{asec}$ wide aperture centered at the center coordinates of the host galaxy. Due to the edge-on orientation of the galaxy, almost all of the galaxy's light falls within the slit, and the effect of slit corrections on the measured fluxes is negligible (see Figure 5.7).

The H$\alpha$ and the redwards line of the N II doublet (rest wavelengths of $6564.6$ Å and $6585.2$ Å) are some of the most detectable lines ( Figure 5.7). Other prominent lines are from Na and Mg absorption (rest wavelengths of $5895.6$ Å and $5176.7$ Å). Fitting a linear combination of Gaussian line profiles to the H$\alpha$ and N II lines yields a redshift of $z = 0.1772(1)$. The uncertainty in the spectroscopic redshift is dominated by the statistical uncertainties in the measured spectrum, which are normalized such that the reduced-$\chi^2$ of the residuals is 1.

To further characterize the galaxy, we combine our Gemini spectra with archival 2MASS [193] and WISE photometry [194]. We use the Spectral Energy Density (SED) fitting code `Prospector` to determine the stellar mass, metallicity, and star formation history of the galaxy [195]. Our modeling and analysis of this host galaxy closely follow a similar effort for the repeater FRB 20181030A [204]. However, because the galaxy is nearly edge-on, dust extinction in the host-galactic center reddens the observed emission. Therefore, we first correct the spectrum for extinction (see Eqs. 10 and 13 of [205]) due to its inclination of $83(3)°$ [189].

Our best-fit model is overlaid on the spectral and photometric data in Figure 5.8. It assumes a delay-τ star formation history $\propto t \exp\left(-t/\tau\right)$, where τ is the characteristic decay time and $t$ is the time since the formation epoch of the galaxy. We set 5 free parameters: present-day stellar mass, metallicity, τ, $t$, and the diffuse dust V-band optical depth (referred to as "dust2" in `Prospector`), which accounts for the attenuation of old stellar light. We use τ and $t$ as determined by `Prospector` to calculate the mass-weighted age of the galaxy. Additionally, we used a standard dust attenuation model [206], and enabled nebular emission and dust emission [207, 208].

Before sampling the likelihood, we choose reasonable priors for each free parameter (Table 5.2). We use Eq. 6 of [209] to obtain an initial estimate of the galaxy's mass and to set a weak prior on the mass range. This prior can be written as follows:

$$\log_{10}(\mathrm{M}^{\star}/\mathrm{M}_{\odot}) = 1.097(g - r) - 4.06 - 0.4(M_r - 4.97) - 0.19z, \tag{5.4}$$

where $g$ and $r$ are the apparent magnitudes in the $g$-band and $r$-band filters, $M_r$ is the absolute magnitude in the $r$-band, and $z$ is the redshift. The prior on $t$ was cut off at 12 Gyr because the age of the Universe at $z = 0.1772(1)$ is only $\sim$12 Gyr. The prior on $\mathrm{Z}/\mathrm{Z}_{\odot}$ and τ were set according to recommendations in `Prospector` [195]. Using these priors, we obtain the fit plotted in Figure 5.7 and list the results in Table 5.3.

Table 5.2: Priors set for SED modelling with `Prospector`.

| **Parameter** | | **Prior** $[\textbf{min}, \textbf{max}]$ |
|---|---|---|
| $\log(M^{\star}/M_{\odot})$ | Present-day Stellar Mass | Log Uniform $[10, 12]$ |
| $\log\left(Z/Z_{\odot}\right)$ | Metallicity | Top Hat $[-2, .19]$ |
| $t$ | Time since formation (Gyr) | Top Hat $[0.1, 12]$ |
| $\tau$ | Star formation characteristic decay rate (Gyr) | Log Uniform $[0.3, 15]$ |
| dust2 | Diffuse dust V-band optical depth | Top Hat $[0, 3]$ |

Finally, to determine the galaxy-integrated SFR, we extract a spectrum with an aperture of $10\,\mathrm{asec}$ in diameter, encompassing all of the galaxy's light within our half-light radius of $\sim 2.5\,\mathrm{asec}$. We calculate the total SFR of the host galaxy using the intensity and line width of the H$\alpha$ line [210]:

$$\mathrm{SFR} = 7.9 \times 10^{-42} \left(\frac{\mathrm{L_{H\alpha}}}{\mathrm{erg\,s^{-1}}}\right) \frac{\mathrm{M_{\odot}}}{\mathrm{yr}}, \tag{5.5}$$

where $\mathrm{L_{H\alpha}}$ is the flux-derived luminosity of the H$\alpha$ emission from our Gemini data. To correct our luminosity measurement for extinction we apply the inclination-angle dependent correction as well as the inclination-independent correction, parameterized as dust2 in `Prospector`. The latter quantifies the amount of V-band extinction of old stellar light in the host galaxy. Optical reddening is characterized by using $\mathrm{R_V}$ = $\mathrm{A_V}$/E(B-V), where E(B-V) is the color index of the galaxy and $\mathrm{A_V}$ is the extinction in the V-band; this equation is thus the ratio of total to selective extinction in the V-band [211]. The dust extinction is taken to be $\mathrm{A_V} = 1.086 \times \mathrm{dust2}$ [195, 212], where we take dust2 to be the best-fit value of $0.79$. With an $\mathrm{R_V}$ value of $3.1$ [211], we calculated E(B-V) to be $0.28$. The H$\alpha$ extinction coefficient can be calculated using $\mathrm{A_{H\alpha}} = \mathrm{R_{H\alpha}} \times$ E(B-V) where we take $\mathrm{R_{H\alpha}} = 2.45$ [213]. The inclination-independent attenuation results in the H$\alpha$ flux being attenuated by a factor of $\exp(\mathrm{A_{H\alpha}}) = 1.97$. Correcting the galaxy-integrated H$\alpha$ flux for extinction yielded a total SFR of $0.24(6)\ \mathrm{M_{\odot} yr^{-1}}$. We may also measure the SFR in the $3\,\mathrm{kpc}$-scale vicinity of the burst. The dominant systematic is the extent of dust extinction in the local vicinity of the FRB ( Figure 5.7), which may differ from the extinction averaged over the galaxy. The local H$\alpha$-derived SFR is $0.02\ \mathrm{M_{\odot} yr^{-1}}$, measured before applying dust (1.97) and inclination-dependent (1.89) extinction corrections, and $0.09\ \mathrm{M_{\odot} yr^{-1}}$ after applying both corrections. We conclude that the star formation in the kiloparsec-scale vicinity of the FRB accounts for between $9$ and $36\%$ of the total star formation in the host galaxy – a substantial fraction of the total.

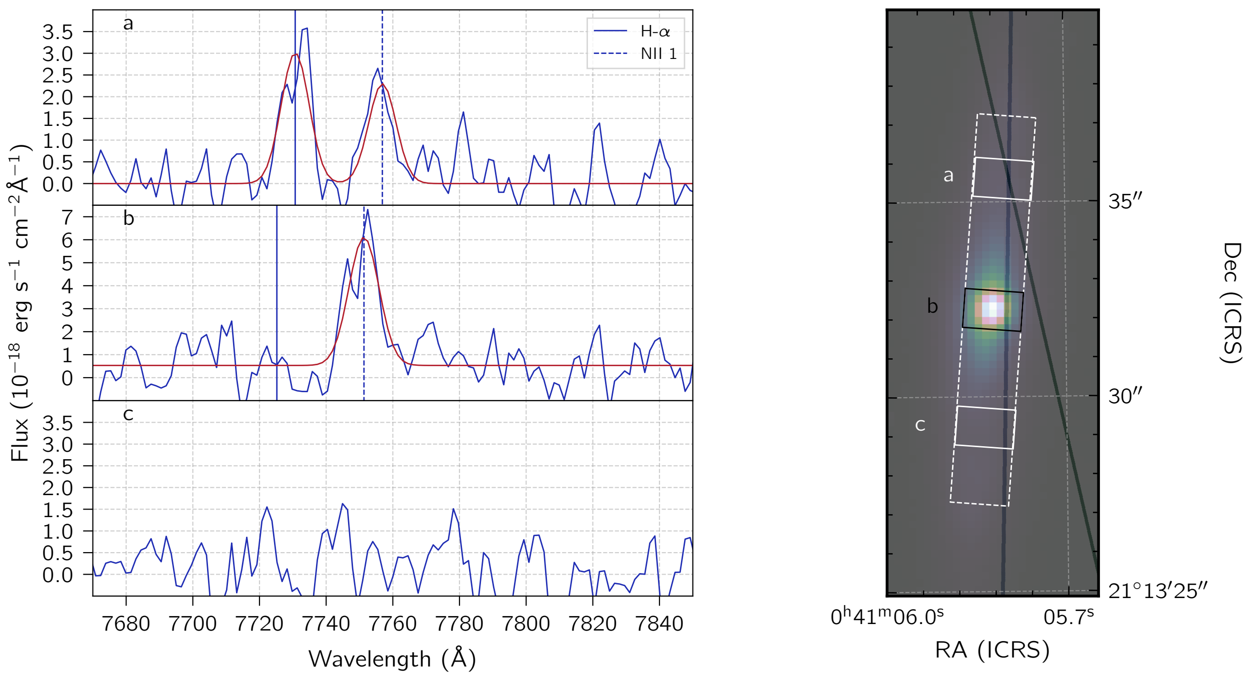


Figure 5.7: **Spatially resolved spectroscopy of the host galaxy.** Top: Optical image and spatially-resolved spectra of the host galaxy of FRB 20210603A acquired using CFHT MegaCAM and Gemini long-slit spectroscopy respectively. Pixel intensities are scaled linearly and normalized to reduce the saturation evident in Figure 5.5. Three spectra are extracted from the vicinity of the FRB, the bulge of the galaxy, and symmetrically from the opposite side of the galaxy at the same projected offset using an aperture size of $1.5 \times 1\,\mathrm{asec}$. The three spectra and Gaussian fits to the H$\alpha$ and one of the NII emission lines are plotted here after correcting for Milky-Way extinction.

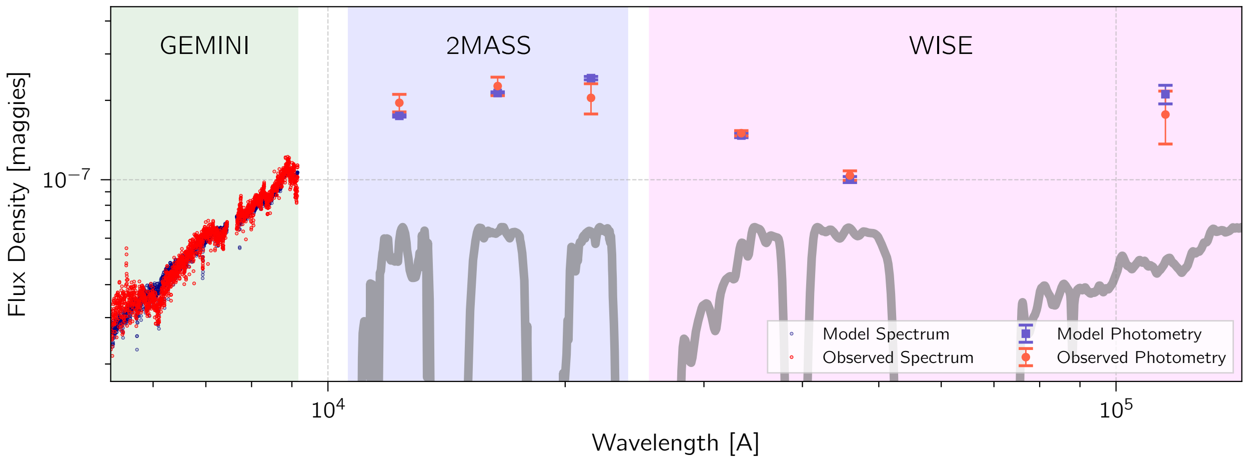


Figure 5.8: **Spectral Energy Density of host galaxy:** Gemini long-slit spectrum, integrated over the galaxy, with archival infrared photometry from 2MASS and WISE, plotted after correcting for extinction due to the host galaxy's inclination angle. Plotted alongside the observations (red) are the best-fit model (blue) from `Prospector`, and the relative passbands for the 2MASS J, H, and $K_s$ and WISE W1-W3 filters.

### 5.4.2 Disk Chance Coincidence Probability

While FRB 20210603A was ostensibly localized to the disk of its host galaxy, the progenitor may be a halo object (as in the case of the globular cluster host of FRB 20200120E [214]) coincidentally aligned with the disk in projection. The probability that this occurs by a chance coincidence is the ratio of the solid angles subtended by the disk and halo. The nearly edge-on disk can be approximated as an ellipse with semi-major and semi-minor axes of 15 and $2.7\,\mathrm{asec}$ respectively, while the halo can be approximated as a circle of radius $r_{\mathrm{vir}} \approx \mathrm{M}^{\star}/\mathrm{M}^{\star}_{\mathrm{MW}} r_{\mathrm{vir,MW}}$. Taking the Milky Way's virial radius to be $r_{\mathrm{vir,MW}} = \sim 200\,\mathrm{kpc}$ [215] and scaling up the host galaxy mass yields the host galaxy's virial radius of $\sim 280\,\mathrm{kpc}$. The low chance coincidence probability of $10^{-3}$ implies a robust association with the disk and favors progenitor models involving disk populations over halo populations.

## 5.5 Summary

We have used VLBI with widefield telescopes to localize an FRB at the time of detection. We restrict the progenitor's location to within the disk of the galaxy SDSS J004105.82+211331.9: a lenticular galaxy with an almost edge-on geometry. This represents a major observational step towards localizing a large sample of FRBs at the time of the first detection. Before this work, VLBI FRB localizations have only been achieved in the targeted follow-up of repeating sources. Such localizations have been to a mix of star-forming regions [216, 217], locations offset from star formation [196], and regions completely devoid of star formation [214]. This has cast doubt on young progenitors being the universal origin of repeating FRBs. In the case of FRB 20210603A, the H$\alpha$ emission in the $\sim 3\,\mathrm{kpc}$ neighborhood of the FRB suggests recent star formation activity. This highlights the need for high-resolution follow-up to discriminate between progenitor models by assessing whether FRBs are spatially coincident with star-forming regions[196]. The instruments and methods used here constitute pathfinders for the CHIME/FRB Outriggers project, which will enable VLBI localizations of large numbers of both repeating and non-repeating sources [141, 145, 151]. Thus, a more complete picture of the diverse host environments of FRBs, and how the environments correlate with other burst properties, will soon be available.

Table 5.3: Parameters associated with FRB 20210603A (upper half of table) and its host galaxy (lower half).

| **Parameter** | **Value** |
|---|---|
| Right Ascension $\alpha$ (ICRS) | $10.274\,034\,0(86)^\circ$, |
| Declination $\delta$ (ICRS) | $21.226\,579(49)^\circ$ |
| CHIME arrival time at (400 MHz) | 2021-06-03 15:51:34.431652 UTC |
| Dispersion Measure, DM | $500.147(4)\,\mathrm{pc\,cm^{-3}}$ |
| $\mathrm{DM}^{\dagger}_{\text{MW-NE2001}}$ | $40(8)\,\mathrm{pc\,cm^{-3}}$ |
| $\mathrm{DM}^{\dagger}_{\text{MW-halo}}$ | $30(20)\,\mathrm{pc\,cm^{-3}}$ |
| $\mathrm{DM}_{\text{cosmic}}$ | $172(90)\,\mathrm{pc\,cm^{-3}}$ |
| $(\mathrm{DM}_{\text{host}})/(1+z) = (\mathrm{DM}_{\text{host-disk}} + \mathrm{DM}_{\text{host-halo}})/(1+z)$ | $257(93)\,\mathrm{pc\,cm^{-3}}$ |
| RM | $-219.00(1)\,\mathrm{rad\,m^{-2}}$ |
| $\mathrm{RM}^{\dagger}_{\text{MW}}$ | $-22.4(3)\,\mathrm{rad\,m^{-2}}$ |
| $\mathrm{RM}^{\dagger}_{\text{iono}}$ | $+1.4\,\mathrm{rad\,m^{-2}}$ |
| $\Pi_{\text{L-800 MHz}}$ | $\gtrsim 96\,\%$ |
| $\Pi_{\text{L-400 MHz}}$ | $\gtrsim 87\,\%$ |
| $\tau_{\text{scatt-600 MHz}}$ | $155(3)\,\mu\mathrm{s}$ |
| $\tau^{\dagger}_{\text{600 MHz-NE2001}}$ | $1.02\,\mu\mathrm{s}$ |
| Fluence | $17.5(30)$ Jy ms |
| Flux | $29.9(48)$ Jy |
| Specific Energy | $1.6 \times 10^{31}$ erg/Hz |
| Specific Luminosity | $2.8 \times 10^{34}$ erg |
| Pulse Width | $220\,\mu\mathrm{s}$ |
| Spectroscopic Redshift, $z$ | $0.1772(1)$ |
| Photometric Redshift, $z^{\dagger}_{\text{phot}}$ | $0.1750(133)$ |
| Inclination angle | $83(3)^\circ$ |
| Present-day Stellar Mass, $\log(\mathrm{M}^{\star}/\mathrm{M}_{\odot})$ | $10.93^{+0.04}_{-0.04}$ |
| Metallicity, $\log\left(\mathrm{Z}/\mathrm{Z}_{\odot}\right)$ | $-0.22^{+0.05}_{-0.04}$ |
| Mass-weighted age | $4.32^{+0.73}_{-0.75}$ Gyr |
| Total Star Formation Rate (SFR) | $\gtrsim 0.24 \pm 0.06 M_{\odot}\mathrm{yr}^{-1}$ |
| Projected offset | $9.5(5)$ kpc |
| $r$-band Half-light Radius | $8.2(9)$ kpc |
| Absolute $r$-band magnitude | $-22.03(2)$ |
| E(B-V) | 0.28 |

Parameters which are derived from external models or measurements are indicated with daggers ($z_{\text{phot}}$, DM, $\tau$, and $\mathrm{RM}_{\text{iono}}$ predictions [154, 162, 163, 166, 168, 185]).

# Chapter 6

# Digital Signal Processing in Radio Astronomy - A Research Experience for Teachers Program

In the vein of enabling landmark discoveries about our universe directly by building your instrument, this chapter describes the Digital Signal Processing in Radio Astronomy (DSPIRA) program. A National Science Foundation (NSF) funded Research Experience for Teachers (RET) project. It leverages the $21\,\mathrm{cm}$ emission from interstellar matter that was first suggested as observable in 1945 [18]. This program allows the teachers to bring landmark discoveries such as detecting dark matter in the Milky Way by measuring its rotation curve [218] and a confirmation of the structure of the Galactic spiral arms [219] as achievable classroom exercises integrated into the usual curriculum. The content of this chapter is adapted from the refereed proceedings in [220].

In the context of fast radio bursts, these horn antennas present an

## 6.1 Introduction

Radio astronomy is inherently multidisciplinary. It was developed by engineers and has now matured into a vast field with specializations such as astrochemistry, astrobiology, and cosmology among others. Moreover, radio telescopes involve almost every aspect of science and engineering – mechanical engineering, electrical engineering, radio frequency engineering, and computer science along with physics, chemistry, and biology (see 6.3).

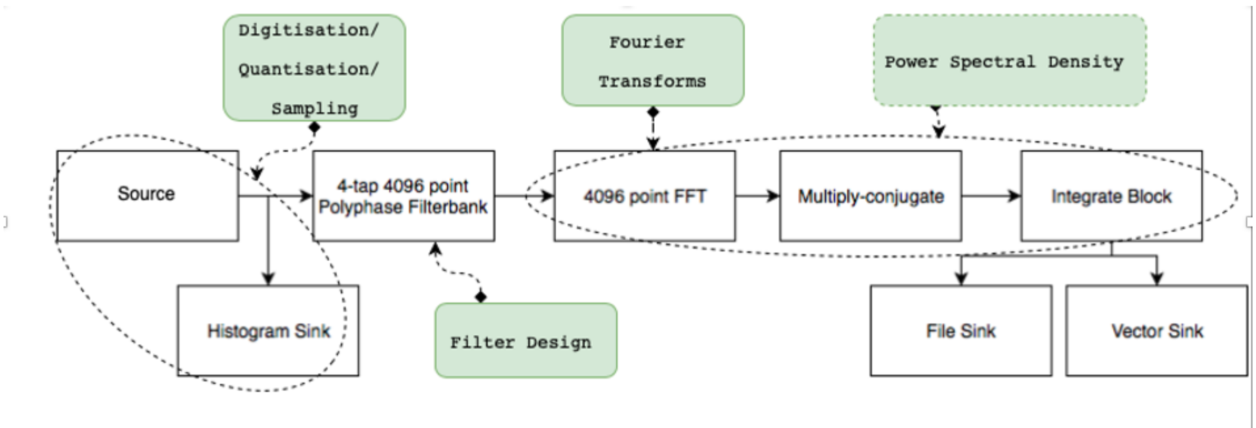


Figure 6.1: **Radio astronomy and DSP topics:**The signal flow of the radio astronomy backend and the digital signal processing topics covered.

DSPIRA aims to leverage this nature of radio astronomy with a focus on digital signal processing. Our primary tool for implementing this is GNURadio [221] – an open-source software development toolkit to process digital signals. We use this to systematically dispense concepts at a level accessible to high school teachers. Teachers disseminate the said concepts to their students within the context of radio astronomy. Through this program, high school teachers are provided the tools they need to design, build and use a miniature radio observatory pictured in Figure 6.2. This horn antenna system is capable of detecting neutral hydrogen. The teachers design their own digital signal processing backend and learn how to reduce the acquired data. Throughout the learning process, the teachers are given a space to design lessons and curricula.

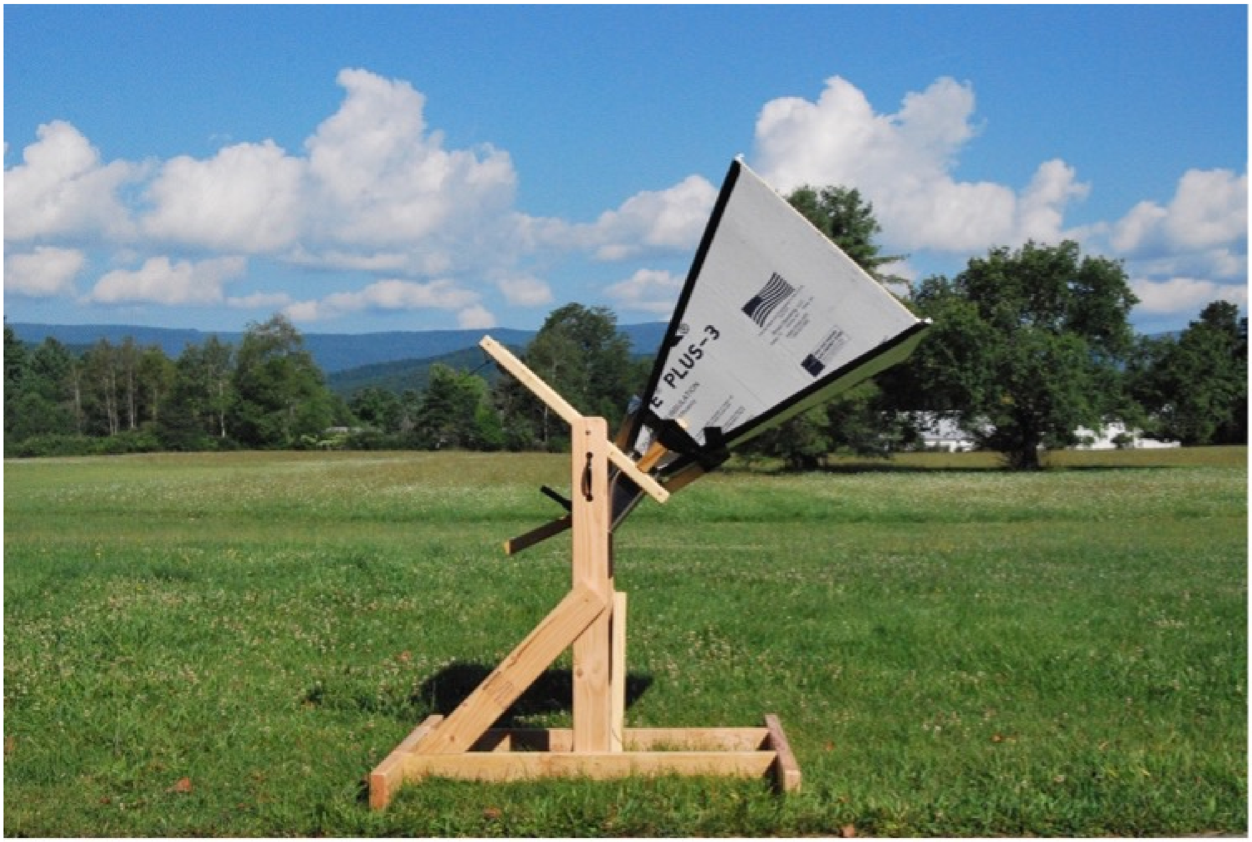


Figure 6.2: **The DSPIRA horn antenna:**The radio telescope built as part of the dspira program.

## 6.2 The RET Program

DSPIRA has been a six-week program held in the summer session. There have been 5 sessions from 2017 to 2021. The first four weeks are spent on-site at West Virginia University (WVU) in the Lane Department of Computer Science and Electrical Engineering. The final two weeks are spent at the Green Bank Observatory. The time in WVU is spent building fundamentals split between acquiring theoretical fundamentals and doing experimental laboratory work. First, a lecture series on descriptive astronomy and digital signal processing provide all the necessary background for the teachers to make sense of all the advanced topics involved in building and usage of the radio telescope. This is followed by a very hands-on laboratory exercise. The DSPIRA program trains the teachers to be able to build a radio astronomy software package from first principle DSP concepts (The laboratory material and exercises are hosted on http://wvurail.org/dspira-lessons/). The flowchart in Figure 6.4 represents our

DSP backend for radio astronomy. For four weeks the teachers are systematically exposed to the concepts driving each block. Critical concepts from sampling through filter design and Fourier analysis are keenly examined (Figure 6.1) through simplified lectures and structured hands-on laboratory exercises using GNURadio as our primary tool. Specialized GNURadio out-of-tree modules have been designed to help acquire radio astronomical data in an easy-to-reduce format (https://github.com/WVURAIL/gr-radio_astro)

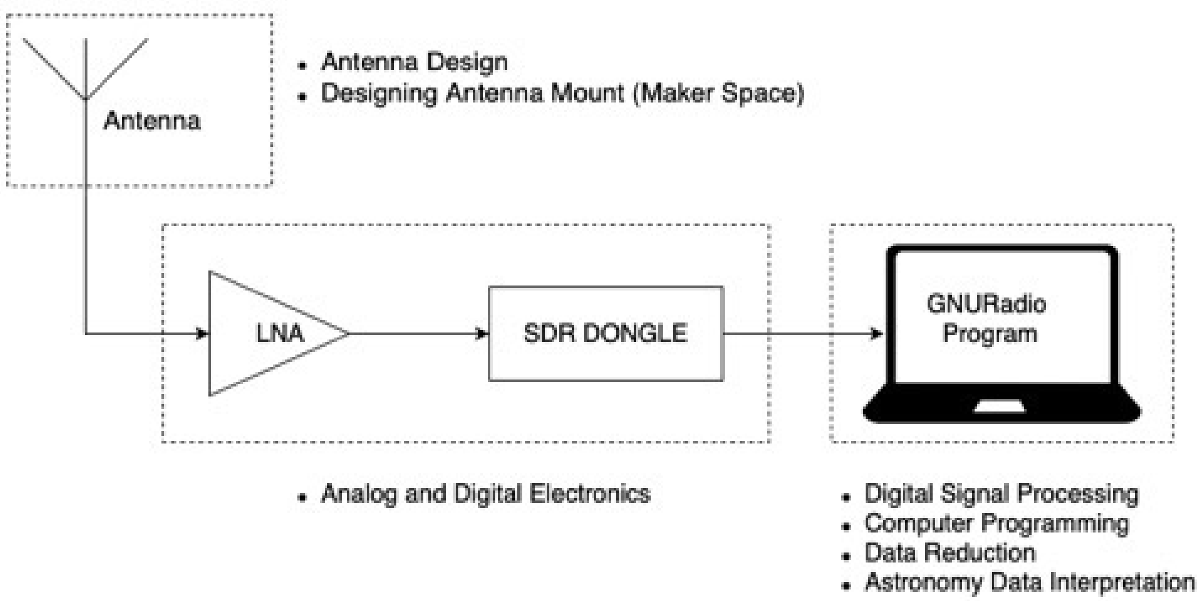


Figure 6.3: **Radio Astronomy and pedagogy:**A typical radio astronomy pipeline and the pedagogical topics associated with each component.

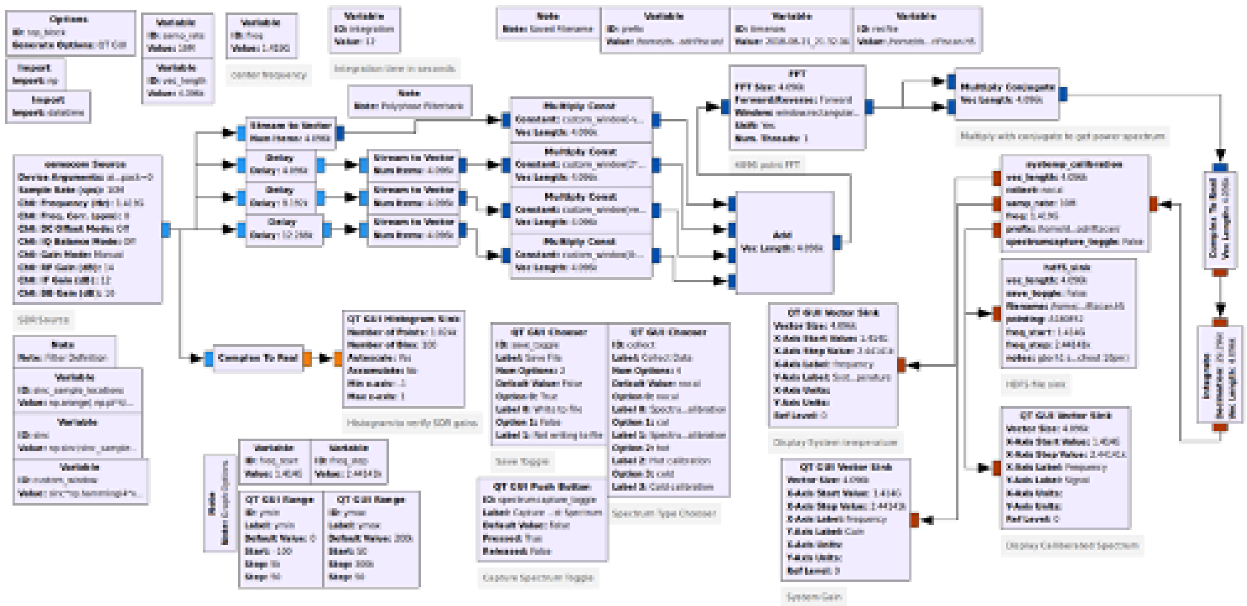

Figure 6.4: **GNURadio Spectrometer:** A GnuRadio flowgraph of a radio astronomy spectrometer

The horn and mount are also designed and built. The design of the horn is reminiscent of the Ewen and Purcell's horn used to detect neutral hydrogen. Its design was driven by two critical constraints – portability and cost. It should be portable enough such that in its fully assembled configuration it could fit through a standard door and it should be constructed out of tools and materials one could easily obtain inexpensively from a hardware store. The collecting horn is a four-sided open pyramid made out of home insulation Styrofoam boards with a metallic reflective lining and a rectangular waveguide made from a paint thinner can (which could be an old used one or empty cans bought from numerous commercial storefronts). The radio signal is picked up from a quarter-wave probe from within the can. It is mounted on a wooden base that is capable of adjusting the elevation of the horn (Figure 6.2). The signal from the horn is amplified using a low noise amplifier (LNA) designed to operate in urban noisy environments (The hardware design is open-sourced on https://github.com/WVURAIL/os_radio_astro_hw). The amplified signal was sent through the Airspy SDR dongle where the signal is mixed down and digitized to be interpreted by the DSP software. The final two weeks are spent at the Green Bank Observatory testing out the miniature radio astronomy observatory and teaching students. The horns constructed by the teachers are used there for a slew of radio astronomy experiments including mapping the neutral hydrogen (HI) in the Milky Way.

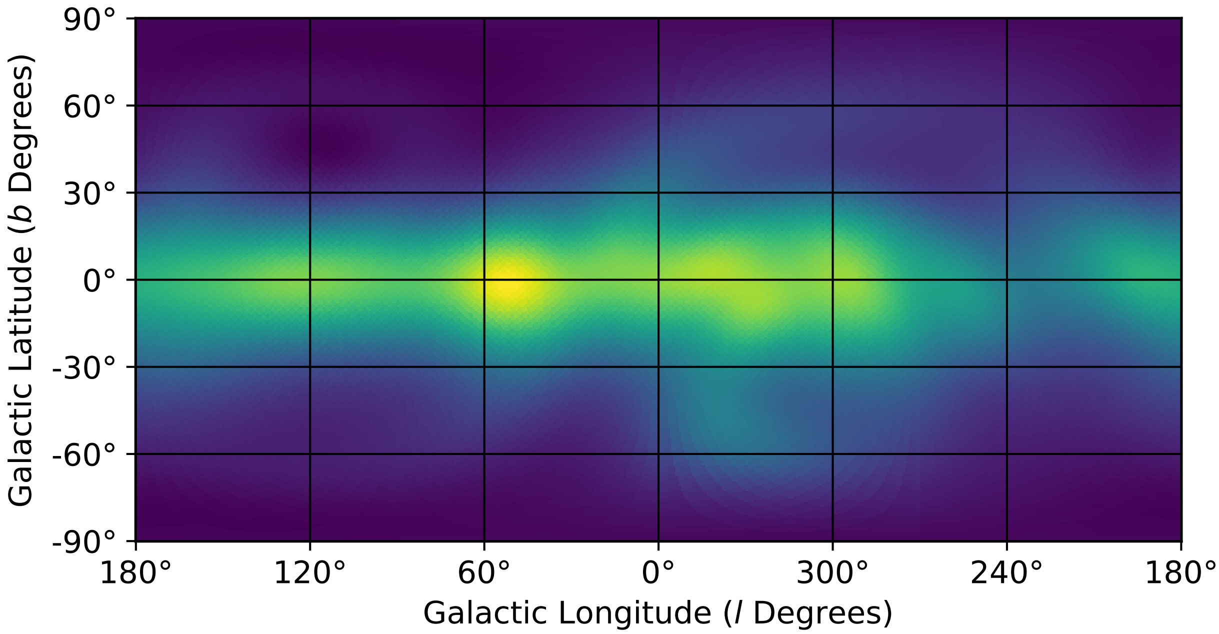


Figure 6.5: **21cm Map:** The map of the neutral hydrogen in the galaxy from data acquired from both the northern and southern hemispheres, reduced and created by the teachers. The data is acquired by pointing horns at different elevations/altitudes and recording the sky drifting past the beam. The image data is smoothed by a Gaussian filter. Any structure shown here is from the lack of calibration and system temperature variations across the day.

## 6.3 Lessons & Curricula

One of the primary mandates of the Research Experience for Teachers (RET) program is to equip teachers with the skills and knowledge to impart said knowledge to their respective students. To its end, time was dedicated to further decimating the lectures and labs into lessons and activities by the teachers.

Many of these activities were tested at Green Bank Observatory. The final two weeks of the DSPIRA program are meant to coincide with several summer camps at Observatory. This allows teachers to try out their lessons and activities with students participating in the camps. Next Generation Science Standards (NGSS)[222] and many state standards expect class curricula to integrate engineering and technology with sciences. DSP and radio astronomy are ripe with topics to be used to approach these requirements. For example, NGSS.HS.ETS.1-4, Cross-Cutting Concepts Engineering and Technology, "Models (e.g., physical, mathematical, computer models) can be used to simulate systems and interactions – including energy, matter, and information flows – within and between systems at different scales.". The horn antennas can thus be used to detect astronomical evidence of matter i.e. neutral hydrogen. Another example includes the concept of red and blue shifts of light that can be tangibly explained by observing the shifts in the HI line.

## 6.4 Observations and Future

The DSPIRA program is currently a vibrant community of at least a dozen educators from across the countries who meet to discuss their experiments and experiences teaching in the classroom. Our program has been adapted to be implemented as short-term workshops involving participants of varying skills and inclinations to increase access. The DSPIRA program has the potential to expand.

Effectively disseminating digital signal processing and radio astronomy topics have been identified as a challenge, mainly due to its complexity. Despite this challenge, the participating teachers have created a living repository of lessons, activities, and guides, which is curated and maintained on the website: http://wvurail.org/dspira-lessons/.

Using the horn antennas as miniature radio observatories has tremendous potential as a citizen science venture. Having as many horn antennas in multiple high schools, amateur astronomy clubs, universities, and personal spaces across the world one could potentially build a broad radio telescope network. This could be aided by an accessible global positioning system (GPS) based on precise timing standards, enabling large-scale citizen science interferometry. Initial experiments with SDR-enabled interferometry are already underway led by the teachers of the DSPIRA cohorts (Makous et. al. in prep.).

In the context of Fast Radio Bursts, these horn antenna radio observatories present an incredible opportunity to detect Galactic FRBs. A combination of a few ($\sim 1-4$) horn antennas with their large field of view and modest system temperature in the L-band can be used as a STARE2 analog [223] to be able to detect Galactic bursts once a year or so. The recent detection of an FRB from a Galactic magnetar [104, 224] has been critical in bringing the community closer to understanding the engines that produce FRBs by providing a strong candidate in magnetars. The 'mini' observatory in every school or backyard with the appropriate virtual observatory event (VOE) system [225] to receive triggers can prove this project as excellent and topical for a teaching and science use case.

To conclude, low-cost materials and open-source hardware and software have contributed to the success of this program. However, true success depends on wide participation and thorough curricular integration. We are working with past teachers to bring this to fruition. Regular meetings and online forums have enabled veteran participants and new teachers to share their continuing efforts in their classrooms. The work of the teachers in this program has so far led to their publications in *The Physics Teacher* [226] and [227] as well as undergraduate research projects [228].

# Chapter 7

# Conclusions and Future

When I heard the learn'd astronomer,
When the proofs, the figures, were ranged in columns before me,
When I was shown the charts and diagrams, to add, divide, and measure them,
When I sitting heard the astronomer where he lectured with much applause in the lecture-room,
How soon unaccountable I became tired and sick,
Till rising and gliding out I wander'd off by myself,
In the mystical moist night-air, and from time to time,
Look'd up in perfect silence at the stars.

— Walt Whitman, "When I Heard the Learn'd Astronomer",
*Drum-Taps, 1865.*

Whitman suggests one needs to experience nature for its true understanding, instead of measuring it. Many might agree with this notion and after some particularly droll months of reading texts and analyzing data for this work, I might be inclined to agree. Of course, I do not. Astronomers peer into the unknown and help reveal the unseen. We take snapshots of the ephemeral, of energies beyond comprehension. The instruments and mathematics reveal and inspire awe, much like the results of our work.

A VLBI pathfinder, TONE, was constructed from scratch as described in §3. A unique delay referencing VLBI calibration technique using a pulsar pulse is described in §4.3.4 which allowed us to localize FRB 20210603A inside an edge on galaxy at redshift $z \approx 0.17$ in §2. Budgeting the propagation properties such as the DM, scattering and RM of the FRB further allowed us to place the FRB inside the ionised disk of the galaxy. Optical follow up indicated star formation in the kilo-parsec vicinity of the FRB hinting at a young population. The breath of the work here presents a truly trans-disciplinary and collaborative effort that not only enables but is required for modern scientific endeavors. This is reflected in the pedagogical efforts described in Chapter 6.

The success of the CHIME/FRB Outrigger pathfinders such as TONE presented in this work is a stepping stone towards the next era of FRB science where we shall have a hundreds of localized FRBs in the coming years. The ability to localize inside the galaxy especially with orientations as we noticed FRB 20210603A near edge on host galaxy will allow us to probe the host galaxy medium of a variety of galaxies. Budgeting the DMs of FRBs similar to §5.3 will allow us to probe the nature of galactic halos [229] as well as magnetic fields of the galaxies for statistically significant number of galaxies. Localization of hundreds of FRBs will provide us with their corresponding redshifts. This will alow us to test the ubiquitousness of the Macquart relation and help put tighter bounds on its variance. Localization to regions within the galaxies will allow us to probe the immediate regions of the FRB with different wavelengths. This would be critical to differentiate different populations progenitors.

## 7.1 Future of the outriggers

This work presents a landmark detection in a field on its cutting edge. The VLBI methods developed and implemented here are critical for the CHIME/FRB and its upcoming outriggers (Figure. 7.1). The CHIME/FRB Outriggers will be a wide-field low-frequency VLBI network of 3 stations building and expanding upon the work of the Outrigger Pathfinders. Much like the pathfinders, they will rely upon CHIME detection of FRBs. They will use the methods described in this work to localize thousands of FRBs within $\sim 50\,\mathrm{mas}$ precision. The three stations will be near Princeton/Allenby, British Columbia, Canada, Green Bank Observatory (GBO), Green Bank, West Virginia, and Har Creek Radio Observatory (HCRO), Hat Creek, California giving us $\sim 67$

km, $\sim$ 3333 km, and $\sim$ 955 km baselines respectively. This will allow us to localise FRBs to $\sim$ 50mas. The outrigger station at Princeton is a single $20\,\mathrm{m}$ wide and $40\,\mathrm{m}$ long cylindrical reflector with 64 CHIME-like cloverleaf feeds and the outriggers GBO and HCRO will consist of a single $20\,\mathrm{m}$ wide and $64\,\mathrm{m}$ long cylindrical reflectors equipped 128 CHIME like cloverleaf antennas each. These sites are at various stages of construction. The Princeton cylinder as of July 2022 is in its commissioning phase and Green Bank cyclinder is under construction.


Figure 7.1: **A map of the outriggers under construction.** Credit: Jane Kaczmerak/CHIME/FRB Outrigger

# Bibliography


1. Maxwell, J. C. XXV. On physical lines of force. *The London, Edinburgh, and Dublin Philosophical Magazine and Journal of Science* **21,** 161–175. eprint: https://doi.org/10.1080/14786446108643033. https://doi.org/10.1080/14786446108643033 (1861).

2. Maxwell, J. C. XLIV. On physical lines of force. *The London, Edinburgh, and Dublin Philosophical Magazine and Journal of Science* **21,** 281–291. eprint: https://doi.org/10.1080/14786446108643056. https://doi.org/10.1080/14786446108643056 (1861).

3. F.R.S., J. C. M. III. On physical lines of force. *The London, Edinburgh, and Dublin Philosophical Magazine and Journal of Science* **23,** 12–24. eprint: https://doi.org/10.1080/14786446208643207. https://doi.org/10.1080/14786446208643207 (1862).

4. F.R.S., J. C. M. XIV. On physical lines of force. *The London, Edinburgh, and Dublin Philosophical Magazine and Journal of Science* **23,** 85–95. eprint: https://doi.org/10.1080/14786446208643219. https://doi.org/10.1080/14786446208643219 (1862).

5. Maxwell, J. C. A Dynamical Theory of the Electromagnetic Field. *Philosophical Transactions of the Royal Society of London* **155,** 459–512. ISSN: 02610523. http://www.jstor.org/stable/108892 (2022) (1865).

6. Einstein, A. Considerations concerning the fundaments of theoretical physics. *Science* **91,** 487–492 (1940).

7. Hertz, H. Ueber die Ausbreitungsgeschwindigkeit der electrodynamischen Wirkungen. *Annalen der Physik* **270,** 551–569 (Jan. 1888).

8. HEAVISIDE, O. Encyclopaedia Britannica 10. *Aufl. Bd* **88** (1902).

9. Kennelly, J. Research in telegraphy. *Elect. World & Eng* **6,** 473 (1902).

10. Planck, M. On the theory of the energy distribution law of the normal spectrum. *Verh. Deut. Phys. Ges* **2,** 237–245 (1900).

11. Planck, M. On an Improvement of Wien's Equation for the Spectrum. *Ann. Physik* **1,** 719–721 (1900).

12. Jansky, K. Directional Studies of Atmospherics at High Frequencies. *Proceedings of the Institute of Radio Engineers* **20,** 1920–1932 (1932).

13. Jansky, K. G. Radio waves from outside the solar system. *Nature* **132,** 66–66 (1933).

14. Jansky, K. A Note on the Source of Interstellar Interference. *Proceedings of the Institute of Radio Engineers* **23,** 1158–1163 (1935).

15. Reber, G. Cosmic Static. *Proceedings of the IRE* **28,** 68–70 (Feb. 1940).

16. Reber, G. Notes: Cosmic Static. ApJ **91,** 621–624 (June 1940).

17. Reber, G. Cosmic Static. ApJ **100,** 279 (Nov. 1944).

18. van de Hulst, H. C. Radiogolven uit het wereldruim: II. Herkomst der radiogolvenRadiogolven uit het wereldruim: II. Herkomst der radiogolvenRadio waves from space. *Nederlandsch Tijdschrift voor Natuurkunde* **11,** 210–221 (Jan. 1945).

19. Ewen, H. I. & Purcell, E. M. Observation of a Line in the Galactic Radio Spectrum: Radiation from Galactic Hydrogen at 1,420 Mc./sec. Nature **168,** 356 (Sept. 1951).

20. Muller, C. A. & Oort, J. H. Observation of a Line in the Galactic Radio Spectrum: The Interstellar Hydrogen Line at 1,420 Mc./sec., and an Estimate of Galactic Rotation. Nature **168,** 357–358 (Sept. 1951).

21. Pawsey, J. L., Payne-Scott, R. & McCready, L. L. Radio-Frequency Energy from the Sun. Nature **157,** 158–159 (Feb. 1946).

22. Ryle, M. & Vonberg, D. D. Solar Radiation on 175 Mc./s. Nature **158,** 339–340 (Sept. 1946).

23. Ryle, M. & Hewish, A. The synthesis of large radio telescopes. MNRAS **120,** 220 (Jan. 1960).

24. Penzias, A. A. & Wilson, R. W. A Measurement of Excess Antenna Temperature at 4080 Mc/s. ApJ **142,** 419–421 (July 1965).

25. Hewish, A., Bell, S. J., Pilkington, J. D. H., Scott, P. F. & Collins, R. A. Observation of a Rapidly Pulsating Radio Source. Nature **217,** 709–713 (Feb. 1968).

26. Hulse, R. A. & Taylor, J. H. Discovery of a pulsar in a binary system. ApJ **195,** L51–L53 (Jan. 1975).

27. Lorimer, D. R., Bailes, M., McLaughlin, M. A., Narkevic, D. J. & Crawford, F. A Bright Millisecond Radio Burst of Extragalactic Origin. *Science* **318,** 777–780. ISSN: 0036-8075. eprint: https://science.sciencemag.org/content/318/5851/777.full.pdf. https://science.sciencemag.org/content/318/5851/777 (2007).

28. Wilson, T. L., Rohlfs, K. & Hüttemeister, S. *Tools of Radio Astronomy* (2013).

29. Condon, J. J. & Ransom, S. M. *Essential Radio Astronomy* (2016).

30. Weinreb, S. S. *A digital spectral analysis technique and its application to radio astronomy* PhD thesis (Massachusetts Institute of Technology, Jan. 1963).

31. Kellermann, K. I. & Moran, J. M. The Development of High-Resolution Imaging in Radio Astronomy. ARA&A **39,** 457–509 (Jan. 2001).

32. Moore, G. E. Cramming more components onto integrated circuits.

33. Backer, D. C. *et al. PAPER: The Precision Array To Probe The Epoch Of Reionization* in *American Astronomical Society Meeting Abstracts* **211** (Dec. 2007), 133.02.

34. DeBoer, D. R. *et al.* Hydrogen epoch of reionization array (HERA). *Publications of the Astronomical Society of the Pacific* **129,** 045001 (2017).

35. van Haarlem, M. P. *et al.* LOFAR: The LOw-Frequency ARray. A&A **556,** A2. arXiv: `1305.3550 [astro-ph.IM]` (Aug. 2013).

36. Hotan, A. W. *et al.* Australian square kilometre array pathfinder: I. system description. PASA **38,** e009. arXiv: `2102.01870 [astro-ph.IM]` (Mar. 2021).

37. Peterson, J. B., Bandura, K. & Pen, U. L. The Hubble Sphere Hydrogen Survey. *arXiv e-prints,* astro–ph/0606104. arXiv: `astro-ph/0606104 [astro-ph]` (June 2006).

38. Tegmark, M. & Zaldarriaga, M. Fast Fourier transform telescope. Phys. Rev. D **79,** 083530. arXiv: `0805.4414 [astro-ph]` (Apr. 2009).

39. Tegmark, M. & Zaldarriaga, M. Omniscopes: Large area telescope arrays with only NlogN computational cost. Phys. Rev. D **82,** 103501. arXiv: `0909.0001 [astro-ph.CO]` (Nov. 2010).

40. Ng, C. *et al.* CHIME FRB: An application of FFT beamforming for a radio telescope. *arXiv e-prints,* arXiv:1702.04728. arXiv: `1702.04728 [astro-ph.IM]` (Feb. 2017).

41. Burke, B. F. & Franklin, K. L. Observations of a variable radio source associated with the planet Jupiter. *Journal of Geophysical Research* **60,** 213–217 (1955).

42. Klebesadel, R. W., Strong, I. B. & Olson, R. A. Observations of Gamma-Ray Bursts of Cosmic Origin. ApJ **182,** L85 (June 1973).

43. Metzger, M. R. *et al.* Spectral constraints on the redshift of the optical counterpart to the $\gamma$-ray burst of 8 May 1997. Nature **387,** 878–880 (June 1997).

44. Lovell, B. Radio Emission from Flare Stars. Nature **198,** 228–230 (Apr. 1963).

45. Schatzman, E. *On the possibility of observing radio emission from flare stars* in *URSI Symp. 1: Paris Symposium on Radio Astronomy* (ed Bracewell, R. N.) **9** (Jan. 1959), 552.

46. McLaughlin, M. A. *et al.* Transient radio bursts from rotating neutron stars. Nature **439,** 817–820. arXiv: astro-ph/0511587 [astro-ph] (Feb. 2006).

47. Keane, E. F., Kramer, M., Lyne, A., Stappers, B. & McLaughlin, M. Rotating Radio Transients: new discoveries, timing solutions and musings. *Monthly Notices of the Royal Astronomical Society* **415,** 3065–3080 (2011).

48. Olausen, S. A. & Kaspi, V. M. The McGill Magnetar Catalog. ApJS **212,** 6. arXiv: 1309.4167 [astro-ph.HE] (May 2014).

49. Kaspi, V. M. & Beloborodov, A. M. Magnetars. ARA&A **55,** 261–301. arXiv: 1703.00068 [astro-ph.HE] (Aug. 2017).

50. Cordes, J. M. & Lazio, T. J. W. NE2001.I. A New Model for the Galactic Distribution of Free Electrons and its Fluctuations. *arXiv e-prints,* astro–ph/0207156. arXiv: astro-ph/0207156 [astro-ph] (July 2002).

51. Cordes, J. M. & Lazio, T. J. W. NE2001. II. Using Radio Propagation Data to Construct a Model for the Galactic Distribution of Free Electrons. *arXiv e-prints,* astro–ph/0301598. arXiv: astro-ph/0301598 [astro-ph] (Jan. 2003).

52. Thornton, D. *et al.* A Population of Fast Radio Bursts at Cosmological Distances. *Science* **341,** 53–56. ISSN: 0036-8075. eprint: https://science.sciencemag.org/content/341/6141/53.full.pdf. https://science.sciencemag.org/content/341/6141/53 (2013).

53. Spitler, L. G. *et al.* Fast Radio Burst Discovered in the Arecibo Pulsar ALFA Survey. ApJ **790,** 101. arXiv: 1404.2934 [astro-ph.HE] (Aug. 2014).

54. Linscott, I. R. & Erkes, J. W. Discovery of millisecond radio bursts from M 87. ApJ **236,** L109–L113 (Mar. 1980).

55. McCulloch, P. M., Ellis, G. R. A., Gowland, G. A. & Roberts, J. A. Failure to detect millisecond radio pulses from M 87. ApJ **245,** L99–L101 (May 1981).

56. PHINNEY, S. & Taylor, J. A sensitive search for radio pulses from primordial black holes and distant supernovae. *Nature* **277,** 117–118 (1979).

57. Cortiglioni, S. *et al.* A Systematic Search for Radio Pulses Associated with Gamma-Ray Bursts. Ap&SS **75,** 153–161 (Mar. 1981).

58. Amy, S., Large, M. & Vaughan, A. A search for transient events at 843 MHz. *Publications of the Astronomical Society of Australia* **8,** 172–175 (1989).

59. Tendulkar, S. P. *et al.* The Host Galaxy and Redshift of the Repeating Fast Radio Burst FRB 121102. *apjl* **834,** L7. arXiv: 1701.01100 [astro-ph.HE] (Jan. 2017).

60. Petroff, E. *et al.* FRBCAT: The Fast Radio Burst Catalogue. *pasa* **33,** e045. arXiv: 1601.03547 [astro-ph.HE]. http://www.frbcat.org (Sept. 2016).

61. Petroff, E., Hessels, J. W. T. & Lorimer, D. R. Fast radio bursts. *aapr* **27,** 4. arXiv: 1904.07947 [astro-ph.HE] (May 2019).

62. Cordes, J. M. & Chatterjee, S. Fast Radio Bursts: An Extragalactic Enigma. *araa* **57,** 417–465. arXiv: 1906.05878 [astro-ph.HE] (Aug. 2019).

63. Ravi, V. *et al.* Fast Radio Burst Tomography of the Unseen Universe. *baas* **51,** 420. arXiv: 1903.06535 [astro-ph.HE] (May 2019).

64. McQuinn, M. Locating the "Missing" Baryons with Extragalactic Dispersion Measure Estimates. *apjl* **780,** L33. arXiv: 1309.4451 [astro-ph.CO] (Jan. 2014).

65. Masui, K. W. & Sigurdson, K. Dispersion Distance and the Matter Distribution of the Universe in Dispersion Space. *prl* **115,** 121301. arXiv: 1506.01704 [astro-ph.CO] (Sept. 2015).

66. Macquart, J. .-. *et al.* A census of baryons in the Universe from localized fast radio bursts. *nat* **581,** 391–395. arXiv: 2005.13161 [astro-ph.CO] (May 2020).

67. Josephy, A. *et al.* No Evidence for Galactic Latitude Dependence of the Fast Radio Burst Sky Distribution. *The Astrophysical Journal* **923,** 2. ISSN: 1538-4357. http://dx.doi.org/10.3847/1538-4357/ac33ad (Dec. 2021).

68. The CHIME/FRB Collaboration *et al.* The First CHIME/FRB Fast Radio Burst Catalog. *arXiv e-prints,* arXiv:2106.04352. arXiv: 2106.04352 [astro-ph.HE] (June 2021).

69. Pleunis, Z. *et al.* Fast Radio Burst Morphology in the First CHIME/FRB Catalog. *The Astrophysical Journal* **923,** 1. ISSN: 1538-4357. http://dx.doi.org/10.3847/1538-4357/ac33ac (Dec. 2021).

70. Kulkarni, S. R. Dispersion measure: Confusion, Constants & Clarity. *arXiv e-prints,* arXiv:2007.02886. arXiv: 2007.02886 [astro-ph.HE] (July 2020).

71. Hankins, T. H. & Rickett, B. J. Pulsar signal processing. *Methods in Computational Physics* **14,** 55–129 (Jan. 1975).

72. Yao, J. M., Manchester, R. N. & Wang, N. A New Electron-density Model for Estimation of Pulsar and FRB Distances. ApJ **835,** 29. arXiv: 1610.09448 [astro-ph.GA] (Jan. 2017).

73. Keating, L. C. & Pen, U.-L. Exploring the dispersion measure of the Milky Way halo. MNRAS **496,** L106–L110. arXiv: 2001.11105 [astro-ph.GA] (July 2020).

74. Yamasaki, S. & Totani, T. The Galactic Halo Contribution to the Dispersion Measure of Extragalactic Fast Radio Bursts. ApJ **888,** 105. arXiv: 1909.00849 [astro-ph.HE] (Jan. 2020).

75. Prochaska, J. X. & Zheng, Y. Probing Galactic Halos with Fast Radio Bursts. *Monthly Notices of the Royal Astronomical Society.* https://doi.org/10.1093%2Fmnras%2Fstz261 (Jan. 2019).

76. Platts, E., Prochaska, J. X. & Law, C. J. A Data-driven Technique Using Millisecond Transients to Measure the Milky Way Halo. ApJ **895,** L49. arXiv: 2005.06256 [astro-ph.GA] (June 2020).

77. Inoue, S. Probing the cosmic reionization history and local environment of gamma-ray bursts through radio dispersion. *Monthly Notices of the Royal Astronomical Society* **348,** 999–1008 (2004).

78. Ioka, K. The Cosmic Dispersion Measure from Gamma-Ray Burst Afterglows: Probing the Reionization History and the Burst Environment. ApJ **598,** L79–L82. arXiv: astro-ph/0309200 [astro-ph] (Dec. 2003).

79. Macquart, J. .-. *et al.* A census of baryons in the Universe from localized fast radio bursts. Nature **581,** 391–395. arXiv: 2005.13161 [astro-ph.CO] (May 2020).

80. Pleunis, Z. *et al.* LOFAR Detection of 110-188 MHz Emission and Frequency-dependent Activity from FRB 20180916B. ApJ **911,** L3. arXiv: 2012.08372 [astro-ph.HE] (Apr. 2021).

81. Gajjar, V. *et al.* Highest Frequency Detection of FRB 121102 at 4-8 GHz Using the Breakthrough Listen Digital Backend at the Green Bank Telescope. ApJ **863,** 2. arXiv: 1804.04101 [astro-ph.HE] (Aug. 2018).

82. Masui, K. *et al.* Dense magnetized plasma associated with a fast radio burst. Nature **528,** 523–525. arXiv: 1512.00529 [astro-ph.HE] (Dec. 2015).

83. Drake, F. D. & Craft, H. D. Second Periodic Pulsation in Pulsars. Nature **220,** 231–235 (Oct. 1968).

84. Colegate, T. M. & Clarke, N. Searching for Fast Radio Transients with SKA Phase 1. *Publ. Astron. Soc. Austral.* **28,** 299. arXiv: 1106.5836 [astro-ph.IM] (2011).

85. Chime/Frb Collaboration *et al.* Periodic activity from a fast radio burst source. *nat* **582,** 351–355. arXiv: 2001.10275 [astro-ph.HE] (June 2020).

86. Platts, E. *et al.* A living theory catalogue for fast radio bursts. *physrep* **821,** 1–27. arXiv: 1810.05836 [astro-ph.HE] (Aug. 2019).

87. Peterson, J. B., Bandura, K. & Sanghavi, P. *Optimization of Radio Array Telescopes to Search for Fast RadioBursts* 2020. arXiv: 2001.06526 [astro-ph.IM].

88. CHIME/FRB Collaboration *et al.* The CHIME Fast Radio Burst Project: System Overview. *apj* **863,** 48. arXiv: 1803.11235 [astro-ph.IM] (Aug. 2018).

89. Condon, J. J. & Ransom, S. M. *Essential Radio Astronomy* ISBN: 9780691137797 (Princeton University Press, 2016).

90. CHIME/FRB Collaboration *et al.* Observations of fast radio bursts at frequencies down to 400 megahertz. *nat* **566,** 230–234. arXiv: 1901.04524 [astro-ph.HE] (Jan. 2019).

91. Metzger, B. D., Margalit, B. & Sironi, L. Fast radio bursts as synchrotron maser emission from decelerating relativistic blast waves. *mnras* **485,** 4091–4106. arXiv: 1902.01866 [astro-ph.HE] (May 2019).

92. CHIME/FRB Collaboration *et al.* A second source of repeating fast radio bursts. *nat* **566,** 235–238. arXiv: 1901.04525 [astro-ph.HE] (Jan. 2019).

93. CHIME/FRB Collaboration *et al.* CHIME/FRB Discovery of Eight New Repeating Fast Radio Burst Sources. *apjl* **885,** L24. arXiv: 1908.03507 [astro-ph.HE] (Nov. 2019).

94. Fonseca, E. *et al.* Nine New Repeating Fast Radio Burst Sources from CHIME/FRB. *apjl* **891,** L6. arXiv: 2001.03595 [astro-ph.HE] (Mar. 2020).

95. CHIME/FRB Collaboration *et al.* A second source of repeating fast radio bursts. *nat* **566,** 235–238. arXiv: 1901.04525 [astro-ph.HE] (Jan. 2019).

96. The CHIME Collaboration *et al.* An Overview of CHIME, the Canadian Hydrogen Intensity Mapping Experiment. *arXiv e-prints,* arXiv:2201.07869. arXiv: 2201.07869 [astro-ph.IM] (Jan. 2022).

97. Bandura, K. *et al.* ICE: A Scalable, Low-Cost FPGA-Based Telescope Signal Processing and Networking System. *Journal of Astronomical Instrumentation* **5,** 1641005. arXiv: 1608.06262 [astro-ph.IM] (Dec. 2016).

98. Denman, N. *et al.* A GPU Spatial Processing System for CHIME. *Journal of Astronomical Instrumentation* **9,** 2050014–2. arXiv: 2005.09481 [astro-ph.IM] (Jan. 2020).

99. Renard, A. *et al.* *Kotekan: A framework for high-performance radiometric data pipelines* version 2021.11. Nov. 2021.

100. CHIME/FRB Collaboration *et al.* The CHIME Fast Radio Burst Project: System Overview. ApJ **863,** 48. arXiv: 1803.11235 [astro-ph.IM] (Aug. 2018).

101. Michilli, D. *et al.* An Analysis Pipeline for CHIME/FRB Full-array Baseband Data. ApJ **910,** 147. arXiv: 2010.06748 [astro-ph.HE] (Apr. 2021).

102. Chime/Frb Collaboration *et al.* Periodic activity from a fast radio burst source. Nature **582,** 351–355. arXiv: 2001.10275 [astro-ph.HE] (June 2020).

103. CHIME/FRB Collaboration *et al.* A bright millisecond-duration radio burst from a Galactic magnetar. Nature **587,** 54–58. arXiv: 2005.10324 [astro-ph.HE] (Nov. 2020).

104. Bochenek, C. D. *et al.* A fast radio burst associated with a Galactic magnetar. Nature **587,** 59–62. arXiv: 2005.10828 [astro-ph.HE] (Nov. 2020).

105. CHIME/FRB Collaboration *et al.* The First CHIME/FRB Fast Radio Burst Catalog. ApJS **257,** 59. arXiv: 2106.04352 [astro-ph.HE] (Dec. 2021).

106. Josephy, A. *et al.* No Evidence for Galactic Latitude Dependence of the Fast Radio Burst Sky Distribution. ApJ **923,** 2. arXiv: 2106.04353 [astro-ph.HE] (Dec. 2021).

107. Pleunis, Z. *et al.* Fast Radio Burst Morphology in the First CHIME/FRB Catalog. ApJ **923,** 1. arXiv: 2106.04356 [astro-ph.HE] (Dec. 2021).

108. Rafiei-Ravandi, M. *et al.* CHIME/FRB Catalog 1 Results: Statistical Cross-correlations with Large-scale Structure. ApJ **922,** 42. arXiv: 2106.04354 [astro-ph.CO] (Nov. 2021).

109. The CHIME/FRB Collaboration *et al.* Sub-second periodicity in a fast radio burst. *arXiv e-prints,* arXiv:2107.08463. arXiv: 2107.08463 [astro-ph.HE] (July 2021).

110. Kader, Z. *et al.* A High-Time Resolution Search for Compact Objects using Fast Radio Burst Gravitational Lens Interferometry with CHIME/FRB. *arXiv e-prints,* arXiv:2204.06014. arXiv: 2204.06014 [astro-ph.HE] (Apr. 2022).

111. Leung, C. *et al.* Constraining Primordial Black Holes using Fast Radio Burst Gravitational-Lens Interferometry with CHIME/FRB. *arXiv e-prints,* arXiv:2204.06001. arXiv: 2204.06001 [astro-ph.HE] (Apr. 2022).

112. Newburgh, L. B. *et al. HIRAX: a probe of dark energy and radio transients* in *Ground-based and Airborne Telescopes VI* (eds Hall, H. J., Gilmozzi, R. & Marshall, H. K.) **9906** (Aug. 2016), 99065X. arXiv: 1607.02059 [astro-ph.IM].

113. Crichton, D. *et al.* Hydrogen Intensity and Real-Time Analysis Experiment: 256-element array status and overview. *Journal of Astronomical Telescopes, Instruments, and Systems* **8,** 011019. arXiv: 2109.13755 [astro-ph.IM] (Jan. 2022).

114. Vanderlinde, K. *et al. The Canadian Hydrogen Observatory and Radio-transient Detector (CHORD)* in *Canadian Long Range Plan for Astronomy and Astrophysics White Papers* **2020** (Oct. 2019), 28. arXiv: 1911.01777 [astro-ph.IM].

115. Eftekhari, T. & Berger, E. Associating fast radio bursts with their host galaxies. *The Astrophysical Journal* **849,** 162 (2017).

116. Deng, M. & Campbell-Wilson, D. The cloverleaf antenna: A compact wide-bandwidth dual-polarization feed for CHIME. *arXiv e-prints,* arXiv:1708.08521. arXiv: 1708.08521 [astro-ph.IM] (Aug. 2017).

117. Bandura, K. *et al.* ICE: A Scalable, Low-Cost FPGA-Based Telescope Signal Processing and Networking System. *Journal of Astronomical Instrumentation* **5,** 1641005. arXiv: 1608.06262 [astro-ph.IM] (Dec. 2016).

118. Bandura, K. *et al.* ICE-Based Custom Full-Mesh Network for the CHIME High Bandwidth Radio Astronomy Correlator. *Journal of Astronomical Instrumentation* **5,** 1641004. arXiv: 1608.04347 [astro-ph.IM] (Dec. 2016).

119. Perley, R. A. & Butler, B. J. An Accurate Flux Density Scale from 50 MHz to 50 GHz. ApJS **230,** 7. arXiv: 1609.05940 [astro-ph.IM] (May 2017).

120. Mena-Parra, J. *et al.* A Clock Stabilization System for CHIME/FRB Outriggers. AJ **163,** 48. arXiv: 2110.00576 [astro-ph.IM] (Feb. 2022).

121. Allan, D. W. Statistics of atomic frequency standards. *Proceedings of the IEEE* **54,** 221–230 (1966).

122. Event Horizon Telescope Collaboration *et al.* First M87 Event Horizon Telescope Results. II. Array and Instrumentation. ApJ **875,** L2. arXiv: 1906.11239 [astro-ph.IM] (Apr. 2019).

123. Thompson, A. R., Moran, J. M. & Swenson George W., J. *Interferometry and Synthesis in Radio Astronomy, 3rd Edition* (2017).

124. *Synthesis Imaging in Radio Astronomy II* **180** (Jan. 1999).

125. Van Trees, H. L. *Optimum array processing: Part IV of detection, estimation, and modulation theory* (John Wiley & Sons, 2004).

126. Van Veen, B. & Buckley, K. Beamforming: a versatile approach to spatial filtering. *IEEE ASSP Magazine* **5,** 4–24 (1988).

127. Bandura, K. *Pathfinder for a neutral hydrogen dark energy survey* PhD thesis (Carnegie Mellon University, 2011).

128. Recnik, A. *et al.* An Efficient Real-time Data Pipeline for the CHIME Pathfinder Radio Telescope X-Engine. *arXiv e-prints,* arXiv:1503.06189. arXiv: 1503.06189 [astro-ph.IM] (Mar. 2015).

129. Bandura, K. *et al.* *Canadian Hydrogen Intensity Mapping Experiment (CHIME) pathfinder* in *Ground-based and Airborne Telescopes V* (eds Stepp, L. M., Gilmozzi, R. & Hall, H. J.) **9145** (July 2014), 914522. arXiv: 1406.2288 [astro-ph.IM].

130. Newburgh, L. B. *et al. Calibrating CHIME: a new radio interferometer to probe dark energy* in *Ground-based and Airborne Telescopes V* (eds Stepp, L. M., Gilmozzi, R. & Hall, H. J.) **9145** (July 2014), 91454V. arXiv: 1406.2267 [astro-ph.IM].

131. Broten, N. W. *et al.* Diameters of Some Quasars at a Wavelength of 66.9 cm. Nature **216,** 44–45 (Oct. 1967).

132. Broten, N. W. *et al.* Long Base Line Interferometry: A New Technique. *Science* **156,** 1592–1593 (June 1967).

133. Broten, N. W. *et al.* Observations of Quasars using Interferometer Baselines up to 3,074 km. *Nature* **215,** 38–38 (1967).

134. Broten, N. W. *et al.* Long baseline interferometer,observations at 408 and 448 MHz-I. The observations. MNRAS **146,** 313 (Jan. 1969).

135. Chatterjee, S. *et al.* A direct localization of a fast radio burst and its host. Nature **541,** 58–61. arXiv: 1701.01098 [astro-ph.HE] (Jan. 2017).

136. Marcote, B. *et al.* A repeating fast radio burst source localized to a nearby spiral galaxy. Nature **577,** 190–194. arXiv: 2001.02222 [astro-ph.HE] (Jan. 2020).

137. Nimmo, K. *et al.* Milliarcsecond localisation of the repeating FRB 20201124A. *arXiv e-prints,* arXiv:2111.01600. arXiv: 2111.01600 [astro-ph.HE] (Nov. 2021).

138. Bannister, K. W. *et al.* A single fast radio burst localized to a massive galaxy at cosmological distance. *Science* **365,** 565–570. arXiv: 1906.11476 [astro-ph.HE] (Aug. 2019).

139. Ravi, V. *et al.* A fast radio burst localized to a massive galaxy. Nature **572,** 352–354. arXiv: 1907.01542 [astro-ph.HE] (Aug. 2019).

140. Law, C. J. *et al.* A Distant Fast Radio Burst Associated with Its Host Galaxy by the Very Large Array. ApJ **899,** 161. arXiv: 2007.02155 [astro-ph.HE] (Aug. 2020).

141. Cassanelli, T. *et al.* Localizing FRBs through VLBI with the Algonquin Radio Observatory 10 m Telescope. AJ **163,** 65. arXiv: 2107.05659 [astro-ph.IM] (Feb. 2022).

142. Et al., P. S. *TONE: A CHIME/FRB Outrigger Pathfinder for Sub-arcsecond Localizations of Fast Radio Bursts on Discovery* In preparation. 2022.

143. Lyne, A. G. *et al.* 45 years of rotation of the Crab pulsar. MNRAS **446,** 857–864. arXiv: 1410.0886 [astro-ph.HE] (Jan. 2015).

144. Deng, M. & Campbell-Wilson, D. The cloverleaf antenna: A compact wide-bandwidth dual-polarization feed for CHIME. *arXiv e-prints,* arXiv:1708.08521. arXiv: 1708.08521 [astro-ph.IM] (Aug. 2017).

145. Mena-Parra, J. *et al.* A Clock Stabilization System for CHIME/FRB Outriggers. AJ **163,** 48. arXiv: 2110.00576 [astro-ph.IM] (Feb. 2022).

146. Cary, S. *et al.* Evaluating and Enhancing Candidate Clocking Systems for CHIME/FRB VLBI Outriggers. *Research Notes of the American Astronomical Society* **5,** 216. arXiv: 2109.05044 [astro-ph.IM] (Sept. 2021).

147. Hankins, T. H. & Rickett, B. J. Pulsar signal processing. *Methods in Computational Physics* **14,** 55–129 (Jan. 1975).

148. Lorimer, D. R. & Kramer, M. *Handbook of Pulsar Astronomy* (2012).

149. Kulkarni, S. R. Dispersion measure: Confusion, Constants & Clarity. *arXiv e-prints,* arXiv:2007.02886. arXiv: 2007.02886 [astro-ph.HE] (July 2020).

150. Lobanov, A. P., Horns, D. & Muxlow, T. W. B. VLBI imaging of a flare in the Crab nebula: more than just a spot. A&A **533,** A10. arXiv: 1107.0182 [astro-ph.HE] (Sept. 2011).

151. Leung, C. *et al.* A Synoptic VLBI Technique for Localizing Nonrepeating Fast Radio Bursts with CHIME/FRB. *aj* **161,** 81. arXiv: 2008.11738 [astro-ph.IM] (Feb. 2021).

152. Rogers, A. E. Very long baseline interferometry with large effective bandwidth for phase-delay measurements. *Radio Science* **5,** 1239–1247 (1970).

153. Foreman-Mackey, D., Hogg, D. W., Lang, D. & Goodman, J. emcee: The MCMC Hammer. PASP **125,** 306. arXiv: 1202.3665 [astro-ph.IM] (Mar. 2013).

154. Mevius, M. *RMextract: Ionospheric Faraday Rotation calculator* June 2018. ascl: 1806.024.

155. Mevius, M. *et al.* Probing ionospheric structures using the LOFAR radio telescope. *Radio Science* **51,** 927–941. arXiv: 1606.04683 [astro-ph.IM] (July 2016).

156. Vedantham, H. K. & Koopmans, L. V. E. Scintillation noise in widefield radio interferometry. MNRAS **453,** 925–938. arXiv: 1412.1420 [astro-ph.IM] (Oct. 2015).

157. Bernardo, J. M., Berger, J. O., Dawid, A. & Smith, A. F. *Bayesian Statistics 6: Proceedings of the Sixth Valencia International Meeting* (Oxford University Press, 1999).

158. Hogg, D. W. & Foreman-Mackey, D. Data Analysis Recipes: Using Markov Chain Monte Carlo. ApJS **236,** 11. arXiv: 1710.06068 [astro-ph.IM] (May 2018).

159. Seymour, A., Michilli, D. & Pleunis, Z. *DM_phase: Algorithm for correcting dispersion of radio signals* Astrophysics Source Code Library, record ascl:1910.004. Oct. 2019. ascl: 1910.004.

160. Collaboration, T. C. *et al.* The First CHIME/FRB Fast Radio Burst Catalog. *The Astrophysical Journal Supplement Series* **257,** 59. ISSN: 1538-4365. http://dx.doi.org/10.3847/1538-4365/ac33ab (Dec. 2021).

161. Ahn, C. P. *et al.* The Tenth Data Release of the Sloan Digital Sky Survey: First Spectroscopic Data from the SDSS-III Apache Point Observatory Galactic Evolution Experiment. ApJS **211,** 17. arXiv: 1307.7735 [astro-ph.IM] (Apr. 2014).

162. Cordes, J. M. & Lazio, T. J. W. NE2001.I. A New Model for the Galactic Distribution of Free Electrons and its Fluctuations. *arXiv e-prints,* astro–ph/0207156. arXiv: astro-ph/0207156 [astro-ph] (July 2002).

163. Cordes, J. M. & Lazio, T. J. W. NE2001. II. Using Radio Propagation Data to Construct a Model for the Galactic Distribution of Free Electrons. *arXiv e-prints,* astro–ph/0301598. arXiv: astro-ph/0301598 [astro-ph] (Jan. 2003).

164. Masui, K. *et al.* Dense magnetized plasma associated with a fast radio burst. *Nature* **528,** 523–525. ISSN: 1476-4687. http://dx.doi.org/10.1038/nature15769 (Dec. 2015).

165. Akahori, T., Ryu, D. & Gaensler, B. M. Fast Radio Bursts as Probes of Magnetic Fields in the Intergalactic Medium. ApJ **824,** 105. arXiv: 1602.03235 [astro-ph.CO] (June 2016).

166. Yamasaki, S. & Totani, T. The Galactic Halo Contribution to the Dispersion Measure of Extragalactic Fast Radio Bursts. ApJ **888,** 105. arXiv: 1909.00849 [astro-ph.HE] (Jan. 2020).

167. Macquart, J. .-. *et al.* A census of baryons in the Universe from localized fast radio bursts. Nature **581,** 391–395. arXiv: 2005.13161 [astro-ph.CO] (May 2020).

168. Batten, A. J. *et al.* The cosmic dispersion measure in the EAGLE simulations. MNRAS **505,** 5356–5369. arXiv: 2011.14547 [astro-ph.CO] (Aug. 2021).

169. Trujillo, I., Chamba, N. & Knapen, J. H. A physically motivated definition for the size of galaxies in an era of ultradeep imaging. MNRAS **493,** 87–105. arXiv: 2001.02689 [astro-ph.GA] (Mar. 2020).

170. Licquia, T. C. & Newman, J. A. Improved Estimates of the Milky Way's Stellar Mass and Star Formation Rate from Hierarchical Bayesian Meta-Analysis. ApJ **806,** 96. arXiv: 1407.1078 [astro-ph.GA] (June 2015).

171. Ocker, S. K., Cordes, J. M. & Chatterjee, S. Electron Density Structure of the Local Galactic Disk. ApJ **897,** 124. arXiv: 2004.11921 [astro-ph.GA] (July 2020).

172. Ocker, S. K., Cordes, J. M. & Chatterjee, S. Constraining Galaxy Halos from the Dispersion and Scattering of Fast Radio Bursts and Pulsars. ApJ **911,** 102. arXiv: 2101.04784 [astro-ph.GA] (Apr. 2021).

173. Cordes, J. M., Wharton, R. S., Spitler, L. G., Chatterjee, S. & Wasserman, I. Radio Wave Propagation and the Provenance of Fast Radio Bursts. *arXiv e-prints,* arXiv:1605.05890. arXiv: 1605.05890 [astro-ph.HE] (May 2016).

174. James, C. W. *et al.* The z-DM distribution of fast radio bursts. MNRAS **509,** 4775–4802. arXiv: 2101.08005 [astro-ph.HE] (Feb. 2022).

175. Olausen, S. A. & Kaspi, V. M. The McGill Magnetar Catalog. ApJS **212,** 6. arXiv: 1309.4167 [astro-ph.HE] (May 2014).

176. Miller, G. E. & Scalo, J. M. The Initial Mass Function and Stellar Birthrate in the Solar Neighborhood. ApJS **41,** 513 (Nov. 1979).

177. Fonseca, E. *et al.* Nine New Repeating Fast Radio Burst Sources from CHIME/FRB. ApJ **891,** L6. arXiv: 2001.03595 [astro-ph.HE] (Mar. 2020).

178. Bhardwaj, M. *et al.* A Nearby Repeating Fast Radio Burst in the Direction of M81. ApJ **910,** L18. arXiv: 2103.01295 [astro-ph.HE] (Apr. 2021).

179. Burn, B. J. On the depolarization of discrete radio sources by Faraday dispersion. MNRAS **133,** 67 (Jan. 1966).

180. Brentjens, M. A. & de Bruyn, A. G. Faraday rotation measure synthesis. A&A **441,** 1217–1228. arXiv: astro-ph/0507349 [astro-ph] (Oct. 2005).

181. Mckinven, R. *et al.* Polarization Pipeline for Fast Radio Bursts Detected by CHIME/FRB. *The Astrophysical Journal* **920,** 138. https://doi.org/10.3847/1538-4357/ac126a (Oct. 2021).

182. Vedantham, H. K. & Ravi, V. Faraday conversion and magneto-ionic variations in fast radio bursts. MNRAS **485,** L78–L82. arXiv: 1812.07889 [astro-ph.HE] (May 2019).

183. Gruzinov, A. & Levin, Y. Conversion Measure of Faraday Rotation-Conversion with Application to Fast Radio Bursts. ApJ **876,** 74. arXiv: 1902.01485 [astro-ph.HE] (May 2019).

184. Beniamini, P., Kumar, P. & Narayan, R. Faraday depolarization and induced circular polarization by multipath propagation with application to FRBs. MNRAS **510,** 4654–4668. arXiv: 2110.00028 [astro-ph.HE] (Mar. 2022).

185. Hutschenreuter, S. *et al.* The Galactic Faraday rotation sky 2020. *arXiv e-prints,* arXiv:2102.01709. arXiv: 2102.01709 [astro-ph.GA] (Feb. 2021).

186. Manchester, R. N., Hobbs, G. B., Teoh, A. & Hobbs, M. The Australia Telescope National Facility Pulsar Catalogue. AJ **129,** 1993–2006. arXiv: astro-ph/0412641 [astro-ph] (Apr. 2005).

187. Pitkin, M. psrqpy: a python interface for querying the ATNF pulsar catalogue. *Journal of Open Source Software* **3,** 538. https://doi.org/10.21105/joss.00538 (Feb. 2018).

188. Boulade, O. *et al. Megacam: the next-generation wide-field imaging camera for CFHT* in *Optical Astronomical Instrumentation* (ed D'Odorico, S.) **3355** (July 1998), 614–625.

189. Kourkchi, E. *et al.* Cosmicflows-4: The Catalog of ∼10,000 Tully-Fisher Distances. ApJ **902,** 145. arXiv: 2009.00733 [astro-ph.GA] (Oct. 2020).

190. Hook, I. M. *et al.* The Gemini-North Multi-Object Spectrograph: Performance in Imaging, Long-Slit, and Multi-Object Spectroscopic Modes. PASP **116,** 425–440 (May 2004).

191. Planck Collaboration *et al.* Planck 2018 results. VI. Cosmological parameters. A&A **641,** A6. arXiv: 1807.06209 [astro-ph.CO] (Sept. 2020).

192. Bhandari, S. *et al.* Characterizing the FRB host galaxy population and its connection to transients in the local and extragalactic Universe. *arXiv e-prints,* arXiv:2108.01282. arXiv: 2108.01282 [astro-ph.HE] (Aug. 2021).

193. Skrutskie, M. F. *et al.* The Two Micron All Sky Survey (2MASS). AJ **131,** 1163–1183 (Feb. 2006).

194. Wright, E. L. *et al.* The Wide-field Infrared Survey Explorer (WISE): Mission Description and Initial On-orbit Performance. AJ **140,** 1868–1881. arXiv: 1008.0031 [astro-ph.IM] (Dec. 2010).

195. Johnson, B. D., Leja, J., Conroy, C. & Speagle, J. S. Stellar Population Inference with Prospector. ApJS **254,** 22. arXiv: 2012.01426 [astro-ph.GA] (June 2021).

196. Tendulkar, S. P. *et al.* The 60 pc Environment of FRB 20180916B. ApJ **908,** L12. arXiv: 2011.03257 [astro-ph.HE] (Feb. 2021).

197. Magnier, E. A. & Cuillandre, J. .-. The Elixir System: Data Characterization and Calibration at the Canada-France-Hawaii Telescope. PASP **116,** 449–464 (May 2004).

198. Prunet, S., Fouque, P. & Gwyn, S. *Photometric calibration of Megacam data* (2014).

199. Graham, A. W. *et al.* Total Galaxy Magnitudes and Effective Radii from Petrosian Magnitudes and Radii. *The Astronomical Journal* **130,** 1535–1544. ISSN: 1538-3881. http://dx.doi.org/10.1086/444475 (Oct. 2005).

200. Fitzpatrick, E. L. & Massa, D. An Analysis of the Shapes of Interstellar Extinction Curves. V. The IR-through-UV Curve Morphology. ApJ **663,** 320–341. arXiv: 0705.0154 [astro-ph] (July 2007).

201. Chilingarian, I. V., Melchior, A.-L. & Zolotukhin, I. Y. Analytical approximations of K-corrections in optical and near-infrared bands. MNRAS **405,** 1409–1420. arXiv: 1002.2360 [astro-ph.IM] (July 2010).

202. Tody, D. *The IRAF Data Reduction and Analysis System* in *Instrumentation in astronomy VI* (ed Crawford, D. L.) **627** (Jan. 1986), 733.

203. Tody, D. *IRAF in the Nineties* in *Astronomical Data Analysis Software and Systems II* (eds Hanisch, R. J., Brissenden, R. J. V. & Barnes, J.) **52** (Jan. 1993), 173.

204. Bhardwaj, M. *et al.* A Local Universe Host for the Repeating Fast Radio Burst FRB 20181030A. *The Astrophysical Journal Letters* **919,** L24. https://doi.org/10.3847/2041-8213/ac223b (Sept. 2021).

205. Shao, Z. *et al.* Inclination-dependent Luminosity Function of Spiral Galaxies in the Sloan Digital Sky Survey: Implications for Dust Extinction. *The Astrophysical Journal* **659,** 1159–1171. https://doi.org/10.1086/511131 (Apr. 2007).

206. Calzetti, D. *et al.* The Dust Content and Opacity of Actively Star-forming Galaxies. ApJ **533,** 682–695. arXiv: astro-ph/9911459 [astro-ph] (Apr. 2000).

207. Byler, N., Dalcanton, J. J., Conroy, C. & Johnson, B. D. Nebular Continuum and Line Emission in Stellar Population Synthesis Models. ApJ **840,** 44. arXiv: 1611.08305 [astro-ph.GA] (May 2017).

208. Draine, B. T. & Li, A. Infrared Emission from Interstellar Dust. IV. The Silicate-Graphite-PAH Model in the Post-Spitzer Era. ApJ **657,** 810–837. arXiv: astro-ph/0608003 [astro-ph] (Mar. 2007).

209. Bernardi, M. *et al.* Galaxy luminosities, stellar masses, sizes, velocity dispersions as a function of morphological type. MNRAS **404,** 2087–2122. arXiv: 0910.1093 [astro-ph.CO] (June 2010).

210. Kennicutt Robert C., J., Tamblyn, P. & Congdon, C. E. Past and Future Star Formation in Disk Galaxies. ApJ **435,** 22 (Nov. 1994).

211. Fitzpatrick, E. L. Correcting for the Effects of Interstellar Extinction. PASP **111,** 63–75. arXiv: astro-ph/9809387 [astro-ph] (Jan. 1999).

212. Conroy, C., Gunn, J. E. & White, M. The Propagation of Uncertainties in Stellar Population Synthesis Modeling. I. The Relevance of Uncertain Aspects of Stellar Evolution and the Initial Mass Function to the Derived Physical Properties of Galaxies. ApJ **699,** 486–506. arXiv: 0809.4261 [astro-ph] (July 2009).

213. Schlafly, E. F. & Finkbeiner, D. P. Measuring Reddening with Sloan Digital Sky Survey Stellar Spectra and Recalibrating SFD. ApJ **737,** 103. arXiv: 1012.4804 [astro-ph.GA] (Aug. 2011).

214. Kirsten, F. *et al.* A repeating fast radio burst source in a globular cluster. Nature **602,** 585–589. arXiv: 2105.11445 [astro-ph.HE] (Feb. 2022).

215. Dehnen, W., McLaughlin, D. E. & Sachania, J. The velocity dispersion and mass profile of the Milky Way. MNRAS **369,** 1688–1692. arXiv: astro-ph/0603825 [astro-ph] (July 2006).

216. Marcote, B. *et al.* The Repeating Fast Radio Burst FRB 121102 as Seen on Milliarcsecond Angular Scales. ApJ **834,** L8. arXiv: 1701.01099 [astro-ph.HE] (Jan. 2017).

217. Niu, C. .-. *et al.* A repeating fast radio burst in a dense environment with a compact persistent radio source. *arXiv e-prints,* arXiv:2110.07418. arXiv: 2110.07418 [astro-ph.HE] (Oct. 2021).

218. Brand, J. & Blitz, L. The velocity field of the outer galaxy. A&A **275,** 67–90 (Aug. 1993).

219. van de Hulst, H. C., Muller, C. A. & Oort, J. H. The spiral structure of the outer part of the Galactic System derived from the hydrogen emission at 21 cm wavelength. Bull. Astron. Inst. Netherlands **12,** 117 (May 1954).

220. Sanghavi, P., Bandura, K., Makous, J. & Chun, H. *Digital Signal Processing in Radio Astronomy: An Interdisciplinary Experience* in *2019 IEEE Integrated STEM Education Conference (ISEC)* (2019), 362–366.

221. Website, G. R. 2012. http://www.gnuradio.org.

222. States, N. L. Next generation science standards: For states, by states (2013).

223. Bochenek, C. D. *et al.* STARE2: Detecting Fast Radio Bursts in the Milky Way. PASP **132,** 034202. arXiv: 2001.05077 [astro-ph.HE] (Mar. 2020).

224. A bright millisecond-duration radio burst from a Galactic magnetar. *Nature* **587,** 54–58. https://doi.org/10.1038%2Fs41586-020-2863-y (Nov. 2020).

225. Petroff, E. *et al. VOEvent Standard for Fast Radio Bursts* 2017. https://arxiv.org/abs/1710.08155.

226. Makous, J. L. & Bandura, K. Using a Radio Telescope for Developing Models in an Introductory Physics Course. *The Physics Teacher* **59,** 38–40 (2021).

227. Herman, T. Measuring the Speed of Earth Around the Sun Using a Classroom-Built Radio Horn Telescope. *The Physics Teacher* **60,** 105–109 (2022).

228. Nix, B., Sherwood, D., Chen, A., Guerin, S. & Nedvidek, B. Measuring the mass of the Milky Way using observations of radio waves emitted by neutral hydrogen. *JUEPPEQ: Journal of Undergraduate Engineering Physics and Physics Experiments at Queen's* **2,** 1–16 (2021).

229. Connor, L. & Ravi, V. The observed impact of galaxy halo gas on fast radio bursts. *Nature Astronomy* (July 2022).

# Appendices

## A Sensitivity of Radio Telescopes

In radio astronomy signals can be expressed in terms of the equivalent temperature $T$ of a resistor matched at the receiver. We have the power from a black body the Rayleigh-Jeans approximation of the Planck radiation,

$$P = k_{\mathrm{B}} T \Delta\nu, \tag{A.1}$$

where $k_{\mathrm{B}}$ is the Boltzmann constant and $\Delta\nu$ is the observing bandwidth. This power is amplified by $g^2$ where $g$ is the voltage gain of the analog chain of the radio telescope. For the antenna temperature $T_{\mathrm{a}}$ and system temperature $T_{\mathrm{sys}}$, have the power from the voltage induced by the source $s_i$,

$$P_a = \langle s_i s_i^* \rangle = g^2 k_{\mathrm{B}} T_a \Delta\nu, \tag{A.2}$$

and the power from the voltage induced by the system noise $n_i$,

$$P_N = \langle n_i n_i^* \rangle = g^2 k_{\mathrm{B}} T_{\mathrm{sys}} \Delta\nu. \tag{A.3}$$

Here $T_{\mathrm{sys}}$ includes receiver noise, losses, spillover, atmosphere and cosmic background. The power received from the a single channel receiver only accepts half of the total radiation from an unpolarised source,

$$P_a = \frac{1}{2} g^2 A_{\mathrm{e}} S \Delta\nu = g^2 k_{\mathrm{B}} G S \Delta\nu. \tag{A.4}$$

The factor $G = A_\mathrm{e}/2k_\mathrm{B}$ is the forward gain in K/Jy. The system equivalent flux density (SEFD) is defined as,

$$\mathrm{SEFD} = \frac{T_\mathrm{sys}}{G}, \tag{A.5}$$

it is the flux density of a source that emits the same power as a system to temperature $T_\mathrm{sys}$. Since the frequency-dependent system temperature and forward gain depends on system calibration however the SEFD can be computed by measuring the change in power on and off a known source.

## A.1 Signal to Noise Ratios of an array of antennas

We can now consider complex voltage from the $i^{th}$ antenna, $v_i = s_i + n_i$. Where $s_i$ is the voltage induced by the signal from the source and $n_i$ is the voltage induced by the system noise. We assume they are zero mean gaussian random variables. We can also assume, that signal and noise from different antennas are uncorrelated i.e. $\langle s_i n_j \rangle$. We also assume in this derivation that the antennas are identical.

### A.1.1 Incoherent Arrays

In incoherent arrays, the powers from individual antennas are summed together such as,

$$P = \sum_{i=1}^{N} P_i = \sum_{i=1}^{N} v_i v_i^*. \tag{A.6}$$

so the expected value of the power

$$\begin{aligned}\langle P \rangle &= \sum_i \langle (s_i + n_i)(s_i + n_i)^* \rangle \\ &= \sum_i (\langle s_i s_i^* \rangle + \langle n_i n_i^* \rangle) \\ &= cN(GS + T_\mathrm{sys}) = cN(T_a + T_\mathrm{sys}).\end{aligned} \tag{A.7}$$

The variance of the power is a representation of the noise $\sigma^2(P) = \langle P^2 \rangle - \langle P \rangle^2$. We have,

$$\begin{aligned}
\langle P^2 \rangle &= \langle P \cdot P \rangle \\
&= \langle \sum_i v_i v_i^* \sum_j v_j v_j^* \rangle \\
&= \langle \sum_i (s_i + n_i)(s_i + n_i)^* \sum_j (s_j + n_j)(s_j + n_j)^* \rangle.
\end{aligned} \tag{A.8}$$

For fourth order moment of jointly gaussian random variables, we have the Isserlis' theorem, $\langle X_1 X_2 X_3 X_4 \rangle = \langle X_1 X_2 \rangle \langle X_3 X_4 \rangle + \langle X_1 X_3 \rangle \langle X_2 X_4 \rangle + \langle X_1 X_4 \rangle \langle X_2 X_3 \rangle$, we have,

$$\begin{aligned}
\langle P^2 \rangle &= \langle \sum_i \sum_j (s_i + n_i)(s_i + n_i)^* (s_j + n_j)(s_j + n_j)^* \rangle \\
&= \sum_i \sum_j \langle (s_i + n_i)(s_i + n_i)^* \rangle \langle (s_j + n_j)(s_j + n_j)^* \rangle \\
&\quad + \langle (s_i + n_i)(s_j + n_j) \rangle \langle (s_i + n_i)^* (s_j + n_j)^* \rangle \\
&\quad + \langle (s_i + n_i)(s_j + n_j)^* \rangle \langle (s_j + n_j)(s_i + n_i)^* \rangle.
\end{aligned}$$

For a complex zero mean gaussian random variables the second term of the above expanded equation is zero. Simplifying,

$$\langle P^2 \rangle = \sum_i \sum_j \Big[ \langle s_i s_i^* + n_i n_i^* \rangle \langle s_j s_j^* + n_j n_j^* \rangle + \langle s_i s_j^* + n_i n_j^* \rangle \langle s_j s_i^* + n_j n_i^* \rangle \Big]. \tag{A.9}$$

Considering two cases, for the first case we have terms of summed power for $N$ terms where $i = j$ and $N(N-1)$ terms where $i \neq j$, the noise from different antennas are uncorrelated i.e.,

$$\langle P^2 \rangle = \sum_i 2 \langle s_i s_i^* + n_i n_i^* \rangle^2 = 2c^2 N (GS + T_{\mathrm{sys}})^2, \tag{A.10}$$

and for the fully correlated sky signal $s_i = s_j$

$$\langle P^2 \rangle = c^2 N(N-1)[(GS + T_{\mathrm{sys}})^2 + (GS)^2]. \tag{A.11}$$

So, we have for all summed terms,

$$\langle P^2 \rangle = c^2 \Big[ 2N(GS + T_{\text{sys}})^2 + N(N-1)[(GS + T_{\text{sys}})^2 + (GS)^2] \Big]. \tag{A.12}$$

Similarly, we can calculate the variance

$$\sigma^2(P) = c^2 N \Big[ (GS + T_{\text{sys}})^2 + (N-1)[(GS + T_{\text{sys}})^2 + (GS)^2] \Big]. \tag{A.13}$$

The SNR of the incoherent array which is scaled given for a band limited signal power by the square root of the number of independent samples ($\Delta\nu\tau$). This leads to the result that,

$$\begin{aligned} \text{SNR} &= \frac{\sum_i \langle s_i s_i^* \rangle \times \sqrt{\Delta\nu\tau}}{\sigma(P)} \\ &= \frac{GS\sqrt{N\Delta\nu\tau}}{\sqrt{(GS + T_{\text{sys}})^2 + (N-1)(GS)^2}}. \end{aligned} \tag{A.14}$$

If the system noise dominates, i.e. $GS \ll T_{\text{sys}}$, for a minimum detectable flux $S_{\text{min}}$

$$\text{SNR} = S_{\text{min}} \times \sqrt{N\Delta\nu\tau} \times \frac{G}{T_{\text{sys}}} \tag{A.15}$$

i.e. for an array of identical antennas,

$$S_{\text{min}} = \frac{\text{SNR} \times \text{SEFD}}{\sqrt{N\Delta\nu\tau}}. \tag{A.16}$$

For dissimilar antennas, the above derivation obtains the SEFD of the combined instrument as $\sqrt{\prod_i \text{SEFD}_i}$ and therefore,

$$S_{\text{min}} = \frac{\text{SNR} \times \sqrt{\prod_i \text{SEFD}_i}}{\sqrt{N\Delta\nu\tau}}. \tag{A.17}$$

### A.1.2 Phased Arrays

In a phased array we sum individual voltages from the $N$ antennas and compute the expected power,

$$\langle P\rangle = \langle\sum_{i=1}^{N} v_i \sum_{j=1}^{N} v_j^*\rangle. \tag{A.18}$$

Expanding both voltage terms, we see that

$$\begin{aligned}\langle P\rangle &= \langle\sum_{i=1}^{N}(s_i+n_i)\sum_{j=1}^{N}(s_j+n_j)^*\rangle \\ &= \langle\sum_{i=1}^{N}\sum_{j=1}^{N}(s_i+n_i)(s_j^*+n_j^*)\rangle \\ &= \sum_{i=1}^{N}\sum_{j=1}^{N}\left[\langle s_i s_j^*\rangle + \langle n_i n_j^*\rangle\right].\end{aligned} \tag{A.19}$$

We have two cases, one where we have $N$ terms where $i=j$ and $N(N-1)$ terms where $i \neq j$ i.e. the signal from different antennas with a phase difference $\phi_{ij}$. We have for $i=j$ the power

$$\langle P\rangle = cN(GS+T_{\text{sys}}) \tag{A.20}$$

and for $i \neq j$,

$$\begin{aligned}\langle P\rangle &= \sum_{i=1}^{N}\sum_{j=1}^{N}(cGS\langle e^{i\phi_{ij}} + n_{ij}) \\ &= c(N(N-1)GS\langle e^{i\phi_{ij}}\rangle + N_{ij}).\end{aligned} \tag{A.21}$$

So for all $N$ antennas,

$$\langle P\rangle = c[N(GS+T_{\text{sys}}) + N(N-1)GS\langle e^{i\phi_{ij}}\rangle + N_{ij}] \tag{A.22}$$

Now we compute the variance of the power, $\sigma^2(P) = \langle P^2 \rangle - \langle P \rangle^2$. We have

$$\langle P^2 \rangle = \langle \sum_i v_i \sum_j v_j^* \sum_i v_i \sum_j v_j^* \rangle \tag{A.23}$$

i.e.,

$$\begin{aligned}\langle P^2 \rangle = &\langle \sum_i v_i \sum_j v_j^* \rangle \langle \sum_i v_i \sum_j v_j^* \rangle \\ &+ \langle \sum_j v_j^* \sum_i v_i \rangle \langle \sum_i v_i \sum_j v_j^* \rangle + \langle \sum_i v_i \sum_i v_i \rangle \langle \sum_j v_j^* \sum_j v_j^* \rangle.\end{aligned} \tag{A.24}$$

For zero mean gaussians the final term is zero. So we are left with

$$\langle P^2 \rangle = 2\big(\langle \sum_i v_i \sum_j v_j^* \rangle\big)^2 = 2\langle P \rangle^2. \tag{A.25}$$

Therefore,

$$\sigma^2(P) = \langle P \rangle^2 = c^2 \big[N(GS + T_{\text{sys}}) + N(N-1)GS\langle e^{i\phi_{ij}} \rangle + N_{ij}\big]^2. \tag{A.26}$$

The SNR ratio of the phased array which is scaled given for a band limited signal voltage by the square root of the number of independent samples ($2\Delta\nu\tau$) therefore

$$\begin{aligned}\text{SNR} &= \frac{\sum_i \sum_j \langle s_i s_j^* \rangle \times \sqrt{\Delta\nu\tau}}{\sigma(P)} \\ &= \frac{\big[(GS) + (N-1)GS\langle e^{i\phi_{ij}} \rangle + N_{ij}\big] \times \sqrt{\Delta\nu\tau}}{\big[(GS + T_{\text{sys}}) + (N-1)GS\langle e^{i\phi_{ij}} \rangle + N_{ij}\big]}.\end{aligned} \tag{A.27}$$

We can the cross-correlation of noise from different antennas very small $N_{ij}$ and that we have achieved perfect phasing of our antennas $\langle e^{i\phi_{ij}} \rangle = 1$ , and therefore

$$\text{SNR} = \frac{\big[(GS) + (N-1)GS\big] \times \sqrt{\Delta\nu\tau}}{\big[(GS + T_{\text{sys}}) + (N-1)GS\big]}. \tag{A.28}$$

We have two limiting cases. First, system noise dominates i.e., $GS \ll T_{\text{sys}}$,

$$\begin{aligned} \text{SNR} &= \frac{NGS \times \sqrt{2\Delta\nu\tau}}{T_{\text{sys}}} \\ &= \frac{NS_{min} \times \sqrt{\Delta\nu\tau}}{\text{SEFD}} \end{aligned} \tag{A.29}$$

i.e., the minimum detectable flux

$$\boxed{S_{\text{min}} = \frac{\text{SNR} \times \text{SEFD}}{N \times \sqrt{\Delta\nu\tau}}}. \tag{A.30}$$

The other limiting case where $N \times G$ tends to the forward gain of a single dish with the effective area $N$ times the effective area of the array feed, effectively giving us the radiometer equation of a single dish.

### A.1.3 Correlator

Finally we consider the summed power of correlated voltages,

$$\langle P \rangle = \sum_{i,j=1}^{N} \langle v_i \cdot v_j^* \rangle. \tag{A.31}$$

Taking the summation inside the integral we observe that the above expression is the same as what we began with for the phased array feed. A classical interferometer differs in practice since it discards autocorrelated power terms, however, modern instruments would like to preserve the power from individual feeds. Thus, despite the signal processing for a correlator and a phased array feed being different, a correlator that preserves the autocorrelation power has the same sensitivity as a phased array. For dissimilar antennas, the above derivation obtains the SEFD of the combined instrument as $\sqrt{\prod_i \text{SEFD}_i}$ and therefore,

$$S_{min} = \frac{\text{SNR} \times \sqrt{\prod_i \text{SEFD}_i}}{N\sqrt{\Delta\nu\tau}}. \tag{A.32}$$

### A.1.4 Other Systems

We can conjecture and prove the SNRfor identical N-element M-phased array feeds incoherently added scales as $N\sqrt{M}$ and $N$, $M$-element phased array feeds used as a phased array as $MN$ for the limit of the system noise dominating.

# B VLBI Localization Likelihood Function

Traditional VLBI usually concerns creating 'images' of the sky brightness. Several deeply mature methods have been developed. For localizing FRBs the key parameter we determine is just the source vector $\widehat{\mathbf{n}}$ defined by the right ascension and declination of the sky position of the FRB. It depends on just the geometry of the interferometer and is encoded in what is called the geometric delay $\tau_{\text{geo}}$. However the visibilities measure a delay, $\tau_{\text{measured}}$, which is decomposed as,

$$\tau_{\text{measured}} = \tau_{\text{geo}} + \tau_{\text{iono}} + \tau_{\text{clock}}\tau_{\text{inst}} + \epsilon, \tag{B.1}$$

where $\tau_{\text{clock}}$ can be determined using methods described in §4.3.2. Slowly varying instrumental and other delays $\tau_{\text{inst}} + \epsilon$ are corrected by employing a differential astrometric approach by dividing the measured visibility of the FRB by the visibility of a source whose sky position is a very well-known source which in our case is the Crab pulsar. Since these delays are in the phase of the visibilities they are nearly canceled out (see §4.3.4. We are now left with a measured differential delay that depends on the difference in the difference in dispersion measure due to the ionosphere at the time of the detection of the FRB and the difference in the geometric delay from the FRB position and the Crab pulsar, as

$$\tau_{\text{measured,FRB}} - \tau_{\text{measured,Crab}} = \tau_{\text{geo,FRB}} - \tau_{\text{geo, Crab}} + \tau_{\text{iono, FRB}} - \tau_{\text{iono, FRB}}. \tag{B.2}$$

For every baseline $i$ and every frequency index $k$ in our data this delay can be written as the phase

$$\phi\left[i,k\right] = 2\pi\nu_k \mathbf{b}_i \cdot (\widehat{\mathbf{n}} - \widehat{\mathbf{n}}_0)/c + 2\pi k_{\text{DM}}\Delta\text{DM}_i/\nu_k. \tag{B.3}$$

This phase can be used as a model to estimate the source vector $\widehat{\mathbf{n}}$ provided we know the position of the Crab pulse $\widehat{\mathbf{n}}_0$ and the prior distribution of possible $\Delta\text{DM}_i$ values. We use a maximum likelihood technique to determine this estimate.

If we assume our measured values follow a gaussian distribution,

$$\mathrm{prob}(\mathcal{V}) = \frac{1}{\sigma\sqrt{2\pi}}\exp\left[-\frac{(\mathcal{V}-\mu)^2}{2\sigma^2}\right] \tag{B.4}$$

then the sample mean statistic of the data is an estimator of the actual mean of the gaussian. For data drawn from a gaussian distribution will also have a gaussian distribution. Thus we can calculate the probability of the mean of the data given our data as,

$$\mathrm{prob}(\mathcal{V}|\phi) = \frac{1}{\sigma\sqrt{2\pi}}\exp\left[-\frac{(\mathcal{V}-\widehat{\mathcal{V}}_{\text{model}}(\phi))^2}{2\sigma^2}\right]. \tag{B.5}$$

We model our differential visibilities as the function of the phase $\phi$ in equation B.3 as

$$\widehat{\mathcal{V}}_{\text{model}}(\phi) = F(\phi\,[i,k]) + \text{noise} \sim A\,[i,k]\exp(i\phi\,[i,k]) \tag{B.6}$$

We can determine the posterior on the parameters encoded in the phase $\phi$ using Bayes theorem,

$$\begin{aligned}\mathrm{prob}(\phi|\mathcal{V}) &\propto \mathrm{prob}(\mathcal{V}|\phi)\times\mathrm{prob}(\phi)\\ &\propto \prod_i \frac{1}{\sigma\sqrt{2\pi}}\exp\left[-\frac{(\mathcal{V}-\widehat{\mathcal{V}}_{\text{model}}(\phi))^2}{2\sigma^2}\right]\times\mathrm{prob}(\phi)\end{aligned} \tag{B.7}$$

This posterior probability from Bayes theorem is called the likelihood function, so for every baseline '$i$' and frequency indices '$k$',

$$
\begin{aligned}
\mathcal{L} &\propto \exp\left[-\frac{1}{2}\sum_{i,k}\frac{||\mathcal{V}[i,k] - A[i,k]\exp(i\phi[i,k])||^2}{\sigma[i,k]^2}\right] \\
&\propto \exp\left[-\frac{1}{2}\sum_{i,k}\frac{||\mathcal{V}[i,k]\exp(-i\phi[i,k]) - A[i,k]||^2}{\sigma[i,k]^2}\right] \\
&\propto \exp\left[-\frac{1}{2}\sum_{i,k}\frac{Re\left(\left(\mathcal{V}[i,k]\exp(-i\phi[i,k])\right)^2 - A[i,k]^2\right) + Im\left(\mathcal{V}[i,k]\exp(-i\phi[i,k])\right)^2}{\sigma[i,k]^2}\right]
\end{aligned}
\tag{B.8}
$$

The amplitude of the model $A[i,k]$ is real. Since the phase information of the complex number is encoded in the imaginary part, for baselines CT and CA we have the log-likelihood function,

$$
\log\mathcal{L} \propto \sum_{i=\mathrm{CA,CT}}\sum_{k=0}^{1023}\mathrm{Im}\left(\mathcal{V}[i,k]\exp\left(-\mathrm{i}\phi[i,k]\right)/\sigma[i,k]\right)^2. \tag{B.9}
$$

Using equation B.3 and B.9 we can thus compute a posterior on the source vector $\widehat{\mathbf{n}}$ defined by the sky position of the FRB. Maximizing the likelihood function or minimizing the log-likelihood allows us to determine the localization of the FRB. This is an example of the maximum likelihood estimation. For localizing the FRB we calculate the posterior probably of equation B.9 given the sky location of the FRB by sampling the parameter space of the right ascension and declination using a markov chain monte carlo sampling method. This implementation is described in §4.3.4.